

MASTER OF SCIENCE THESIS



Aerodynamic Analysis Tool for Dynamic Leading Edge Inflated Kite Models

A Non-Linear Vortex Lattice Method

R.H.M. van Kappel BSc

31-10-2012

Faculty of Aerospace Engineering · Delft University of Technology



Aerodynamic Analysis Tool for Dynamic Leading Edge Inflated Kite Models

A Non-Linear Vortex Lattice Method

MASTER OF SCIENCE THESIS

For obtaining the degree of Master of Science in Aerospace
Engineering at Delft University of Technology

R.H.M. van Kappel BSc

31-10-2012

"When once you have tasted flight, you will forever walk the earth with your eyes turned skyward, for there you have been, and there you will always long to return."
Leonardo Da Vinci (1452-1519)



Delft University of Technology

Copyright © R.H.M. van Kappel BSc
All rights reserved.

DELFT UNIVERSITY OF TECHNOLOGY
DEPARTMENT OF
AERODYNAMICS - APPLIED SUSTAINABLE SCIENCE, ENGINEERING AND TECHNOLOGY

The undersigned hereby certify that they have read and recommend to the Faculty of Aerospace Engineering for acceptance a thesis entitled “**Aerodynamic Analysis Tool for Dynamic Leading Edge Inflated Kite Models**” by **R.H.M. van Kappel BSc** in partial fulfillment of the requirements for the degree of **Master of Science**.

Dated: 31-10-2012

Professor ASSET:

Prof. Dr. W. Ockels

Supervisor:

Dr. R. Schmehl

Aeroelastics:

Dr. Ir. S. van Zuijlen

Kite modeling:

PhD. J. Breukels

Summary

Kite Aerodynamics Airborne Wind Energy (AWE) systems operate at high altitudes, where wind velocities are higher in magnitude and more constant with respect to lower heights at which for example wind turbines operate. The ASSET department of the Delft University of Technology uses a concept which consists of a flexible Leading Edge Inflated (LEI) kite, which is connected through a tether to a drum on a ground station. By autonomously flying the kite in crosswind patterns, high tension forces in the tether cause it to be unwound from the drum, this mechanical energy is converted into electricity via a generator. This kite power system has the potential of becoming a new player in the wind energy sector.

The development of such systems creates a demand for kite models, which can be used to optimize the performance of tethered wings. By using aeroelastic models, which simulate the Fluid-Structure-Interaction (FSI), the flight dynamics of a flexible wing can be studied. In this thesis an aerodynamic analysis tool is presented, which can serve as part of a quasi-steady aeroelastic model for kites.

The New Tool The Vortex Lattice Method (VLM) and 3D panel method were identified as acceptable aerodynamic modeling methods with the best balance between model complexity and computation time. Because the tethered wings in AWE systems mostly fly at high angles of attack, close to stall, an extension is implemented. This extension corrects for the non-linear aerodynamic phenomena that occur at high angles of attack. A non-linear potential flow solver is used, where viscous corrections on both lift and drag are implemented by using airfoil data of the analyzed wing. The method combines the capability of a VLM and 3D panel method to incorporate effects of finite, non-planar wings with the capability of viscous airfoil analysis to predict non-linear effects, including stall. The method is implemented in an already existing analysis tool for airfoils, wings and planes, named XFLR5 which is programmed in C++. Several approaches within the method are considered where, with a trade-off validation procedure, the method with the best performance is selected.

Because the applied corrections in the method largely depend on viscous airfoil data, an investigation is performed on the single membrane airfoils used in LEI kites. Results are compared for high-fidelity 2D CFD simulations, the 2D integral boundary layer panel

method XFOIL and an existing polynomial regression model based on single membrane airfoil CFD simulations. The polynomial regression model is considered most promising, though improvements on the current available model could significantly increase accuracy of the non-linear methods. For the chordwise pressure distribution, an approach is given where XFOIL is used on-the-fly.

Results and Conclusion For analysis of LEI kites, the VLM has better performance than the 3D panel method. predicted aerodynamic loads with the new tool are more realistic than those from Breukels' method (Breukels, 2011), which is currently the most advanced aerodynamic load solver used for dynamic kite models. This is because the model incorporates effects of finite wings and has a higher flexibility in predicting chordwise pressure distributions.

The computation time for determining the aerodynamic loads of an LEI kite with the new approach is approximately 5 seconds, consisting of 96% for the determination of the chordwise pressure distribution with XFOIL. Less than 0.2 seconds is required for the non-linear VLM calculation. This tool can be incorporated in a FSI kite model to analyze pumping cycles and simulate load cases for kite design. For both applications a 60 second real-time simulation is required, this will cost roughly 19 hours of computation time. When a simpler chordwise load model is used, simulation times are reduced to 1 hour.

Regarding the performance of the developed software, it can be concluded that it has higher fidelity with respect to competitive aerodynamic methods used in dynamic kite modeling, while maintaining acceptable computation times. Therefore, the developed method is able to significantly increase the accuracy of the current FSI models that simulate flight dynamics and aeroelastic phenomena of LEI kites,

Concluding, it can be said that the developed method is very promising for future work and fosters a new generation of kite models that improve development of AWE systems. The applicability of the tool extends however much further than kites alone, as is shown by the variety of wing configurations in the validation cases.

Acknowledgements

Despite the somewhat difficult start of this project, where it was unclear for a long time what kind of model should be developed, it was a very good choice to graduate at this department. During this thesis my interest for kites, and especially for kite power systems, strongly grew. I really hope I can stay involved with this project and make kite power a success.

Now, I would like to thank a few people for their support during my research. Special thanks to Roland Schmehl, my supervisor, for guidance during the project and for bringing me in contact with persons of interest. Very helpful have been Rolf van der Vlugt, Aart de Wachter and John van den Heuvel, who provided guidance during my graduation project and gave both general and specific knowledge of the KitePower system. Also thanks to Wubbo Ockels for making the KitePower project possible and for passing out the combination of vividness and sustainability.

Furthermore, I would like to express my gratitude to Nando Timmer, Leo Veldhuis, Loek Boermans, Sander van Zuijlen for providing aerodynamic knowledge and material on the topic. Thank to Momchil Demchev for giving insight to xflr5 source code, Michiel Haanschoten with helping me using the computer cluster, Joost Schwoll for giving instructions on Rhinoceros and Ansys, Allert Bosch and Marien Ruppert for our continuous discussion on aeroelastic modeling of kites and Melvin Agten for the close collaboration during our project on developing the new tool. Thanks to management assistant Nana Saaneh for the organization within ASSET. Finally, I would like to thank Jelle Reichert for his practical insights and my brothers Eric and Marc for reading and checking the final report.

Delft, The Netherlands
31-10-2012

R.H.M. van Kappel BSc

Contents

Summary	v
Acknowledgements	vii
Nomenclature	xiii
1 Introduction	1
1.1 Kite aerodynamics	1
1.2 Research objectives	3
1.3 Research structure	3
2 Kite Power Systems	5
2.1 Fundamentals	5
2.1.1 Airborne Wind Energy	5
2.1.2 Traction power kite theory	10
2.2 The role of kite dynamics	12
2.2.1 System sensitivity to kite dynamics	12
2.2.2 Current and future kite design	15
2.2.3 Low and high resolution models	18
2.3 Simulating aeroelasticity of kites	18
2.3.1 Steady and dynamic aeroelastics	19
2.3.2 Solver types	19
2.3.3 Deformation models for kites	21
2.3.4 Aerodynamic models for kites	22
2.3.5 Aeroelastic models for kites	24
2.3.6 Computation time	26
2.4 Concluding remarks	27

3	Aerodynamic Analysis Methods	29
3.1	Available methods	29
3.1.1	Breukels' method	29
3.1.2	Potential flow methods	31
3.1.3	High-fidelity CFD	33
3.1.4	Selection	36
3.2	Background theory	37
3.2.1	Vortex lattice method	37
3.2.2	3D panel method	39
3.3	Software	40
3.3.1	XFOIL	41
3.3.2	XFLR5	42
3.4	Recap and introduction to a new aerodynamic method	43
4	Nonlinear VLM and 3D Panel Method	47
4.1	Implementing non-linearity by using lift correction	47
4.1.1	Effective angle of attack	47
4.1.2	Angle shift on lift curve	48
4.2	3D analysis methodology	49
4.2.1	Reference literature on lift correction methods	49
4.2.2	Determination angle shift: 3D panel method vs VLM	50
4.2.3	Implementation in XFLR5	50
4.3	Program features of the adapted XFLR5 software	55
4.3.1	Inviscid 2D lift curve	55
4.3.2	Trefftz plane calculations	55
4.3.3	Local effective angle of attack and Reynolds number	57
4.3.4	Implementation angle shift	57
4.3.5	Viscous drag calculation	58
4.4	Program settings	58
4.4.1	Grid discretization study	58
4.4.2	Boundary condition	58
4.4.3	Wake direction	59
4.4.4	Applying twist	60
5	Software Validation and Selection	63
5.1	Program versions	63
5.2	Reference data	64
5.2.1	Flat wing	64
5.2.2	Swept wings	65
5.2.3	Winglet configurations	67
5.2.4	Arc shaped kite	69

5.2.5	Model discretization in XFLR5	70
5.2.6	Airfoil data	70
5.3	Program trade-off	72
5.3.1	Procedure	72
5.3.2	Trade-off criteria	73
5.3.3	Trade-off results	73
5.4	Results of validation cases	76
5.4.1	Lift and drag coefficient	76
5.4.2	Improvement on original XFLR5	77
5.4.3	Spanwise distributions	81
5.4.4	Winglet configurations	81
5.4.5	Arc shaped kite	85
5.5	Software performance	93
5.5.1	Impact of number of iterations	93
5.5.2	Computational time	93
6	Aerodynamic Analysis of LEI Kites	97
6.1	Fluent grid and parameter study for 2D CFD analysis	97
6.1.1	Solver	97
6.1.2	Meshing	98
6.1.3	Boundary Conditions	102
6.1.4	Error and uncertainty analysis	102
6.2	2D Analysis of LEI kite profiles	108
6.2.1	Lift and drag curves	108
6.2.2	Chordwise pressure distribution	116
6.3	Simulation results of a LEI kite	123
6.3.1	DUT-MutinyV2 kite	123
6.3.2	Experimental data from flight test	123
6.3.3	Comparison of results	124
6.4	Computation times	130
6.4.1	Aerodynamic load solver	130
6.4.2	Estimation for the aeroelastic solver	131
7	Conclusions	133
8	Recommendations	135
	References	137
A	Power kites and their applications	145
A.0.3	Foil kites vs LEI kites	145
A.0.4	Sport kites	146
A.0.5	Kite propelled marine systems	148

B	Example of conventional kite design: 'designing the DUT power kites'	153
B.1	MutinyV1 25m ²	154
B.2	MutinyV2 25m ²	155
B.3	GenetrixV1 Hydra 14m ²	155
B.4	GenetrixV2 25m ²	156
C	Theory of aerodynamic methods	159
C.1	General theories	159
C.1.1	Kutta-Joukowski theorem and Kutta-condition	159
C.1.2	Vortex filament, Biot-Savart law and Helmholtz's vortex theorems	160
C.2	Thin airfoil theory	160
C.3	2D panel method	162
C.3.1	2D boundary layer correction	163
C.4	Lifting line theory	163
D	Airfoil section validation	165
D.1	NACA - 64 ₂ (A)015	165
D.2	NACA - 65 ₁ (A)012	166
D.3	NACA - 64 ₁ (A)612	169
D.4	NACA - 0012	170
D.5	NACA - 64-418	172
E	VLM/3D panel method validation	175
E.1	Flat wing	175
E.2	Swept wing AR5_012	178
E.3	Swept wing AR5_612	185
E.4	Swept wing AR10_012	190
E.5	Swept wing AR10_612	197
F	Simulation results final versions	203
F.1	Flat wing	203
F.2	Swept wing AR5_012	205
F.3	Swept wing AR5_612	208
F.4	Swept wing AR10_612	209
F.5	Arc shaped kite	211
G	Fluent mesh properties	213
	List of Figures	224
	List of Tables	225

Nomenclature

Latin Symbols

AR	Aspect Ratio	—
C_D	Drag coefficient	—
C_L	Lift coefficient	—
C_M	Moment coefficient	—
C_{D_i}	Profile drag coefficient	—
C_{D_p}	Profile drag coefficient	—
$C_{L_{max}}$	Maximum lift coefficient	—
D	Drag	N
e	Wing span efficiency	—
L	Lift	N
M	Mach number	—
n	Amplification factor	—
P	Power	W
Re	Reynolds number	—
S	Surface area	m^2
t	Thickness	—
TI	Turbulence level/intensity	—
V_∞	Freestream velocity	m/s
V_{app}	Apparent wind speed	m/s
V_C	Crosswind speed	m/s
V_L	Cable velocity	m/s

V_W	Wind speed	m/s
y^+	Wall distance	–

Greek Symbols

α	Angle of attack	rad
α_s	Angle shift	rad
α_∞	Freestream angle of attack	rad
α_{eff}	Effective angle of attack	rad
α_i	Induced angle of attack	rad
α_{twist}	Twist angle	rad
β	Sideslip angle	rad
Γ	Dihedral angle	rad
κ	Camber	–
μ	Dynamic viscosity	Ns/m^2
ν	Kinematic viscosity	m^2/s
ω	Downwash	m/s
ρ	Density	kg/m^3
φ	Velocity potential	m^2/s

Abbreviations

ASSET	Applied Sustainable Science Engineering and Technology
AVL	Athena Vortex Lattice
AWE	Airborne Wind Energy
BC	Boundary Condition
CFD	Computational Fluid Dynamics
CSD	Computational Structure Dynamics
DES	Detached Eddy Simulation
DNS	Direct Numerical Simulation
DoF	Degrees of Freedom
DUT	Delft University of Technology
FEM	Finite Element Method
FSI	Fluid-Structure-Interaction
FVM	Finite Volume Method
HAWP	High Altitude Wind Power
IMU	Inertial Measurement Unit

KCU	Kite Control Unit
LEI	Leading Edge Inflated
LES	Large-Eddy Simulation
LLT	Lifting Line Theory
MAC	Mean Aerodynamic Chord
MAD	Mean Absolute Deviation
MAPD	Mean Absolute Percentage Deviation
OFAT	One-Factor-at-A-Time
RANS	Reynolds-Averaged NavierStokes
RHS	Right-Hand-Side
RMS	Root-mean-square
TAT	Thin Airfoil Theory
TI	Turbulence Intensity
VLM	Vortex Lattice Method

Introduction

1.1 Kite aerodynamics

Though kites date back to 3000 years ago, there have been many recent developments in the performance and application of kites. Mostly they are regarded as toys and sport devices: kites are used on sailboats, for skydiving, parasailing and in the Olympics of 2016 kitesurfing will even replace windsurfing (BBC, 2012). The use for these kind of applications demonstrates that kites can generate high forces, e.g. sail speeds records were broken and freestyle kiteboarders jump many times higher and longer than any wind surfer.

Kites serve well for recreational purposes, but can also be used to save on fuel or generate clean energy. Opposed to wind turbines, which are structurally limited to altitudes of 200 meters, kites can harvest wind energy at high altitudes where wind is stronger and more continuous. By flying these light-weight structures crosswind the apparent wind speeds can easily increase by a factor of five (Heuvel, 2010). As forces scale quadratically with speed they become 25 times higher (Loyd, 1980). The principle of crosswind is also used in wind turbines where the rotation of the blades increase apparent wind speeds. However, only the tips of the blades experience high speeds and as a results the outer most 20% of a rotor blade generates more than 50% of the power. The rest of the blade serves more as a support structure and is far less efficient. In a kite power system the kite acts as the efficient high speed rotating tip where the traction power is transferred via cables to a generator on the ground, replacing the need for a hub in the air, see Figure 1.1. The principle of traction kites is already used to provide propulsion for large container ships where it can replace up to 2MW from the main engine, which allows it to save up to 35% on fuel (SkySails, 2012a). Currently, there are several institutions developing systems which use crosswind flying kites to generate clean wind energy, one of them is the KitePower Group at the ASSET institute of Delft University of Technology (DUT). This system connects the kite to the ground by a single tether and, even though it is a demonstration system, the kite can already go up to 1000m.

The core element of producing power with a kite comes from its capability of extracting kinetic energy from wind, which can be converted into mechanical power. In this process the achievable aerodynamic wing loading plays a key roll. To make kite power systems commercially attractive, the performance of the tethered wing should be optimized.

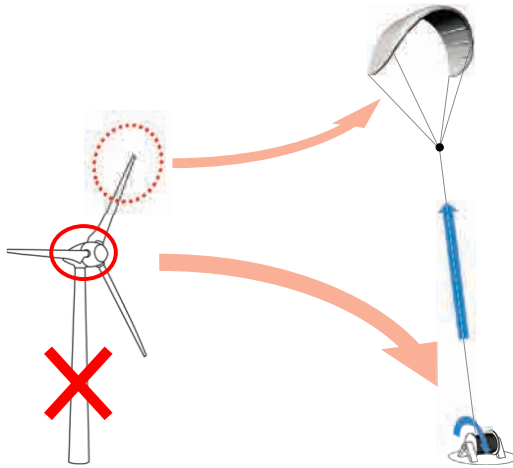


Figure 1.1: A kite power system can be seen as an evolution of a wind turbine (Schmehl, 2012b).

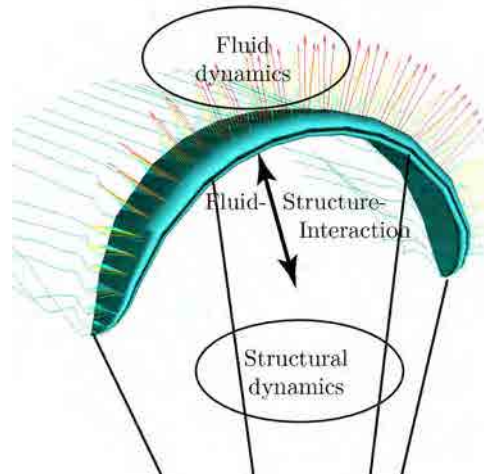


Figure 1.2: Aeroelastic models are required to capture the interaction between fluid and structural dynamics.

The study of kite aerodynamics is challenging, because the inflatable membrane wing is lightweight and very flexible and the shape deforms due to the interaction of aerodynamic wing loading on the one hand and discrete line forces and internal structural forces on the other hand. Its low inertia and flexibility make the behavior of the tethered wing very sensitive to control commands, variations in apparent wind velocity and changes in geometry. By using aeroelastic models, which simulate the Fluid-Structure-Interaction (FSI) as shown in Figure 1.2, the flight dynamics of the complete wing can be studied. Simulation of the flight dynamics is important for autonomous controller development and optimization of system components, but also to serve as basis for the kite design process.

To model this aeroelastic behavior constant evaluation of the aerodynamic forces is required, and thus software should be available capable of determining the aerodynamic loads in a very short time frame. In this report such a tool is presented, which can be used to improve and develop aeroelastic models of kites. Though there exist numerous aerodynamic analysis methods, there is a growing demand for one capable of handling kite shapes, which differ in a great extent with those used for aircraft. In the current KitePower system the wing has inflatable tubes and its planform shape is strongly curved in both chord and spanwise direction, as depicted in Figure 1.2. The combination of a round inflated tube and single membrane canopy result in unique profile shapes, which make the prediction of aerodynamic forces even more complex.

Because of the growing kite industry and the potential of kites power systems to be a new player in the wind energy sector, the development of aeroelastic kite models is of great importance. Improving these models will make it possible to more accurately predict flight behavior and bring kite and kite system design to a higher level.

1.2 Research objectives

The research goal of this thesis is formulated as follows:

To develop a model, which predicts the aerodynamic loads within the framework of aeroelastic simulations of leading edge inflated kites.

This project goal implies an investigation of the specific demands for aerodynamic kite models, where computation time and accuracy will play major rolls. Since kites are highly deformable the validation of such a tool brings difficulties, since the shape of a kite and its corresponding load distribution is hard to determine in measurements. Validation is however necessary to see if we get closer to imitation of real kite behavior.

1.3 Research structure

In order to achieve the research goal in an efficient way the process is split into three parts, each consisting of several elements.

The first part starts with a preliminary study on kite systems discussed in Chapter 2. It is explained how these systems work and what the role is of kite dynamics. Current literature on already performed research on dynamic kite models is consulted. In Chapter 3 a selection is made between available aerodynamic analysis methods based on the criteria for aeroelastic kite models. The selected methods will serve as a basis for the new developed method.

The second part of this thesis outlines the development and validation of a new aerodynamic analysis software tool applicable to aeroelastic kite models. In Chapter 4 the theory behind the method is described and how this is implemented in the software. Chapter 5 makes a trade-off between variants of the method, for which validation with experimental data is used.

The third part, Chapter 6, deals with the difficulties when applying the new tool to leading edge inflated kites and simulates the model of an

Finally, chapter 7 gives conclusions and recommendations on the developed tool and it is checked whether the research goal is achieved.

Kite Power Systems

2.1 Fundamentals

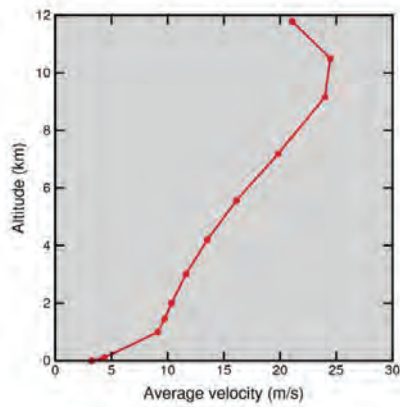
The goal of a kite power system is to: 'Harvest wind energy with kites in a sustainable manner and offer it against a competitive market price.' From this goal it follows that performance should be defined as having high power output and low cost. When striving for high performance, boundary conditions should be met. It is the nature of human beings to *sustain* themselves, and to ensure our offspring can continue to live on earth, our energy use should be sustainable as well. This way an important boundary condition is set on the system.

2.1.1 Airborne Wind Energy

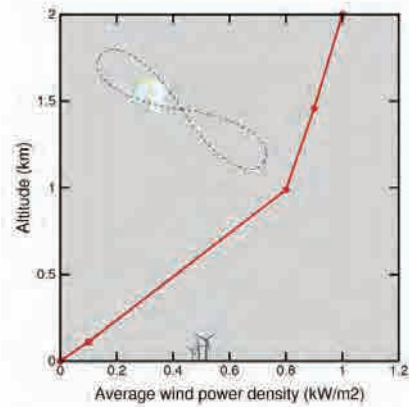
A relatively new field of research is electricity generation with flying devices, called Airborne Wind Energy (AWE). One advantage of using airborne devices is the fact that at higher altitudes wind is stronger and more consistent (also known as High Altitude Wind Power HAWP) as can be seen in Figure 2.1. Wind power scales cubically with speed, that is: $P \sim V^3$ (Loyd, 1980) and therefore these high altitude winds offer huge potential to the energy market. HAWP is impossible to access with conventional wind turbines, since they require a supporting tower and are, due to their own weight and high loads, restricted to a certain height.

AWE concepts

There are several ideas how to exploit these high altitude powerful winds, for example using a wind turbine tethered to the ground by a conductive cable to transport the generated energy (Cohn, 2006). A variant on this idea is currently investigated by the American company 'Makani Power', which additionally uses crosswind flying with a tethered wind turbine (Makani, 2011), seen at the left of Figure 2.2. In the right picture the 'Laddermill' concept developed by Ockels (Ockels, 2001) is visualized. In his concept multiple kites are stacked and connected by a tether, which form a large loop. By controlling the pitch of the kite one side of the loop generates more lift than the other side: the loop starts turning and when connected to a generator on the ground it generates energy.



(a) Wind speed at high altitude



(b) Wind power density at high altitudes.

Figure 2.1: High altitude wind power in The Netherlands (*KitePower*, 2012).

(a) Makani M1



(b) Laddermill

Figure 2.2: Two airborne wind energy kite concepts of which the Makani M1 is a rigid kiteplane with generators on board (Makani, 2011) and the Laddermill consists of flexible kites with a generator on the ground (*Laddermill Kites Wind Energy*, 2011).

Currently the most explored concept in AWE is the use of tethered wings where the kinetic energy of the moving tether is converted to electrical energy at the ground. Though there are universities and companies which use rigid wings (Sieberling & Rüterkamp, 2011), see Figure 2.2b, mostly kites are used in currently investigated AWE concepts. Kite powered energy generation has advantages and disadvantages compared to conventional wind turbines (Baldwin, 2008; Bonne, 2010):

- Less material is required to obtain the same amount of energy, mainly because no supporting tower is required. This makes the system lighter and cheaper in many applications.
- They can access wind at higher altitudes, therefore higher capacity factors (easily 60%) and relatively more energy generation can be achieved.
- Easy deployment in remote areas.
- Lower environmental footprint.
 - Less material is required.
 - Reduced visual impact since kites are smaller and fly higher.
 - Reduced acoustic impact; the most significant (or even only) contribution heard on the ground originates from the winch and flow moving past the tether, which is far less than noise from rotating blades.
 - Because kites are smaller, less bird hazards will occur.
- Less experience and far fewer reliability data.
- The airspace (and possibly ground area) required is larger.
- When a cyclic power generation is used (see Section 2.1.1), power output is interrupted and thus either buffers or multiple out-of-phase kites are required.

The structure of a kite system is much cheaper than for wind turbines, but the maintenance costs for kite systems might be higher due to for instance the replacement of kites, batteries and tethers. It is hard to accurately predict costs and benefits for kite powered energy generation and therefore not much is known yet about the economic viability of these systems (Hassan, 2011). All AWE concepts are still under development and not yet commercially available. It is also not yet known which of these concept(s) will survive; more research is required to see how they compete economically and environmentally with conventional energy sources and wind turbines.

Pumping kite at DUT KitePower

One of these kite power energy concepts is the **pumping cycle technique** of the 'KitePower' research group (DUT) from the Applied Sustainable Science Engineering and Technology (ASSET) department. This research group originates from the Ladder-mill concept, but already soon it became clear that controlling and understanding the behavior of a single kite is already quite complex. Therefore the research group decided to focus on a single kite system, which uses mainly crosswind as the power source.

Crosswind is induced by flying the kite in optimized trajectories perpendicular to the direction of the wind, which (depending on system and operation parameters) look roughly as asymmetrical Figures of 8 (Diehl & Houska, 2009). Flying crosswind easily increases the apparent wind speed of the kite and substantially increases the aerodynamic forces, lift and drag, which depend on the square of the relative wind velocity that the

kite experiences. Crosswind speed is generally much higher than wind speed, typically up to 5 times as high depending on kite performance, therefore it is the core contribution to power in kite propelled marine systems (Appendix A) and most kite energy generating systems. In the next section, the mathematical foundation of crosswind power is given. At the moment, DUT KitePower uses symmetrical Figures-of-eight for crosswind flying; this is not proven to be a most efficient path, though it shows quite some resemblance with the path determined by Diehl & Houska (2009) and was also proposed by Furey & Harvey (2008) and Williams et al. (2008). This pattern does not result in flying excessively close to the ground and thus a certain safety perimeter from the ground is maintained. Further it has the advantage of being a simple shape, thus making it more easy to control. In higher level control this path should be optimized such that the overall power in time is maximal.

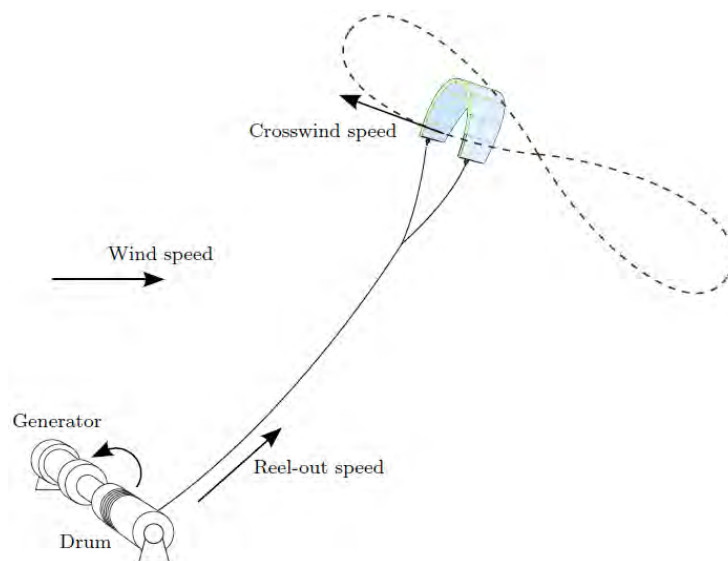


Figure 2.3: A pumping kite system using crosswind by flying Figures-of-eight (Groot, 2010).

In June 2012 the DUT KitePower group officially demonstrated their 20kW prototype system. In this system wind energy is, via mechanical energy, converted into electrical energy by means of pumping cycles. These cycles consist of a reel-out or traction phase and a reel-in or retraction phase. During reel-out phase the kite flies crosswind Figure-of-eight patterns (Figure 2.3) to obtain high traction forces. This way the tether is pulled from a drum where a winch automatically regulates the force and speed. As a consequence the drum is rotating and driving an electrical generator. At a certain height or tether length the kite is depowered: by changing the length of the front and rear lines the pitch angle becomes lower and as a result the traction force decreases, see Figure 2.4. Now the generator on the ground is used as a motor and starts to reel-in the tether until a certain height is reached. This way the kite is pumping up and down and theoretically could continue forever. Although the reel-in phase will cost some energy, there is a significant netto energy gain in the whole pumping cycle, as shown by real test data in Figure 2.5. Storage capacity is provided by batteries and could also function as a buffer to equalize output energy over time.

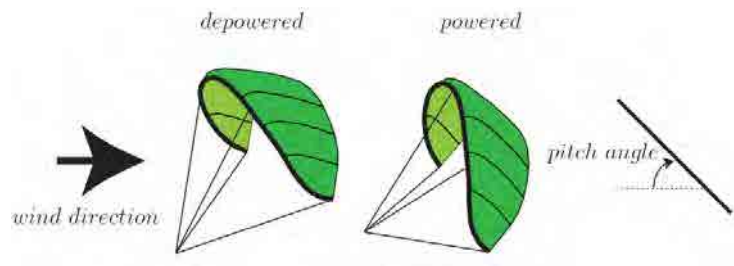


Figure 2.4: Powering and depowering of the kite by changing the pitch angle resulting from a difference in lengths of the steering lines and power lines (Bosch, 2012a).

A custom-made Leading Edge Inflated (LEI) kite (more on kite design in Section 2.2.2) with a surface area of 25m^2 generates the traction force and is fully automatically controlled by an autopilot algorithm. The control pod, or kite control unit (KCU), is suspended about 10m below the kite incorporating two small but strong motor winches for steering and depowering of the wing. This way it makes it possible to only use one line between the kite plus controller and ground station therefore reducing tether drag. It has two redundant wireless connections to the ground station and if necessary the KCU can be manually controlled. The KCU increases the weight of the flying system making it less efficient. However it improves safety and stability since it functions as a stabilizing weight in depowered flight, by shifting the center of gravity far below the kite.

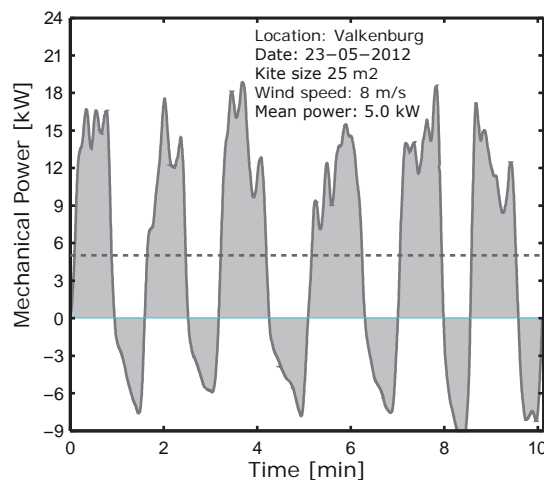


Figure 2.5: The power production of six consecutive pumping cycles with the 20kW prototype system (Bosch et al., 2012).

The prototype is a 20kW system, but during demonstration peak values went as high as 34kW. The nominal average cycle power is 4kW. During reel-out the flight velocity of the kite is between 70-90km/h with cable forces between 250-400kg. In the reel-in phase this force can be lowered to 60kg at a reel-in speed of 5m/s. The maximal cable length is 1000m resulting in a height of the kite of about 850m. Depending on wind speed this system could provide 12-18 households. Such a system could be scaled up and as with

wind turbines possibly MegaWatt systems could be build. (Schmehl, 2012a)

2.1.2 Traction power kite theory

The aerodynamic performance of a kite is mainly determined by the forces it can generate. These forces depend on the kite's inertia, orientation, motion, free stream properties and wing configuration, which are discussed shortly.

The *inertia* of a kite is significantly lower than a rigid aircraft, because of their light-weight structures. Momentum caused by aerodynamic and cable forces are in many cases much larger than the resistance of the kite to a change in motion. Inertia of the kite might become important when steering maneuvers are performed at low speeds.

Orientation of kites is defined according to reference frames that are found in basic flight dynamics theory. It is extensively discussed by Groot (2010) and Terink (2009). The orientation defines in which direction the kite is pointing with respect to a predefined reference frame. With orientation known it can be determined what the angle of attack α and slide slip angle β are; these are the angles between the wing and apparent wind speed, see Figure 2.6.

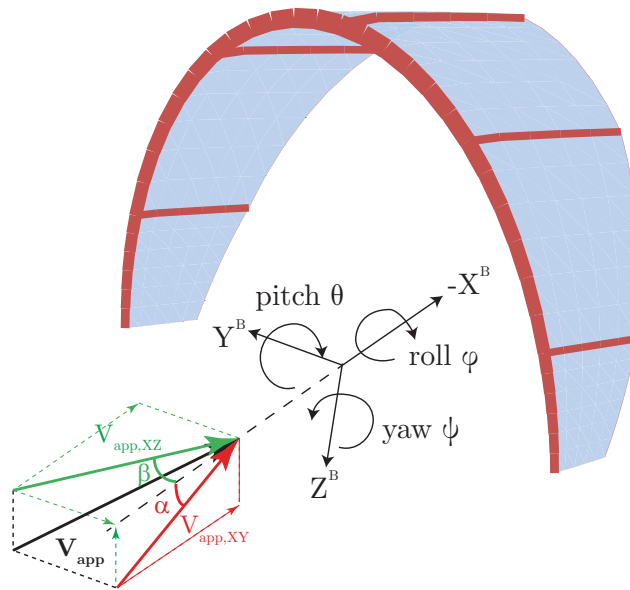


Figure 2.6: Definition of angle of attack and slide slip angle in the body-fixed reference frame.

The apparent wind speed V_{app} of a kite is dependent on wind speed V_W , cable velocity V_L and crosswind speed V_C . The idea of using *crosswind* motion to increase the force in the tether originates from Loyd (1980). Moving in the plane normal to the wind direction allows the apparent wind velocity to become (many times) larger than the wind velocity itself. Since the force in the tether is approximately proportional to the square of the apparent wind velocity, this crosswind motion causes a strong increase in tether force. From the free-body-diagram in Figure 2.7 it follows that for a weightless kite going

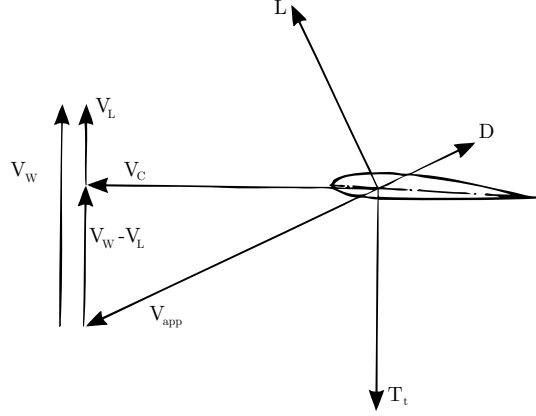


Figure 2.7: Forces and velocities on a kite in crosswind motion (Breukels, 2011).

through the point of maximum power:

$$V_{app} \approx V_C = (V_W - V_L) \frac{L}{D} \quad (2.1)$$

where a massless tether with zero drag, constant uniform wind and steady flight is assumed. Lift L and drag D are the forces in respectively perpendicular and parallel direction to the flow and are defined as:

$$L = C_L \frac{1}{2} \rho V_{app}^2 S \quad (2.2)$$

$$D = C_D \frac{1}{2} \rho V_{app}^2 S \quad (2.3)$$

where C_L and C_D are respectively the lift and drag coefficient, ρ is the air density and S the projected surface area of the kite. Lift and drag coefficients are mainly dependent on angle of attack, Reynolds number and wing configuration. The drag coefficient can be defined as:

$$C_D = C_{Dp} + C_{Di} \quad (2.4)$$

Profile drag C_{Dp} is drag due to the form of a body (pressure drag) and due to the friction of the surface (skin friction drag). Induced drag C_{Di} is drag due to lift and is given by:

$$C_{Di} = \frac{C_L^2}{\pi A R e} \quad (2.5)$$

where AR and e are respectively the aspect ratio and wing span efficiency (or Oswald factor) of the wing. Loyd (1980) assumes that lift L and traction force T are approximately equal in magnitude:

$$T \approx L = C_L \frac{1}{2} \rho S (V_W - V_L)^2 \left(\frac{L}{D} \right)^2 \quad (2.6)$$

Loyd (1980) then determined that the power produced by a kite unwinding a tether on a drum is given as:

$$P = T \cdot V_L \approx C_L \frac{1}{2} \rho V_W^3 S \cdot F \quad (2.7)$$

where F in the case of crosswind is given by:

$$F_{crosswind} = \left(\frac{L}{D}\right)^2 \left(\frac{V_L}{V_W}\right) \left(1 - \frac{V_L}{V_W}\right)^2 \quad (2.8)$$

Argatov et al. (2009) derived the same formulas only included centrifugal and gravity forces and tether weight and drag. He shows by example that these effects are typically less than 1% on the optimum reel-in speed. The maximum value of the relation in Equation 2.8 is $F_{crosswind,max} = \frac{4}{27} \left(\frac{L}{D}\right)^2$ with a corresponding cable speed of $V_L/V_W = 1/3$. For fixed lift coefficient the lift to drag ratio L/D is the parameter to maximize to extract the most energy in crosswind motion. From equation 2.7 and 2.8 and using that $L/D = C_L/C_D$ it follows that the generated power of a crosswind flying kite is proportional to:

$$P \sim \frac{C_L^3}{C_D^2} \quad (2.9)$$

Therefore in general C_L^3/C_D^2 is the parameter to maximize to obtain maximum power generation.

An important flow characterizing variable for wings is the Reynolds number Re :

$$Re = \frac{\rho V l}{\mu} \quad (2.10)$$

It is a dimensionless number containing flow velocity V , density ρ , viscosity μ and a characteristic length of the wing l . Reynolds numbers give a measure of the ratio of inertial and viscous forces. The Mach number M determines the amount of compressibility of the flow. For kites Mach numbers are low: $0 \leq M \leq 0.3$. In this region flow is considered incompressible.

2.2 The role of kite dynamics

When developing a kite power system, it should be clear what the system and its components should do to reach the objectives. In this section the role of kite dynamics with respect to system design and optimization is given. The interdependencies between kite dynamics and other system components are discussed. Next to this, the kite design process is considered, since high level engineering kite design is required to maximize aerodynamic performance. Finally, the role of using low and high resolution kite models is discussed.

2.2.1 System sensitivity to kite dynamics

The aerodynamics of the kite are critical in the system: it is the only power input of the system, everything else can be considered as waste. To obtain high power output, high power input is required with low loss. Therefore high system performance can be defined as having a large amount of aerodynamic power versus a low waste for supporting components. This waste consists of material use, power losses, system support, but also restrictions due to regulations and safety can set limits on performance.

In the previous section a description of the KitePower prototype system was given, for which a more elaborate visualization is given in Figure 2.8. For optimal performance

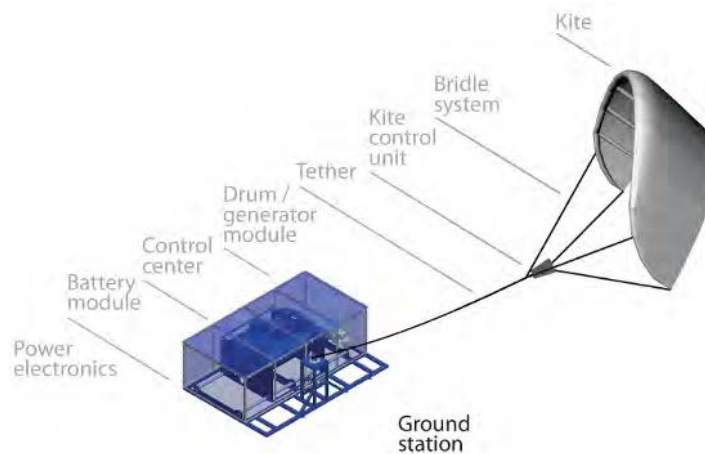


Figure 2.8: System layout of the current system at DUT KitePower (*KitePower*, 2012).

the right balance between power output and cost should be found. This is determined by the sensitivity and impact of the system components. When for instance a larger kite is used to generate more power, other components need to be upscaled as well: the tether and support structure should be stronger and the winch and electronics should become more powerful. When it is known how each component reacts on changes somewhere else in the system, an optimal design can be found.

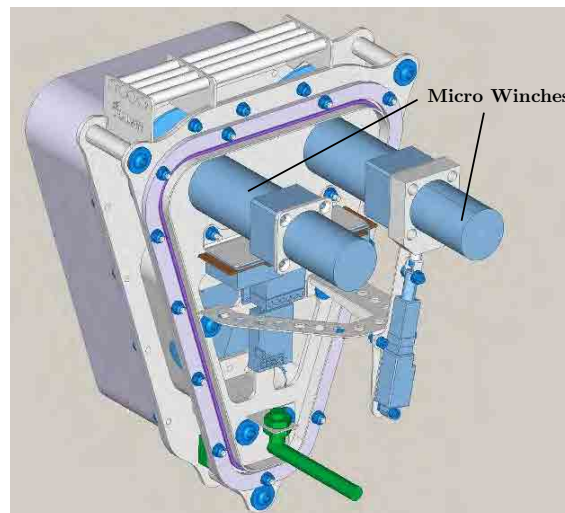
This thesis puts a focus on the aerodynamics of the kite and it is therefore of critical importance to understand the sensitivity of each component to the dynamic behavior of the kite. For convenience, this behavior is split up in global and detailed dynamics: global dynamics give an indication of the average, minimum and maximum forces during flight, while detailed dynamics determine how exactly the kite deforms and what the forces are on a much smaller scale. The system component sensitivity to these two types of kite dynamics are given in Table 2.1.

The table clearly shows that all components are highly dependent on the global dynamic behavior of the kite, which follows from the fact that the generated aerodynamic power is the only input to the system and is therefore of critical importance for the rest of the system. The detailed dynamics have however small influence on tether design and ground station components, except for the kite controller. The kite controller determines the ability of the kite to fly a desired trajectory and to accurately control the kite, detailed information should be known on kite behavior. When the kite can accurately fly a desired, optimized path, the cycle efficiency increases. The bridle system is the component closest to the kite and is therefore strongly dependent on the local forces during flight. The core component of the KCU are the steering and depower motors or micro winches. These should react fast and efficient to the dynamic behavior of the kite. Mainly the maximum force and speed determine the type of micro winch. The power supply of these micro winches is provided by batteries in the KCU. Accurately knowing the dynamics of the kite, such that steering and depower forces can be determined, makes optimization of the KCU possible. This could reduce power supply by 50% and lifetime by a factor 4, according to Fechner (2012).

Table 2.1: System sensitivity to kite dynamics of the KitePower prototype system.

Component	Sensitivity to changes in:	
	global dynamics	detailed dynamics
Bridle system	high	high
KCU hardware	high	medium
Tether	high	low
<i>Ground station:</i>		
Drum/generator module	high	low
Power electronics	high	low
Winch controller	high	low
Kite controller	high	medium/high
Support structure	high	low

Other key factors to the success of the system are safety and reliability. When a kite breaks or collapses, most likely it becomes uncontrollable and will crash. As a result reparations and replacements are required, but also surrounding objects can get damaged. These could be other kite systems, but when placed in urban areas also humans could get in danger. With accurate knowledge about kite dynamics, safe and reliable kites could be designed and hazards can be avoided.

**Figure 2.9:** The KCU without protection cover shows that the micro winches greatly determine the size of the pod (*KitePower*, 2012).

2.2.2 Current and future kite design

During power cycles the kite should generate high traction forces, have large depower to minimize forces during reel-in, have high maneuverability and it should be stable. Opposed to rigid kites, such as the Ampyx PowerPlane given at the left of Figure 2.10, inflatable membrane wings are highly flexible, which makes design a challenging task. Currently, most flexible kites for energy generation are designed in a similar way as commercial sport kites. This manner of design process is explained, after which a vision on future kite design is given.

Current kite design

The design of highly flexible kites is not a highly structured design process as it is with aircraft design. Just as in the beginning of aircraft design, design information for kites is mostly provided by basic knowledge of analytic theory combined with a fair amount of experimentation. Kites are designed and improved by adaptations on current kite designs of which the designer thinks that they could be of positive influence on the required performance.

The following information on kite design is obtained from Pealinck (2012), working at the R&D division of the foil kite manufacturer Flysurfer. After only 2-3 days of making design adaptations with the use of a computer, the production recommendations are documented. Then it takes 2 weeks to produce the kite, continued by 1 week of testing and optimizing. In total a prototype life cycle is about one month. This process can be done simultaneously for 2 kites, resulting in the manufacturing of approximately 25 prototypes per year with 2,5 full-time developers. Then after several years, a handful designs are launched on the market.

To see the independent effect of each design adaptation, it is tried to only vary one aspect of the design. Their design is then tested and evaluated and, when not satisfied, adapted again. This procedure repeats itself until the designer is satisfied or out of resources. There are good reasons why kite design is performed in this way and not by using complex models and analysis tools. The dynamic behavior of kites is such a complex process, it is very expensive and time consuming to develop a suitable FSI solver for kite design. It already took many years of PhD and Master thesis' to arrive at the current state of dynamic kite models, and the most advanced design tool (Breukels, 2011) currently available has still too strong limitations with respect to flexibility, bridle design and user-friendliness (and possibly) accuracy. The development of a suitable design analysis tool is just too expensive for a commercial company. In the currently used trial and error process the designer slowly gains more knowledge on flow and kite behavior. This process depends however largely on the skills and experience of the designer. Moreover, observing if the kite operates better after a design adaptation is the only measure for a designer and it does not necessarily mean you will know which aerodynamic or aeroelastic phenomena are causing the desired effects. It is then difficult to predict on the performance of future designs.

Finding a highly optimized design with the current design process is highly implausible: only a few test models can be build and tested due to limited resources and therefore it is difficult to know how optimal a design is. Just as a Darwinian process one could argue kite design slowly converges to an optimum in time. However the process of natural selection could take up to thousands of generations before closing in to an optimum.

Next to this, current kite designs mainly originate from sport kites. As sport kiting is mostly recreational, it favors those designs which are economically most favorable and that does not necessarily mean the design has optimal performance since also other factors play a role in the buyer's choice. Furthermore different applications each have their own optimum design, therefore requiring their own selection process. The trial and error procedure used in the current process is just not sufficient to find a kite with engineering level performance.

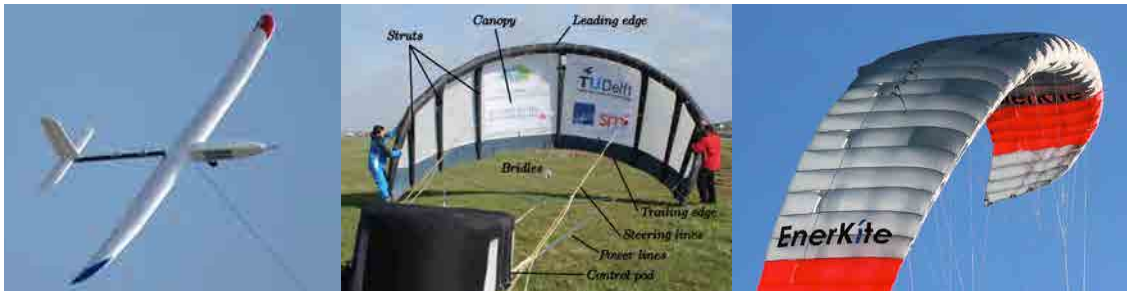


Figure 2.10: Left: Prototype of the 10kW PowerPlane design (LabS55, 2011). Middle: DUT-MutinyV2 LEI kite (Bosch, 2012a). Right: Ram-air wing of EnerKite (EnerKite, 2012).

In Figure 2.10 examples of the three main type of kites are depicted, including rigid, semi-rigid and flexible wings. LEI kites are semi-rigid, because they are reinforced by inflatable tubes. Ram-air kites, or foil kites, have almost no rigidity, but generally have higher L/D ratio.

Next to the geometry of the wing, the dynamics of the kite are strongly influenced by the configuration of the lines and bridle system, see Figure 2.11. Bridle design is therefore an integrated part of the kite design process. The bridle system balances the local forces in the kite by a collection of smaller lines and redirects them to the power and steering lines. It gives rigidity to the kite by setting constraints to local deformations and should minimize stress concentrations. Power lines are lines at the front of the kite through which the greater part of the generated pulling force of the kite is transferred to the pilot or system on the ground. Steering lines are the rear lines connected to the tips and control the angle of attack of the kite. Increasing the angle of attack is called powering since it results in high loading of the wing. When increasing the angle of attack, the flow cannot stay attached anymore and flow separation becomes more dominant and eventually the wing will stall causing a drop in lift and increase in drag. This is very unfavorable for aerodynamic performance and the wing can even become uncontrollable. Decreasing the kite's angle of attack is called depowering and results in low force. The capability of a kite to depower is an important feature: it determines safety and power cycle efficiency in energy generation applications (Heuvel, 2010).

In Appendix B an extensive description is given on the conventionally designed LEI kites that are used at DUT KitePower and more can be found on depower and bridle design.

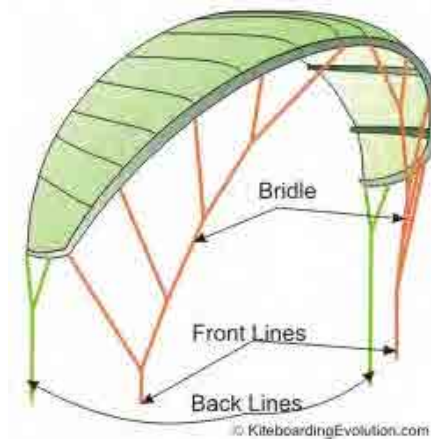


Figure 2.11: The bridles and lines of a LEI play an important part in the dynamic behavior (Slingshot, 2009).

Future kite design

Now the era of sustainable power generating kites has begun the current kite design process demands for a revolution. As showed in the previous section conventional kite design is relatively slow, unstructured and does not result in highly optimized designs and detailed understanding of fluid-structure interaction. With a growing demand for high performance kites the design process requires methods capable of accurately determine aeroelastic behavior within acceptable resources. Enhancing our understanding of fluid-structure interaction expands our ability to predict kite behavior. With the advent of the digital computer and the fast development of the field of numerical analysis, a variety of complex calculation methods have become available to the designer. With high-fidelity computer models it is possible to develop a detailed understanding of the dynamic kite behavior to support the design process.

Multiple phases can be distinguished when flying a power kite, each involving a different state of deformation and aerodynamic forces. In order to analyze the aerodynamics of all these phases a fast and accurate tool is required. Around 12 load cases are used when testing new designs, each consisting of ± 5 seconds during maneuvers (Pealinck, 2012). This results in:

$$\text{effective test time} \approx 12\text{load cases} \times 5\text{sec} = 60\text{sec} \quad (2.11)$$

If now real test flights could be replaced with simulations, one can only imagine the possibilities. The entire process of drawing the design, making a design ready for production, two weeks of waiting on the product and one week testing and optimizing, can be replaced by drawing, fast simulations and redrawing on the computer. Assuming 4 years (last three years Flysurfer did not commercialize new designs) required for making and evaluating about 25 prototypes per new design product could be reduced to a fraction.

The current knowledge of kites is limited and still many aspects of kite design should be investigated. Making CFD and FEM calculations has very high information value, but are simply to time consuming to efficiently find high performance designs. A tool is needed that can quickly give results on how a kite performs when adaptations are made to

airfoil shapes, aspect ratio, planform shape, spanwise camber and bridle design. Having such a tool will result in evaluation of more designs in a shorter time frame and ultimately increases competitiveness and lowers design and production costs.

2.2.3 Low and high resolution models

Design and optimization should always be about the performance of the entire system, therefore the dependencies within the system require constant evaluation. It is critical to have models which can quickly evaluate the effect of any change in the system on the performance. In other words, modeling is required to close in to an optimum system as soon as possible. However, when models increase in complexity, they tend to get slow. The art of design and optimization is to find a proper balance between the use of low and high resolution models to close in to an optimum as fast as possible.

Though you would like to model the whole system at once, it is often not efficient to do so. With low resolution models you get an impression of how the entire system, or at least a part of it, will look like. Then this part can be isolated and higher resolution models can be used for optimization. For instance, from the low sensitivity between the detailed dynamic behavior of the kite and the ground support structure follows that for detailed design of the support structure no high resolution dynamic kite models are required.

Low resolution models are used at least in the beginning of a project, as part of larger models and possibly later as baseline for more complex models. These models have little degrees of freedom, but they are fast and therefore many possible combinations of model components can be quickly evaluated. Knowing that a prototype design life cycle of a kite is one month, underlines the importance of having fast models (Pealinck, 2012). Very low resolution kite models are analytical models, which can be found in the work of Loyd (1980), Terink (2009) and Argatov et al. (2009). The formulas given in Section 2.1.2 form the basis of these models.

High resolution models are generally used for detailed design and optimization. They are able to simulate the dynamic effects, but are slower than lower resolution models. They can also serve as validation of the lower order models.

Already early in the design process dynamic kite models are required, mainly for control purpose. At KitePower currently linear feedback models are used for control and optimization, but the goal is to have on-line optimization of the flight path trajectory by using nonlinear adaptive trajectory tracking control (Fechner & Schmehl, 2012). Another possibility is to pre-calculate the trajectory for each cycle and impose that on the system. In both cases a nonlinear dynamic kite model is required. In the case of on-line optimization the model should be at least as fast as real-time, but also for pre-calculated path trajectory optimization fast models are required.

2.3 Simulating aeroelasticity of kites

It is shown in previous sections that the aerodynamic performance of a kite is critical for kite power systems. Because of their flexible structure the aerodynamics of a kite cannot be studied independently of its structural deformations. This interaction between aerodynamic and structural dynamics, called aeroelasticity, and the modeling aspects of this behavior is discussed in this section.

2.3.1 Steady and dynamic aeroelastics

How much force a kite can generate can be influenced by changing the wing configuration of the kite. The shape of the profile, struts, planform shape and surface roughness all influence lift and drag. Rigid wings don't deform (much) during flight making it relatively simple to model aerodynamic forces. For a lightweight membrane wing however, the shape is continuously changing due to its flexibility: steer inputs, accelerations, change in line tension or fluctuations in air flow or air density all make the kite deform. For these highly flexible wings it is essential to include the strong coupling between the aerodynamic forces and the deformations of the flexible structure in the model to achieve realistic simulation results.

These FSI phenomena involve inertial, elastic and aerodynamic forces, which are studied in the field of aeroelasticity. Aeroelasticity can be divided in two fields of study: (quasi-)steady or static and dynamic aeroelasticity. In steady aeroelastics the inertia is not significant and interaction is mainly between aerodynamic and elastic forces on an elastic structure. In dynamic aeroelastics also inertial forces become significant, which makes analysis and modeling more complicated.

The weight of the DUT Power Kite is approximately 100N, which is small compared to the generated forces during reel-in and reel-out phase, generally between 1000-4000N. Using smooth transitions between these phases, will ensure the forces not get much smaller. The short moments where apparent velocities are small and inertia forces become relatively high, are not of high interest for current modeling purposes. The micro-scale FSI phenomena that can occur during these short phases, strongly complicate the aeroelastic problem and are therefore neglected.

Of high interest are the macro-scale FSI phenomena, such as wing torsion and bending induced by steering inputs. This steady aeroelastic behavior significantly affects the flight dynamics and are the reason for the steering abilities of the kite.

When the kite stalls and recovers, hysteresis effects can occur. The aeroelastics are in those cases unsteady. Stall is avoided during flight and therefore the analysis of the specific behavior after stall is not of high interest to model at this moment.

It is however important to know, at which point the wing starts to stall. From flight tests was concluded that the wing generally flies at very high angles of attack, close to stall. This way generated forces are as high as possible. It is then important to know when stall occurs, such that it can be avoided.

Other dynamic aeroelastic behavior can occur, such as canopy flapping, see Figure 2.12. These micro-scale FSI phenomena have no important effects on the general flight dynamics. They are important to model when addressing stresses in the material, because these could lead to fatigue or even failure of the structure. However, if a kite gets damaged during flight it is most probably due to high load (divergence) and not because of excessive vibration. With reinforcements and good kite and bridle design, canopy flapping is avoided.

2.3.2 Solver types

An aeroelastic model contains an aerodynamic and deformation model. Numerical methods are often used to study and model fluid and structure dynamics, named Computational Fluid Dynamics (CFD) and Computational Structure Dynamics (CSD). There are two main approaches to construct an aeroelastic model: the monolithic approach

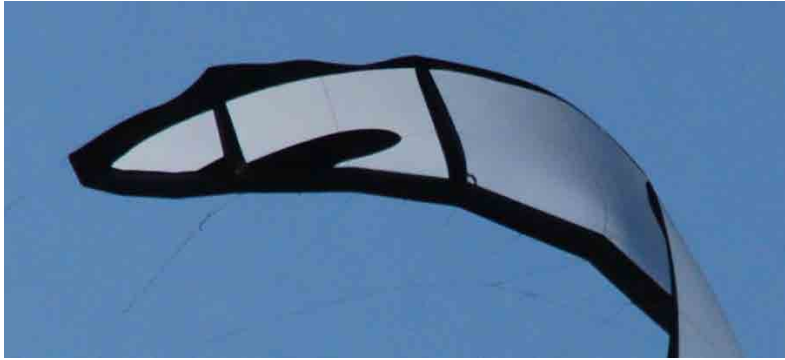


Figure 2.12: The TUD-MutinyV1 has a sharp trailing edge corner near the tip causing flapping of the canopy.

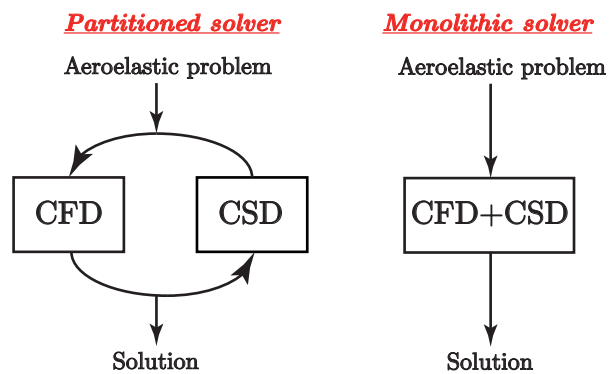


Figure 2.13: Two types of aeroelastic solvers: flow and displacement equations can be solved simultaneous (monolithic) or separately (partitioned).

which involves simultaneous coupling of CFD and CSD by using a single solver and the partitioned approach which involves segregated coupling of CFD and CSD by using two distinct solvers, see Figure 2.13.

In simultaneous coupling of an aeroelastic problem a unique set of equations is required, which includes both material and fluid description. The partitioned approach solves the flow equations and the structural equations with two different solvers. Their advantage is that for the separate CFD and CSD solvers more efficient techniques have been developed. Monolithic solvers are less flexible, because they are developed for one specific problem. For large 3D problems monolithic solvers are more difficult to set up (Heil et al., 2008). The important advantages of monolithic solvers is that they are more accurate and robust. Regarding computation time, the segregated coupled model for ram air wings used by Chatzikonstantinou (1989) was found to be 50% less compared to simultaneous coupling.

Most available dynamic kite models are partitioned solvers, in which various deformation models are used. Together with the advantages just mentioned, makes it attractive to develop an aerodynamic model applicable to partitioned solvers.

2.3.3 Deformation models for kites

This section shortly discusses currently available deformation models used in dynamic kite modeling.

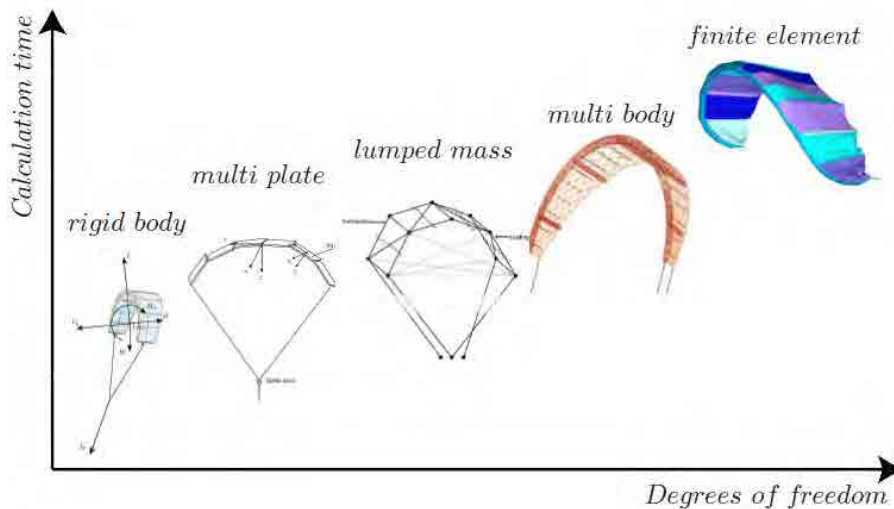


Figure 2.14: Currently available models that simulate kite dynamics.

Figure 2.14 shows currently available dynamic kite models. Analytical and point mass models are not included, because they neglect attitude dynamics and flexible modes. Point mass models only have 3 degrees of freedom (DoF), making real-time modeling possible.

Rigid body models do also not incorporate flexibility of the kite, but can change in orientation (Williams et al., 2008). It is very questionable whether such models can realistically capture the dynamics of a kite (Groot, 2010). A rigid body has typically six

degrees of freedom, though semi-rigid body models have been developed with 4 (Knappskog, 2011), 5 (Terink, 2009) and 9 (Houska, 2009) DoF.

Lumped mass (Furey & Harvey, 2007) and multi-plate models (Williams et al., 2007a,b) are able to deform to some extent, however the individual components are rigid and modeling requires artificial fine-tuning. It can be difficult to establish equilibrium configurations and the models easily become unstable, therefore small time steps are required (4ms for lumped mass model). Typical number of DoF is 30.

The multi-body framework developed by Breukels (2011) uses some realistic properties determined by experiments for the inflated tubes. It nicely simulates the flexibility of the kite by using approximately 400 DoF and can use realistic steering inputs. Unfortunately, it still contains artificial elements e.g. springs and hinges for which parameters need to be tuned. Another disadvantage of this method is that it is quite hard to implement a new kite.

By far the most advanced CSD solver is the Finite Element Method (FEM). FEM solves complex partial differential equations by discretizing the wing into a finite number of deformable elements. Each element deforms under load according to material properties and therefore artificial parameters are not required. Schwoell (2012) made a FEM model of the DUT-MutinyV2 kite with approximately 30,000 elements, while Bosch (2012a) recently developed a FEM kite model with 400 elements. Accuracy of FEM can be very high, unfortunately so are computation times.

2.3.4 Aerodynamic models for kites

The remainder of this report will focus on the modeling of fluid dynamics for kites. This section discusses the parameters of interest for these models and briefly considers available methods.

Parameters of interest

In order to accurately determine the complete instantaneous aerodynamic force distribution sufficient information on the instantaneous shape of the kite should be known. The accuracy of an aerodynamic force model is therefore dependent on information quality and quantity of the wing shape. The resulting geometry generated by a deformation model serves as input to CFD analysis.

Other inputs are orientation and velocity which give the necessary information on flow direction and magnitude. Flow direction and magnitude vary over the wing when the kite is rotating which makes analysis more complex. For many cases however these effects are small, since the rotational velocity is small with respect to the velocity of the kite. Sometimes it could be interesting to consider this rotation, e.g. when investigating the local effects when giving a steer input.

Other required inputs for aerodynamic analysis are flow properties. This is mainly determined by the Reynolds number. The characteristic length of the wing is in general defined as the mean aerodynamic chord (MAC) of the wing. Air properties such as wind speed, density and viscosity vary with altitude for which wind models are available (Figure 2.1a). The apparent wind speed can change due to air fluctuations. For kite design it would be interesting to know how strongly these fluctuations could effect kite behavior when flying slowly, for instance in depower mode.

Lookup tables

Using an aerodynamic lookup table is very fast, but requires the build up of a database that contains experimental data. It is an empirical approach which does not require any knowledge about the internal system; only the state of the system (input) and the corresponding aerodynamic coefficients (output) are of interest. Especially for point mass and rigid body models these tables can be very handy to use. The disadvantage is that they don't incorporate flexibility and therefore lookup tables cannot be used for aeroelastic analysis.

Aerodynamic derivatives

Aerodynamic derivatives are widely used in the dynamics of aircrafts. They are a fast way to compute the aerodynamic forces based on experience and the history of the states of the model. The derivation of these coefficients is explained in Mulder et al. (2006). Aerodynamic derivatives are not applicable to flexible models, because they determine the total forces and moments, not locally.

Breukels' aerodynamic model

Breukels (2011) used a variant of aerodynamic derivatives for kite models, though not to describe the whole wing at once. He divides the kite in quasi 2D sections of which the properties are found in mathematical descriptions build up from detailed CFD analysis. The generated section forces and moments can therefore be considered as aerodynamic derivatives. The advantage is that in this way flexibility can be incorporated. This aerodynamic model is currently the only available model applied to LEI kites incorporating variable pressure distribution, therefore an extensive description is given in Section 3.1.1. Because only simple equations have to be solved, the model is fast with respect to other models that can incorporate flexible behavior.

Potential flow methods

Potential flow methods use a highly simplified flow, therefore reducing the problem to a linear one. These low-fidelity CFD methods are not able to model terms involving viscosity and rotational flow, since these terms are nonlinear. They are reasonably accurate in the linear flow regime, but do not predict nonlinear effects such as separated flow or stall, see Figure 2.15. There are however potential flow methods that use corrections to incorporate nonlinear effects. Potential flow methods only determine aerodynamic loads on the wing's surface, not in the surrounding domain. Most potential flow methods have the ability to predict chordwise variations in pressure. The DoF's can roughly vary between 300-2500. Calculation times are typically less than a second.

High-fidelity CFD

For more advanced fluid dynamics analysis numerous nonlinear methods can be used. They differ mainly in discretization technique and are able to model turbulence and viscosity effects. These high-fidelity methods solve the unknowns throughout a predefined domain that is surrounding a wing, therefore making it possible to investigate local flow

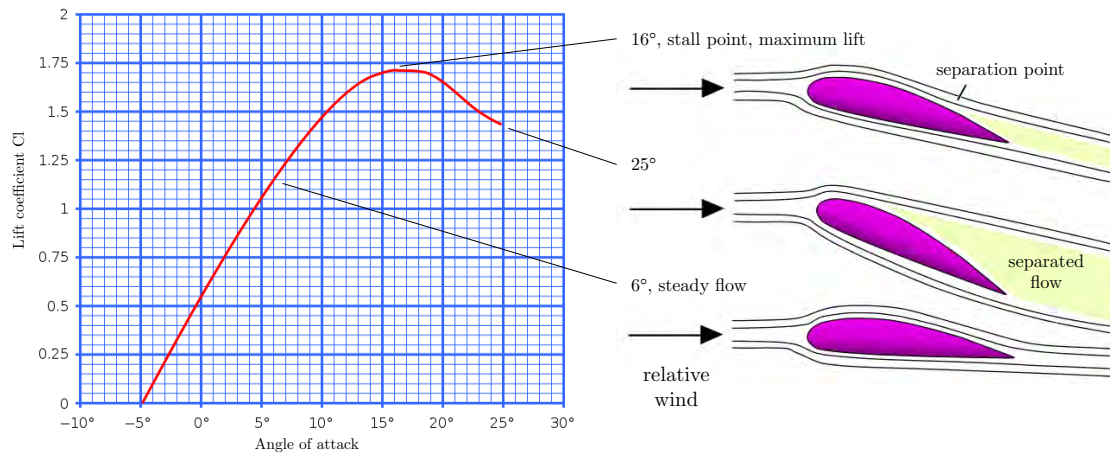


Figure 2.15: A typical lift curve including a linear regime and a nonlinear regime (Wikipedia, 2006).

phenomena and wakes. Computational costs are much higher than low-fidelity CFD methods, though they can vary drastically with the choice of mathematical model. Luckily, with the fast development of numerical analysis and computer capacity the computational cost of CFD is still strongly decreasing in time. The performed CFD calculations in this thesis took approximately one hour for a grid with 200,000 elements using 12 processors. Considering that not even drawing and meshing is included in these run times and a cluster of processors is used, makes these type of CFD solvers (almost) impossible to use for the currently used dynamic kite models.

2.3.5 Aeroelastic models for kites

After the introduction of the computer, many numerical aeroelastic models have been developed for aircrafts and aircraft wings. Unfortunately, most of these models consider dynamic aeroelastics and are not useful when considering quasi-steady behavior of kites. With the assumption of quasi-steady behavior unsteady terms disappear from the equations to solve, significantly simplifying the problem. As a result many aeroelastic models are not of particular interest to power kite analysis. This Section briefly discusses several available aeroelastic models, which are either developed or could potentially be used for highly flexible wings and power kites.

The following list contains aeroelastic models of which an overview of characteristics is given in Table 2.2. In this table VLM and RANS stand for respectively vortex lattice method and Reynolds-averaged NavierStokes. The fundamentals of these CFD methods are elaborated in chapter 3.

- Williams et al. (2007a); Furey & Harvey (2008) developed lumped mass and multi-plate models for kites.
- Gal-Rom & Raveh (2011) made a simplified model for analysis of the aerostructural characteristics of multi-cell baffled inflated wings.
- Zhu et al. (2001) presented a method to model the dynamics of parafoils. It is an

intermediate step towards a fully-coupled simulation.

- Chatzikonstantinou (1993) presents a numerical model for predicting the behavior of ram air wings under aerodynamic loading.
- Breukels (2011) constructed a multi-body framework to model behavior of inflatable tube kites.
- Bosch (2012a) presented a reduced approach to model flying flexible inflatable tube kites that represents the global dynamics and deformation modes of the kite.
- Bungart (2009) modeled a ram-air wing by coupling a FEM and RANS solver.

As expected, from the table follows that the computational cost increases when the level of detail is increased. The model with the lowest computation cost are those of Williams et al. (2007a) and Furey & Harvey (2008). The structural and aerodynamic models used in lumped mass and multi-plate models only simulate flexible behavior in a very limited way. The aerodynamics are simplified to 2D sections for which lift and drag coefficients are determined from a lookup table. These models are constructed to more realistically determine the general forces in the kite, not so much to simulate the local aeroelastic behavior. Chordwise the plates and lumped masses are fixed. These could be used when doing preliminary design on for example trajectory control.

The model of Gal-Rom & Raveh (2011) is highly simplified and serves as preliminary investigation on characteristics of single-cell and multi-cell inflated wings of various aspect ratios, airfoil thickness ratios, and membrane thicknesses. In the paper it is stated that future work will involve improvement of the aeroelastic model to better handle low-aspect-ratio configurations and expansion of the structural model to handle asymmetrical airfoils and more complex geometries.

Zhu et al. (2001) and Chatzikonstantinou (1993) proposed models for ram air wings. The latter uses a more advanced CFD solver, but is not able to simulate nonlinear effects as friction, turbulence, separation and stall. Zhu et al. (2001) uses a prescribed pressure field which is calibrated with experimental flight data. A certain amount of preliminary knowledge about the used wing and its behavior in certain flight conditions should be known, which makes his method not very flexible and appropriate to test new designs and predict local behavior.

The aeroelastic models of Breukels (2011) and Bosch (2012a) both simulate behavior of LEI kites, though the latter uses FEM and has therefore a more realistic model. The multi-body framework of Breukels contains several components that are rigid or only flexible in one direction. This model is therefore a more artificial approach to simulate aeroelastic behavior. Linear springs simulate canopy movements for which a self-developed aerodynamic method is used. The aerodynamic model of Breukels was never validated, but the aeroelastic models showed reasonable correlation with measured data. The same aerodynamic method was used in the FEM model of Bosch (2012a), though he omitted a 3D correction. For the FEM model of Chatzikonstantinou (1993) a VLM is used.

The most computational intensive and most accurate models use FEM and finite volume methods. A recent investigation was performed by Bungart (2009) to investigate ram air kites. Other calculations on ram air wings have been performed by Kalro et al. (1997), Garrard et al. (1995) and Lingard (1995). Such models are very useful when investigating local flow phenomena and can give much understanding of kite behavior. For fast dynamic kite modeling, they seem not very effective: the fine volume discretization results in millions of equations for every iteration, which requires a lot of computational

power and the user should be well trained in setting up these type of CFD and CSD calculations.

Table 2.2: Characteristics of existing aeroelastic kite models.

Aeroelastic model	Deformations	Aerodynamics	Level of detail	Computation cost	Applied to
Furey & Harvey (2008); Williams et al. (2007a)	Lumped mass, multi-plate	lookup table for 2D sections	global	low	kite
Gal-Rom & Raveh (2011)	Multicell box beam	2D thin airfoil theory	global	low	ram air (simplified, high AR, planar)
Zhu et al. (2001)	FEM	Prescribed pressure field (requires calibration)	local	intermediate	ram air
Chatzikonstantinou (1993)	FEM	VLM	local	intermediate	ram air
Breukels (2011)	Multi-body	Self-developed method (Section 3.1.1)	local	intermediate	LEI
Bosch (2012a)	FEM	Fitting method of Breukels	local	intermediate	LEI
Bungart (2009)	FEM	RANS	detailed	high	ram air

2.3.6 Computation time

Having fast kite models allows for rapid evaluation of both changes in system design as path trajectories for control purposes. Setting hard criteria on allowed computation time is difficult, since there are so many parameters which could easily be changed. The type of programming language, algorithm efficiency, computer power and type of problem under investigation have all influence on the criteria.

To give an indication of computation time criteria the FEM model of Bosch (2012a) is used as baseline. This is the latest developed model at DUT KitePower and showed realistic dynamic behavior of kites. For his simulations he used:

- Intel core i5 750 @ 2.8GHz, 4GB memory
- Matlab code with some parts compiled to C++

In a 30s during simulation of the traction phase, the average time step was 4.5ms, and the speed of the simulation is between 25 and 30 times slower than real time on a wing with 400 elements. Bosch states that when a lower level programming language is used the computation time could get 10 times faster. The evaluation of the aerodynamic load for each deformation took approximately 10ms (Bosch, 2012b). Note that he keeps the aerodynamic forces constant during each time step, which makes it a loosely coupled solver. The relation between FEM and aerodynamic load computation time is approximately 10:1.

This computation time applies to a non-optimized algorithm on a normal laptop: improving these two factors could result in a dynamic kite model much closer to real time.

2.4 Concluding remarks

Power kites often try to produce as much power as possible, for which high lift values and angles of attack are required. Modeling of the nonlinear behavior occurring at these high angles is therefore an important aspect for power kites and without it an important part of flight prediction becomes unreliable.

Considering the type of aeroelastic behavior of the kite, it is shown that unsteady effects are not of high interest when modeling the general behavior of kites, where mostly quasi-steady effects are dominant. Assuming quasi-steady aeroelastics makes the computation times much shorter, which is an important criteria for FSI solvers. Therefore, in the remainder of this report **kite aeroelastics are considered quasi-steady**.

Computation time and accuracy play major roles when choosing a suitable aerodynamic model. For design and optimization of system components, dynamic simulations of a large part of the energy cycle could be required. For on-line nonlinear feedback control, real-time models of the kite are necessary. For these purposes fast models are a prerequisite. Currently, the most advanced aerodynamic model (that of Breukels) at KitePower, which serves as part of an aeroelastic kite model, has a computation time of about 10ms. It is programmed in Matlab and runs about 25 times real-time on a normal desktop computer (specifications defined in Section 2.3.6).

Summarized, there is a shortage of aerodynamic models that:

- are able to predict nonlinear behavior at high angles of attack, including stall point
- have low calculation times, so that it can be used for dynamic kite models that simulate quasi-steady aeroelastic phenomena.
- can serve as basis or validation for the lower resolution models.
- can be used for kite design purposes.

In the next chapter, methods are discussed that can potentially fulfill these roles. Also the computational costly CFD solvers are discussed, because they will provide critical information for the method, which is going to be developed.

Mark that for the simulations performed in this report, the following laptop specifications apply:

- Intel core i7-2630QM @ 2.0GHz, 4GB memory, 64-bit

Aerodynamic Analysis Methods

In the previous chapter it is explained what the requirements are for the aerodynamic model. Methods that are possible candidates, are shortly discussed after which a selection is made. Finally, an introduction to the method proposed in the next chapters is given.

3.1 Available methods

A variety of computational analysis methods that are available could be used for modeling flexible behavior of kites. These range from linear methods, concerned with solving the velocity potential equation, to more complicated methods that involve solving the Euler (inviscid) or Navier-Stokes (viscous) equations at various points on and around the wing to determine the nature of the flow. A selection is made based on the criteria on accuracy and computational speed required for aeroelastic kite models.

3.1.1 Breukels' method

Breukels (2011) developed a method specifically for kites to determine the aerodynamic forces on his multi body kite model. The most important requirements consisted of analytical flexibility and reasonable results at low computation cost.

The aerodynamic loads of the kite are approximated according to the finite strip approach, which is based on the assumption that the aerodynamics of the wing can be approximated by modeling the wing as an assembly of a finite number of connected two-dimensional single membrane airfoils in the spanwise direction. The aerodynamic load for each of these wing sections is determined separately, depending on its shape, angle of attack α and apparent wind velocity V_a . The shape of the wing profile is described by the chord length c , camber $\kappa = b/c$, thickness $t = d/c$ as depicted in Figure 3.1.

The section's lift, drag and moment coefficients are approximated by an algorithm which produces these coefficients as a function of airfoil thickness t , camber κ and angle of attack α . He performed 2D CFD simulations with a RANS solver in Fluent on airfoils with different characteristics (thickness 15%, 20%, 25%; camber 0%-12%; angle of attack 0°-25°) and from the obtained data a polynomial regression model is made for lift, drag and moment coefficients: the depending variables (C_L , C_D and C_M) are expressed as polynomial functions of the independent variables (κ , t , α).

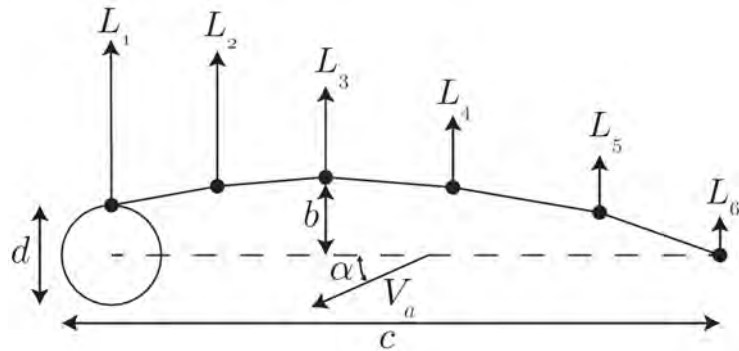


Figure 3.1: Side view of a wing section.

The fitted function can now produce these aerodynamic coefficients as function of airfoil characteristics, hence:

$$\begin{aligned} C_L &= f(\kappa, t, \alpha) \\ C_D &= f(\kappa, t, \alpha) \\ C_M &= f(\kappa, t, \alpha) \end{aligned} \quad (3.1)$$

Bosch (2012a) pointed out that the resultant aerodynamic coefficient curves of Breukels obtained regression model showed some peculiarities. Lift coefficient values were found to be relatively high compared to normal aircraft wings and the drag does not always increase with an increasing camber. Furthermore the moment coefficient curve is linear while the CFD results from Breukels show non linear behavior.

Breukels distributes the total aerodynamic force resulting from his fitted functions over a number of nodes, which are equally divided over the chord, see Figure 3.2. Changing flight conditions will vary the airfoil lift, drag and moment. This variation is represented by a variation of weight factors. Per section he selects constant weight factors w_i and variable weight factors $u_i \cdot a$ which, for changing flight conditions, can be altered by a single parameter a .

One of the main drawbacks of Breukels procedure is the fact that he has to choose one set of constant coefficients w_i and u_i , which will determine how the shape of his pressure distribution can vary. The fact that the determination of pressure distribution is reduced to a one dimensional operation gives the model its simplicity, but also limits the flexibility.

Breukels incorporates the effects of having a finite wing by using a VLM. He finds that the relation between lift curve slope and anhedral angle is independent of airfoil shape. With the relation between spanwise station and lift curve slope known, you can determine the local 3D lift coefficient for any location and any angle of attack *where the lift curve is linear*. This 3D correction has three main drawbacks:

- This correction is based on flight in the linear regime i.e. at low angles of attack. Power kites however, fly mostly at high angles of attack.
- It considers constant shape for increasing angle of attack, while in reality the entire kite deforms when flight conditions change.
- A different wing would require a new VLM analysis with resulting lift slopes per spanwise stations, since for changing wing configuration the 3D aerodynamic effects

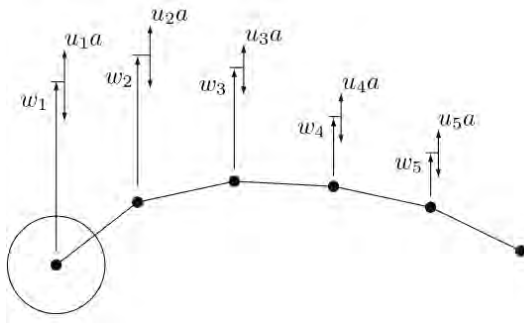


Figure 3.2: A schematic representation of the modeled pressure distribution (Breukels, 2011).

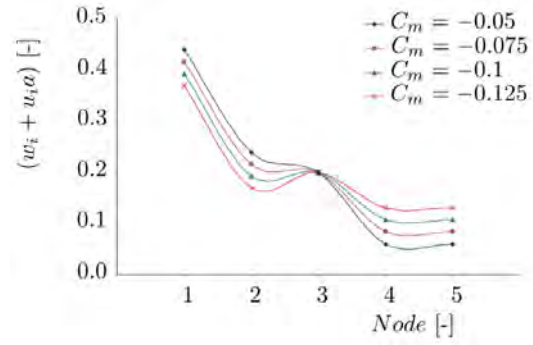


Figure 3.3: The values for the weight factors $w_i + u_i a$ for different values of airfoil moment coefficient C_M (Breukels, 2011).

will be different.

3.1.2 Potential flow methods

Due to its simplicity and its ability to predict the most important dynamics in flows it was and still is popular under aerodynamici. It does not include all the characteristics of flows that are encountered in the real world e.g. turbulence and boundary layers. Yet, there are ways to introduce non-potential flow aspects, at least in a certain degree. This, and the fact that potential flows are easy and quickly to solve, makes them a potential candidate for aeroelastic models.

Assumptions

In potential flow theory the flow field is described as the gradient of the velocity potential function $\varphi = \varphi(x, y, z, t)$:

$$\vec{v} = \nabla\varphi \quad (3.2)$$

Knowledge of φ directly relates to the velocity components:

$$u = \frac{\partial\varphi}{\partial x}, \quad v = \frac{\partial\varphi}{\partial y}, \quad w = \frac{\partial\varphi}{\partial z} \quad (3.3)$$

Because the curl of a gradient is equal to zero, it follows that vorticity is zero and therefore potential flow is *irrotational*.

$$\nabla \times (\nabla\varphi) = \nabla \times \vec{v} = 0 \quad (3.4)$$

Combining the definition of the velocity potential with the principle of mass conservation for incompressible flow results in the Laplace equation:

$$\nabla^2\varphi = 0 \quad (3.5)$$

A consequence of incompressible, potential flow is that viscous terms vanish, therefore incompressible potential flow implies absence of viscosity¹.

Potential flow theory can also be extended to compressible and unsteady flows resulting in the nonlinear *full potential equation*. The dynamics of kites is assumed to be quasi-steady and incompressible, hence the full potential equation is for thesis not of further interest.

Lifting line theory

The Lifting Line Theory (LLT) predicts the aerodynamic properties of a finite wing and is the first practical theory incorporating the three-dimensional geometry of a wing (Anderson, 2001). According to LLT, the wing is considered to be a single vortex line, at which the bound vortex is bound to, see Figure 3.4. Next to this, the wing tips generate so called tip vortices, resulting in a closed system, which is a result of the conservation of circulation (Kelvin's circulation theorem). It gives reasonable results for straight wings at moderate to high aspect ratio. However, for low aspect ratio straight wings, swept wings and delta wings, lifting line theory is inappropriate (Anderson, 2001). As a matter of fact, the theory assumes that the wing lies in the xy-plane only and sweep and dihedral are not even taken into account for the calculation of lift. Inviscid conditions are assumed, which results in significant errors when predicting drag at high angles of attack. LLT does not predict chordwise pressure distribution, it only determines spanwise lift values.

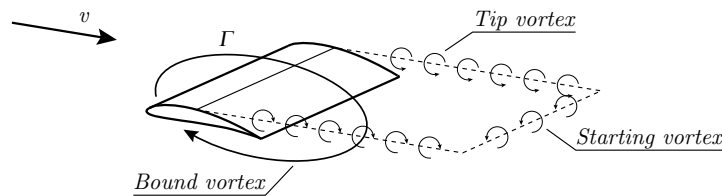


Figure 3.4: Development of a closed circulation vortex system behind a finite wing section.

Nonlinear lifting line method

The classical LLT assumes a linear variation of the lift coefficient versus effective angle of attack. Nonlinear LLT corrects this assumption by using experimental data of the lift curves for each spanwise station.

About this method Anderson (1980) states that solutions give reasonable preliminary engineering results for the high-angle-of-attack post-stall region (within 20% compared to experiment), though "it is wise not to stretch the applicability of LLT too far". The 3D effects at high angles of attack, such as spanwise flow and mushroom shaped flow separation regions, cannot be included in this method.

¹From Stokes (1851) it actually follows that viscous stresses do not have to be zero in irrotational flow. However the terms containing viscous stresses disappear in the Navier-Stokes equations since they only contain derivatives of the viscous stresses which are zero in potential flow. Potential flow can be used for considering viscous effects in cases where shear stresses are negligible, but normal stresses exist (where the orientation of the stresses is taken with respect to the orientation of the flow field). This is however only valid in some special cases. (Joseph, 2003)

Vortex lattice method

Since LLT has quit some limitations considering wing geometry, methods are developed that give more accurate results when for example using low aspect ratios, sweep and dihedral. Such a method is the VLM, which is widely used for preliminary design considerations. VLM takes into account the span and chordwise variations in geometry, but does not take into account airfoil thickness. The unknowns are solved at the mean camber line.

3D panel method

Next to the VLM, which already has significant improvements with respect to LLT, 3D panel methods are developed. In contrast to the VLM, these methods take into account the thickness and camber of an airfoil and therefore also gives results on pressure distributions on upper and lower surfaces. Next to wings also bodies (eg. fuselage) can be modeled with a 3D panel method, such that total airplanes can be analyzed.

Attempts have been made to correct the inviscid calculation by using a *3D inviscid-viscous interaction*. Results obtained with these tools are still limited (Lock & Williams, 1987). The development of a 3D boundary layer correction method proves difficult due to the complexity of the boundary layer equations. Furthermore, in the presence of flow separation these methods run into difficulties: the algorithm becomes instable and ceases to converge as a singularity is encountered in the boundary layer formulation. There are some methods which overcome these problems, but when significant separation is present the inviscid and viscous solutions are mismatched and an efficient update procedure for rectifying this has yet to be developed. (Coenen et al., 2000)

Boundary element method

Panel methods and boundary element methods are similar in the way that they both use a surface mesh with singularities and are based on potential flow theory. The boundary element method is however not restricted to determination of flow properties on only the surface. It uses Green's Second Identity to map a potential flow problem from dimension x to dimension $x - 1$. Using this identity each point in the domain is expressed in terms of the boundary values, once all boundary values are known any potential value within the domain can now be found.

The boundary element method is often more efficient than other volume-discretization methods in terms of computational resources for problems where there is a small surface/volume ratio. However, for many problems boundary element methods are significantly less efficient than volume-discretization methods. This method can give insight in flow characteristics around a wing, however, it is based on potential flow theory and has therefore the same limitations.

3.1.3 High-fidelity CFD

In high-fidelity CFD methods the entire flow domain is discretized. Three classical discretization choices are available: the finite difference method, the finite element method and the Finite Volume Method (FVM). Though they all have (dis)advantages regarding efficiency, accuracy, theory, stability and handling of complex geometries the finite volume

method is mostly used for advanced CFD and is generally the most robust method. This section briefly gives the general equations, assumptions and sub-models of high-fidelity CFD.

Assumptions

The governing equations of fluid dynamics are the conservation laws of mass, momentum, and energy. This set of conservation laws are called the Navier-Stokes equations. When solving the complete complete form, no assumptions to the flow are made and the problem is completely solved. However, these equations are highly complex and some assumptions can strongly simplify the problem. Considering incompressible flow, the three momentum equations (in x-,y- and z-direction) can be written in vector form by:

$$\rho \left(\overbrace{\frac{\partial \vec{v}}{\partial t} + \vec{v} \cdot \nabla \vec{v}}^{\text{Inertia (per volume)}} \right) = \overbrace{-\nabla p + \mu \nabla^2 \vec{v}}^{\text{Divergence of stress}} + \underbrace{\vec{f}}_{\text{Other body forces}} \quad (3.6)$$

Unsteady acceleration
Convective acceleration
Pressure gradient
Viscosity

The viscosity term can be written in this format, because at low Mach number the flow is assumed to be incompressible, homogeneous and Newtonian. For incompressible flow the conservation of mass simplifies to:

$$\nabla \cdot \vec{v} = 0 \quad (3.7)$$

In contrast to compressible flow, in incompressible flow the energy equation is decoupled from the continuity and momentum equations. For solid walls there is, unlike potential flow, a *no-slip condition*: the tangential velocity at the wall should be zero. This implies a boundary layer must exist, which is indeed made possible by the presence of viscosity.

For inviscid flow the viscous term from equation 3.6 disappears resulting in the **Euler equations**. This implies that boundary layers are not modeled. Therefore the need for fine grids in boundary layers which they normally require don't have to be present in Euler solvers, resulting in lower computation times. Unlike potential flow, Euler equations do include rotational flow.

An overview of the linear and non-linear fluid dynamic analysis methods is given in Figure 3.5.

Turbulence models

Turbulent flows are time dependent, three dimensional, irregular and vortical, which makes them highly complex to model. Describing the turbulence can be done in many ways, and the choice of the method depends on the application at hand and on computational resources. The most famous of these methods are shortly discussed. More on turbulence models can be found in many literature and at CFD-Online (2011a).

RANS stands for **Reynolds-average Navier-Stokes** and is a concept introduced by Reynolds in 1895. It is the most commonly used approach in industry. The Reynolds decomposition separates the flow variable into a mean (time-averaged) component (\vec{u}) and a fluctuating component (\vec{u}'). Using the Reynolds decomposition the Navier-Stokes

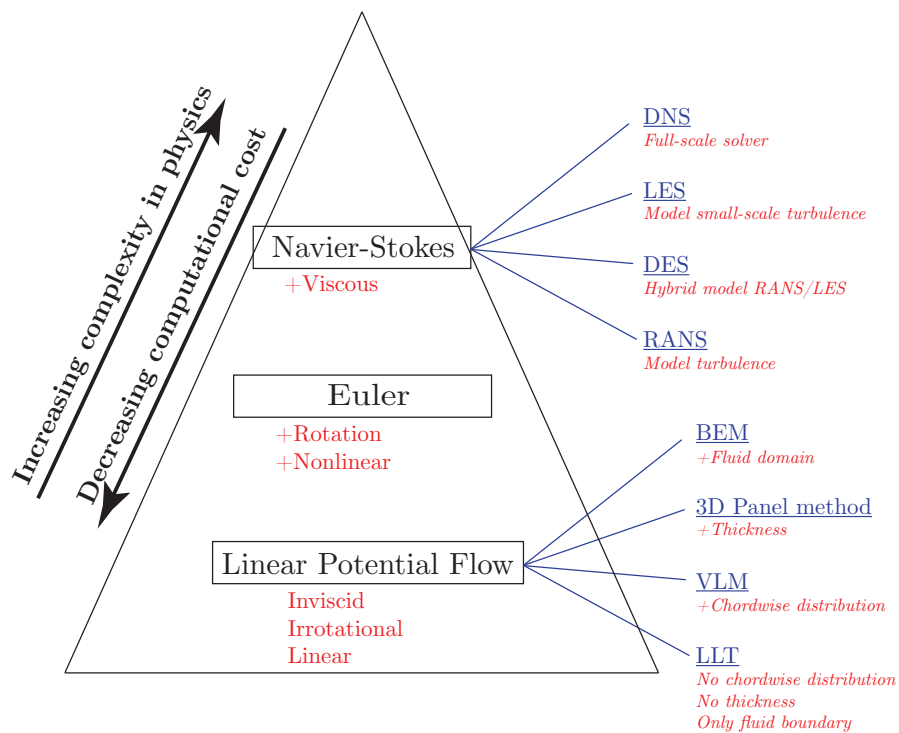


Figure 3.5: An overview of the discussed aerodynamic analysis methods. Breukels' method is omitted, because it uses fractions of both VLM as CFD. Also nonlinear potential flow is omitted here, because the unsteady and full potential equation contain respectively time and density differential terms, while in this report these effects are neglected in the modeling of kite aeroelastics.

equations can be rewritten as

$$\frac{\partial \vec{u}}{\partial t} + (\vec{u} \cdot \nabla) \vec{u} = \nabla \cdot \left(-\frac{1}{\rho} \nabla p + \nu \nabla^2 \vec{v} - \overline{\vec{v}' \otimes \vec{v}'} \right) + \vec{f} \quad (3.8)$$

The Reynolds stress term $\overline{\vec{v}' \otimes \vec{v}'}$ is an artificial stress term and results from the decomposition. It contains a nonlinear term with fluctuations, and its effect requires additional modeling. Many models use one or more transport equations, involving turbulence (eddy) viscosity, turbulent kinetic energy and (specific) dissipation. Examples are Spalart-Allmaras, $k - \epsilon$ and $k - \omega$ models. The Reynolds stress model (RSM) is a higher level, elaborate turbulence model requiring more computational resources.

In **Large-Eddy Simulation** (LES) the time and space dependence of the fluid motions are resolved down to some prescribed length-scale. LES is a higher fidelity CFD method than RANS, but also more costly. Since it models the smallest scales of the solution, LES is far less expensive than DNS.

Detached eddy simulation (DES) is a hybrid method between RANS and LES and attempts to combine the best aspects of their methodologies. DES uses RANS in near-wall regions and regions where the turbulent length scale is less than the maximum grid dimension and assigns LES to the rest of the flow. Grid generation is more complicated than for a simple RANS or LES case, but when applied properly it can significantly improve accuracy of RANS or, decrease calculation times of LES.

When using **Direct Numerical Simulation** (DNS) all spatial and temporal scales in are resolved without a turbulence model. This includes the Kolmogorov microscales, which are so small that extremely fine grids and time steps are required, resulting in a tremendous amount of calculations. "(...) the number of operations grows as Re^3 ." (CFD-Online, 2012) Therefore, the computational cost of DNS is very high, even at low Reynolds numbers. For the Reynolds numbers encountered in power kite applications, it would require more than 1^{18} (quintillion) operations. This is unachievable, even the most powerful computers currently available would not suffice.

3.1.4 Selection

Breukels' method is fast and specifically designed for dynamic kite models, however it has some critical points:

- The approach of using polynomial regression models allows the use of experimental data, as well as numerical data giving it added flexibility.
- In the regression models only camber, thickness and angle of attack influence the forces. Neglecting Reynolds numbers and determining camber by only one variable, limits prediction capability.
- It has limited capability in predicting the varying chordwise loads, which is an important feature when predicting aeroelastic phenomena.
- It has a very limited correction for finite wings and is based on linear regime only, while nonlinear and 3D effects become increasingly important for the at high angle of attack flying, low aspect ratio wings. Bosch (2012a) regarding this 3D correction: "Discussions with the author of the model led to the conclusion that the uncertainty

of the three dimensional correction is so significant that it is not clear whether this correction actually improves the model or not.”

- Induced drag is not included in the model.
- Bosch (2012a) also pointed out that the regression model showed some peculiarities and states: ”A better aerodynamic model would (..) give more reliable results of the total simulation. This model acts at the moment as a limitation to the total validity.”

These limitations suggest a more accurate method should be found. Ideally, the accuracy of the high-fidelity CFD methods are achieved, but they are much too computationally intense to solve as part of the flexible kite model. Potential flow methods are much faster, although they have their limitations. LLT seems not useful for predicting aeroelastic behavior of kites, because the canopy shape is determined by the chordwise pressure distribution and without it the airfoil characteristics cannot be known. Next to this, it is not capable to incorporate the non-planar shape of a kite. BEM wastes effort by projecting the aerodynamic surface loads to the surrounding domain.

The most promising methods are the VLM and 3D panel method, where the latter incorporates the thickness of the wing making it slower. At this stage it is unclear if the expected higher accuracy of the 3D panel method matches the extra computational effort that is required, therefore both methods will be considered as possible candidate. These methods predict forces over non-planar wings and include both chord- and spanwise variations. In their natural form they are linear and do not incorporate rotational and viscous effects. However, nonlinear LLT showed there is a way to correct for viscosity and as a result nonlinear behavior can be predicted. Before announcing a nonlinear VLM and 3D panel method in Section 3.4, a section is spent on the background theory of these methods. The new method is thereafter extensively discussed and developed in the upcoming chapters.

3.2 Background theory

In this section background theory is given on the VLM and 3D panel method as these are used in the remainder of this report. In Appendix C more can be found thin airfoil theory and the 2D panel method.

3.2.1 Vortex lattice method

VLM is used to model the wake behind a wing by means of placing a number of vortices on the wing planform. For each of these vortices, the strength is determined such that the boundary conditions are satisfied. Instead, the mean camber line is taken as a basis, such that only the upper surface pressure distribution can be determined. Two methods are distinguished considering a VLM, which are based on a slightly different theory. The first one is shown in Figure 3.6, where a horseshoe vortex is placed on every quarter chord panel with a control point at the three quarter chord panel. This control point refers to the boundary condition that states the non penetration condition on the surface of the body.

The second method is recommended by Katz & Plotkin (1991) and uses so called ring vortices or quad vortices, as shown in Figure 3.7. Also here, the vortex is placed on the

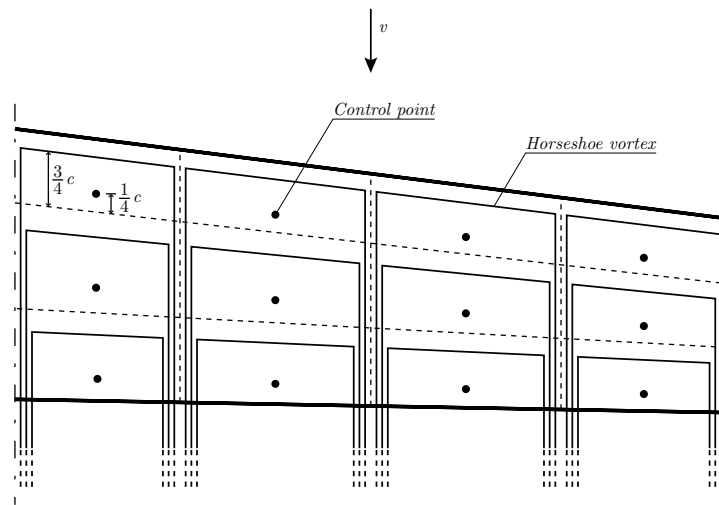


Figure 3.6: Top view of a semi-span wing illustrating the vortex lattice method using horseshoe vortices.

quarter chord panel with a control point at the three quarter chord panel. However, in this case only the trailing vortices extend to infinity, which strength is equal to the trailing edge ring vortex. This is due to the condition that the wake is force free. Besides the fact that these methods use a different approach, the outcomes are expected to be similar.

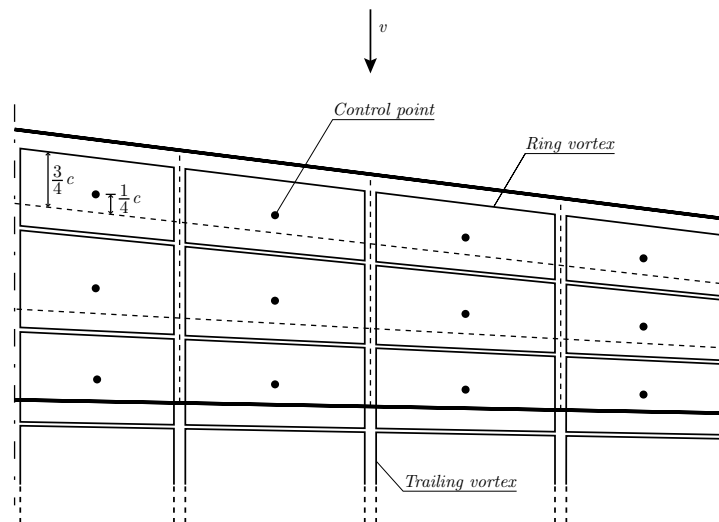


Figure 3.7: Top view of a semi-span wing illustrating VLM using ring vortices.

As mentioned earlier, the VLM uses the mean camber line of the considered airfoil to perform calculations on, neglecting thickness effects. In a 3D space, such a lay-up can be visualized as shown in Figure 3.8.

Considering a single panel on this surface, the lift force and coefficient can be deter-

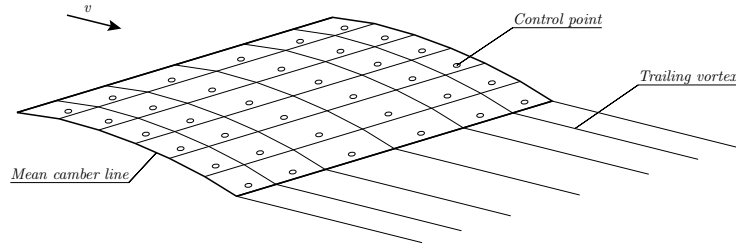


Figure 3.8: Lay-up of a 3D wing using VLM.

mined from the force acting on this panel. This force is defined as

$$F_{panel} = \rho v \Gamma_c \quad (3.9)$$

Here, Γ is the vortex strength multiplied by the vortex length. Therefore, this force is acting in normal direction with respect to the panel. The lift coefficient can then be determined as shown in Equation 3.10, where S_{panels} is the total panel area and F_{wz} force projected on the vertical wind axis. From this, the lift force can be determined, which is in turn used to calculate the position of the center of pressure and pitching moments.

$$C_L = \frac{1}{\rho S_{panels} v^2} \sum_{panels} F_{wz} \quad (3.10)$$

3.2.2 3D panel method

In a 3D panel method, a wing or plane is discretized into panels distributed over the span and chord of the airfoil. As with the VLM, each panel contains one or multiple singularities and a control point. Popular are sources and doublets; the latter is equivalent to a distribution of vortices and can therefore generate lift, as opposed to sources (Paraschivoiu, 2003).

In addition to covering the body with panels, also the wake behind the body can be modeled with panels. The idea is that each of the wing's chordwise strip sheds a column of wake panels. The doublet strength of each panel in this wake strip is the difference of the doublet strength of the top and bottom panels of the wing's strip. This is a consequence of the fact that the wake cannot sustain load. In addition, being a thin surface, the wake panels have a zero source strength. Again here, the singularity strengths are determined, satisfying the boundary conditions.

The resulting Equations which are solved in case Neumann boundary conditions are applied, are principally the same as those of the 2D panel method (Appendix C). However, for multiple programs, such as XFLR5 and VSAERO, the format of the Equation is somewhat different. The boundary condition considers sources and doublets on each surface panel (σ_s and μ_s) and only doublets on each wake panel (μ_{wake}), such that the induced velocity v_i is obtained for the Neumann boundary condition as:

$$\bar{v}_i = [A]\bar{\mu}_s + [B]\bar{\sigma}_s + [C]\bar{\mu}_{wake} = -\bar{V}_\infty \cdot \bar{n} \quad (3.11)$$

The singularities represent the jump in conditions across the boundary; the doublet density represents the local jump in potential and the source density represents the local jump in the normal component of velocity.

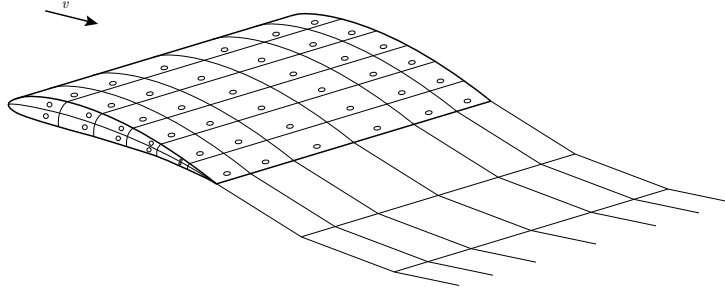


Figure 3.9: Lay-up of a three-dimensional wing using a panel method.

For the Dirichlet boundary condition, the Equation is slightly different when rewritten. This results in

$$[D]\bar{\mu}_s + [E]\bar{\sigma}_s + [F]\bar{\mu}_{wake} = 0 \quad (3.12)$$

In the relations above, the matrices $A - F$ represent influence matrices completely determined by the geometry of the surface. Furthermore, the doublets and sources are defined as:

$$\mu = \frac{1}{4\pi} (\varphi - \varphi_0) \quad (3.13)$$

$$\sigma = -\frac{1}{4\pi} (\bar{V}_\infty \cdot \bar{n}) \quad (3.14)$$

In the definition of σ , it is assumed that no transpiration velocity is used (which can be the case when coupling boundary layer calculations). In the case of a VLM, only vortices are placed on each surface panel, such that no wake panels exist (no sources). The wake therefore completely consists of shedded horseshoe vortices, where there is no jump in velocity across the wake. In the case of a panel method, the source strength on each wake panel is zero. Furthermore, the definition of μ implies the Kutta condition at the trailing edge, such that $(\varphi_{u_{TE}} - \varphi_{l_{TE}})$ is constant on the wake shedded by these panels. Finally, a full-matrix Equation is obtained as

$$\begin{bmatrix} A_{1,1} & \dots & A_{1,N} \\ \vdots & \ddots & \vdots \\ A_{N,1} & \dots & A_{N,N} \end{bmatrix} \begin{bmatrix} \mu_1 \\ \vdots \\ \mu_N \end{bmatrix} = \begin{bmatrix} RHS_1 \\ \vdots \\ RHS_N \end{bmatrix} \quad (3.15)$$

influence matrix (geometry) $\cdot \mu = \sigma, V_\infty, \alpha$ (boundary conditions)

Once the doublet and source strengths in spanwise and chordwise direction are known, the associated derivative is used to determine the pressure distribution.

3.3 Software

The VLM and 3D panel method are selected as most promising to fulfill the requirements for the dynamic kite model. Until now, these methods are purely theoretical. This section

compares a selection of available software, in which these methods are implemented. Also software which analyses the flow over 2D airfoils is discussed, because for the new developed tool, airfoil data is required.

3.3.1 XFOIL

Maughmer & Coder (2010) performed a comparison between various methods for airfoil analysis, including the integral boundary-layer methods XFOIL6.94, PROFIL07, MSES3.05 and RANS solvers OVERFLOW 2.1AE (Spalart-Allmaras) and FLUENT 12.1.2 (4-eq transition SST). It was concluded that XFOIL was overall in the closest agreement to the measured values. The average error in prediction of maximum lift $C_{L_{max}}$ was within 11%. Furthermore, it was found that the ones incorporating boundary-layer methods provide a more reliable drag prediction than does OVERFLOW. FLUENT predictions of maximum lift agree very well with those measured and correspond to the same critical angle of attack, while XFOIL tends to overpredict the stall point. XFOIL is very accurate in predicting the point of transition, though FLUENT is also quite good in predicting transitional boundary-layer behavior.

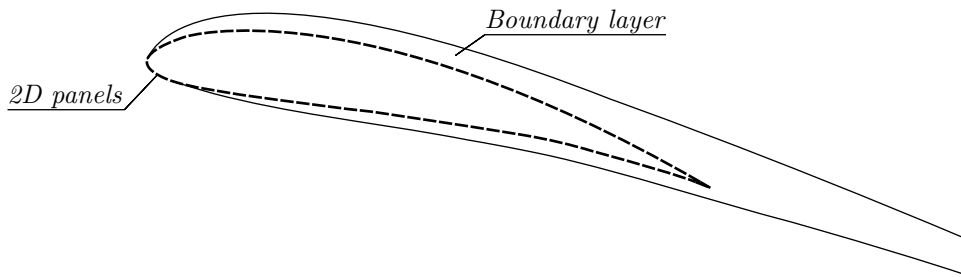


Figure 3.10: The thickness of the boundary layer is added to the airfoil geometry.

This shows that XFOIL is very good in predicting the aerodynamics around airfoils, even when compared to the high-fidelity RANS solvers. It is however unclear whether it is also accurate when predicting flow around profiles of LEI kites.

XFOIL is a 2D panel method with inviscid-viscous interaction, as shown in Figure 3.10 and can be used for design and analysis of subsonic airfoils. A surface transpiration method (two-Equation lagged dissipation) is used to represent the viscous layers. Both laminar and turbulent layers are treated, where an approximate e^n method determines the transition point. This approximate method tracks only the most amplified frequency of the Tollmien-Schlichting waves at a given point on the airfoil downstream from the point of instability to obtain the amplitude of that disturbance. Transition is assumed when this integrated amplitude reaches an empirically determined value. The boundary layer and transition Equations are solved simultaneously with the inviscid flow field by a global Newton method. In addition to calculating the total drag from the wake momentum thickness, XFOIL also determines the friction and pressure drag components. (Drela & Giles, 1987)

3.3.2 XFLR5

A comparison of several potential flow solvers was made, because it is important to know the possibilities and limitations of such programs. Three open-source programs are considered: Tornado, AVL and XFLR5.

Comparison with other software

Tornado (Melin, 2000) is an open-source VLM implemented in the user-friendly technical computing language Matlab, which makes it relatively easy to understand and adapt. As Matlab is a high level programming language it is the slowest of the three. Airfoil sections can be read in via simple coordinate files (.dat).

Athena Vortex Lattice (AVL), programmed by Drela & Youngren (2011), employs a VLM for the lifting surfaces, together with a slender-body model for fuselages and nacelles. The software is written in FORTRAN77 and can be run as an executable in Windows. XFOIL generated airfoil files can be read in.

XFLR5 has three main features: foil design, foil analysis and wing and plane analysis. The foil analysis is performed by an implemented version of XFOIL for which a user-friendly interface is build in. The 3D wing analysis feature of XFLR5 incorporates LLT, a VLM and a 3D panel method. The code is programmed in C++; one of the most popular programming languages nowadays (*TIOBE Programming Community Index*, 2009).

In contrast to XFLR5, AVL and Tornado does not take into account a profile drag correction. The incorporated features including XFOIL, the user-friendly graphical user interface and the programming language make XFLR5 the best candidate to use in further investigations.

Next to the availability of either the LLT, VLM and 3D panel method, one can choose in XFLR5 to implement inertia properties, and the direction of the wake. Next to this, 3 polar types can be chosen, considering either fixed speed, fixed lift or fixed angle of attack. For VLM discretization horseshoe vortices (VLM1) or ring vortices (VLM2) can be used, which are explained in Section 3.2.1.

Guidelines

Considering the meshing of a wing (plus tail), either for the VLM or 3D panel method, several methods are recommended in the guidelines manual that comes with the program (XFLR5, 2011). It is advised to consider the following approaches when defining a wing:

- Use a panel distribution where the mesh density near geometrical breakpoints is higher, such as the root and tips of the wings. There is, however, a lower limit size for the panels. Below this limit, the calculation becomes unstable or leads to non-physical results. This can typically occur with a sine spanwise panel distribution.
- An increased mesh density at the leading and trailing edges can be obtained by using a cosine panel distribution in the chordwise direction. In general, more precise calculations and shorter computational times are obtained with a well refined mesh.
- The aspect ratio of the panels should be low, since large panel length differences in streamwise and chordwise directions can result in numerical instabilities for a 3D

panel method analysis.

- Considering a panel method, all corners of each panel should be in the same plane, since first order panels are used. This is not possible for twisted geometries, however for small twist angles errors will be acceptable.
- Considering the VLM, use the same amount of chordwise panels along the wing span with a similar distribution. This way, all connected panels have the same edges and nodes. As a result errors due to discretization will be smaller when determining surface velocity, which is defined as the gradient of doublet strengths between adjacent panels.

Trefftz-plane analysis

Since these methods are all potential flow based and thus inviscid, only the induced drag part can be determined directly. For this, a Trefftz-plane analysis is used, which is a far-field method based on the balance of the momentum on a control surface far downstream of the body. As mentioned in the guidelines of XFLR5 (XFLR5, 2011), it is generally reported that the drag and lift results from near-field analysis are significantly higher and less representative than those resulting from a calculation in the Trefftz-plane. This is reported for almost all VLM and panel codes (Smith, 1996). The implementation in XFLR5 for the calculation of lift and drag is therefore the far-field method. Pressure distributions cannot be obtained from a Trefftz-plane analysis, therefore XFLR5 shows the panel pressures obtained by near-field analysis. As a consequence the integral of the pressure distribution might be different from the values obtained by Trefftz-plane analysis.

3.4 Recap and introduction to a new aerodynamic method

In the preceding chapters knowledge is gained about the currently available aeroelastic kite models and the characteristics and (dis)advantages of several aerodynamic analysis methods. This information lead to the development of a new aerodynamic analysis method which is presented in the upcoming chapters. It includes those properties required for the current demand of dynamic kite models.

In this chapter it is shown that potential flow based methods incorporate 3D aerodynamic effects and are therefore capable of predicting the inviscid aerodynamics of non-planar wings. They only have to solve one linear differential equation, instead of four nonlinear differential Equations required for Navier-Stokes and Euler. Moreover potential flow requires only a boundary grid, not a full fluid space discretization. As a result the effort of grid generation is considerably reduced. On the other hand, potential flows assume no vorticity and viscosity, making it impossible to model turbulence, separated flow and boundary layers. Since these nonlinear effects strongly influence the behavior of power kites they should be incorporated in the aerodynamic model. Nonlinear LLT uses a lift correction to incorporate nonlinear effects where the characteristics of the spanwise sections are determined by predefined lift curves. Unfortunately LLT does not hold for non-planar wings. Breukels' aerodynamic model contains functions based on CFD results and offers a reliable way to obtain viscous data of the non-conventional shape of kite airfoils. His model is however limited in incorporating 3D effects and variations in chordwise direction.

Given that the aerodynamic model requires short calculation times and reasonable

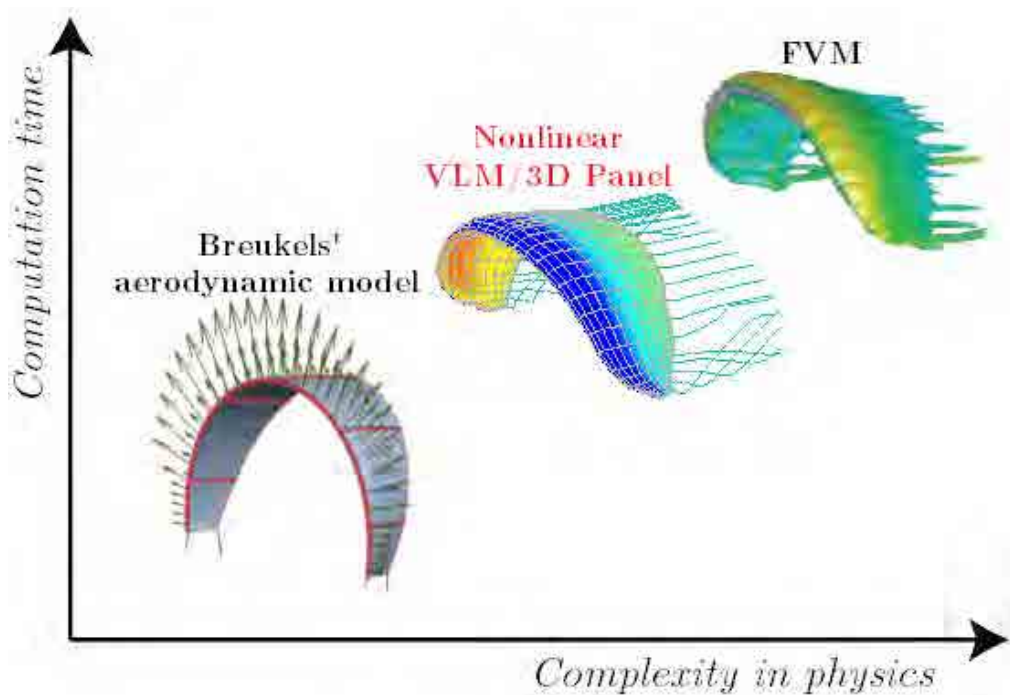


Figure 3.11: The relative position of the new method, a nonlinear VLM/3D panel method, with respect to other available aerodynamic methods.

accuracy a method is developed which is based on a potential flow method and additionally implements nonlinear effects in an iterative manner. The new method uses a similar type of correction as the one used in nonlinear LLT, only the viscous characteristics of the spanwise sections are implemented in a different manner. The correction of sectional lift in an iterative manner improves the capability of predicting realistic pressure distributions at high angles of attack. Since almost no experimental data on typical profiles of LEI kites is available, XFOIL, CFD data and regression models are used to serve as 2D sectional data source. In this way the method combines the features of potential flow, nonlinear LLT, high-fidelity CFD and Breukels' method.

The computation times of the proposed method are in the order of those used in a VLM and 3D panel method. The accuracy is higher than those of a normal VLM, 3D panel method, nonlinear LLT or Breukels' method, but of course lower than those obtained by high-fidelity CFD. Figure 3.11 shows how the new proposed method relates to other available methods. It fills the gap between simple linear analytical methods and complex Euler and Navier-Stokes Equation solvers and therefore reduces lagging of CFD/CSD based aeroelastic methods for kites, see Figure 3.12. It can be used for as simple models such as multi-plate, but also for lower order FEM models. The degrees of freedom are however limited, therefore it would not be able to generate variable forces for all elements in a detailed 3D FEM model.

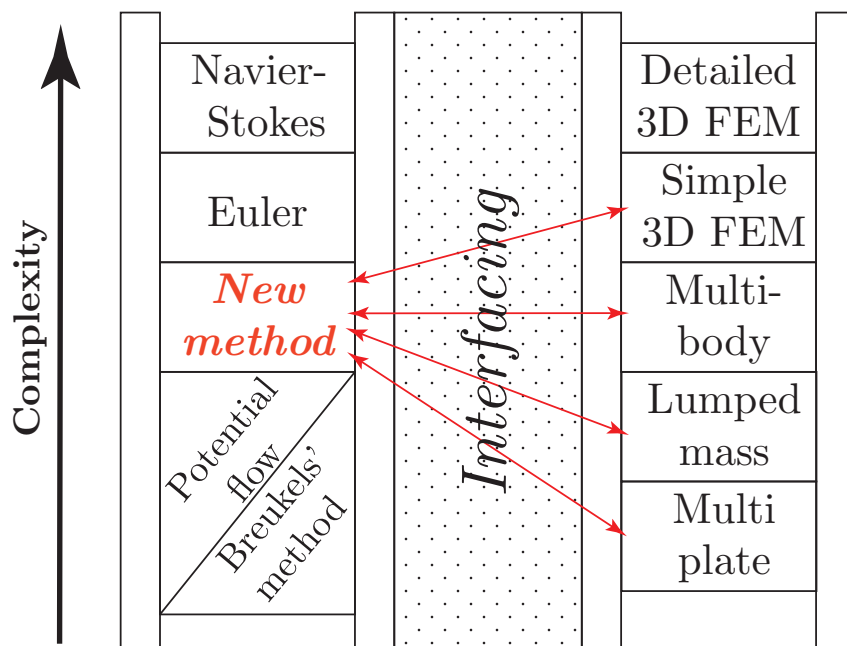


Figure 3.12: Levels of fidelity used in fluid-structure interaction computations.

Nonlinear VLM and 3D Panel Method

Regarding the aerodynamic tool study in the previous chapter, XFLR5 is chosen to work with. By default, the VLM and 3D panel method ignore profile drag, though XFLR5 uses interpolation, based on the results of 3D wing analysis, on predetermined 2D viscous lift to drag polars. Especially for kites, which often fly close to stall, it is of great importance to have a tool which is able to determine the aerodynamics in the non-linear regime. In this chapter, methodologies are investigated that use a lift correction to implement this non-linear behavior. Two methods are found in literature, on which several interpretations resulted in a set of different algorithms. The main differences are the determination of induced angles, whether iterative solving is used and the manner in which profile drag is determined.

4.1 Implementing non-linearity by using lift correction

Since 3D panel methods and VLM's are inviscid methods, significant viscous phenomena such as boundary layer transition and separation are neglected. In the VLM a mean camber line is used and thus also thickness effects are neglected. The assumption of neglecting viscosity and thickness will affect lift and drag values. Especially when non-linear behavior occurs, such as separation in the high angle of attack region, predicted values will deviate from reality. By making use of viscous 2D airfoil calculations, lift corrections on multiple spanwise sections can be implemented in a 3D analysis. Though any 2D airfoil data source could be used, in the validation of these methods XFOIL is used. Before explaining the method used to perform such a correction, the definition of the effective angle of attack is explained, which is required for the nonlinear potential flow methods.

4.1.1 Effective angle of attack

By definition, the lift force acting on a wing is directed perpendicular with respect to the velocity vector. In case the wing is under an angle of attack α_∞ , the lift vector should not be taken perpendicular with respect to the freestream velocity vector V_∞ , but with

respect to the induced velocity vector v_i . This is the vector which is deflected with a downwash angle (or induced angle of attack) α_i . As a result, the direction of the lift force is also deflected by this angle, as illustrated in Figure 4.1. It can be seen that this will reduce the magnitude of the lift force, which is therefore called the effective lift. Since the airflow has already been deflected with the induced angle, this angle is not effective in terms of lift production. Therefore, the effective lift is caused only by the difference between the airflow direction and the airfoil, which is called the effective angle of attack.

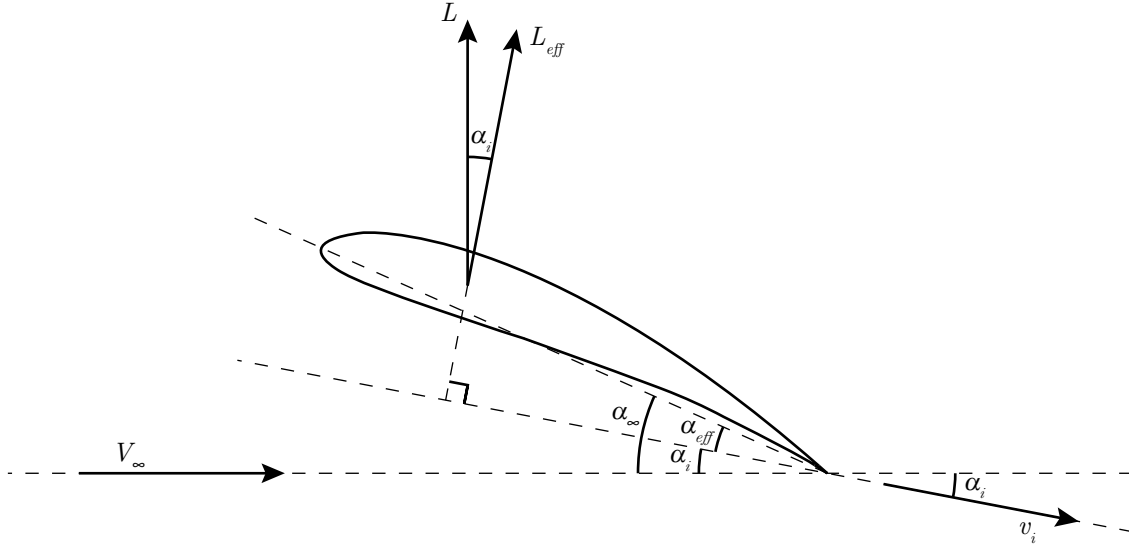


Figure 4.1: Definition of the effective angle of attack, induced angle of attack and effective lift vector.

Adding a spanwise twist distribution (α_{twist}) to the wing can be used to reduce the lift and induced drag near the tips. Taking this into account, the effective angle of attack α_{eff} of an airfoil is defined as

$$\alpha_{eff} = \alpha_{\infty} - \alpha_i + \alpha_{twist} \quad (4.1)$$

4.1.2 Angle shift on lift curve

For the effective angle of attack seen by a section, which is dependent of the downwash created by the trailing wake, the inviscid and viscous lift coefficients can be determined by making use of XFOIL. In Figure 4.2, an example is shown of such an inviscid and viscous $C_l - \alpha$ polar. To account for viscosity in a 3D analysis a shift on the initial effective angle $\alpha_{eff,original}$ is performed. Now, the airfoil works at an angle of attack which has the same lift coefficient as the viscous lift coefficient before the angle shift called $\alpha_{eff,new}$. This can also be defined as shown in Equation 4.2, where $\alpha_{eff,original}$ is defined as in Equation 4.1 and α_s represents the angle shift.

$$\alpha_{eff,new} = \alpha_{eff,original} - \alpha_s \quad (4.2)$$

This method assumes implicitly that the airfoil's behavior on a finite wing is similar to that of an infinite wing, with only a correction for the spanwise induced angles of

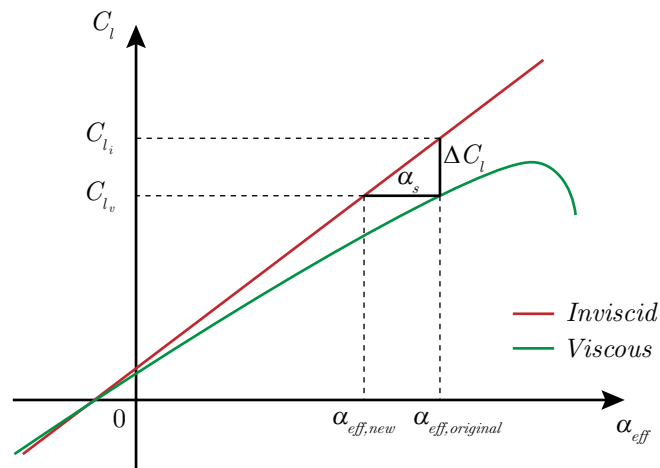


Figure 4.2: Angle shift correction method on 2D lift polars to account for viscous effects in a 3D analysis.

attack. There is no real background, neither theoretical nor experimental, to support this approach. However, the results of Horsten (initial proposer of this method) and Gaunaa show significant improvement on the results when compared to experimental and CFD data.

4.2 3D analysis methodology

In the previous section, the principle of using angle shifts to correct 3D potential flow methods is explained. Both Horsten (Horsten & Veldhuis, 2009) and Gaunaa (Gaunaa et al., 2010) use this method to correct a VLM, each having different characteristics. In this section, these variants are discussed followed by the explanation of the newly developed algorithm.

4.2.1 Reference literature on lift correction methods

As mentioned before, two papers are found that consider the use of angle shifts for lift correction: Horsten (Horsten & Veldhuis, 2009) was the initial proposer of this method, followed by Gaunaa et al. (2010) who developed an equivalent algorithm in cooperation with Carqueija et al. (2010), who have a different approach for the calculations and implementation.

The applications used to validate their methods are a planar wing in the case of Horsten and a highly non-planar, circular arc shaped kite in the case of Gaunaa. They use different programs for the implementation of their methods: Horsten uses Athena Vortex Lattice (AVL) with a 2D viscous airfoil calculation in XFOIL, while Gaunaa combines a VLM written earlier by himself with XFOIL. However, Gaunaa states that 2D airfoil data from any other source works as well. This is shown in his validation, where he actually uses CFD results.

To account for viscosity, a shift on the initial effective angle is performed, as explained in the previous section. Therefore, the calculation of the effective angle will have large impact on the quality of results. The definition, as shown in equation 4.1, is based on

geometrical input, freestream input and resulting induced angles. Horsten determines the induced angles by using Trefftz-plane calculations. Gaunaa indirectly determines the induced angles based on spanwise lift distribution and Thin Airfoil Theory (TAT). Furthermore, they use different implementations of the angle shift: Horsten uses a geometrical change by applying twist, while Gaunaa changes the local inflow angle on every spanwise section, which is defined at the Right-Hand-Side (RHS) of the matrix equation. The latter method is significantly more efficient in terms of computational effort. In the method of Gaunaa, iteration until convergence is used, whereas Horsten only uses one iteration of the correction. For the determination of the viscous drag, Horsten uses the final effective angle of attack after the angle shift. Gaunaa, however, uses the initial effective angle of attack.

4.2.2 Determination angle shift: 3D panel method vs VLM

The proposed correction method by Horsten is to correct a VLM for viscosity effects. Gaunaa states that his correction method introduces the effect of airfoil thickness and viscosity.

The angle correction is based on the difference between a viscous and inviscid 2D panel method calculation. Both these calculations include the thickness of a profile and thus the difference does not include a thickness correction. If, however, TAT would be used to calculate the inviscid lift curve, Gaunaa's statement is correct in the sense that there is a correction for both thickness and viscosity. Therefore, such a method would in theory be more appropriate when correcting a VLM, since it is only applicable for thin surfaces. The method where only viscosity is corrected would be appropriate for a 3D panel method. This viscous/thickness effect methodology is illustrated in Figure 4.3.

4.2.3 Implementation in XFLR5

From the discussed methods and theories, several options for using angle shifts are available. These combinations are not purely theoretical, but represent artificial methods to correct for thickness and viscosity. One can choose between the following options concerning the method of angle shift correction:

- Angle shift calculation:
 - TAT vs XFOIL
 - Induced angle calculation
- Potential flow method: VLM vs 3D panel method
- Number of iterations: convergence vs limited
- Implementation angle shift: RHS vs geometry (twist)
- Viscous drag calculation: initial vs final α_{eff}

The angle shift method is implemented in XFLR5 and above mentioned options are made available, except for the angle shift implementation. For this, changing the local inflow angle defined at the RHS is used. This is far more efficient in terms of computational effort, because the time consuming process of calculating influence matrices is in this

way avoided. The determination of the angle shifts is the core of the implementation of nonlinearity, therefore two algorithms similar to Horsten and Gaunaa's methods are constructed in which the options can be adjusted. The used program structures by Gaunaa and Horsten are given below. As mentioned before, Gaunaa uses TAT for which $C_{l_\alpha} = 2\pi$.

Method of Horsten	Method of Gaunaa
1 Perform an inviscid VLM calculation and calculate the induced angles in the Trefftz plane	1 Perform an inviscid VLM calculation and save the $C_{l,original}$ for each section along the span
2 Calculate $\alpha_{eff} = \alpha_\infty + \alpha_i + \alpha_{twist}$	2 Initialize $\Delta\alpha_i$ as equal to zero
3 Determine angle shift $\alpha_s = \frac{\Delta C_l}{C_{l_\alpha}}$	3 Find α_{eff} each section, from: $\alpha_{eff} = \frac{C_{l,original}}{C_{l_\alpha}} + \alpha_0 - \Delta\alpha_i$
4 Add α_s to RHS	4 Calculate angle shift $\alpha_s = \frac{\Delta C_l}{C_{l_\alpha}}$
5 Return to step 1 and iterate until convergence or a predefined iteration limit	5 Add α_s to RHS
6 Use final α_{eff} to calculate profile drag	6 Perform new VLM calculation and save for each section along the span the new lift coefficient $C_{l,final}$
	7 Calculate $\Delta\alpha_i = \frac{C_{l,original} - C_{l,final}}{2\pi} - \alpha_s$
	8 Return to step 3 until convergence or a predefined iteration limit
	9 Use initial/final α_{eff} to calculate profile drag

The complete program overview in XFLR5 is visualized in Figure 4.4. A more general overview is given in Appendix ??. The program structure of XFLR5 is based on an earlier developed panel method: VSAERO (Maskew, 1987). In the function 'BuildInfluenceMatrix' the unit doublet or vortex influence at the boundary condition points are determined for each panel. To save on computing time, inline functions are used for the vectorial operations, resulting in a longer, but 4 times more efficient code. Then in 'CreateUnitRHS' three unit RHS vectors are generated, one for every direction: u_{RHS} , y_{RHS} and z_{RHS} . By default y_{RHS} is not used in the program, but since angle shifts are applied perpendicular to each section, these components will be present for wings with dihedral. When the 3D panel method is used, doublets are added to the influence matrix for wake contributions. The Kutta-condition is added to the matrix equation. With the matrix of influence coefficients known, a loop is started in which the matrix is solved and accordingly, angle shifts are iteratively applied. In this loop the function 'CreateSourceStrength'

is only required for the 3D panel method, where \hat{V}_∞ is defined as:

$$\hat{V}_\infty = \begin{Bmatrix} u_x \\ u_y \\ u_z \end{Bmatrix} \quad (4.3)$$

In 'CreateDoubletStrength' the unit RHS vectors are scaled with the unit components of the freestream vector, given in equation 4.10. In 'ComputeFarField' the spanwise lift, drag and induced velocities are determined. When the iteration loop is ended, the results are scaled for total speed to give the correct absolute surface velocities, pressures and forces. Lastly viscous drag is added.

Non-linear VLM/3D panel method

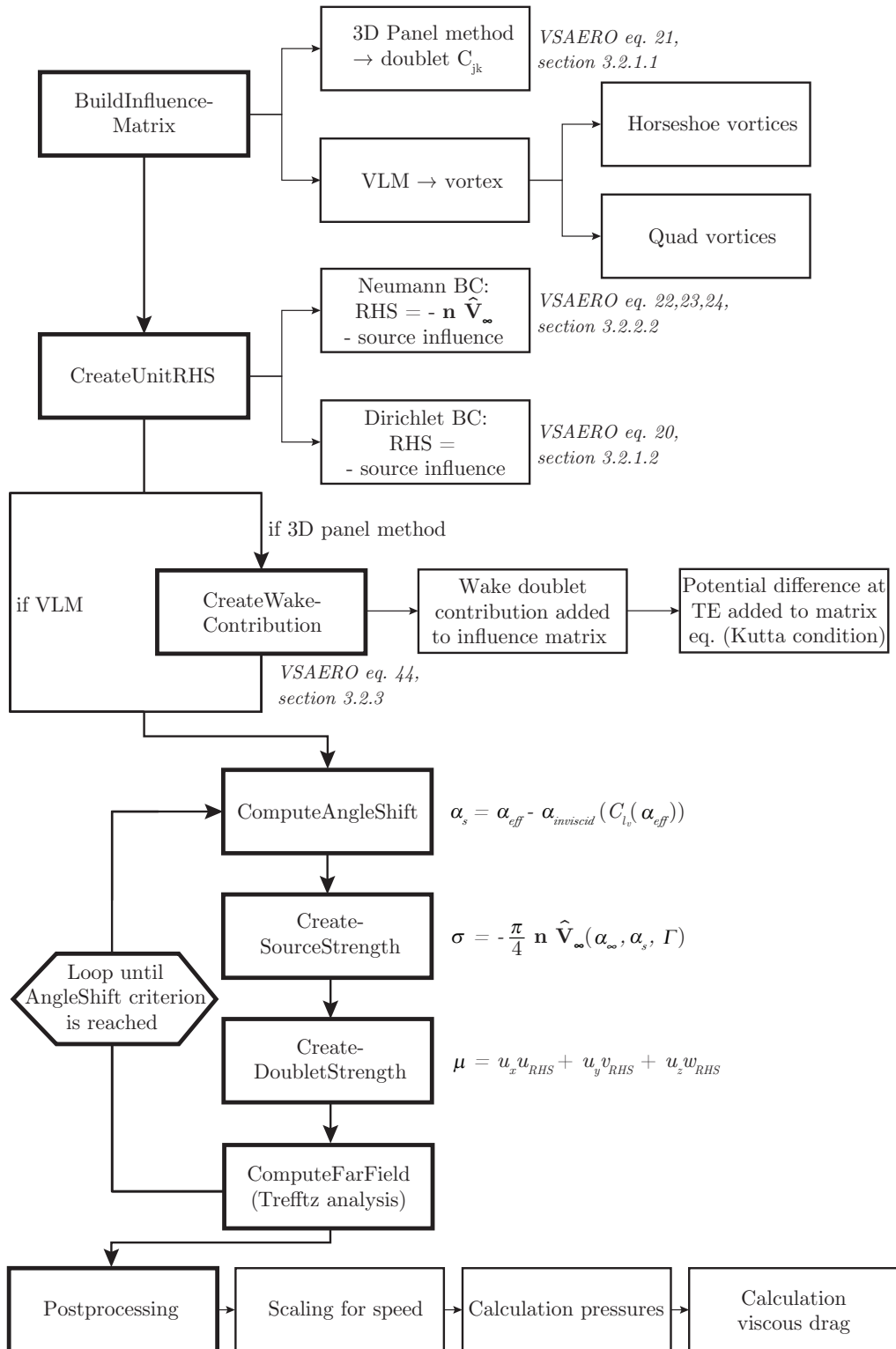


Figure 4.4: Flow diagram of the adapted XFLR5 program structure.

4.3 Program features of the adapted XFLR5 software

Besides the implementation of the angle shift methods, a number of other features have been included in the adapted XFLR5 program. In this section, these adjustments are presented.

4.3.1 Inviscid 2D lift curve

When determining the angle shifts, both the viscous as inviscid lift curve of the airfoils is required. A practical issue is that the build in XFOIL version in XFLR5 is not capable of determining inviscid lift values and polars, though the stand alone version of XFOIL is capable. This feature has been added in the adapted XFLR5 version such that also the inviscid lift value and inviscid $C_l - \alpha$ curve are automatically generated when doing viscous XFOIL calculations. The function for linear interpolation between different airfoil curves and Reynolds numbers is also added for the inviscid lift curves.

When using TAT for the determination of angle shifts, an external program was used, written in Matlab. XFLR5 is adapted such that external inviscid lift values can be imported from simple text files. The theory of the TAT programs can be found in Appendix C.

4.3.2 Trefftz plane calculations

By standard, the induced angles in XFLR5 are measured in the $x - z$ plane, therefore not taking into account out of plane sections. In the adapted version, the induced angles are calculated normal to a section. The induced angle is determined as shown in Equation 4.4, where w represents the downwash and v is the induced velocity. In this section, it is explained what procedure is used to adapt the induced velocity components.

$$\alpha_i = \frac{w}{v} \quad (4.4)$$

An incoming airflow under an angle of attack α can be decomposed in two dimensional velocity vectors in the x and z direction, as shown in Figure 4.5.

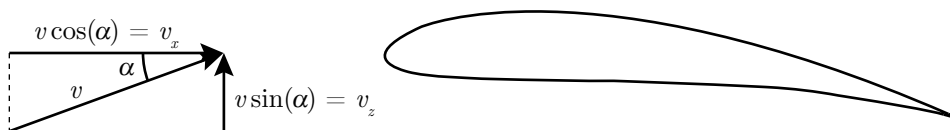


Figure 4.5: Two dimensional airflow acting on an airfoil with a local angle of attack α .

In case a wing has sections with dihedral, the components of the velocity vector acting perpendicular to the section are required to obtain the exact three dimensional total velocity vector. This can be determined with a simple model in the $y - z$ plane (front view), as shown in Figure 4.6. Here, the two dimensional z component is projected on a wing section with a certain dihedral Γ , together with its perpendicular component with respect to the wing surface.

Using the geometry, one can find relations for the y and z components of this perpendicular velocity vector. Now, including the effect of dihedral, the total velocity vector (or

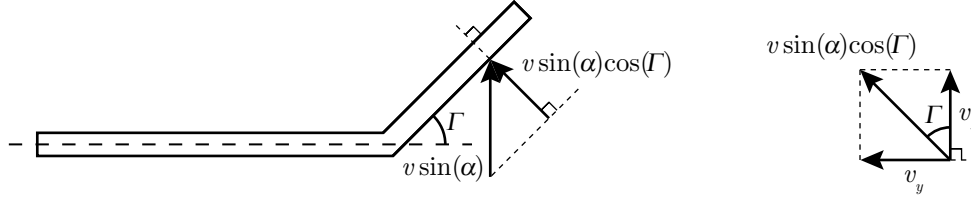


Figure 4.6: Perpendicular velocity vector projected on the wing dihedral.

wind direction) is defined as

$$\mathbf{v}_w = \begin{bmatrix} v \cos(\alpha) \\ v \sin(\alpha) \cos(\Gamma) \sin(\Gamma) \\ v \sin(\alpha) \cos^2(\Gamma) \end{bmatrix} \begin{bmatrix} x \\ y \\ z \end{bmatrix} \quad (4.5)$$

From this, the vector perpendicular to the wind direction and the wing surface can be determined, which is called the wind normal vector. Considering a spanwise section of the dihedral wing as a two dimensional vector (no sweep), the wind normal vector can be computed by means of the cross product method. In other words, this is solving the determinant of the three dimensional velocity vector matrix for both vectors. Considering all three components (\mathbf{i} , \mathbf{j} , \mathbf{k}) of two vectors, which are in this case the wind direction vector and spanwise dihedral wing, the wind normal vector acting in perpendicular direction on both vectors can be determined as

$$\begin{aligned} \mathbf{v}_n &= \mathbf{v}_w \times \Gamma \\ &= \begin{vmatrix} \mathbf{i} & \mathbf{j} & \mathbf{k} \\ \cos(\alpha) & \sin(\alpha) \cos(\Gamma) \sin(\Gamma) & \sin(\alpha) \cos^2(\Gamma) \\ 0 & \cos(\Gamma) & \sin(\Gamma) \end{vmatrix} \\ &= \begin{vmatrix} \sin(\alpha) \cos(\Gamma) \sin(\Gamma) & \sin(\alpha) \cos^2(\Gamma) \\ \cos(\Gamma) & \sin(\Gamma) \end{vmatrix} \mathbf{i} + \begin{vmatrix} \cos(\alpha) & \sin(\alpha) \cos^2(\Gamma) \\ 0 & \sin(\Gamma) \end{vmatrix} \mathbf{j} \\ &\quad + \begin{vmatrix} \cos(\alpha) & \sin(\alpha) \cos(\Gamma) \sin(\Gamma) \\ 0 & \cos(\Gamma) \end{vmatrix} \mathbf{k} \\ &= [\sin(\alpha) \cos(\Gamma) (\sin^2(\Gamma) - \cos^2(\Gamma))] \mathbf{i} + [\cos(\alpha) \sin(\Gamma)] \mathbf{j} + [\cos(\alpha) \cos(\Gamma)] \mathbf{k} \end{aligned} \quad (4.6)$$

Thus, the velocity vector normal to the section and to the freestream velocity vector is defined as

$$\begin{aligned} \mathbf{v}_x &= \sin(\alpha) \cos(\Gamma) (\sin^2(\Gamma) - \cos^2(\Gamma)) \\ \mathbf{v}_y &= \cos(\alpha) \sin(\Gamma) \\ \mathbf{v}_z &= \cos(\alpha) \cos(\Gamma) \end{aligned} \quad (4.7)$$

The wind normal vector affects the induced angle of attack, and will therefore change the effective angle for sections with dihedral.

From performed simulations on a flat wing configuration, results from the VLM showed induced angle distributions with values twice as large with respect to the 3D panel method. From theory, the LLT should give rather accurate results for a flat wing. Therefore, the induced angle distributions are compared with LLT and it showed that the 3D panel method results were similar. An error was present in the calculation of the induced angles and was solved by dividing the induced angle calculations in the VLM code by 2.

4.3.3 Local effective angle of attack and Reynolds number

As given in Equation 4.1, the definition of the effective angle of attack is

$$\alpha_{eff} = \alpha - \alpha_i + \alpha_{twist}$$

Here α is the local freestream angle of attack and therefore dependent on dihedral, as shown in Equation 4.8.

$$\alpha_{local} = atan(tan(\alpha)cos(\Gamma)) \quad (4.8)$$

The induced angle of attack is already defined perpendicular to the panel normal as described in the previous section. Note that side slip angles are not included in the equations. This is because these are by default implemented in XFLR5 by changing the geometry, not by changing the freestream direction.

Besides the spanwise variations in effective angles, also chord length c_{local} varies over span for wings with taper. The angle shift is therefore determined by interpolation on multiple polars for the local Reynolds number defined as:

$$Re_{local} = \frac{V_{\infty}c_{local}}{\nu} \quad (4.9)$$

Here ν is kinematic viscosity.

4.3.4 Implementation angle shift

In Section 4.3.2 a dihedral effect was implemented on the induced angle calculations. A similar approach is used to add the angle shift to the RHS. The RHS represents the freestream velocity normal to a panel. This is normally defined as a scalar V_{∞} multiplied by a vector containing all panel normals. By adding an angle shift to each spanwise station, the scalar V_{∞} becomes a vector acting as a local freestream velocity vector varying in spanwise direction. Here, the local velocity is changed by including an angle shift and is therefore dependent on dihedral. This results in a new local velocity as shown in Equation 4.10, where α_s represent the angle shift.

$$\begin{aligned} \mathbf{u}_x &= \cos(\alpha_s \sin(\Gamma)) \cos(\alpha + \alpha_s \cos(\Gamma)) \\ \mathbf{u}_y &= \cos(\alpha + \alpha_s \cos(\Gamma)) \sin(\alpha_s \sin(\Gamma)) \\ \mathbf{u}_z &= \cos(\alpha_s \sin(\Gamma)) \sin(\alpha + \alpha_s \cos(\Gamma)) \end{aligned} \quad (4.10)$$

4.3.5 Viscous drag calculation

In the original version of XFLR5, the profile drag is based on an interpolation of the $C_l - C_d$ curves from a 2D analysis. This can result in difficulties at high angles of attack, since at certain lift values the solution of viscous drag may not be unique (different drag values for same lift value before and beyond stall). Therefore, in the adapted version, it is avoided to use the lift coefficient when determining profile drag. Instead, the effective angle of attack is used to determine the viscous drag in the $C_d - \alpha$ curve.

In his method, Gaunaa (Gaunaa et al., 2010) calculates the profile drag for the original (initial) effective angle of attack, thus also using the original induced angle of attack. It is however preferred to use the final induced and effective angles (similar to Horsten's algorithm), because these correspond to the viscous lift distribution instead of the uncorrected, initial inviscid lift distribution. Similar as mentioned in Sections 4.3.2 and 4.3.4, the effective angle is determined perpendicular to each spanwise section.

4.4 Program settings

A number of adjustments have been performed on the original XFLR5 program so far. In the uncorrected version, several settings significantly affect the results of 3D analyses. The most important are discussed in this section, using knowledge both from the XFLR5 guidelines and by testing the software.

4.4.1 Grid discretization study

In Figure 4.7 a grid convergence plot is given for the two VLM's and 3D panel method. Not much gain can be obtained by using grid sizes of more than 1,000 panels i.e. less than 1% with respect to the finest grid. Mark that for the same discretization, the panel method uses roughly two times more panels, as it uses panels for the upper and lower surface. For the same discretization, where 512 panels are used for the VLM's and 1056 for the panel method, the latter takes approximately 800ms versus 100ms for the VLM's. Next to this, the computation times of the panel method are higher, because it uses paneling of the wake. VLM2 is slightly faster than VLM1, since it has less computational heavy horseshoe vortices to calculate. When the option 'Tilted Geometry', i.e. a free wake, is disabled the gains of using VLM2 instead of VLM1 for full angle sweeps is many times higher.

4.4.2 Boundary condition

For the VLM, the Neumann boundary condition (BC) is the only option, i.e. the velocity's component normal to the surface must be zero. Considering available BC's for the 3D panel method, the options are the Neumann BC and the Dirichlet BC. In the latter case the velocity's potential on the panel's inside surface is zero, so that the total potential inside the body is equal to the freestream velocity's potential. The Dirichlet BC can be used in cases where there are non-zero normal velocity components, e.g. to model BL displacement effect, entrainment or inflow/outflow for engine inlet/exhaust modeling. These physical phenomena are not studied at the moment, however the resulting formulation which follows from using the Dirichlet BC is "by far the simplest formulation (..), even simpler than the method based on the external Neumann boundary condition" (Hess &

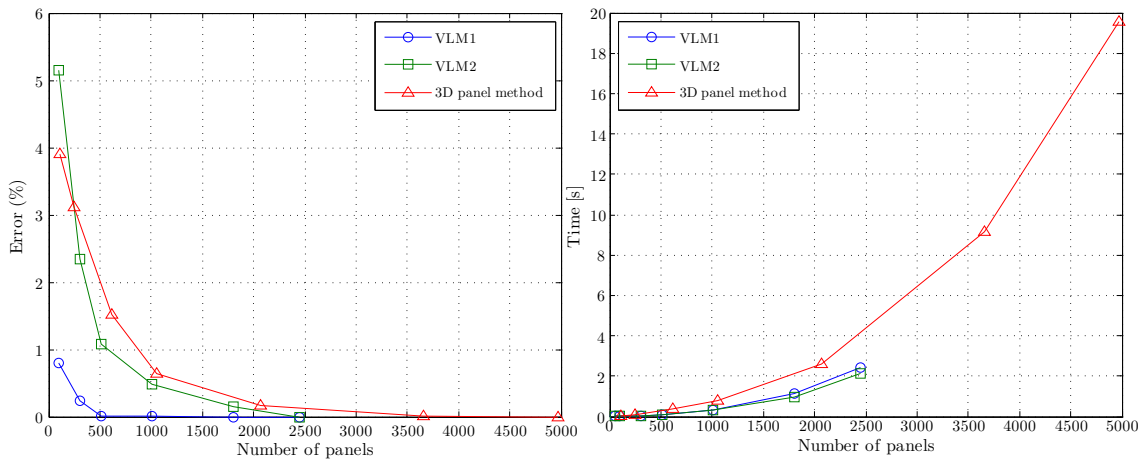


Figure 4.7: Effect of the number of panels on the error with respect to the finest grid and computational time for the flat wing case (see Section 5.2.1), using inviscid calculations. The computational times correspond to the average over an angle of attack sweep of 21 steps.

Smith, 1962). Furthermore, the guidelines of XFLR5 say: "After a trial and error process, the Dirichlet BC have been preferred to the Neumann BC. The latter method is more sensitive to local geometry changes, and leads to less convincing results. This is also the choice used by the developer of VSAERO: Maskew (1987)."

Several simulations with both boundary conditions showed that there is no significant difference in calculation time and lift and drag values (less than 1% smaller). In future calculations the Dirichlet BC will be used, as preferred by Maskew (1987), XFLR5 (2011) and Hess & Smith (1962).

4.4.3 Wake direction

Another calculation setting which can be altered is to use 'Tilted Geometry' (TG) which means the wake is in the direction of the flow (free wake) and not simply parallel to the body's x -axis (fixed wake), see Figure 4.8. The option of a free wake was unfortunately not working in the 3D panel method of XFLR5 and thus a fixed wake will be used.¹ It was observed from simulations, that the inviscid VLM lift curves were slightly non-linear without using the TG option. With TG on, the lift slope became more linear, which is expected of a linear method. The remaining non-linearity is probably due to numerical errors.

A free wake is a more realistic representation of the flow, because the flow gets aligned in free stream direction shortly after it smoothly leaves the trailing edge. Considering that the trailing edge vortices extent to $100 \times \text{MAC}$ behind the wing, the representation of a fixed wake is strongly deviating at high angles of attack. The main purpose of a fixed wake, which is based on a small angle of attack assumption (XFLR5, 2011), is to reduce computational effort when simulating multiple angle of attacks, because then the influence coefficients of the wake remain the same and do not have to be recalculated. This is however not of interest when considering the software should function as part of

¹The current moderator confirmed the bug and in future versions it will be available.

an aeroelastic solver, which requires only one calculation for one geometry.

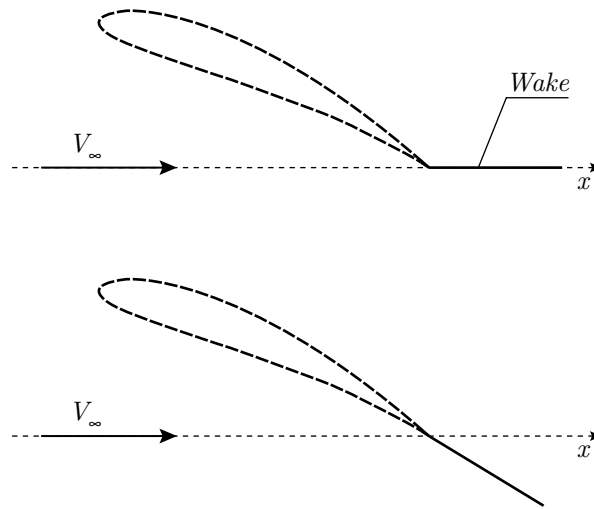


Figure 4.8: Placement of wake direction with (bottom) and without (top) using the tilted geometry setting.

In Figure 4.9 a comparison is made between the inviscid lift curves of XFLR5, where both the curves for fixed and free wake is given. With a comparison between the methods without TG, it is determined whether the results are according to the made assumptions. The curves for VLM1 and VLM2 almost exactly match and have a bit smaller slope than the panel method, which is expected as the latter includes airfoil thickness. To confirm the similarity with the 3D panel method results a wing with only 1% thickness was simulated. This way, the thickness of the profile has minimal effect on the results and thus similar results for all three methods is expected. This was indeed the case, where the panel method showed a difference in lift slope with the two similar VLM's of less than 2%.

In Figure 4.9 stands out that there is a significant difference in lift slope between the two VLM's with a free wake (+TG). At first instance it cannot be determined which method has the highest accuracy, therefore both methods were compared in the validation cases in the next chapter. It was found that the nonlinear method with using VLM2+TG showed (slightly) better results in all validation cases. Therefore only VLM2 is used in future considerations, unless noted otherwise.

4.4.4 Applying twist

A new definition of applying twist to the wing is implemented in the code, since the definition was incorrect for out of plane sections. In the definition, it is assumed twist is applied linear to the panel.

In the XFLR5 version used to implement the algorithms, it was noticed that applying twist makes the chord length smaller and thus local C_l larger. This is a small error in the software, which is fixed in the new version XFLR5 6.07.

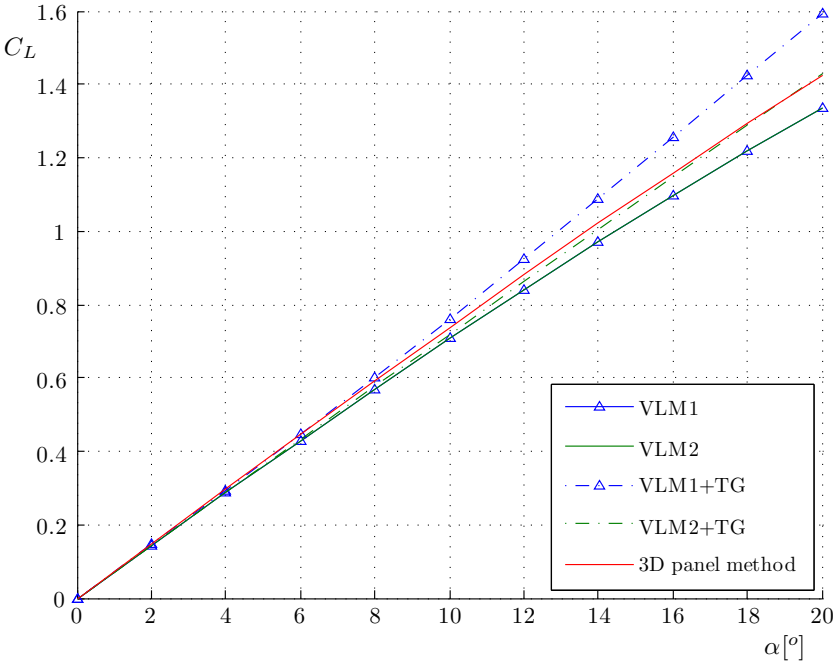


Figure 4.9: Inviscid lift curves of the two VLM's and 3D panel method for the flat wing case.

Software Validation and Selection

In order to prove the quality of the adapted aerodynamic tool, the software needs to be validated. Because the capabilities of the proposed nonlinear potential flow method extend far beyond serving as aerodynamic load model for an FSI solver, validation is performed for several, different wing shapes. An example of its possible use for other wing shapes, is the fact that the developed software was also used as a design tool for the Ampyx PowerPlane, as described by Agten (2012). Next to this, kite design for AWE systems might change significantly in the upcoming years and it would be of great use if this tool can handle a variety of wing shapes. To evaluate the different options within the method, as proposed in the previous chapter, a statistical trade-off procedure is used, based on the cases for which windtunnel data was available.

5.1 Program versions

In Section 4.2.3 several options were identified for implementing the non-linear methods in XFLR5. The core difference is the implementation of the angle shift, for which one approach is described by Gaunaa et al. (2010) and one by Horsten & Veldhuis (2009). Within the method of Gaunaa several possibilities are identified, such that in total four different versions are investigated:

1. Methods of Gaunaa with original effective angle of attack used for viscous drag calculation, as is proposed by Gaunaa. In these methods, induced angles are implicitly determined from lift values. Also, iteration until convergence is used for these versions.
 - (a) Version MG: based on difference between inviscid and viscous lift curve, where a inviscid lift slope value of 2π is used corresponding to thin airfoil theory. This version is therefore equivalent to that of Gaunaa. For the inviscid lift curve Gaunaa originally uses XFOIL's calculation, this will be indicated with version MG (XFOIL). Another possibility is to use TAT to determine the inviscid lift curve, this will be indicated by version MG (TAT).
 - (b) Version MG_a : based on interpolation between inviscid and viscous lift curve and corresponding inviscid lift slope, which can be different than 2π since

XFOIL's inviscid calculation includes thickness. Using TAT for the inviscid lift curve would be equivalent to version MG (TAT) and is therefore omitted.

2. Version MG_b : same as method of Gaunaa, version MG, but with final effective angle of attack used for viscous drag calculation. Using TAT for the inviscid lift curve would be equivalent to version MG (TAT) and is therefore omitted. Also, iteration until convergence is used in this version.
3. Version AK: this version is based on the method of Horsten, for which the inviscid lift curve from XFOIL is used (as in MG_a). The viscous drag is determined as done with version MG_b , using the final effective angle of attack. Induced angles are determined directly from Trefftz-plane calculations and 1 iteration of the angle shift loop is used.

5.2 Reference data

From experimental windtunnel data and CFD results found in literature, four cases are selected to validate the aerodynamic analysis tool and choose the most promising version. First of all, a simple flat wing with no taper, twist or dihedral is used to also compare results with the algorithm of Horsten. This is followed by a set of 4 swept wings, which differ in airfoil section (symmetrical and cambered) and aspect ratio. The third case is again a straight wing on which a winglet is mounted in a range of different dihedral angles. Lastly, an arc shaped wing is considered, which is treated in the fourth case. Since this is the model used by Gaunaa to validate his work, the version in which his algorithm is processed (version MG) can be compared.

5.2.1 Flat wing

The first validation case is the wing configuration found in the work of Horsten (Horsten & Veldhuis, 2009), and used for academic experiments at the Delft University of Technology. It concerns a planar wing with no sweep, twist and taper. Experimental data from this configuration is obtained for $Re = 1 \cdot 10^6$. The wing profile used is the NACA - 64₂(A)015, from which the coordinates and 2D windtunnel data for $Re = 1 \cdot 10^6$ are known (Wirsing, 1999). The wing properties are shown in Table 5.1 and a 3D model in XFLR5 can be seen in Figure 5.1.

Windtunnel data from this configuration is uncorrected for wake blockage effects due to wall interference. This could have an impact on the resulting lift coefficient. Therefore, a correction factor for 3D models in a rectangular closed windtunnel is considered to verify the influence for this particular case. The wake blockage factor is defined as (Garner et al., 1966):

$$\varepsilon_b = \frac{1}{4} \left(\frac{S}{bh} \right) \frac{1}{\beta^2} C_D \quad (5.1)$$

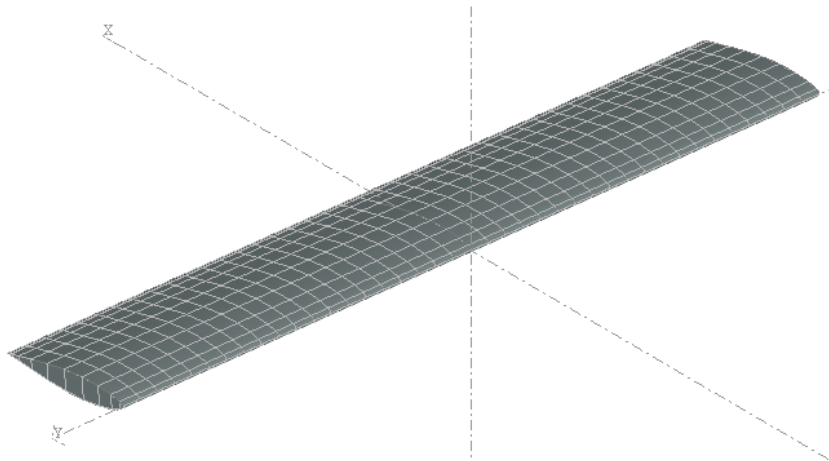
Here, S is the wing surface area, b and h are the width and height of the windtunnel, respectively, β is the Prandtl-Glauert compressibility factor and C_D is the corresponding drag coefficient. Inserting the required parameters results in:

Table 5.1: Flat wing configuration parameters.

Parameter	Value
Airfoil	NACA - 64 ₂ (A)015
Reynolds number	$1 \cdot 10^6$
Wing span	1.28 m
Chord length	0.24 m
Surface area	0.31 m^2
Aspect ratio	5.3

$$\varepsilon_b = \frac{1}{4} \left(\frac{1.28 \cdot 0.24}{1.25 \cdot 1.80} \right) \frac{1}{1 - \left(\frac{62.5}{340} \right)^2} C_D = 0.0353 C_D$$

The drag coefficient is in the range of $0.006 < C_D < 0.12$, so the correction factor is of negligible value ($< 0.5\%$). Therefore no adjustments have been done on the lift curve values. The drag coefficient polar, however, shows an increased constant value. This is due to the profile drag of the plate where the model is attached to. windtunnel tests have been performed while covering this plate, which showed a drag reduction of 0.0092 (Veldhuis, 2012b). This value is therefore subtracted from the windtunnel data. A significant increase in accuracy of the XFLR5 simulations was obtained due to this correction.

**Figure 5.1:** Flat wing configuration in XFLR5.

5.2.2 Swept wings

The second case considers 4 planar wings (Tinling & Kolk, 1951), which all have the same sweep angle of 35° , but vary in aspect ratio, $A = 5$ and $A = 10$, and in airfoil section, namely the NACA - 65₁(A)012 (uncambered) and NACA - 64₁(A)612 (cambered). The

considered airfoil sections are shown in Figure 5.2. With these configurations, the effect of sweep, aspect ratio, as well as the effect of camber are taken into account. Both Reynolds number as Mach number are varied in these cases, which are $2 \cdot 10^6 \leq Re \leq 10 \cdot 10^6$ and $0.25 \leq M \leq 0.92$. For power kites in energy applications, only low Mach numbers are present. Regarding the 25 m² LEI kite of ASSET, Reynolds numbers vary between typically $1 \cdot 10^6 \leq Re \leq 5 \cdot 10^6$. Therefore, only the case where $M = 0.25$ and $Re = 2 \cdot 10^6$ is considered for validation.

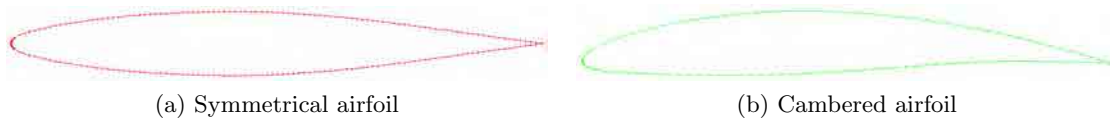


Figure 5.2: A symmetrical NACA - 65₁(A)012 and cambered NACA - 64₁(A)612 airfoil section used for the swept wing configurations.

The configuration parameters of each aspect ratio wing are shown in Table 5.2 and the 3D model in XFLR5 of the configuration with $A = 10$ and cambered profile is shown in Figure 5.3. The cambered profile is a modified version of the NACA - 64₁(A)612 section, where for the NACA mean camber line factor 0.8 was used. Furthermore, the thickness distribution in spanwise direction for each model is constant and no twist is applied. The models are placed on a horizontal turntable, which is connected to a force-balance system directly. Also, windtunnel wall interference corrections are applied to the data.

Table 5.2: Four swept wings configuration parameters.

Parameter	AR5_012	AR5_612	AR10_012	AR10_612
Airfoil (NACA)	65 ₁ (A)012	64 ₁ (A)612	65 ₁ (A)012	64 ₁ (A)612
Reynolds number	$2 \cdot 10^6$		$2 \cdot 10^6$	
Wing span	1.80 m		3.10 m	
Root Chord length	0.41 m		0.41 m	
Tip chord length	0.29 m		0.21 m	
Quarter chord line	0.36 m		0.32 m	
Taper ratio	0.71		0.5	
Surface area	0.32 m ²		0.48 m ²	
Sweep angle	35°		35°	

Since sweep is applied to this configuration, the aerodynamic coefficients are determined from wing sections perpendicular to the quarter-chord line. These sections have a thickness of 14% and a design lift coefficient of 0 and 0.73 for the symmetrical and cambered profile, respectively. The use of a swept-back wing is only preferred for high subsonic flight speeds, since it delays the rise in drag approaching the speed of sound (Jones, 1946). For low velocities as used in this case ($M = 0.25$), sweep has a negative effect such as spanwise flow due to a larger reaction time to push the air towards the tips and a loss in

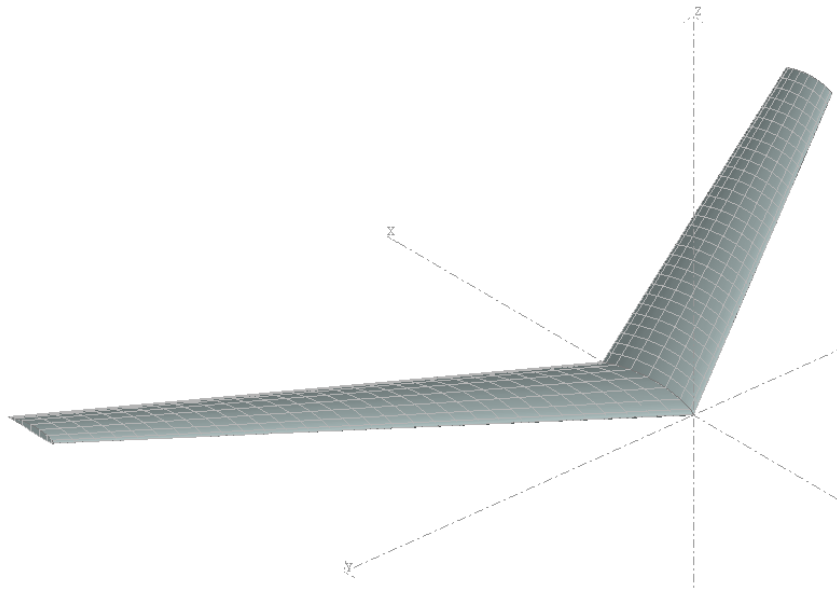


Figure 5.3: Swept wing configuration in XFLR5, with $A = 10$, $\Lambda = 35^\circ$ and a highly cambered profile.

effective aspect ratio since the span is smaller compared to a straight wing. The spanwise flow will result in earlier tip stall, since the effective angles become the largest here. The effect of a lower effective aspect ratio at low speeds results in an increase in drag. The effect of increasing the aspect ratio (in this case from 5 to 10), on the other hand, should result in a higher slope of the lift curve. Furthermore, the difference between the symmetrical and cambered profile added to the wing planforms should result in a vertical shift of the lift curve and therefore has an effect on the zero lift angle. The value and region of $C_{L_{max}}$ and stall conditions are expected to change. The maximum lift coefficient should be higher for a cambered profile, but occurs at a lower angle of attack. It should also be noted that the wing tip of the windtunnel model is formed by a half body with a radius equal to the half thickness of the wing tip section. In case of a VLM analysis, thickness is not taken into account, so there the shape of the wing tip is neglected. The 3D panel method does include thickness, but in the simulation the wing tip is defined as a simple straight section. This assumption will have impact on the tip characteristics, but for the total lift and drag curves this effect should not be significant.

5.2.3 Winglet configurations

The third case discusses a straight flat wing with $A = 10$ on which multiple winglets are applied with different dihedral angles (Yen & Fei, 2011). Only data for one Reynolds number value is considered, $Re = 80,000$. The dimensions of the winglets are significant, namely 20% of the baseline wing span, thus it is expected the winglets have significant effect on the aerodynamic behavior. This validation case could be considered as an intermediate step between a flat wing and an arc shaped kite.

For the windtunnel model, a stainless-steel symmetric NACA - 0012 airfoil is used for both baseline wing and winglets with a winglet dihedral varying from -30° to 135° (Yen

& Fei, 2011). The baseline wing parameters are shown in Table 5.3. This leads to several wing configurations, of which 5 are shown in Figure 5.4, where also surface oil-flow patterns from the windtunnel experiments are shown for an angle of attack $\alpha = 15^\circ$. The aerodynamic performance that is required for the validation, is measured with a JR³ force-moment balance system in an open-loop windtunnel. Lift and drag measurement accuracies are $\pm 1.5\%$ and $\pm 2.0\%$, respectively. For the lift and drag coefficients, these are $\pm 4.5\%$ and $\pm 5.1\%$, respectively.

Table 5.3: Baseline wing configuration parameters excluding winglets.

Parameter	Value
Airfoil	NACA - 0012
Reynolds number	80,000
Wing span	0.6 m
Chord length	0.06 m
Surface area	0.036 m ²
Aspect ratio	10

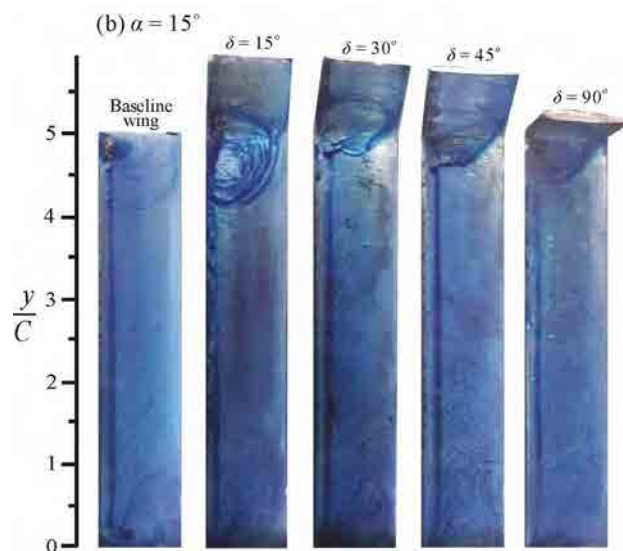


Figure 5.4: Oil flow patterns during a windtunnel test on five different wing configurations, considering a baseline wing and added winglets under various dihedral angles at $\alpha = 15^\circ$ and $Re = 80,000$.

It is expected that winglets will effect the aerodynamic performance such, that there will be a decrease in both induced drag and loss of lift (Smith, 1996). These effects will increase the lift to drag ratio. An increasing dihedral angle for the winglet should decrease the tip vortex strength. However, the windtunnel experiments showed this only holds for dihedral angles larger than 15° . For values between 0 and 15, the vortex even grows stronger and therefore negatively influences the aerodynamic coefficients. Apparently,

the flow momentum here is still high enough to expand the tip vortex to the winglet.

5.2.4 Arc shaped kite

The fourth and last configuration does not include experimental data, but is considered to validate the algorithm of Gaunaa (Gaunaa et al., 2010). In his work, the algorithm is compared with CFD results from an arc shaped kite. Both profile coordinates and 3D model of this kite are obtained to be able to perform a proper validation. The available results are performed at $Re = 3 \cdot 10^6$. In Table 5.4, the kite main dimensions can be found. The planform is of elliptical shape, which is chosen due to the expected induced drag minimization (Munk, 1923). The 3D model in XFLR5 can be seen in Figure 5.5.

Table 5.4: Kite configuration main parameters.

Parameter	Value
Airfoil	NACA - 64-418
Reynolds number	$3 \cdot 10^6$
Wing span	1.0 m
Root chord length	0.3 m
Surface area	0.3 m^2
Aspect ratio	3.33

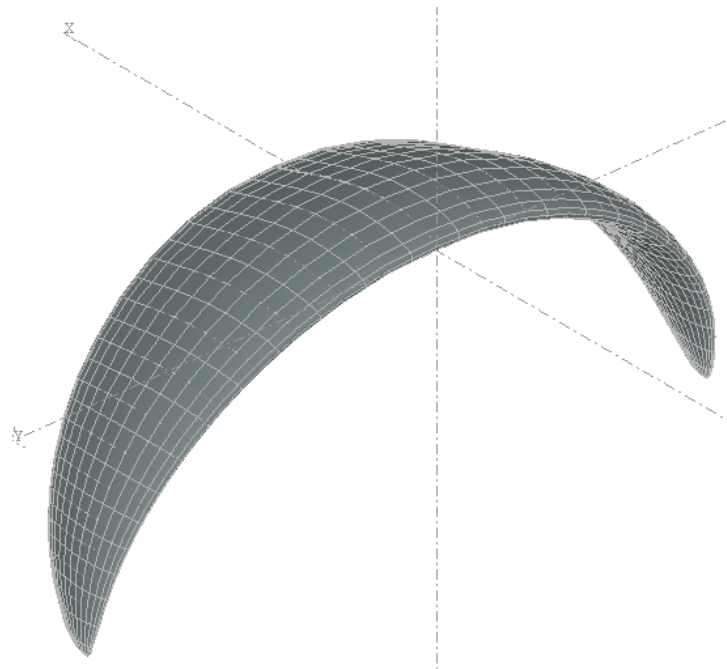


Figure 5.5: Circular arc shaped kite configuration in XFLR5, used to validate the method of Gaunaa.

5.2.5 Model discretization in XFLR5

In Table 5.5, the type of discretization and number of panels are given for every validation case. A cosine panel distribution means a higher concentration of panels near the tips and leading/trailing edges for respectively spanwise and chordwise distribution.

All, but one, used discretizations are equivalent for VLM and 3D panel method, where the latter uses chordwise panels on the upper and lower camber line and extra panels on the tip sides. Only in the swept wing configurations variations are made between both MG vs AK and VLM vs 3D panel method. For version AK there is a calculation error due to discretization for induced angles in VLM calculations, which makes the values at the root unrealistic. Therefore, a *cos* spanwise panel distribution is used for the 3D panel method to avoid dense paneling at the root. However, when there are an equal numbers of panels as used in other versions, the values of the induced and effective angles are too extreme at the tips. Hence, too dense paneling is not favorable at both the root as the tips, therefore only half the number of panels are used with respect to the MG versions.

This type of discretization does, however, not work for the VLM in version AK, since then again there is unrealistic behavior at the tips due to too dense paneling. In the spanwise distribution, the induced angle slope towards the tips suddenly flips from negative to positive. Therefore, for the VLM in version AK a uniform distribution is used with the same amount of panels as in the 3D panel method in version AK. These extreme and unrealistic values could be the result of too high aspect ratio panels, which should be avoided according to the XFLR5 manual.

Table 5.5: Discretization parameters used for the validation cases, where *cos* means cosine and *uni* is uniform.

Method →	VLM			3D panel method		
Configuration ↓	Chordwise	Spanwise	Panels	Chordwise	Spanwise	Panels
Flat wing	<i>cos</i> /13	<i>uni</i> /30	390	<i>cos</i> /13	<i>uni</i> /30	806
Swept wing AR5 MG	<i>cos</i> /12	<i>uni</i> /36	432	<i>cos</i> /12	<i>uni</i> /36	888
Swept wing AR5 AK	<i>cos</i> /12	<i>uni</i> /18	216	<i>cos</i> /12	<i>cos</i> /18	456
Swept wing AR10 MG	<i>cos</i> /12	<i>uni</i> /72	864	<i>cos</i> /12	<i>uni</i> /72	1,752
Swept wing AR10 AK	<i>cos</i> /12	<i>uni</i> /36	432	<i>cos</i> /12	<i>cos</i> /36	888
Baseline wing	<i>cos</i> /10	<i>uni</i> /24	240	<i>cos</i> /10	<i>uni</i> /24	500
Winglet, $\Gamma = 90^\circ$	<i>cos</i> /10	<i>uni</i> /32	320	<i>cos</i> /10	<i>uni</i> /32	660
Arc shaped kite	<i>cos</i> /20	<i>cos</i> /30	600	<i>cos</i> /20	<i>cos</i> /30	1,240

5.2.6 Airfoil data

This section discusses, which 2D sectional airfoil data is used for the angle shift corrections. Preferably, the 2D airfoil data used for the lift correction corresponds to the flow characteristics and airfoil geometry of the 3D windtunnel measurements. Besides wind tunnel data, XFOIL is used to pre-generate viscous airfoil data. An important parame-

ter to consider is the n -factor. This value used in the e^n method quantifies the critical disturbance amplification ratio and determines the point of transition. The n -factor can have significant influence on the overall behavior of the 2D polars.

Flat wing

For the flat wing, reference data of the same airfoil, Reynolds number, Mach number and windtunnel was available from Wirsing (1999). For this case the use of three different n -factors, $n = 7, 11, 13$, in XFOIL are compared to the windtunnel data (polars are given Appendix D). Considering the relation given by Mack (1984), which is similar to that of Van Ingen (2008):

$$n = -8.43 - 2.4 \ln(TI) \quad (5.2)$$

where it is given that turbulence levels TI are between $0.015\% \leq TI \leq 0.07\%$ (*Low Turbulence Wind Tunnel*, n.d.) for the low speed wind tunnel at DUT, the n -factor should be between $9 \leq n \leq 12.7$. Results showed the best agreement for an n -factor of 11 and therefore shows the validity of XFOIL for this airfoil. For the remainder of the algorithm validation procedure, the wind tunnel data is used.

Swept wings

For the swept wings, only airfoil data from other wind tunnels (Abbott et al., 1945) than the one used for the 3D wing measurements were available. Because the swept wings are tapered, the local chord changes over span, and accordingly local Reynolds number varies too. In reference data the only Reynolds number considered is $Re = 3.0 \cdot 10^6$. In this case it is decided to compare the 3D simulation results for two different n -factors:

- $n = 9$: this is a common default value used, which may have been found useful due to the fact that most modern low speed low turbulence wind tunnels had been built according to the same recipe, aiming at a turbulence level of just below 0.1% as had been suggested to be sufficiently low (Van Ingen, 2008).
- $n = 12.4$: at this factor XFOIL results agree closest to the wind tunnel data at $Re = 3.0 \cdot 10^6$.

The results of the 3D simulations for the different methods are shown in figure 5.6, where the errors are given for the linear and non-linear regions of the lift and drag curves, averaged over the 4 sweep cases. In Appendix D, the corresponding XFOIL polars can be found.

From this bar diagram, it can be seen that the differences in error between the 2 values of n are not large: between 0.5% and 2%. Results of $n = 12.4$ consistently shows higher accuracy, which agrees with the fact that the XFOIL results are closest to the windtunnel data for $Re = 3.0 \cdot 10^6$. The results in this graph do, however, not take into account the predicted angle of attack range of the simulated data. This also involves the prediction of stall. For the sweep cases, it showed that for a value of $n = 9$, 37 out of 48 stall points are reached. For $n = 12.4$, this value is 19 out of 48 stall points. This is caused by the convergence problems of XFOIL at angles of attack far beyond stall for the lowest simulated Reynolds numbers. Since there is a significantly larger discrepancy between the amount of reached stall points than the errors in Figure 5.6, $n = 9$ seems

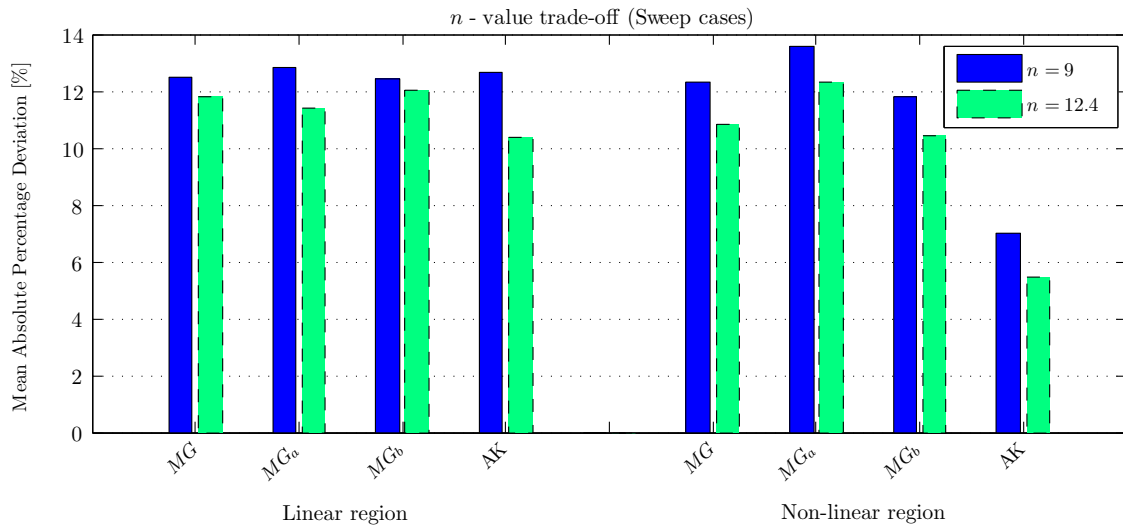


Figure 5.6: Error of the linear and non-linear region for 2 different n -values of all versions for the swept wing configurations.

better to use with respect to the set criteria. This illustrates the limitation of the use of XFOIL: when it is not able to find converged solutions of one of the generated polars, could mean that stall cannot be predicted in the 3D nonlinear VLM analysis.

Winglet configurations and arc shaped kite

For the several winglet configurations, wind tunnel data of the NACA-0012 profile was obtained from Sheldahl & Klimas (1981).

For the arc shaped kite the airfoil inviscid and viscous data is given by Carqueija et al. (2010), where he uses 2D CFD data for one Reynolds number. According to Carqueija: "This data is chosen over XFOIL data solely due to the fact that the algorithm will be validated against CFD results." Unfortunately, nothing can be said about the numerical errors in his 2D CFD calculations. These errors can significantly influence the results of the nonlinear potential flow methods, but the comparison can still give an impression on how the nonlinear regime and stall are predicted by the new software.

5.3 Program trade-off

Before validating the algorithms, it should be noted that the results from 3D simulations are highly dependent on the 2D XFOIL polars. Therefore, the airfoil sections of each validation case are first validated by comparing 2D windtunnel data with XFOIL results. This way, the most promising validation can be performed with 3D simulations.

5.3.1 Procedure

Since there are 4 methods available to perform 3D simulations with, which have been discussed earlier in this chapter, a trade-off scheme will be maintained during the comparison of results. All considered options are shown in Figure 5.7. For each version, the

VLM and 3D panel method are used. In case of the VLM, the 2D inviscid lift curves of XFOIL and TAT can be chosen.

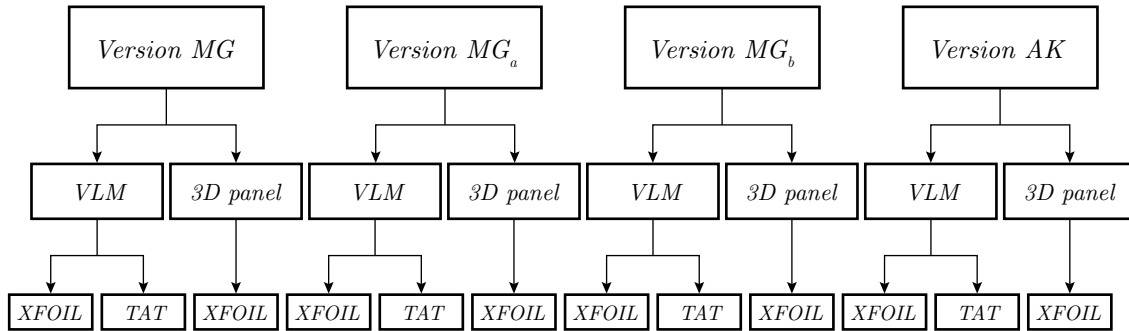


Figure 5.7: Option tree of available methods for each program version.

The trade-off procedure will be performed as follows. First, separate comparisons with experimental data will be done for the MG based VLM's and the AK based VLM's for the flat and swept wing configurations. From this, a most promising VLM will be chosen. A similar analysis will be done with the 3D panel methods based on the methods of MG and AK, from which a most promising version is chosen. These versions are used to analyze the dihedral and arc shaped kite configuration with, to investigate for example the influence of dihedral/winglets. These cases are not used in the program validation, because of the higher uncertainties in windtunnel, airfoil and CFD data.

5.3.2 Trade-off criteria

Due to the large number of polars that resulted from simulations, a trade-off process has been performed to decide which of the program versions gives the most accurate results. In Appendices D and E, all polars can be found which are used to do this analysis. For the trade-off procedure, 3 criteria are selected on which the tool is validated. These concern:

- The linear part of the lift curve with the associated part of the drag curve
- The non-linear part of the lift curve with the associated part of the drag curve
- The determination of stall point, both value ($C_{L_{max}}$) as critical angle of attack

These criteria are also visualized in Figure 5.8. The non-linear part of the lift curve starts when the lift curve slope deviates more than 10% from the lift curve slope at $C_L = 0$. For the first 2 criteria, a Mean Absolute Percentage Deviation (MAPD) is used to determine the error with respect to the windtunnel data. For the third criteria, the values of $C_{L_{max}}$ and α at $C_{L_{max}}$ are normalized with respect to the values of the windtunnel data. The absolute distance of these 2-dimensional points is considered to be the error.

5.3.3 Trade-off results

In Figure 5.9 and 5.10, the trade-off results of criteria 1 and 2 are shown for all validation cases calculated with all VLM and 3D panel method versions, respectively. From both

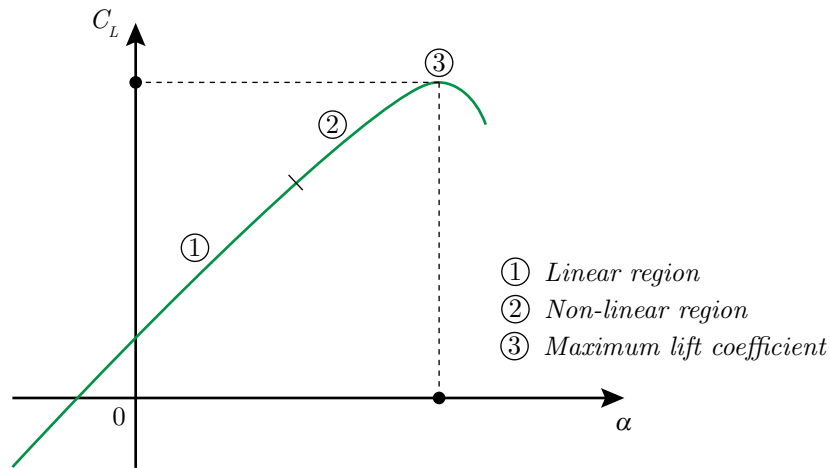


Figure 5.8: Trade-off criteria used for validation.

bar diagrams, it can be seen that there is no large discrepancy in error between all versions regarding the linear region of the lift curve. Considering the non-linear region, AK (XFOIL) shows the lowest error percentage for both VLM and 3D panel method. From the versions based on Gaunaa, MG_b shows the lowest error with a small difference. That MG_b has higher accuracy than version MG is expected, since (profile) drag is based on the corrected values, not on the linear results.

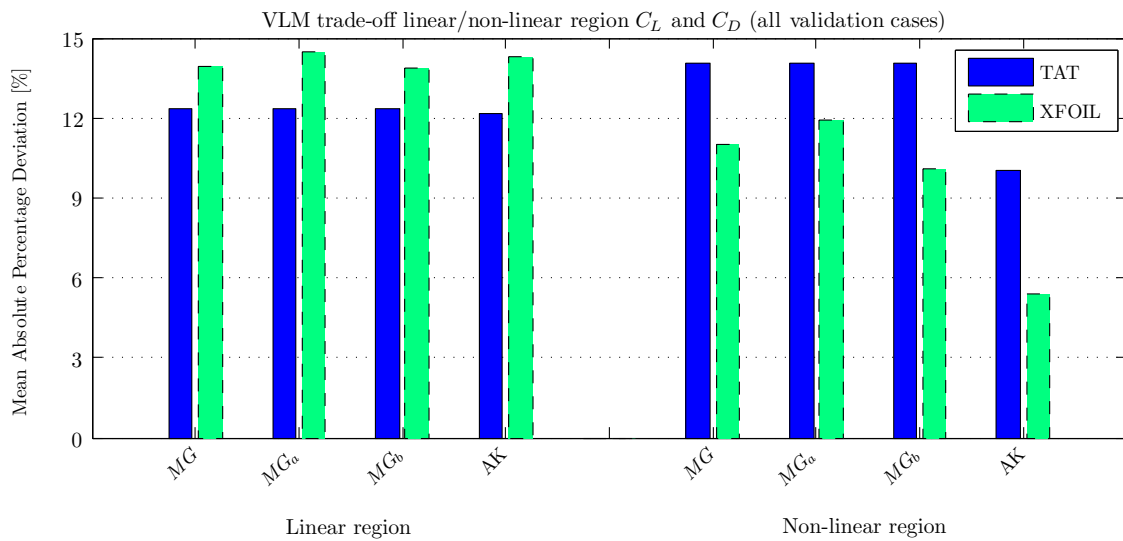


Figure 5.9: Error of the linear and non-linear region of the lift and drag curves of all VLM versions for all validation cases.

In Figure 5.11, the accuracy of stall point predictions (criteria 3) of each version is shown, averaged over the flat wing and swept wings validation cases. Also, the amount of reached stall points are depicted above the bar diagrams. It is directly noted that the XFOIL based methods show a higher accuracy than the TAT based methods for the VLM. This shows that this method, where viscous effects are implemented on basis of 2D theory, has its limitations. In general, it can be concluded that the applied corrections

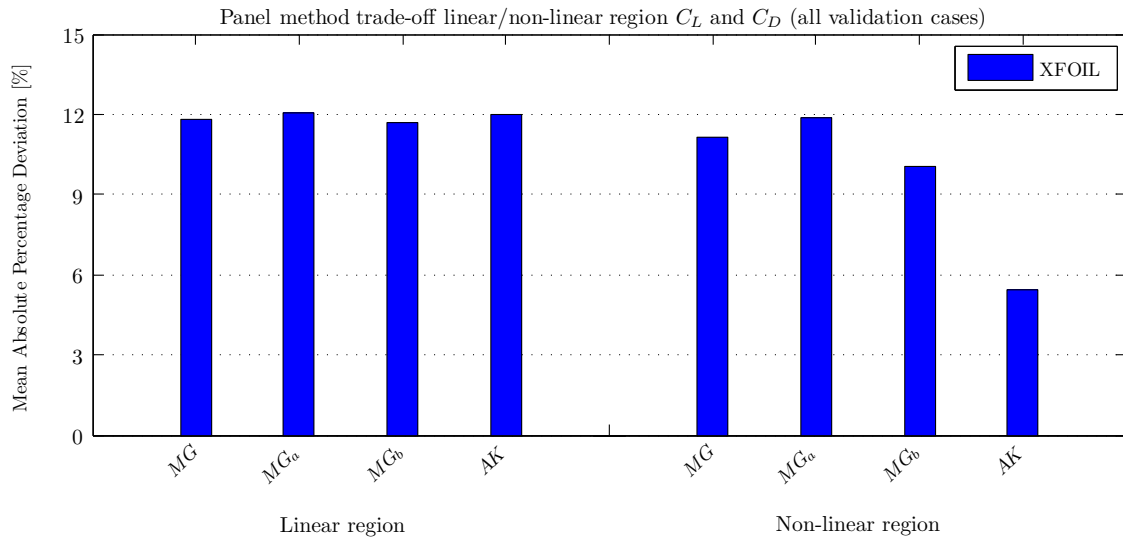


Figure 5.10: Error of the linear and non-linear region of the lift and drag curves of all 3D panel method versions for all validation cases.

are too high in the linear regime and too low in the non-linear regime. Therefore TAT has higher accuracy in the linear regime, and XFOIL better predicts the non-linear regime.

Another important observation is that the Gaunaa based versions determine all stall points, from which MG and MG_b show the lowest error. However, MG_b showed a better performance in drag prediction and is therefore chosen as the most promising version based on Gaunaa’s method. AK shows a similar accuracy in stall point prediction, but not all points are reached.

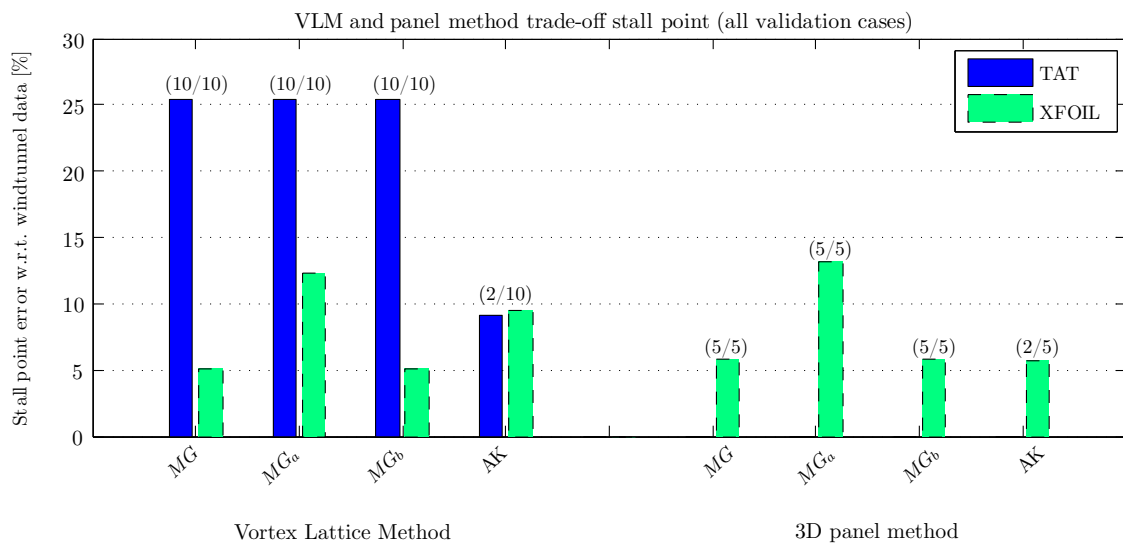


Figure 5.11: Error of the location and value of $C_{L_{max}}$ of all VLM and 3D panel method versions for all validation cases, including the number of reached stall points.

5.4 Results of validation cases

From an extensive trade-off procedure, the versions MG_b and AK came out to be most accurate in predicting lift and drag coefficients up to stall conditions. Although all validation results can be found in Appendix E, in this section the lift and drag polars of version MG_b and AK are shown for all validation cases. From these results, conclusions can be drawn regarding specific phenomena for each different configuration. Also, improvement with respect to the original XFLR5 version is of major importance. Therefore, an analysis is performed on the trade-off criteria (defined in Section 5.3.2) between the original and adapted versions.

5.4.1 Lift and drag coefficient

In Figure 5.12 and 5.13, the lift and drag curve results of the flat wing configuration (Horsten case) are shown for the most promising versions. It can be seen that the results from the adapted programs deviate from the values of Horsten. This is due to the use of a different VLM and implementation of the angle shift and the implementation of interference effects in Horsten's algorithm. In general, the solutions are close to the wind tunnel data, where a non-linearity occurs at $\alpha = 6^\circ$. The simulated values nicely predict a similar non-linearity, which is (necessarily) also observed in the viscous airfoil data. The non-linearity is probably the rapid movement of the transition point.

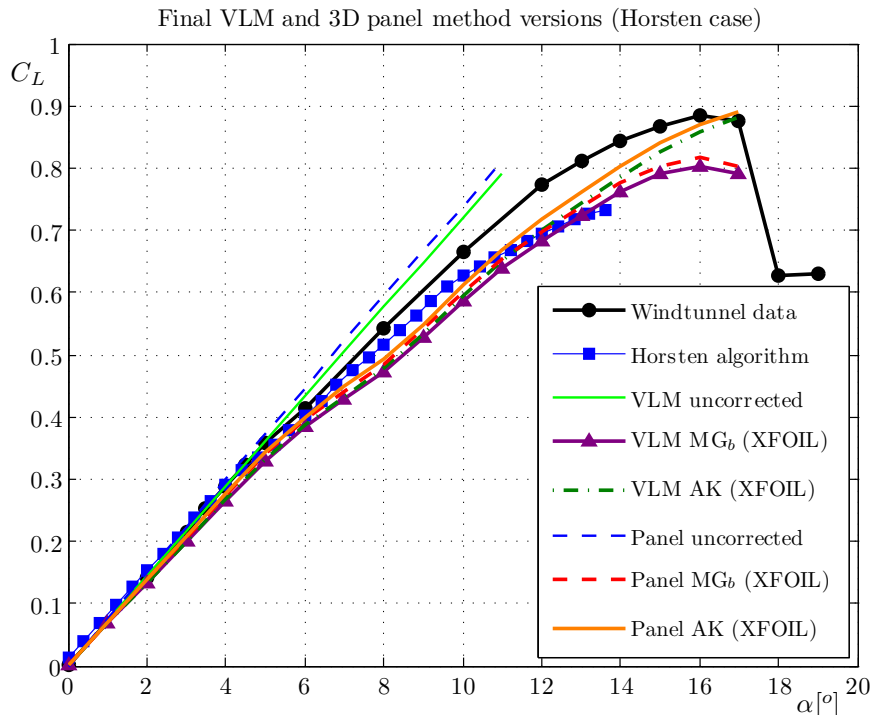


Figure 5.12: The $C_L - \alpha$ curves obtained from wind tunnel experiments and XFLR5 simulations of the flat wing where $Re = 1.0 \cdot 10^6$.

In the experimental data, a similar, but stronger non-linearity is observed in the lift curves for the swept wing configurations. In Figure 5.14, 5.15, 5.16 and 5.17 the

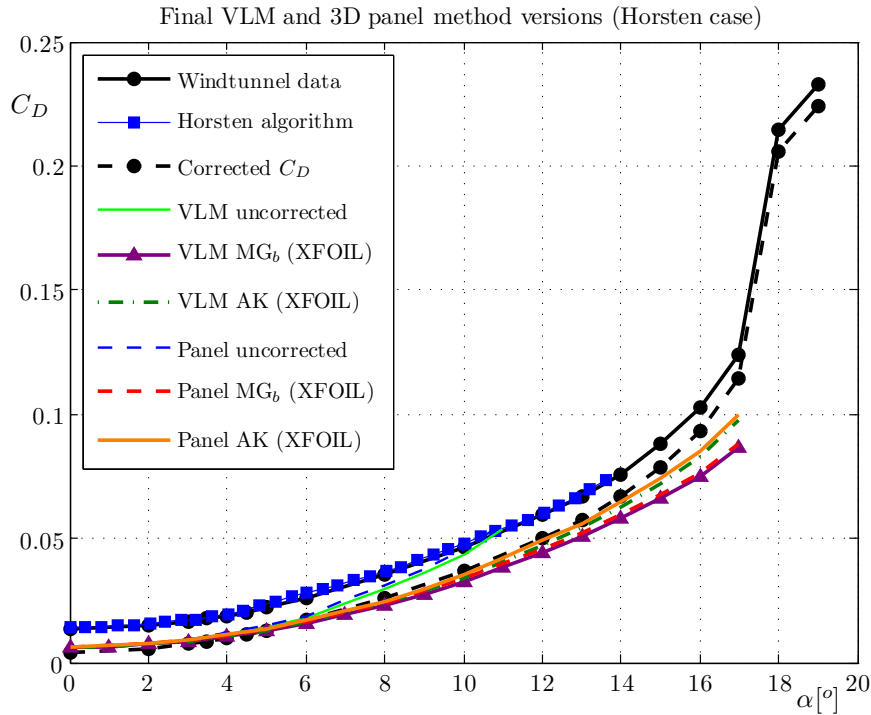


Figure 5.13: The $C_D - \alpha$ curves obtained from wind tunnel experiments and XFLR5 simulations of the flat wing where $Re = 1.0 \cdot 10^6$.

lift, drag, profile drag and induced drag curves of the AR10_012 wing configuration are shown. The lift and drag curves from each adapted version show a good resemblance with the experimental data. The lower accuracy of the drag for high lift values is due to the profile drag, which show an higher increase in windtunnel data. The pressure drag caused by separated flow is probably higher than XFOIL predicts, where the latter is not able to predict the 3D aerodynamics of separated flow. The induced drag coefficients are, however, predicted accurately. It should be noted that the wind tunnel data in Figure 5.17 has a value larger than 0 at $C_L = 0$. This is an error due to low resolution figures from literature. The remaining results of the swept wing configurations can be found in Appendix E.

5.4.2 Improvement on original XFLR5

In Figure 5.18, the Mean Absolute Deviation (MAD) of the linear and non-linear region of the lift curves are shown for the original XFLR5 program and the adapted versions. An average of all validation cases is used here. In the linear region, negligible differences are observed. In the non-linear region, however, an increased accuracy of approximately 0.1 is obtained with respect to the uncorrected XFLR5 version. Since all validation cases have stall points around or below $C_L = 1$, an average error decrease of 0.1 is significant. The value of MAD of the adapted versions is around 0.03.

In Figure 5.19 and 5.20, the MAD of the linear and non-linear region of the drag curves are shown of the standard software and the adapted versions. The profile and induced drag coefficient are considered separately and the average of 2 swept wing configurations

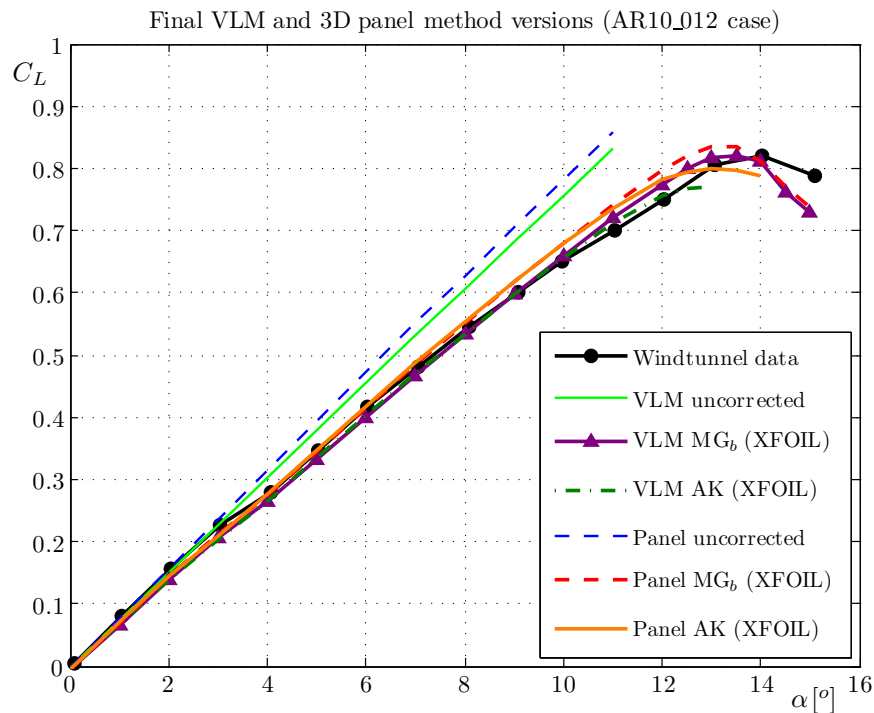


Figure 5.14: The $C_L - \alpha$ curves obtained from wind tunnel experiments and XFLR5 simulations of the swept AR10_012 wing where $Re = 2.0 \cdot 10^6$.

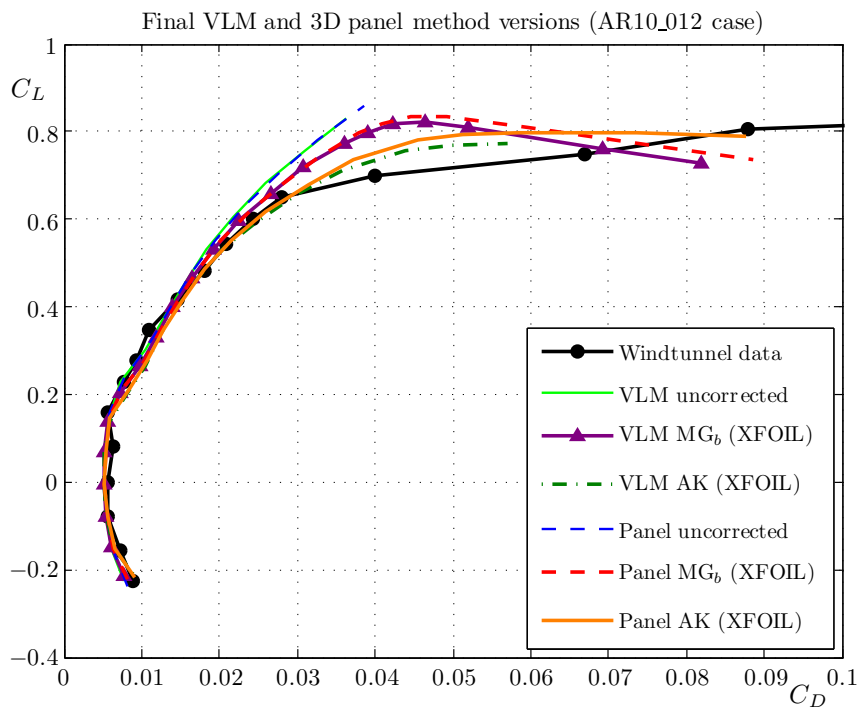


Figure 5.15: The $C_L - C_D$ curves obtained from wind tunnel experiments and XFLR5 simulations of the swept AR10_012 wing where $Re = 2.0 \cdot 10^6$.

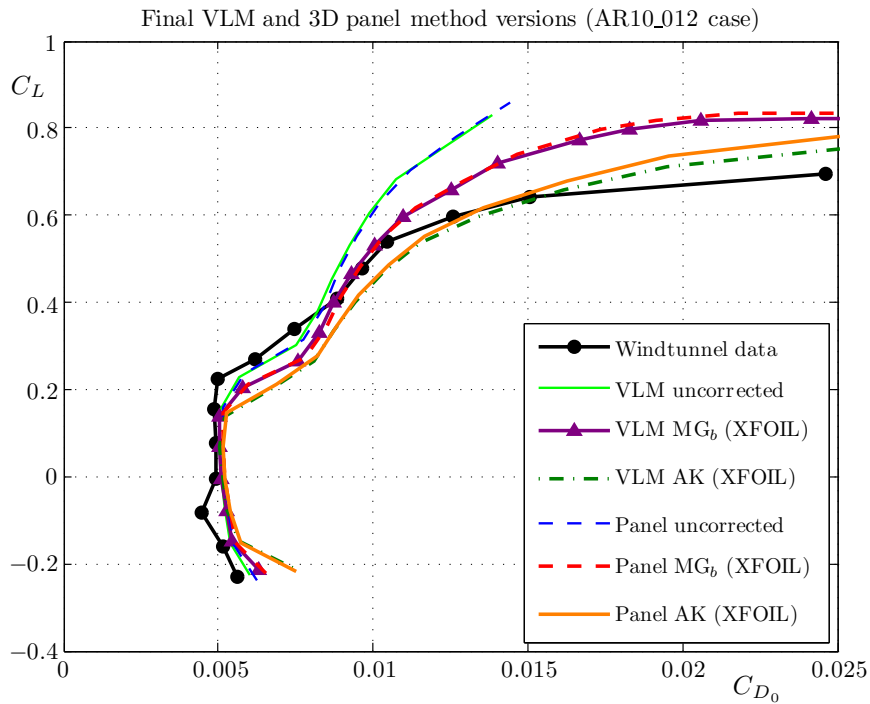


Figure 5.16: The $C_L - C_{D_0}$ curves obtained from wind tunnel experiments and XFLR5 simulations of the swept AR10_012 wing where $Re = 2.0 \cdot 10^6$.

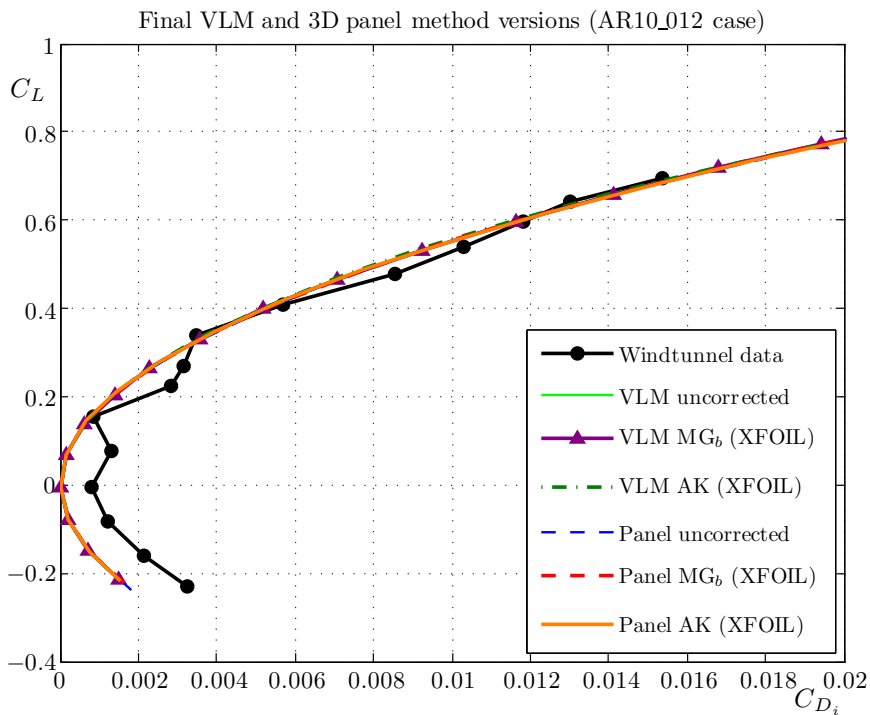


Figure 5.17: The $C_L - C_{D_i}$ curves obtained from wind tunnel experiments and XFLR5 simulations of the swept AR10_012 wing where $Re = 2.0 \cdot 10^6$.

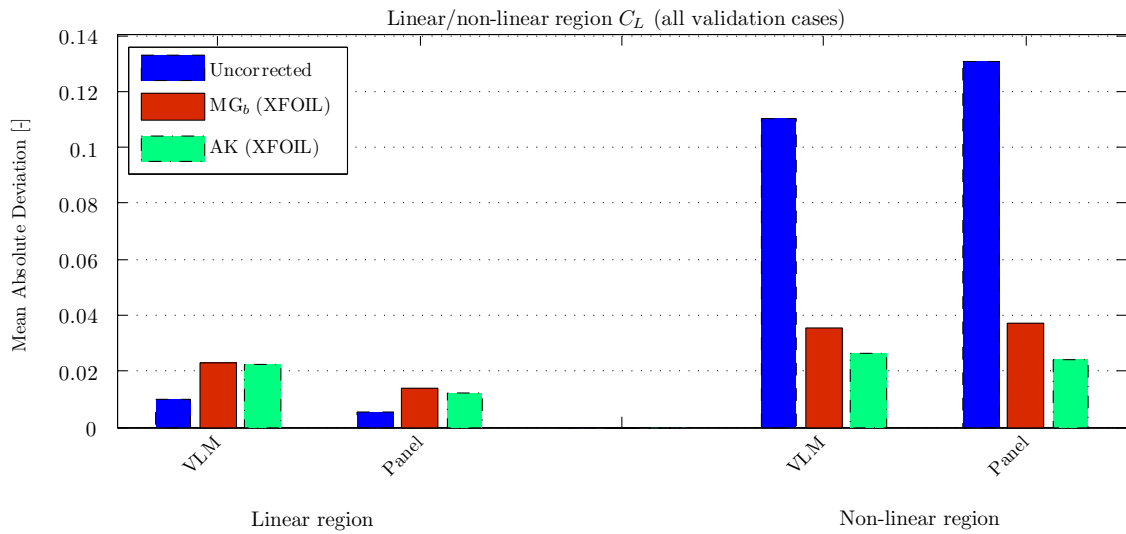


Figure 5.18: MAD of the linear and non-linear region of the lift curves of the uncorrected XFLR5 version and adapted versions for all validation cases.

(AR5_012 and AR10_012) is used. It can be seen that in the linear region the total drag coefficient shows is slightly increased in accuracy with the adapted versions. In profile drag there is a small increase in error, which corresponds to the fact that after correction, lift is lower and thus also drag becomes lower. In overall results do not deviate much. More significant increases in accuracy are shown in the non-linear region (Figure 5.20). Most profit is gained in the total drag with the AK method. But also MG_b shows to produce lower errors for both total drag and profile drag. Thus, concerning the nonlinear region, significant profits are obtained with the adapted XFLR5 programs.

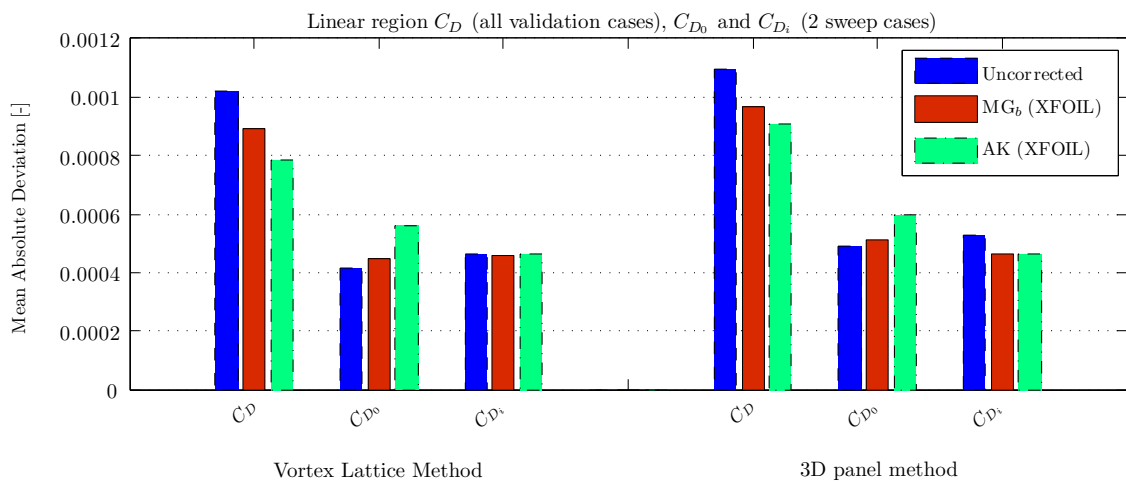


Figure 5.19: MAD of the linear region of the drag (total, profile and induced part) curves of the uncorrected XFLR5 version and adapted versions for all validation cases.

In Figure 5.21 and 5.22, the normalized errors w.r.t. the wind tunnel data of the value and location of the stall points are shown. Each marker denotes a single validation case.

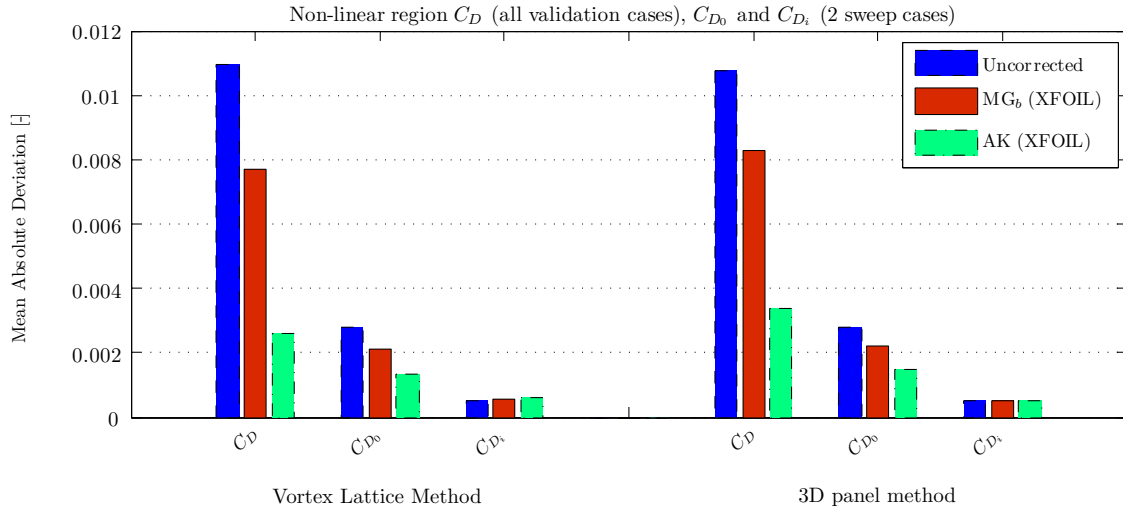


Figure 5.20: MAD of the non-linear region of the drag (total, profile and induced part) curves of the uncorrected XFLR5 version and adapted versions for all validation cases.

It can be seen that each obtained stall point is predicted within an error of 10%, both for critical angle of attack and maximum lift.

5.4.3 Spanwise distributions

In Figure 5.23, the lift and angle shift distributions of the AR10_012 wing are shown for $\alpha = 6^\circ$ and $\alpha = 13.3^\circ$. In Appendix F spanwise distribution results of the flat wing configuration can be found. The results of the swept wing AR10_012 show a significant deviation for the uncorrected VLM and 3D panel method. It is also noted that the different adapted version show different results, especially for the angle shift distribution. This is caused by the different approaches in induced angle determination, where the AK version directly obtains it from Trefftz-plane calculation, while MG_b indirectly determines the angles from the lift distribution. For an increasing angle of attack, the differences become larger. In general, version MG_b shows more realistic distributions: it predicts the expected tip stall and it does not have strong peak values at the root.

In Figure 5.24, the effective angle and drag distributions of the AR10_012 wing are shown for $\alpha = 6^\circ$ and $\alpha = 13.3^\circ$. Similar differences are observed as in Figure 5.23, where the peaks of the effective angles confirm the erroneous induced angle determination in the Trefftz-plane. Concerning the drag distributions for $\alpha = 13.3^\circ$, the uncorrected VLM and 3D panel method results are not shown, since the drag coefficient could not be interpolated anymore at this angle.

5.4.4 Winglet configurations

In Figure 5.25 the lift, drag and induced drag curves are given for both the VLM as 3D panel method. Two notifications should be made to the performed simulations on the winglet configurations:

- A low Reynolds number is used, $Re = 80,000$, and thus viscous forces are relatively

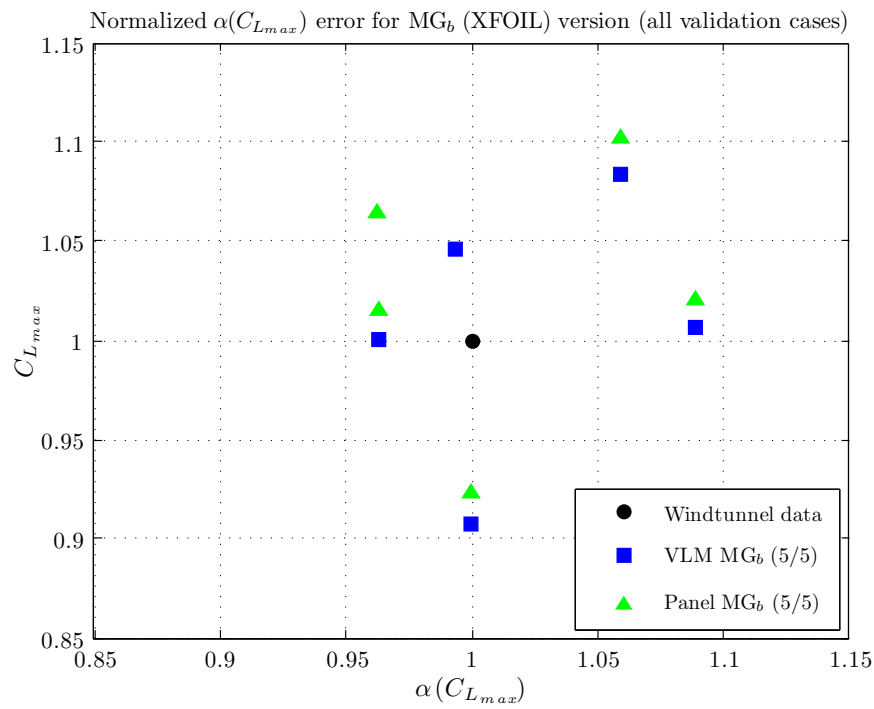


Figure 5.21: Normalized error of the value and location of $C_{L_{max}}$ of version MG_b for all validation cases.

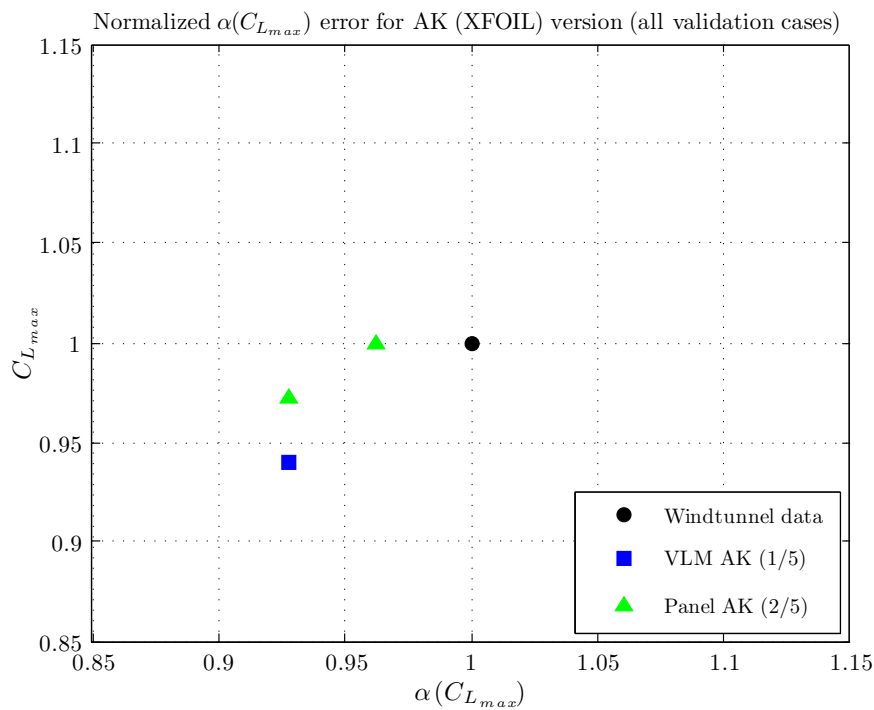


Figure 5.22: Normalized error of the value and location of $C_{L_{max}}$ of version AK for all validation cases.

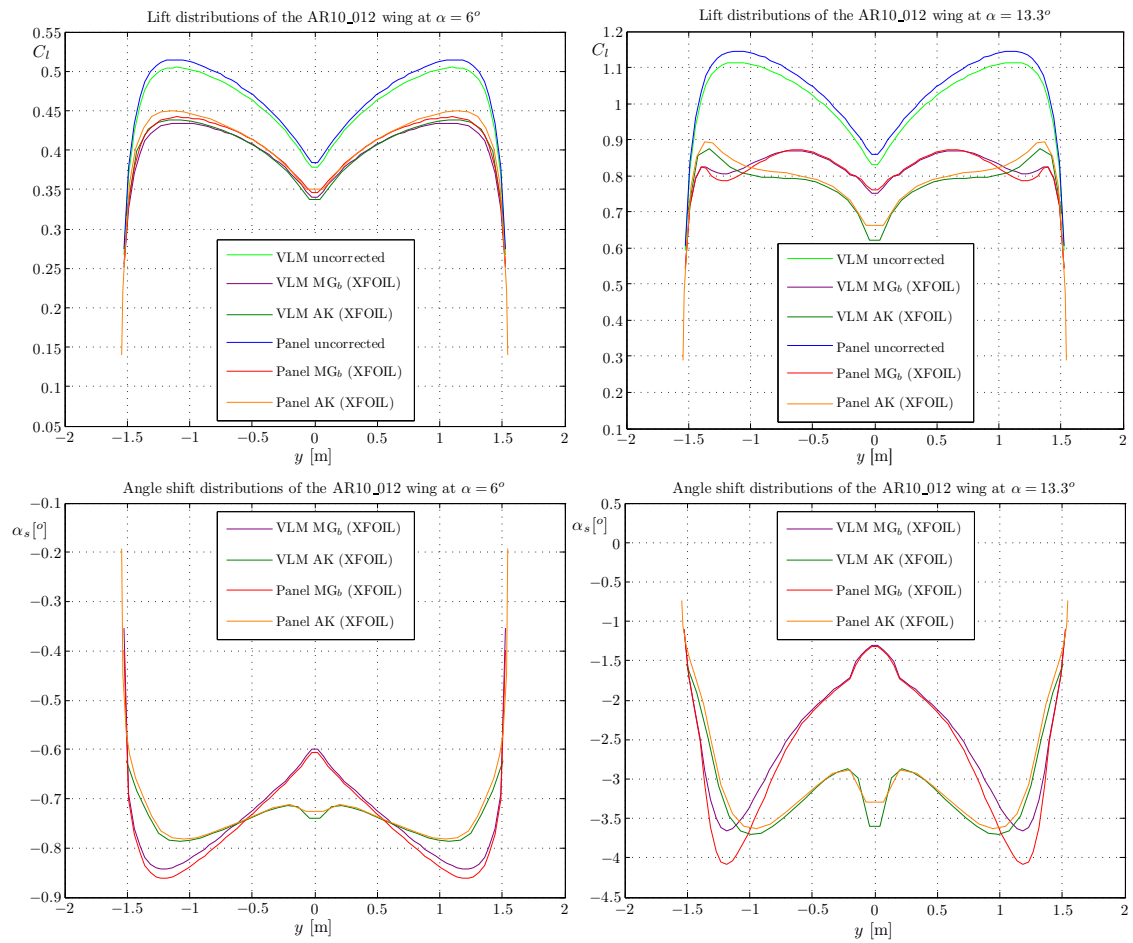


Figure 5.23: The $C_l - y$ and $\alpha_s - y$ distributions obtained from XFLR5 simulations (original, MG_b and AK) for the AR10_012 wing with $\alpha = 6^\circ$ and $\alpha = 13.3^\circ$.

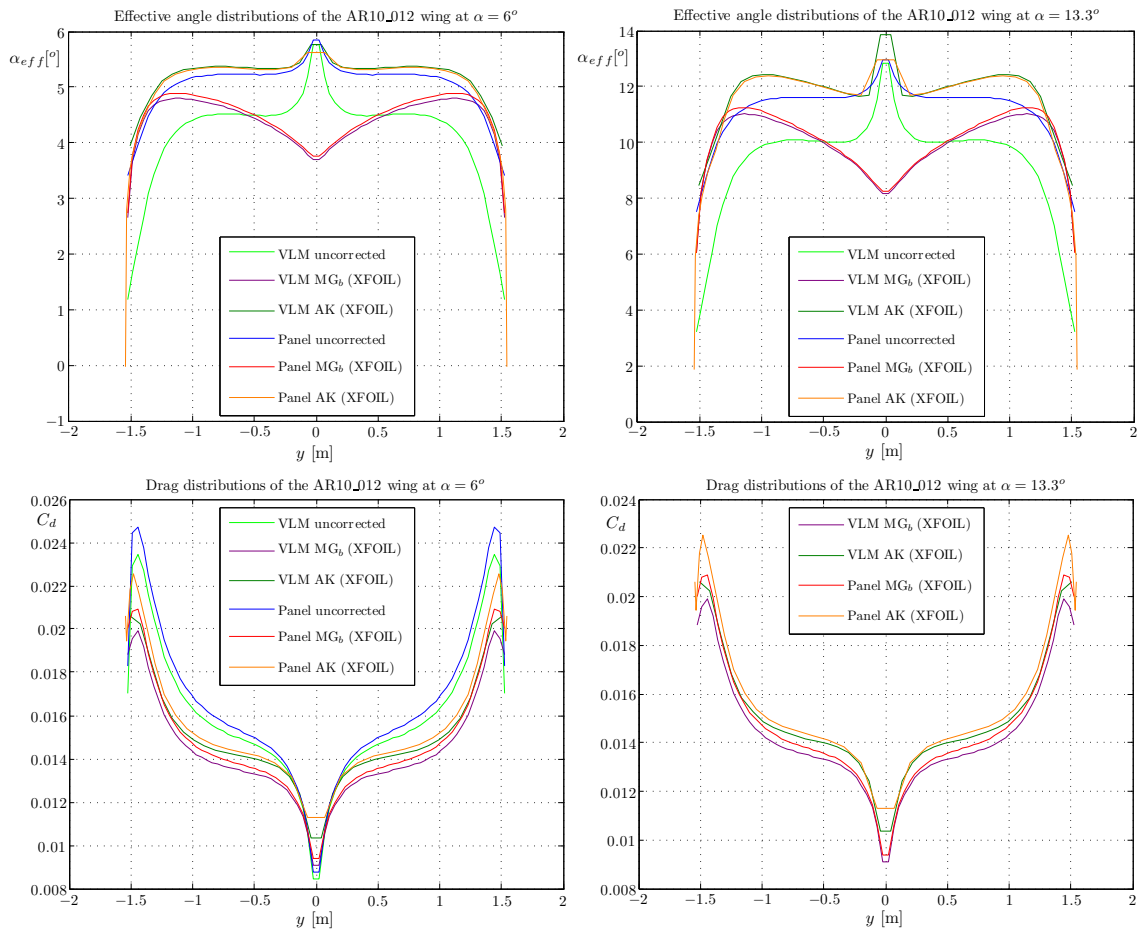


Figure 5.24: The $\alpha_{eff} - y$ and $C_d - y$ distributions obtained from XFLR5 simulations (original, MG_b and AK) for the AR10_012 wing with $\alpha = 6^\circ$ and $\alpha = 13.3^\circ$.

high with respect to inertial forces. These viscous forces are very sensitive to small variations and can strongly influence the transition point. Therefore viscous 2D airfoil data can deviate significant of the behavior which belongs to the airfoil in the experiments.

- The deviations in profile drag, at $C_D(\alpha = 0)$, between the experimental and simulated data arouse suspicion that the experimental drag coefficients are not corrected for wind tunnel effects. Another explanation could be wind tunnel flow quality or that the NACA profile has a different surface roughness and/or camber lines which can significantly affect friction drag and transition point. The NACA - 0012 profile is also known for the many variations in measured lift and drag values at different wind tunnel measurements, as mentioned by Veldhuis (2012b).

The $C_D - \alpha$ curve of the simulated values moves upward when winglets are applied. For $\alpha = 0^\circ$, the induced drag is zero (symmetric profile), which means that the shift is a result of increased profile drag. This is simply because the drag coefficient is calculated with respect to the projected area which remains constant after the addition of winglets of $\Gamma = 90^\circ$ dihedral (while the total profile drag increases). The increase in profile drag is proportionally less compared to the experimental values: 18% vs 38%. The 18% of the simulated values corresponds approximately to the 20% increase in total wing area. The remaining 18% increase in the wind tunnel values is therefore due to viscous 3D effects .

The shape of the simulated $C_D - \alpha$ curve remains approximately the same, whereas it would be expected that the wing with winglets would have relatively less resistance as lift increases, because of reduction in induced drag. This reduction in drag is indeed visible in the experimental data. After inspection, the simulated data did show a reduction in induced drag for increasing angle of attack, but this difference in induced drag is only a fraction of the profile drag and has therefore almost no effect on the total drag. Apparently, the lift distribution, and thus lift slope, is significantly more influenced by the winglets in reality than the potential flow code predicts. This is not surprising, because this theory is not able to simulate viscous 3D effects. In the oil-patterns in Figure 5.4 surface vortices are visible near the wing tip and wing junction, which are caused by the strong wall and finite wing effects. In the corresponding literature, the strong 3D flow structures are also confirmed, where they even call the boundary-layer flow pattern the 3D flow mode. This case shows clearly the limitation of the nonlinear potential flow method, that it is not able to predict the 3D viscous effects that occur for strong variations in dihedral at low Reynolds numbers.

Next to the winglet with $\Gamma = 90^\circ$, a number of other dihedral angles where used for experiments (Yen & Fei, 2011). Here, also a negative dihedral was used of which lift and drag curves deviated significantly from the same positive dihedral. This is due to the wake interference of the negative dihedral winglet with that of the main wing. In simulations, a similar non-symmetrical effect was observed, since a free wake is used. However, the deviations were less notable.

5.4.5 Arc shaped kite

The new algorithm is used to simulate an arc shaped kite. Some comments can be made on this validation case, where originally the algorithm of Carqueija et al. (2010) was compared with the results of a 3D CFD simulation (RANS):

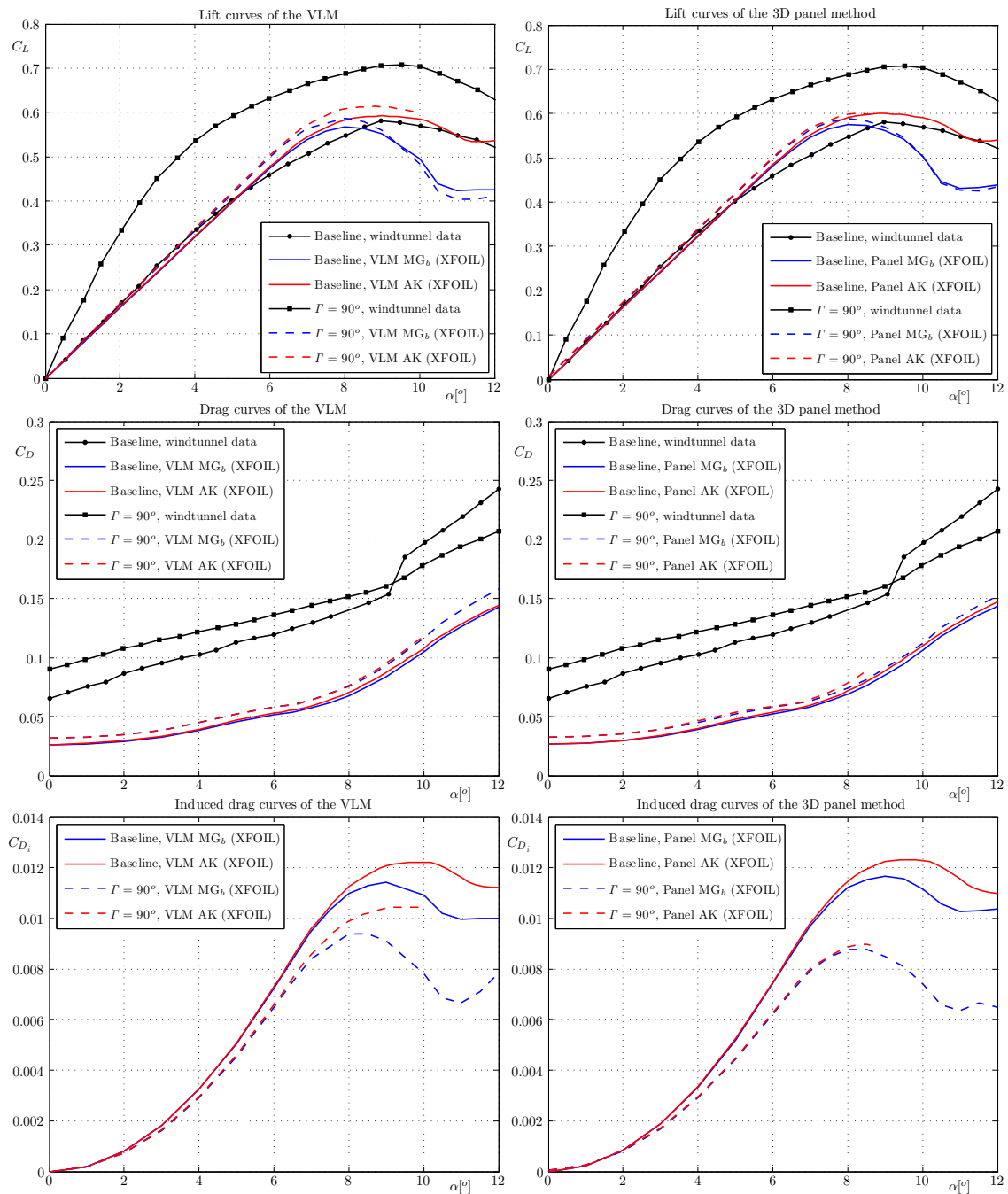


Figure 5.25: The lift, drag and induced drag curves obtained from wind tunnel experiments and XFLR5 simulations of the winglet configuration with ($\Gamma = 90^\circ$) and without winglet for $Re = 80,000$.

- It is difficult to determine how accurate the CFD results are, since nothing is known about the numerical and modeling errors. This is however one of the few cases in which an arc shaped kite is analyzed with a high-fidelity CFD solver. The results can be expected to have higher accuracy than a VLM or 3D panel method, because the solved equations use far less assumptions. Therefore, this comparison is still interesting.
- For the lift and drag curve of the NACA - 64-418 airfoil, results were obtained from a 2D CFD analysis for $Re = 6 \cdot 10^6$. Since this is the only airfoil data used for the correction in the nonlinear potential flow methods, Carqueija makes the assumption that the Reynolds number is constant over span. In contrast, the proposed method in this thesis requires local Reynolds numbers, as defined in Section 4.3.3. The local Reynolds numbers are lower towards the tips and lower Reynolds numbers generally means lower maximum lift. As a result, the generated lift at the tips is expected to be lower when local Reynolds numbers are used. Whether this corresponds better to the 3D CFD results, was not possible to verify for this case.
- Carqueija uses a different VLM, which is not public. Therefore, differences in the inviscid VLM calculations can be expected. It is only known that it uses ring vortices, a free wake (similar as VLM2 with tilted geometry in XFLR5) and TE shed lines of only 1 local chord length opposed to 100 MAC lengths used in XFLR5. Carqueija states that the influence of the TE shed lines is not significant. It is also not given if his results are obtained from near or far-field analysis.
- For the calculation of the effective angles, the spanwise lift distribution is used, however it is not known which definition of the local lift coefficient in his VLM is used. It could be defined with the local or mean aerodynamic chord, which significantly differ and can therefore have large influence on the applied lift correction and final results. It is also not clear whether he uses the local normal force coefficient or the local lift coefficient. The first one would be more logical to use, since the local effective angles of attack and angle shifts should be defined normal to the airfoil section. If not, the algorithms would not be able to apply the angle shifts to a vertical wing (for example an aircraft tail).
- For the spanwise distribution plots, a transformation of the coordinates along the span y was required, because Carqueija uses the coordinates along the projected span Y in his figures.

In the figures in his report, Carqueija uses a different definition for the spanwise lift distribution than the one used in XFLR5: he uses the mean aerodynamic chord instead of the local chord.¹ This arouses suspicion that he uses the same definition of lift to determine the effective angles and in turn the lift corrections. As a result of this difference in lift coefficient definition, the total lift values become smaller at high angles of attack, which is indeed the case when observing the results given in Figures 5.26. Though the results of his algorithm match better with the reference data, it is based on a wrong definition of lift coefficient. The reason that it is wrong, is because a mean value over span is used to determine local corrections, which depend on local flow behavior. Therefore, also local parameters should be used.

¹This can be derived from the spanwise distributions and the corresponding values of total lift from the 3D lift curves.

To still make a proper comparison between spanwise distribution, the values from XFLR5 are transformed such that they match the definition of Carqueija. The results are depicted in Figure 5.31. The 'unsmooth' values of VLM MG_b near the root are caused by numerical errors of VLM2; the results of VLM1 (horseshoe vortices instead of ring) do not show these peaks and are of similar shape as the results of Carqueija.

The total lift and drag related curves in Figures 5.26-5.31 show that lift is over-predicted for high angles of attack, and drag is slightly under-predicted. There is significant improvement for the entire range with respect to the standard VLM. Considering the, for kite systems important, lift-to-drag ratio: the deviations are less than 10% up to $\alpha = 10^\circ$, from this point on it starts to deviate and at $\alpha = 16^\circ$ it is predicted 25% higher ($L/D = 10$ vs $L/D = 7.5$).

The lift curve of the 3D panel method, shown in Figure 5.32, shows a significant higher lift slope than the VLM, while the lift-to-drag ratios in Figure 5.33 are similar (remaining results of the panel method can be found in Appendix F). After investigation on the same wing with a 1% and 20% thick airfoil, it was determined that the difference in lift slope is mainly caused by the difference in modeling, not so much due to airfoil thickness. Thus, after comparing the nonlinear VLM and 3D panel method for a wing with strong spanwise camber, it can be concluded that *the nonlinear 3D panel method has lower accuracy than the VLM for arc shaped wings.*

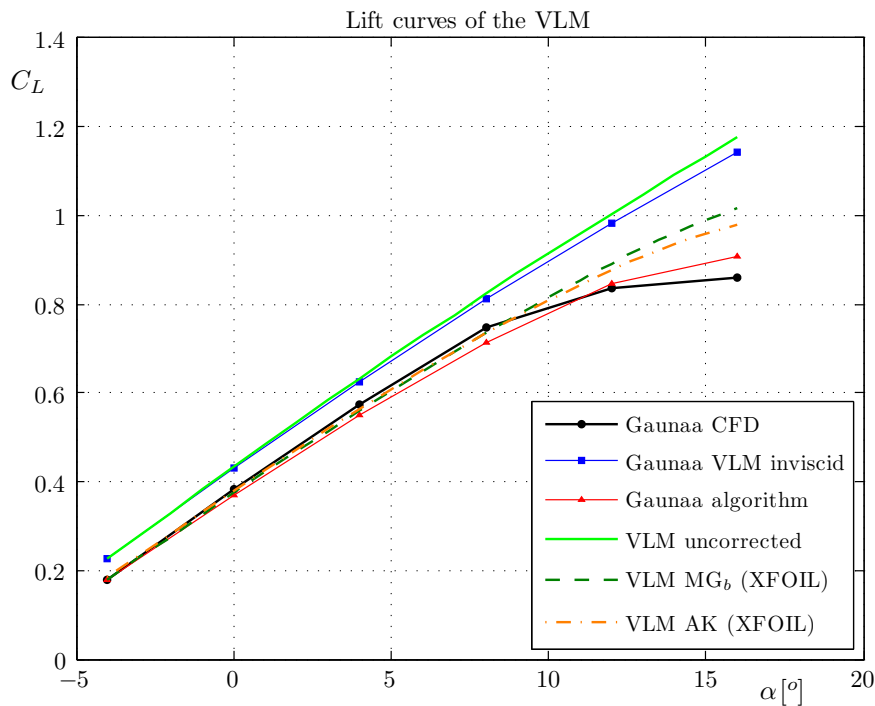


Figure 5.26: Comparison of $C_L - \alpha$ curves obtained from simulations of the arc shaped kite.

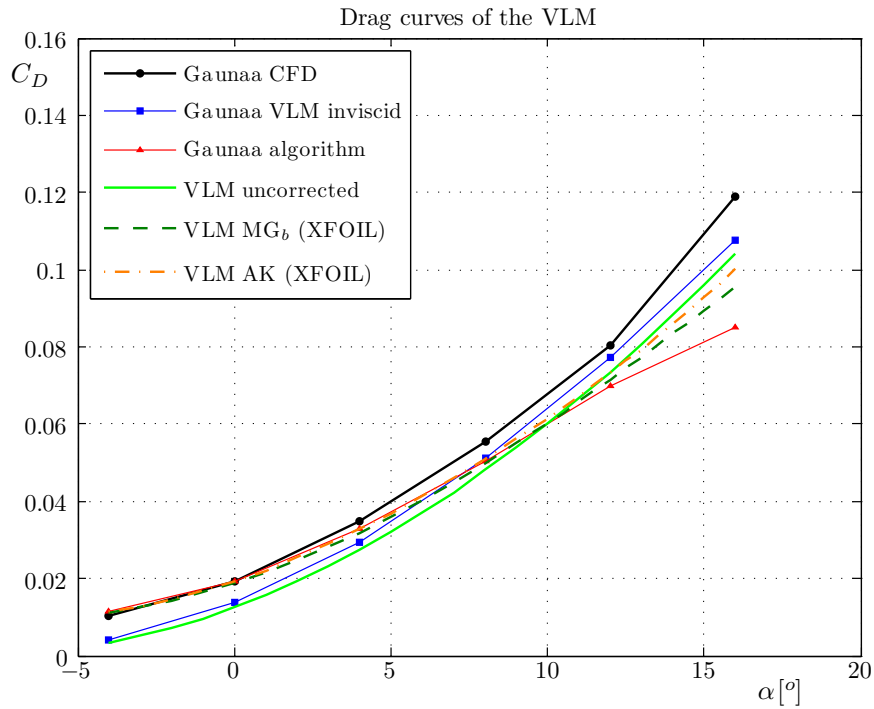


Figure 5.27: Comparison of $C_D - \alpha$ curves obtained from simulations of the arc shaped kite.

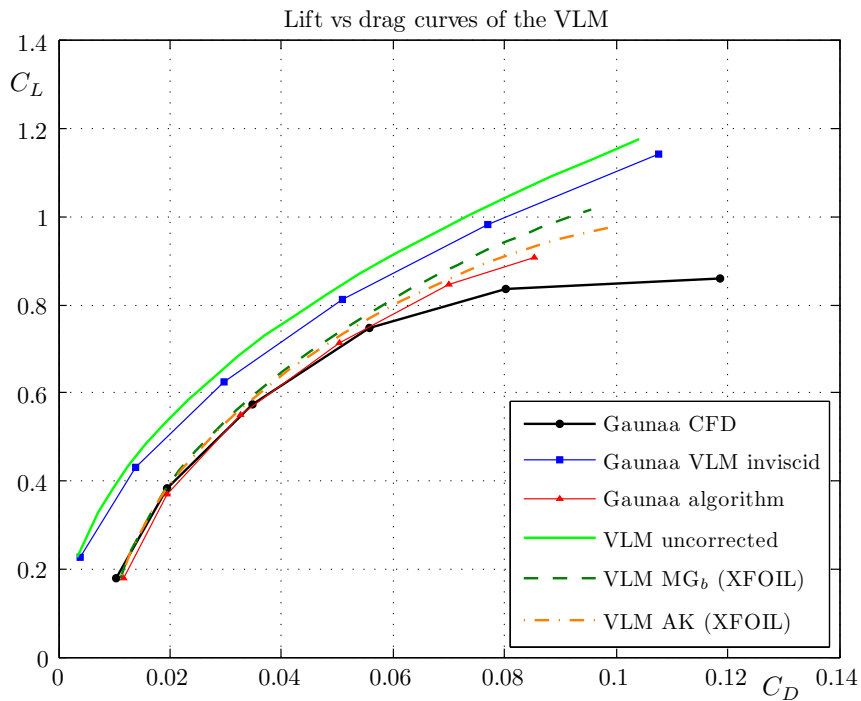


Figure 5.28: Comparison of $C_L - C_D$ curves obtained from simulations of the arc shaped kite.

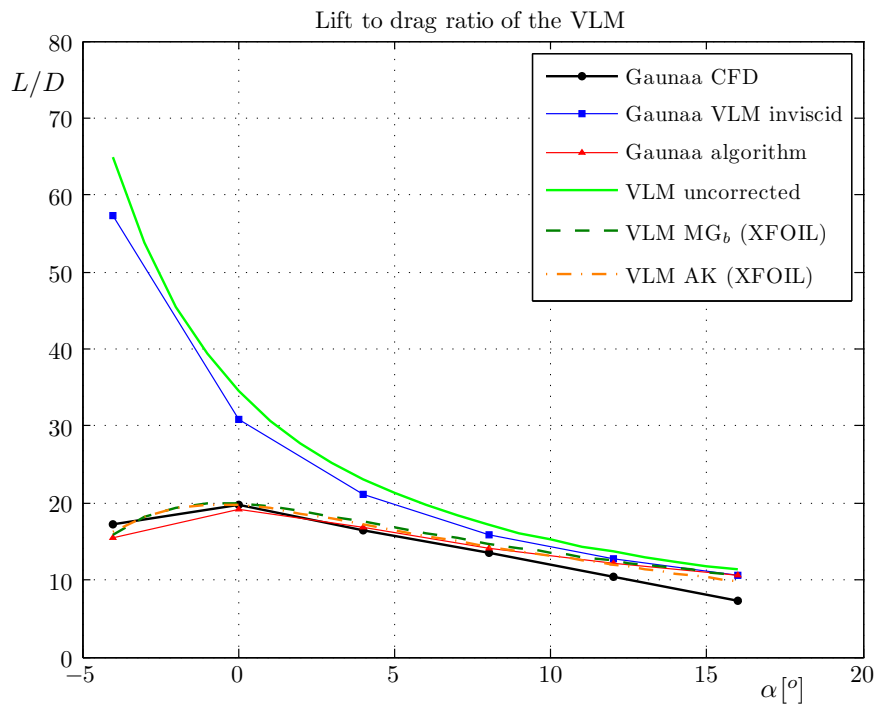


Figure 5.29: Comparison of $L/D - \alpha$ curves obtained from simulations of the arc shaped kite.

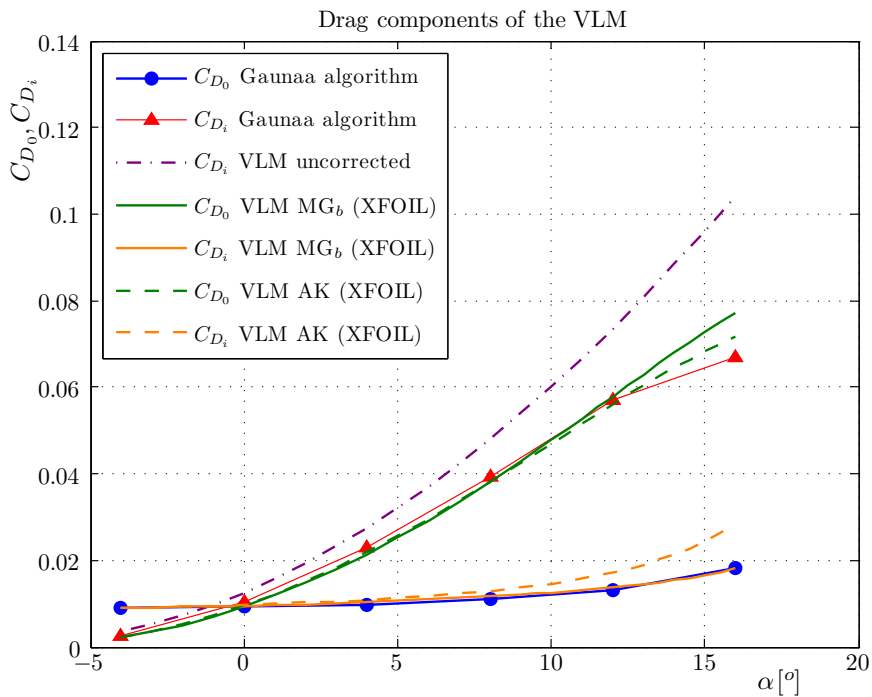


Figure 5.30: Comparison of C_D , C_{D_0} and C_{D_i} as function of α curves obtained from simulations of the arc shaped kite.

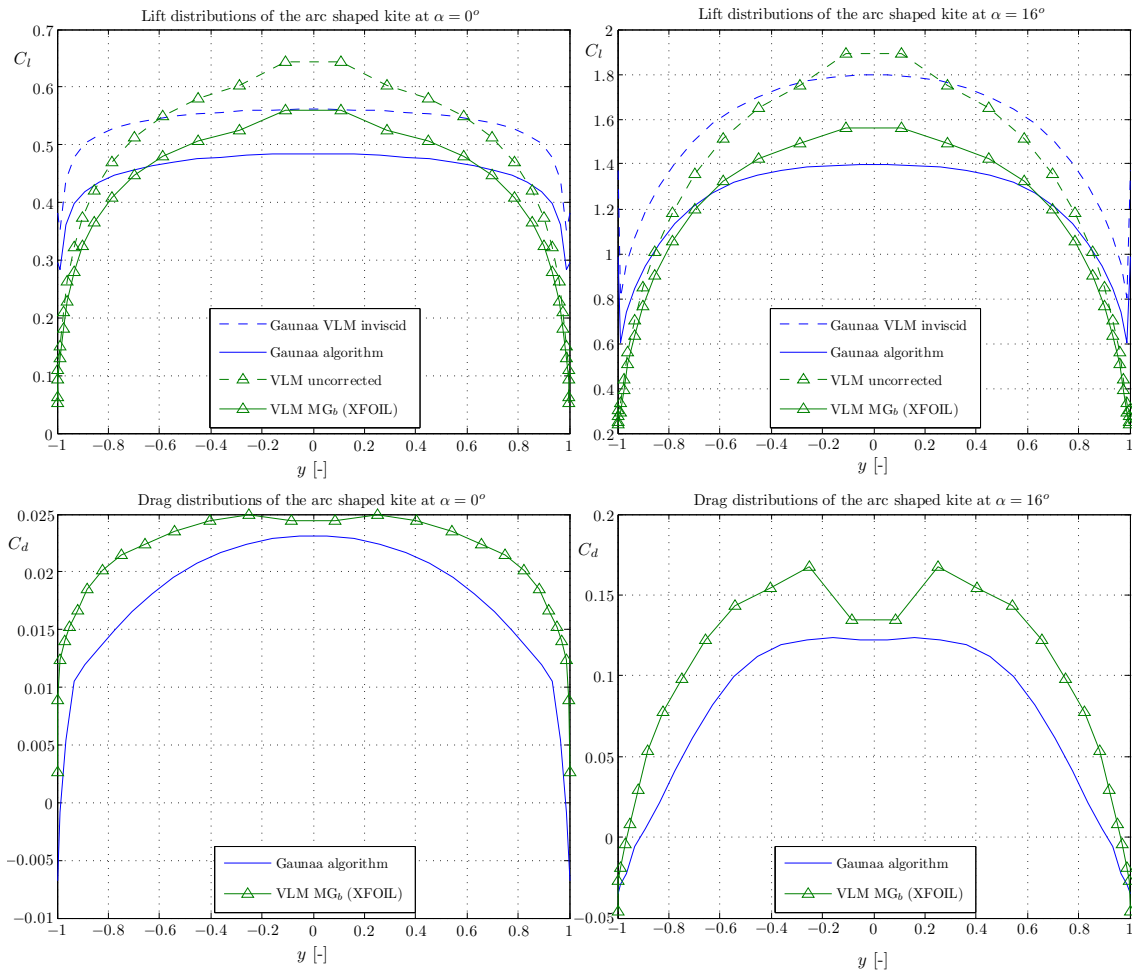


Figure 5.31: The $C_l - y$ and $C_d - y$ distributions obtained from simulations of the arc shaped kite with $\alpha = 0^\circ$ and $\alpha = 16^\circ$.

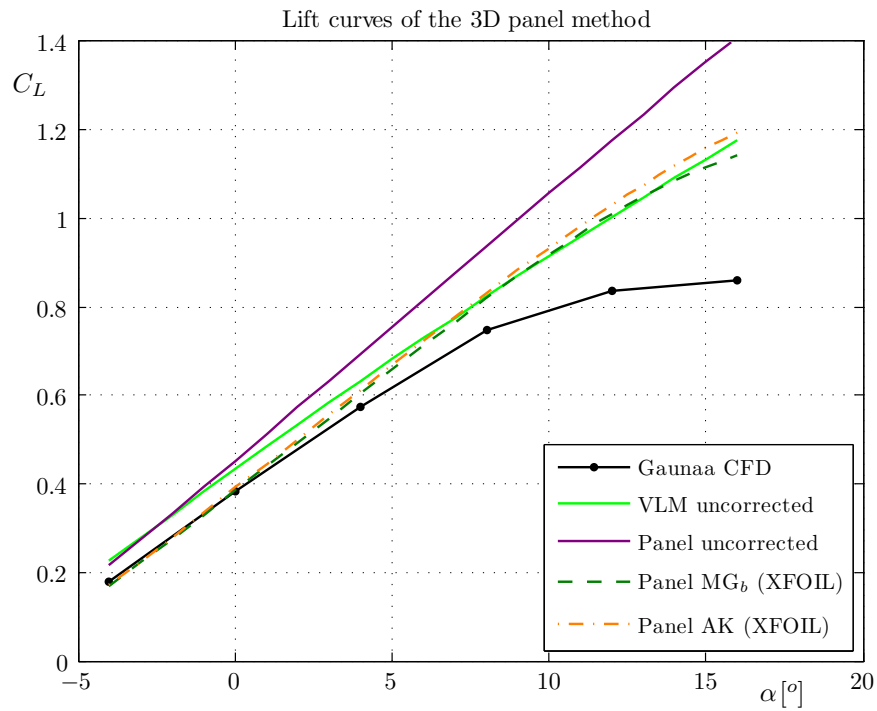


Figure 5.32: Comparison of $C_L - \alpha$ curves obtained from simulations of the arc shaped kite.

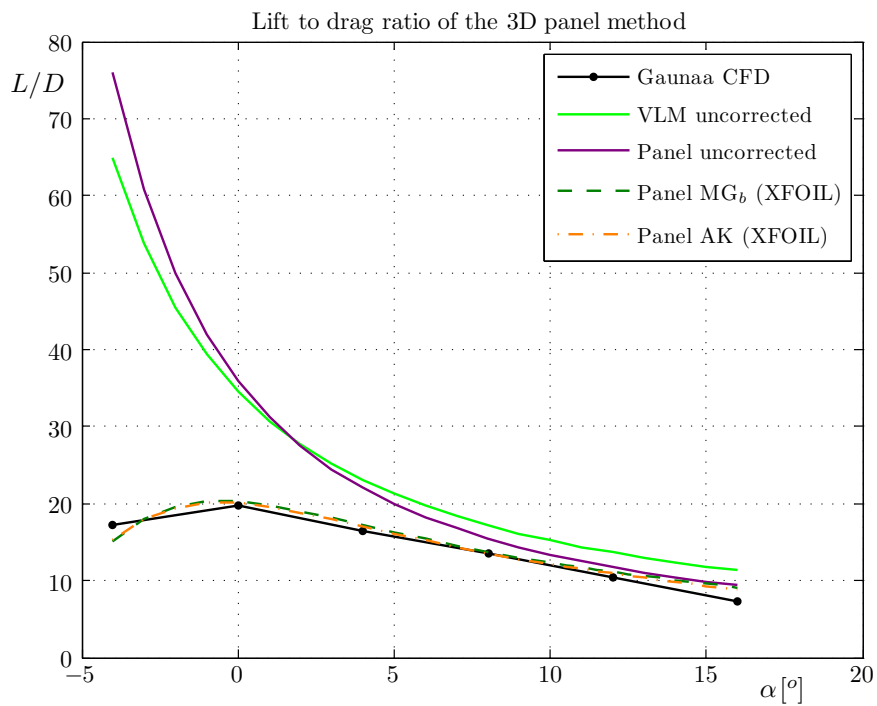


Figure 5.33: Comparison of $L/D - \alpha$ curves obtained from simulations of the arc shaped kite.

5.5 Software performance

So far, the quality of the adapted aerodynamic analysis tool has been proven. Since it concerns a computational program, performance is an important feature. In this section, focus will be laid on the impact of number of iterations on computation time and accuracy.

5.5.1 Impact of number of iterations

The influence of the number of iterations on the accuracy of the results is investigated with the flat wing configuration (see Section 5.2.1), as shown in Figure 5.34. Only the lift coefficient around stall is considered, since there the angle shifts and effect of number of iterations is the highest.

Results are similar for the AK and MG versions, though the AK version diverges for high angles of attack. This is caused by the peaks in spanwise induced angle distributions that become visible after two iterations (see Figure 5.35). The combination of angle shift and the induced angle determination in the Trefftz-plane results in fluctuating distributions and occurs for every type and number of paneling. The MG version determines the induced angles from the lift distribution and does not show this behavior.

An exponential decay in the relative error is observed: the error with respect to the converged value is already less than 3% after two iterations. Using one iteration with AK is sufficient for having a maximum error of about 10% at stall and less for smaller angles. Two iterations would result in higher accuracy but, as mentioned above, peaks will become visible in spanwise distributions.

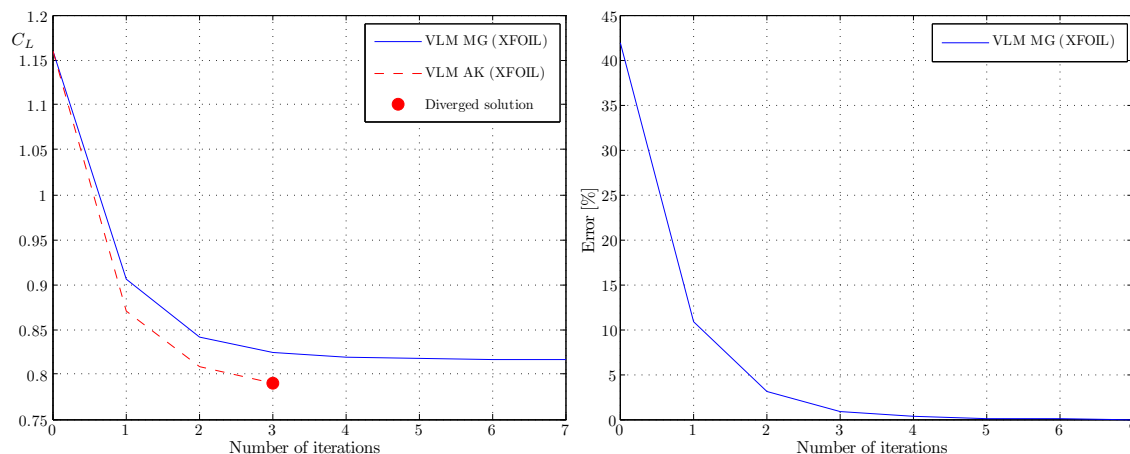


Figure 5.34: Convergence and accuracy of C_L vs number of iterations of the flat wing for $\alpha = 16^\circ$.

5.5.2 Computational time

The computational times are determined at multiple discrete angles of attack, consequently for varying number of iterations, and by doing a full angle of attack sweep from which an average time per angle of attack follows. The results are given in Table 5.6 for which the arc shaped kite with 600 panels is used.

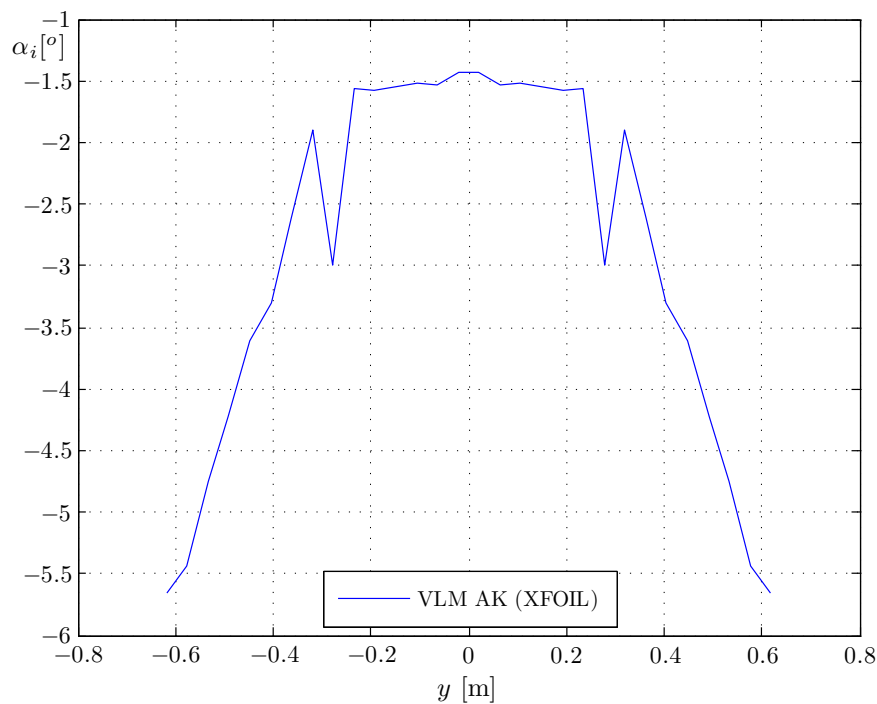


Figure 5.35: Induced angle distribution (VLM AK (XFOIL)) of the flat wing for $\alpha = 16^\circ$.

Carqueija et al. (2010) states about the computational time of his VLM algorithm: "In average, the algorithm takes around 1.5 minutes to compute one angle". The algorithm presented in this method, which is written in C++, uses only about **100 ms** (clock resolution of 15 ms) to compute one angle in VLM2 and therefore presents a huge reduction in computational time. The same computation time per angle of attack was observed when doing a full angle of attack sweep. It was found that the number of iterations have negligible influence on the computational time.

For VLM1 computational times are higher, since it uses trailing vortices instead of quad vortices. For 6 and 14 iterations, required calculation times are respectively 307 ms and 561 ms, hence an increase in computational time with increasing iterations is observed. This is probably caused by the relatively time consuming process of calculating the influence of the trailing edge vortices.

The 3D panel method uses 1,240 panels and as a result computational times are significantly higher: 1,148-1,196 ms for 7-13 iterations. The influence of the number of iterations is very small. The average time per angle of attack of an angle sweep gives a much lower value of 680 ms. For the 3D panel method, the TG option (free wake) was not available, therefore the influence coefficients of the wake do not change for varying angle of attack. Thus it can be said that the calculation of the wake influence consumes a significant portion of computational time.

Table 5.6: Effect of the number of iterations on the computational time for the flat wing, using version MG_b .

	VLM1		VLM2		3D panel method	
<i>discrete α</i>						
α [°]	Iterations	Time [ms]	Iterations	Time [ms]	Iterations	Time [ms]
0	6	307	6	109	7	1,148
3	6	306	7	105	6	1,147
6	5	273	6	108	6	1,173
9	6	306	6	104	6	1,150
12	7	329	6	103	8	1,158
15	14	561	8	106	13	1,196
18	-	-	12	109	-	-
20	-	-	22	115	-	-
<i>α-sweep for [0:1:20]</i>						
Time [ms]	7,614		2,162		14,285	
Average time per α [ms]	363		103		680	

Aerodynamic Analysis of LEI Kites

This chapter points out how to handle the proposed nonlinear potential flow method for LEI kites. Profiles with a round leading edge and single canopy (called single membrane airfoils) are discussed and an approach is given for obtaining realistic chordwise pressure distributions. First, the preliminary study required for 2D CFD analysis is discussed. The results of these CFD simulations are later used as validation for faster airfoil analysis tools.

6.1 Fluent grid and parameter study for 2D CFD analysis

Breukels (2011) already performed many CFD simulations on kite profiles, however no grid and parameter study was performed, which are considered essential for CFD simulations. From these initial studies a large part of the uncertainties and errors that result from using computer models can be addressed.

For the 2D CFD analysis in Ansys Fluent (v13.0.0) a study is performed such that modeling, discretization and iterative errors are addressed and, when possible, reduced to a minimum. If not obtained by this study the choice of settings are obtained from, or by a combination of: earlier 2D CFD analysis (Breukels, 2011; Wachter, 2008; Vos, 2006), Fluent user manual, literature and expertise from CFD specialists S. Van Zuijlen and S. Hulshoff (DUT).

6.1.1 Solver

As LES and higher order CFD solvers were not available and are probably not time efficient, RANS modeling is used. Due to the shape of the profile and the typical high Reynolds numbers of kites ($0.5M \leq Re \leq 5M$) turbulent flow and separation will be present substantially. The use of LES or the Reynolds Stress Model were not considered, because of their high computational demand. It was decided to use the $k - \omega$ SST (Shear Stress Transport) model, which combines the best of two far developed turbulence models: $k - \epsilon$ and $k - \omega$. This two equation linear eddy viscosity model uses the Boussinesq hypothesis, which states that the momentum transfer caused by turbulent eddies can be modeled with an eddy viscosity (Schmitt, 2007). The SST model is one of the most widely used models for aerodynamic flows, according to B. Menter (1989). By default the $k - \omega$

model uses enhanced wall treatment.

The solver was conFIGured as pressure-based, steady, two-dimensional with pressure-velocity coupling by a SIMPLEC scheme. A Green-Gauss node based gradient discretization is used with second order pressure and second order upwind momentum, turbulent kinetic energy and specific dissipation rate spatial discretization.

6.1.2 Meshing

For meshing Ansys ICEM CFD (v13.0) is used. Before meshing in ICEM, the CAD program Rhinoceros (v4) was used to adapt the geometry. Both geometry simplification as mesh properties are discussed in this section.

Geometry simplifications

Some simplifications with respect to reality were made. An example of the mesh close to the profile is given in Figure 6.1. A perfect smooth profile is assumed, having no surface roughness. Seams, stitches and local reinforcements are thus neglected. Many kites contain a zigzag seam on the leading edge tube. This seam could induce turbulence in the flow making it more prone to transition. It is difficult to predict what the exact effect is on the boundary layer, but since Reynolds number are in general high for kites it is expected that the flow transitions to turbulent close to the LE. Therefore it is expected that the influence of the presence of a seam is small. This is however not verified.

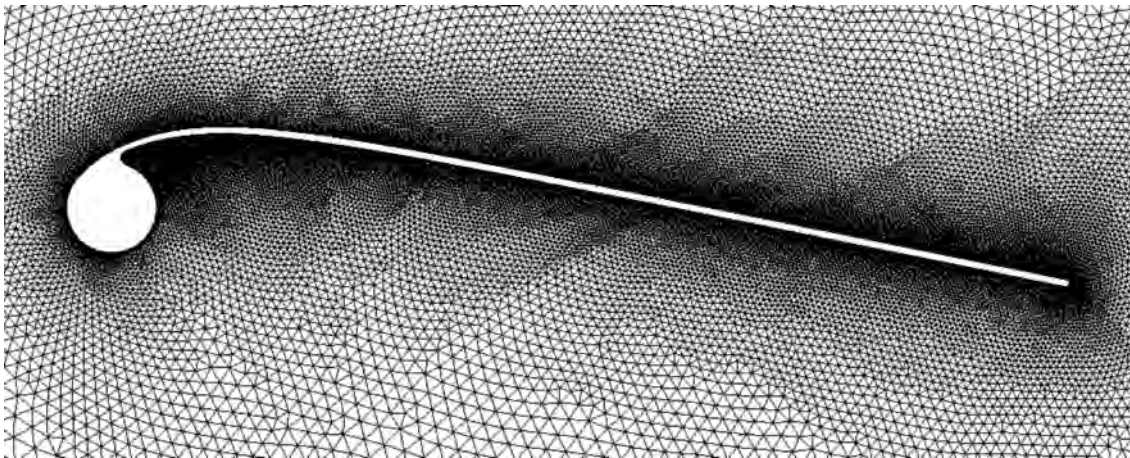


Figure 6.1: A zoom-in on the two dimensional grid around the center profile of the DUT-MutinyV2 kite.

The sharp corner behind the leading edge connecting the canopy to the leading edge tube is modeled as an arc with finite radius, as shown in Figure 6.2. This corner behind the leading edge is not an important part of the flow dynamics of a kite; the flow is more or less standing still. Pressure forces near this corner at the lower side are small and dominated by the flow at the upper side, caused by the large separation area. The reason for changing this corner is to simplify the boundary layer mesh, which consists of prism elements. If a constant thickness boundary layer mesh is used, the corner should be large enough to let the prisms turn in the corner without intersecting each other. In this case

the radius should be larger than the prism mesh thickness.

The boundary layer is build up from prism elements, which should be aligned with the local flow direction. Preferably, the prism mesh is continued behind the airfoil in the direction of the wake. However, problems were experienced with the gradual decrease of prism layers ('stair stepping'). Due to time constraint this was solved by using a larger canopy thickness than in reality: approximately 2mm. This way the prism mesh can be curved around the TE with constant thickness, as shown in Figure 6.3. Assuming a circular cylinder the drag caused by the trailing edge is less than 2% of the total drag for Reynolds numbers $1 \cdot 10^6 \leq Re \leq 6 \cdot 10^6$ (Anderson, 2001).

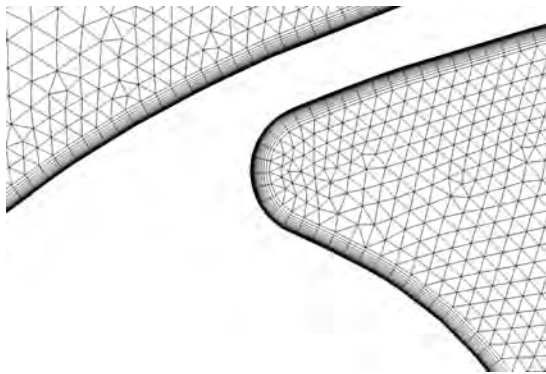


Figure 6.2: The sharp corner between the leading edge tube and canopy is modeled with a finite radius arc to simplify boundary layer meshing.

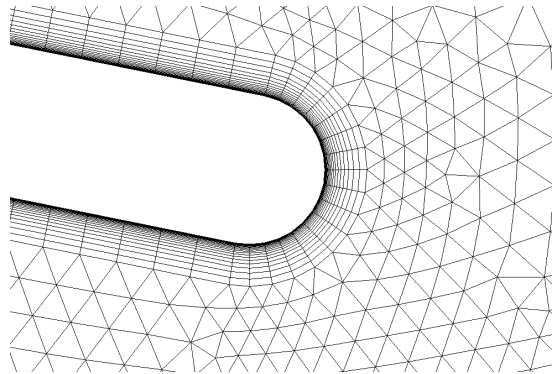


Figure 6.3: The prism mesh at the trailing edge.

Mesh properties

An unstructured mesh with triangular elements is used, which are more flexible and easy to handle than structured meshes. As already mentioned, the boundary layer is build up from multiple layers consisting of prism elements. Both type of elements can be seen in Figure 6.2 and 6.3. The size of the prism elements are discussed in the next section. More Figures of the mesh are given in Appendix G.

A fine mesh is used near the profile to properly solve the high gradients in flow parameters. Going outwards to the boundaries the flow is aligned with the free stream and a coarser grid is sufficient. To obtain an efficient mesh three different grid density areas are defined¹ Using different grid density areas resulted in a more gradual increasing mesh. As a result, only the parts of the domain in which there is high disturbance, contain small elements. This way there can be saved on number of grid cells and thus on computational effort.

After mesh generation, smoothing of the triangular elements is applied based on element quality. A poor quality mesh can display results that are more mesh dependent than model dependent, and the solution could have more difficulties to converge. Mesh

¹There were problem with the control of mesh density around curves. ICEM constructs areas with a certain element density and uses hard boundaries at which these densities are increased. Therefore there is only limited control of the mesh density on and around curves.

quality is solely defined by geometry, where a maximal value of 1 corresponds to a perfect triangular shape.

Lastly, solution based grid adaptations are applied after 500 and 1000 iterations. These adaptations are performed by Fluent, where the mesh is locally refined in high gradient areas. Two types of adaptations were applied, one based on pressure coefficient and one on TI. Typical values of these parameters around kite profiles are given in Figure 6.4 and 6.5. After the two grid adaptations there is approximately a 85% increase in cells with respect to the starting mesh.

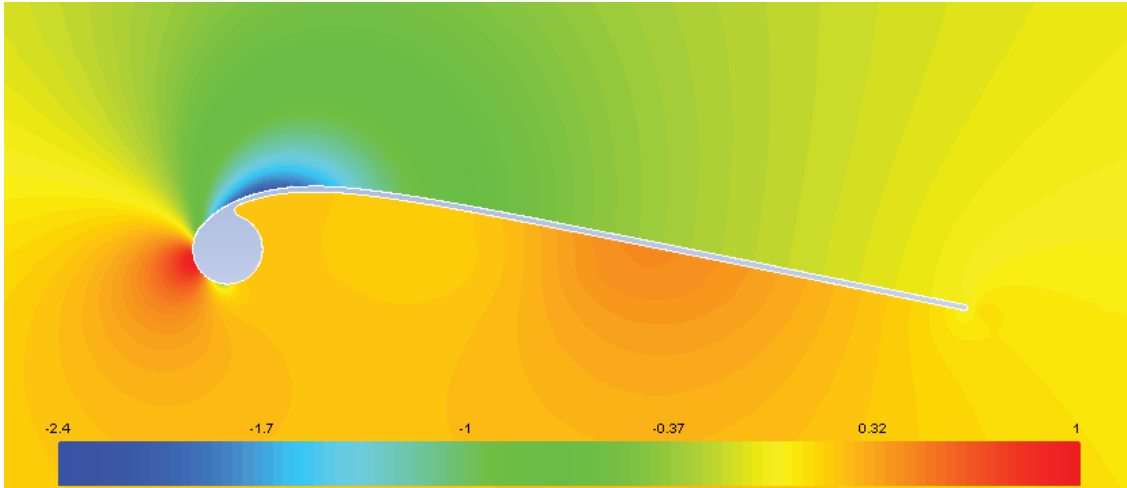


Figure 6.4: Contours of pressure coefficient for the DUT-MutinyV2 center profile at $\alpha = 4^\circ$ and $Re = 2.9 \cdot 10^6$.

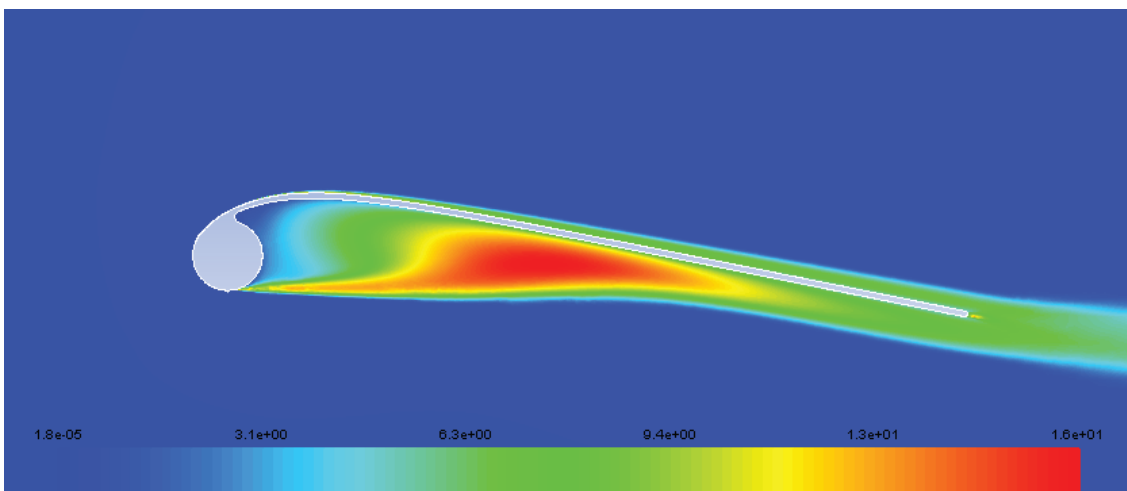


Figure 6.5: Contours of turbulence intensity for the DUT-MutinyV2 center profile at $\alpha = 4^\circ$ and $Re = 2.9 \cdot 10^6$.

Wall distance estimation: y^+

The boundary layer is meshed with multiple prisms layers. The structured nature of the prisms in the normal to surface direction offer good orthogonality and clustering capabilities, making them fast and efficient. To determine what the height of the initial cells should be a wall distance estimation is performed. The size of the prism elements in the wall normal direction is given by the non dimensional parameter y^+ :

$$y^+ = \frac{\rho u_\tau y_P}{\mu} \quad (6.1)$$

where $u_\tau = \sqrt{\tau_w / \rho_w}$ is the friction velocity and y_P is the distance from point P to the wall. The requirements for this parameter are (Fluent manual):

- "When the enhanced wall treatment is employed with the intention of resolving the laminar sublayer, y^+ at the wall-adjacent cell should be on the order of $y^+ = 1$. However, a higher y^+ is acceptable as long as it is well inside the viscous sublayer ($y^+ \leq 4 - 5$)."
- "You should have at least 10 cells within the viscosity-affected near-wall region ($Re_y \leq 200$) to be able to resolve the mean velocity and turbulent quantities in that region."

A prism exponential growth factor of 1.2 is used with 20 layers. From equation 6.1 it follows that the initial height decreases with increasing wall shear stress τ_w . Since skin friction increases with free stream velocity, the higher Reynolds number limit of the performed CFD simulations is used: $Re_L = 4.2 \cdot 10^6$ corresponding to $U_e = 22\text{m/s}$ for a profile with a chord of 2.72m. The skin friction is approximated (CFD-Online, 2011b) using the Schlichting skin-friction correlation for a turbulent boundary layer (Schlichting & Gersten, 2000):

$$\begin{aligned} c_f &= (2 \cdot \log_{10}(Re_L) - 0.65)^{-2.3} \\ &= 3.77 \cdot 10^{-3} \end{aligned} \quad (6.2)$$

The friction velocity becomes:

$$\begin{aligned} \tau_w &= c_f \cdot \frac{1}{2} \rho U_e^2 \\ &= 0.87 \end{aligned} \quad (6.3)$$

An estimation of the first grid point to obtain $y^+ = 1$ follows from:

$$\begin{aligned} y_1 &= \frac{y^+ \nu}{u_\tau} \\ &= \nu \sqrt{\frac{\rho}{\tau_w}} \\ &= 1.42 \cdot 10^{-5} \sqrt{\frac{1.225}{0.87}} \\ &= 1.7 \cdot 10^{-2} \text{mm} \end{aligned} \quad (6.4)$$

Using these settings y^+ values of smaller than 1 were found. To save on computational effort a somewhat higher value of $y_1 = 3 \cdot 10^{-2} \text{mm}$ is used for the performed simulations, which results in $y^+ \approx 1$. The relative thickness of the prism mesh is 0.2% chord.

6.1.3 Boundary Conditions

The boundary conditions are defined by type and corresponding required values. For the $k - \omega$ model values for turbulence and dissipation should be set at the inlet and outlet. This influence is discussed in Section 6.1.4.

Types

Five boundaries are identified for this problem:

- *Inlet*: A velocity inlet is the only suitable candidate to use.
- *Upper and lower wall*: A symmetry plane is applied. A symmetry plane is a zero shear stress wall, for which normal velocity and gradients are all zero. In theory this is the case for flow infinitely far away from the wing. Since in CFD there is a bounded domain in which the flow is calculated, the symmetry BC will have a consequence on the results. These could be understood in the same way as some of the wall effects present in wind tunnels. By using a domain study these effects can be minimized
- *Outlet*: A pressure outlet is used. Compared to an outflow boundary condition it often results in a better rate of convergence when back flow occurs during iteration.
- *Wing*: This is set as a wall for which a no-slip condition is enforced.

Free stream values

Standard atmospheric values are taken for pressure p_0 , density ρ_0 , temperature T_0 , viscosity ν and specific heat ratio γ :

$$\begin{aligned}
 p_0 &= 101325 Pa \\
 \rho_0 &= 1.225 kg/m^3 \\
 T_0 &= 288.16 K \\
 \nu &= 1.79 \cdot 10^{-5} m^2/s \\
 \gamma &= 1.4
 \end{aligned}
 \tag{6.5}$$

For the DUT-MutinyV2 kite the apparent wind velocities during flight, including retraction phase, vary between approximately 5-22m/s (Ruppert, 2010). Simulations are performed within these extremes.

6.1.4 Error and uncertainty analysis

In Chapter 5 the smallest error of all correction methods in the trade-off was approximately 5% (stall point of MG_b (XFOIL)). On average the same amount is obtained for the total numerical errors in the performed CFD simulations. Many of the modeling errors can only be addressed when performing validation, such as the used physical models and geometrical simplifications. But as benchmark data is not available, this is not possible. Therefore, a part of the physical approximation error between simulated and 'true' data will remain unknown. This could be a task for future work.

Convergence studies are performed to assess the uncertainty due to iteration and numerical errors caused by discretization. Furthermore, the influence of the artificial

boundaries on the parameters of interest is studied, therefore partly capturing geometrical modeling errors. Lastly, the effect of using different values of turbulence and dissipation is addressed. Computer round-off errors are not considered significant when compared with other errors (Slater, 2008).

Iterative convergence

To obtain a steady state simulation it is ensured that the solution satisfies the following three conditions:

- Residual (RMS) error values have reduced to $\epsilon_{RMS} = 10^{-5}$ for x- and y-velocities, continuity, turbulent kinetic energy and specific dissipation rate.
- Lift, drag and moment coefficients have reached a steady solution.
- The mass flow imbalance (difference between mass flow at inlet and outlet) in the domain is less than 1%.

To prevent divergence, relaxation factors are applied. These were set at 0.6 for pressure and 0.7 for momentum, k and ω .

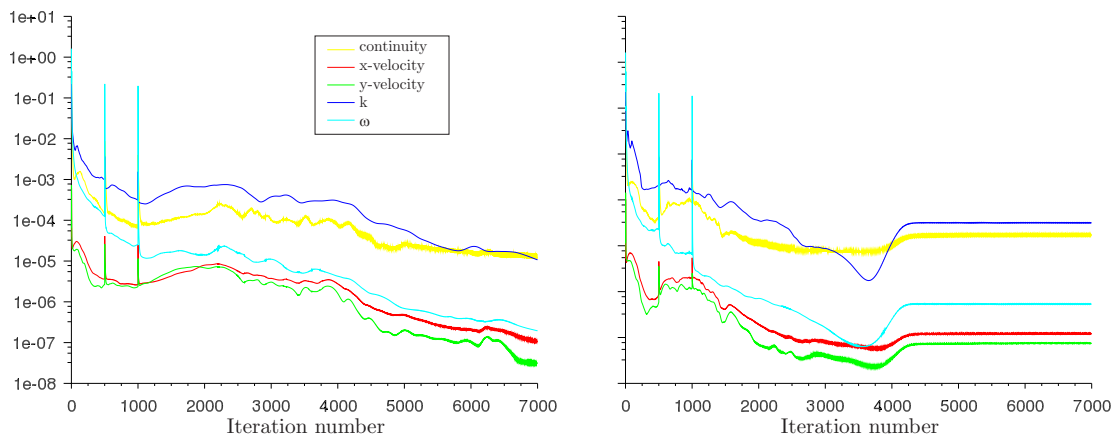


Figure 6.6: Residuals during iteration. Left: $\alpha = 0^\circ$, right: $\alpha = 10^\circ$

In the left plot of Figure 6.6 it is nicely seen that for an angle of attack $\alpha = 0^\circ$ the residuals decrease to the desired values. For an high angle of attack ($\alpha = 10^\circ$) the residuals reach a steady-state value (right plot), probably caused by unsteady flow. For this case the convergence criteria were not achieved, however the iterative behavior of the steady solver is oscillatory convergent, as shown in Figure 6.7.

The discussed results of the CFD simulations are obtained as the mean values of the converged oscillations. An indication of the uncertainty of the parameter of interest can be expressed by the relative standard deviation of the oscillatory converged solution. The uncertainty in Figure 6.7 was found to be $\sigma_{C_l} = 0.03\%$ for lift and $\sigma_{C_d} = 0.7\%$ for drag. The amplitudes of oscillation were $A_{C_l} = 1.7 \cdot 10^{-3}$ and $A_{C_d} = 4.8 \cdot 10^{-4}$.

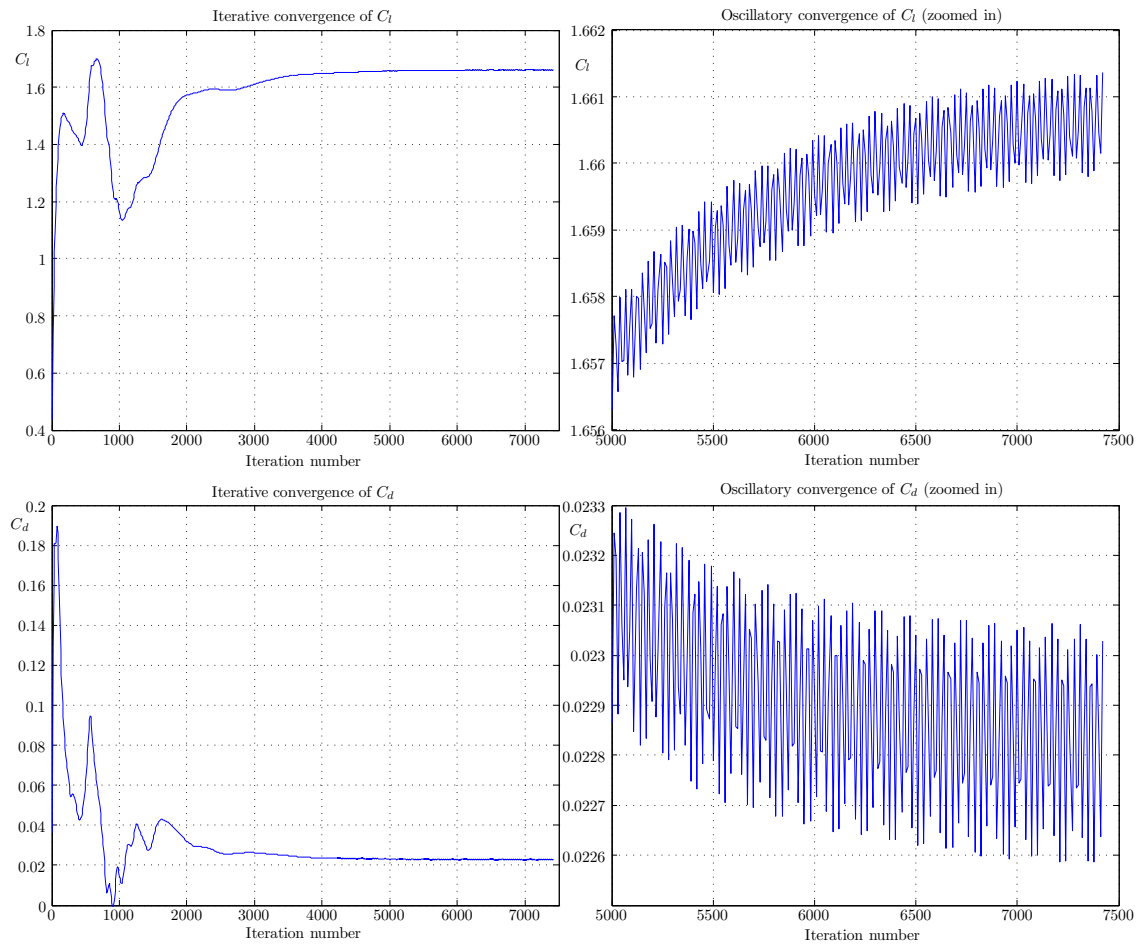


Figure 6.7: Iterative behavior of lift and drag coefficient for a kite profile with thickness 9% and camber 5% at an angle of attack of 10° .

Grid convergence study

A grid convergence study is performed in order to find an efficient mesh and quantification of the numerical error due to a discretization of the domain. An efficient mesh is obtained when having a small computational time and small discretization error. The parameters of interest are C_l , C_d and C_m . Different simulations are performed from coarse to dense grids. Their behavior as function of grid size is shown in Figure 6.8. For a grid of 215,373 cells, the numerical discretization error is approximately 1% for lift and drag and less than 3% for moment. This seems acceptable considering the total numerical discretization error should not be larger than 5%. The slope of the numerical errors ϵ (measured with respect to the finest grid) as function of the number of cells, is on average -1.3 on a loglog-scale, which is slightly higher than the theoretical value of -1 corresponding to second order discretization. The difference could originate from the type of solver, numerical errors and mesh properties.

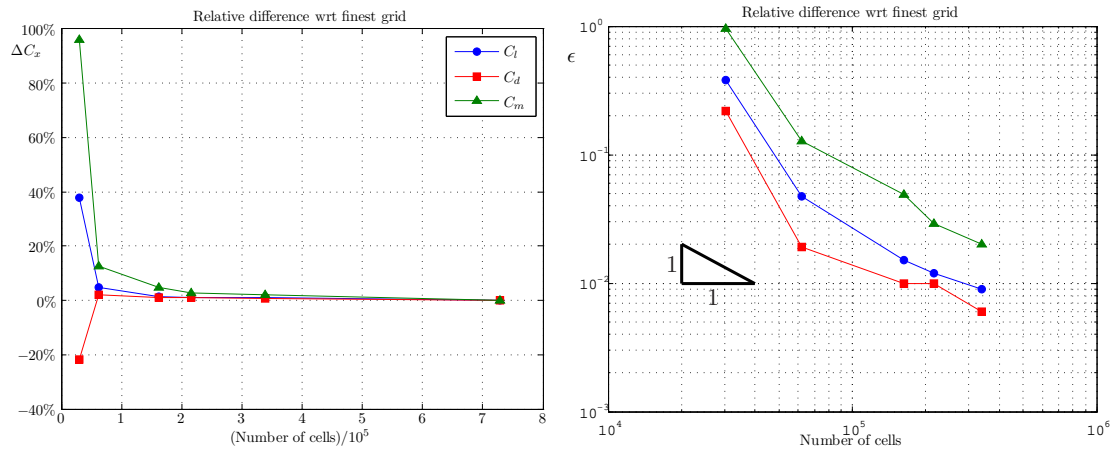


Figure 6.8: Effect of the number of cells on lift, drag and moment coefficients, using a kite profile with 9% thickness and 5% camber at $\alpha = 0^\circ$.

Domain size

The influence of the artificial boundary distances to the profile is investigated. Lift and drag coefficients are observed for increasing distance to the inlet, outlet and walls, which together determine the domain size of the CFD problem. The influence of the boundaries increases for increasing lift and drag. A profile is chosen which has maximum total lift and drag force with respect to the other performed CFD calculations: the center profile of the DUT-MutinyV2 kite (same as grid convergence study), which has a chord of 2.72m. This foil will be the limiting factor when determining your computation domain, since all smaller airfoils are relatively further away from the walls when the same domain size is used. Results are obtained for both a low and high angle of attack (the high angle of attack, $\alpha = 10^\circ$, is just before stall according to the interpolation model of Breukels (2011)). The uncertainty in converged values due to transient behavior at high angles of attack is accounted for, as discussed in section 6.1.4.

The results of the domain size study are given in Figure 6.9. All coefficients for both

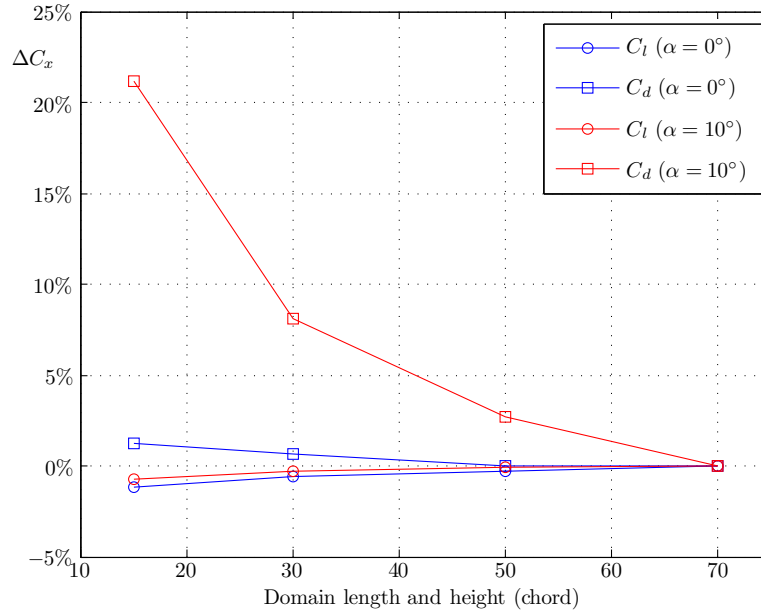


Figure 6.9: Lift and drag coefficients for increasing domain size. The difference is taken with respect to the values for the largest domain.

angles of attack differ not more than 1.3% at the most coarse grid, except for the drag coefficient for the high angle of attack. Even at a domain size of 70 chord lengths, drag is still not totally converged. From extrapolation follows that there will be an approximate 3% further decrease.

For the remaining results a domain of 50 chord lengths in height and length will be used. The maximum error due to artificial boundaries is then approximately 5.7%, following from $\Delta C_d = 2.7\%$ plus the additional estimated 3%. For most cases this error will be smaller, for the reasons mentioned above.

The dependence of the domain size on the number of cells is given in table 6.1. Only a 16% increase in cells is required for a domain size which is 21.8 times as big with respect to the smallest domain. This is possible due to the use of coarser cells when moving away from the wing.

Table 6.1: Domain size influence on the number of cells. The number of cells are determined after grid adaption. Increase factor is taken with respect to the smallest domain.

Domain length & height (chord)	Volume (m ²)	Number of cells	Volume increase factor	Cell increase factor
15	1,665	205,488	-	-
30	6,659	215,373	4.0	1.05
50	18,496	237,947	11.1	1.16
70	36,252	262,159	21.8	1.28

Turbulence Intensity and length scale

Inherent when using the $k-\omega$ model, is defining parameters for turbulence and dissipation. In this case they were defined by a combination of turbulence intensity (TI) and turbulence length scale. These values need to be defined at the inlet; turbulence is 'released' at this boundary and from there on a certain amount is dissipated (F. Menter, 1992).

The value of TI and length scale varies with location, height and time. Atmospheric boundary layer profiles or measurement data can be used to find common values for TI (Stull, 2000). Both Wachter (2008) and Miller et al. (2007) used TI= 3% in their CFD simulations on wing profiles. The length scale is a physical quantity describing the size of the large energy-containing eddies in a turbulent flow and generally increases with increasing height. The Fluent manual gives the following statements regarding TI and length scale:

- "Physically correct values for the turbulence intensity should be achieved near the location of transition." Because of the relatively high Reynolds numbers that apply to kites, the circular profile and the zigzag stitching line, transition will occur near the LE.
- "A TI of 1% or less is generally considered low and a TI greater than 10% is considered high. Ideally, you will have a good estimate of the TI at the inlet boundary from external, measured data."
- "For flows using (...) the $k-\omega$ models, the converged solutions should be independent of the initial values for k and ω . For better convergence, however, it is beneficial to use a reasonable initial guess for k and ω ."

Since it is unknown which length scale to use and what the effect is on convergence, investigations of several combinations of TI and length scale were performed. During the iteration process no grid adaptations were applied, since these adaptations are based on turbulence intensity values in the domain. These values can significantly vary when different TI and length scale values are used. As a result the additional number of cells generated by the grid adaption can vary too.

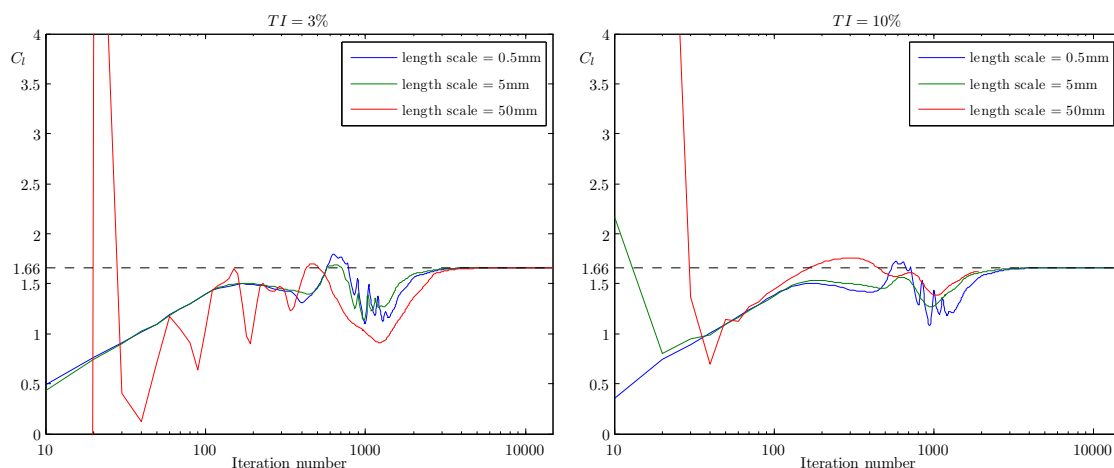


Figure 6.10: Iterative behavior of different values for TI and length scale.

The iterative behavior of lift is given in Figure 6.10. The plots confirm that the converged solutions are independent of the initial values for k and ω , since all plots converge to the same lift value of $C_l = 1.66$. For much larger length scales the solution badly converged or did not converge at all. In future calculations a length scale of 5mm is used, because in this case the oscillations of the residuals for k and ω were small and low fluctuating.

6.2 2D Analysis of LEI kite profiles

The correction for viscous effects in the non-linear VLM is based on airfoil data. This section discusses several possibilities to obtain the required airfoil data and compares results of different airfoil analysis methods. Furthermore, it proposes how to obtain the chordwise pressure loads.

6.2.1 Lift and drag curves

In the proposed method, lift and drag are corrected for viscous effects by using angle shifts and viscous drag, which are both obtained from airfoil analysis. Airfoil lift and drag curves are used and the accuracy of these curves will determine the quality of the 3D wing calculation. If available it is always recommended to use experimental data for viscous coefficients of airfoils, however be aware that not all experimental data is necessarily of high quality. Other options are to use results from CFD solvers such as XFOIL or Fluent. This section investigates how available airfoil analysis methods perform when applied to LEI kite airfoils.

Inviscid lift curve

The inviscid lift curves of the profiles can be determined by XFOIL. Currently both the inviscid as viscous solution are not given in XFLR5 when the boundary layer correction does not converge. A small adaption to the program should be required to make the plug-in version of XFOIL output the inviscid lift values regardless whether the solution converges. Due to time constraint this was not implemented during this thesis, but since the stand-alone XFOIL version is capable of performing inviscid calculations for any angle of attack, this should not be a problem in possible future work on this subject. Calculation times were tested with the stand-alone version and were found to be 2.5ms per angle of attack.² In the FEM model of Bosch (2012a) 38 spanwise sections were used. For constructing a linear inviscid lift curve only 2 angle of attacks are required. Then, the total computation time for each simulation step for constructing all inviscid lift curves by using XFOIL would be $2 \times 38 \times 2.5\text{ms} = 190\text{ms}$. However, with the use of polynomial regression models or lookup tables this could be reduced to the order of milliseconds, considering that the entire aerodynamic model of Breukels only takes (on average) 10ms in Matlab.

²This followed from using 100,000 angles of attack measured in 40 seconds.

Breukels' regression model

The aerodynamic tool should serve as part of an aeroelastic solver, therefore fast and accurate airfoil data should be available. The non-linear VLM requires complete lift and drag curves for all the airfoil shapes varying over the span of the wing. It is much too computational intensive to generate this large amount of data by doing Fluent or XFOIL simulations for each time step in the aeroelastic solver. Currently, the only existing viscous data generator for single membrane airfoil, which is fast enough, is the polynomial regression model of Breukels. This section gives an indication on how accurate this model. Unfortunately, windtunnel data was not available, but it can be assumed that the high-fidelity 2D CFD simulations in Fluent give the most accurate results (less assumptions and solves entire flow domain with roughly 200,000 cells instead of ± 200).

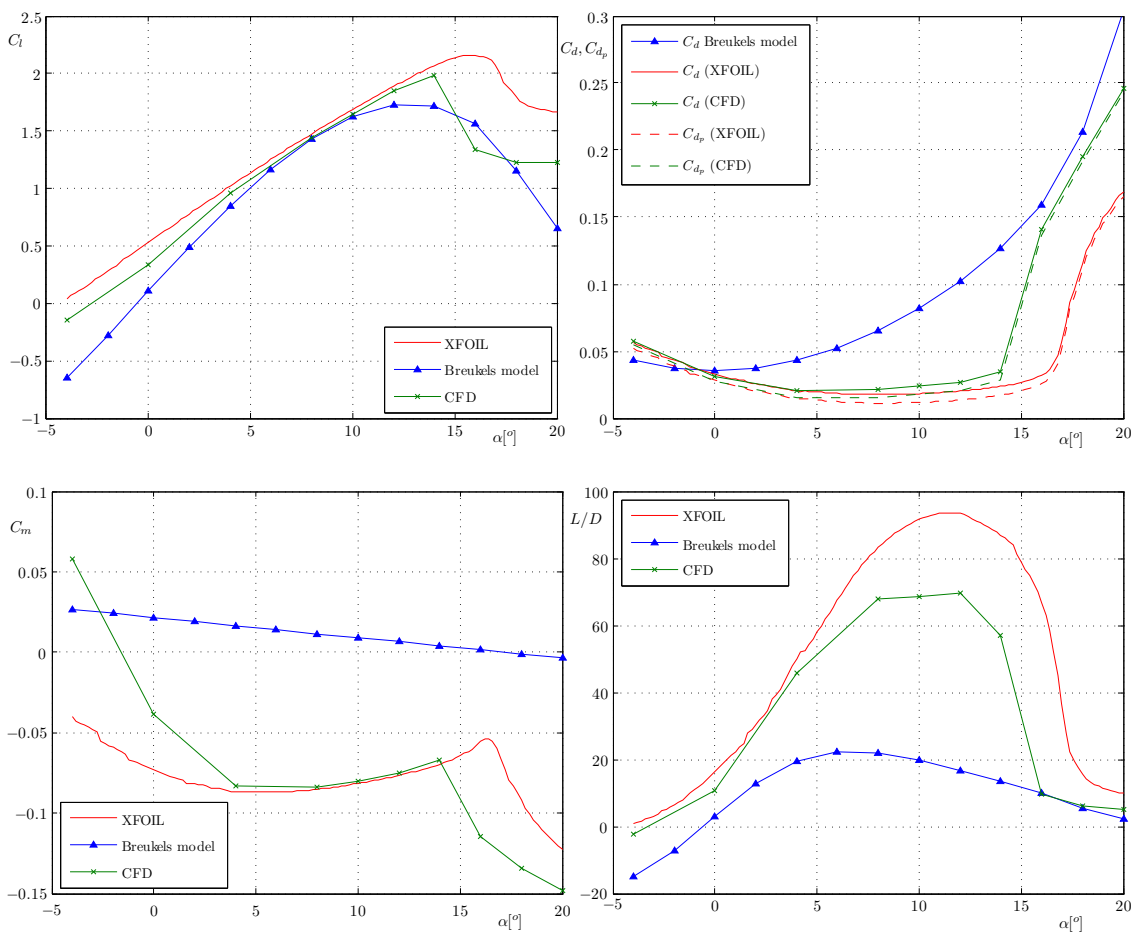


Figure 6.11: Lift, drag and moment curves of the root profile (camber 5%, thickness 9%) of the DUT-MutinyV2 kite for $Re = 2.9 \cdot 10^6$ ($V_\infty = 15m/s$). In XFOIL simulations $n = 9$ is used.

The results of the comparison can be seen in Figure 6.11 and 6.12 for two different single membrane airfoils, where the airfoil shapes are given in Figure 6.14 and 6.15. There is quite some resemblance between the results, though some differences are visible.

The lift curve of the regression model has a higher lift slope and lower zero lift angle. In

his work, he compared his results with wind tunnel data of a single membrane airfoil, which confirms his predicted lift curve slopes are indeed higher than in reality. Furthermore, these experiments showed his drag predictions were too high for angles of attack larger than 0° . The drag curves of the new CFD simulations are indeed lower. Furthermore, the CFD curves show more abrupt stall behavior. This is caused by a rapid movement of the separation point towards the leading edge, which results in a strong increase of pressure drag. This separation point movement is also shown by the velocity contours generated by Fluent simulations in Figure 6.13. The regression model of Breukels is not capable to include these strong changes in lift, drag and moment curve, because the relations in his model are of too low order.

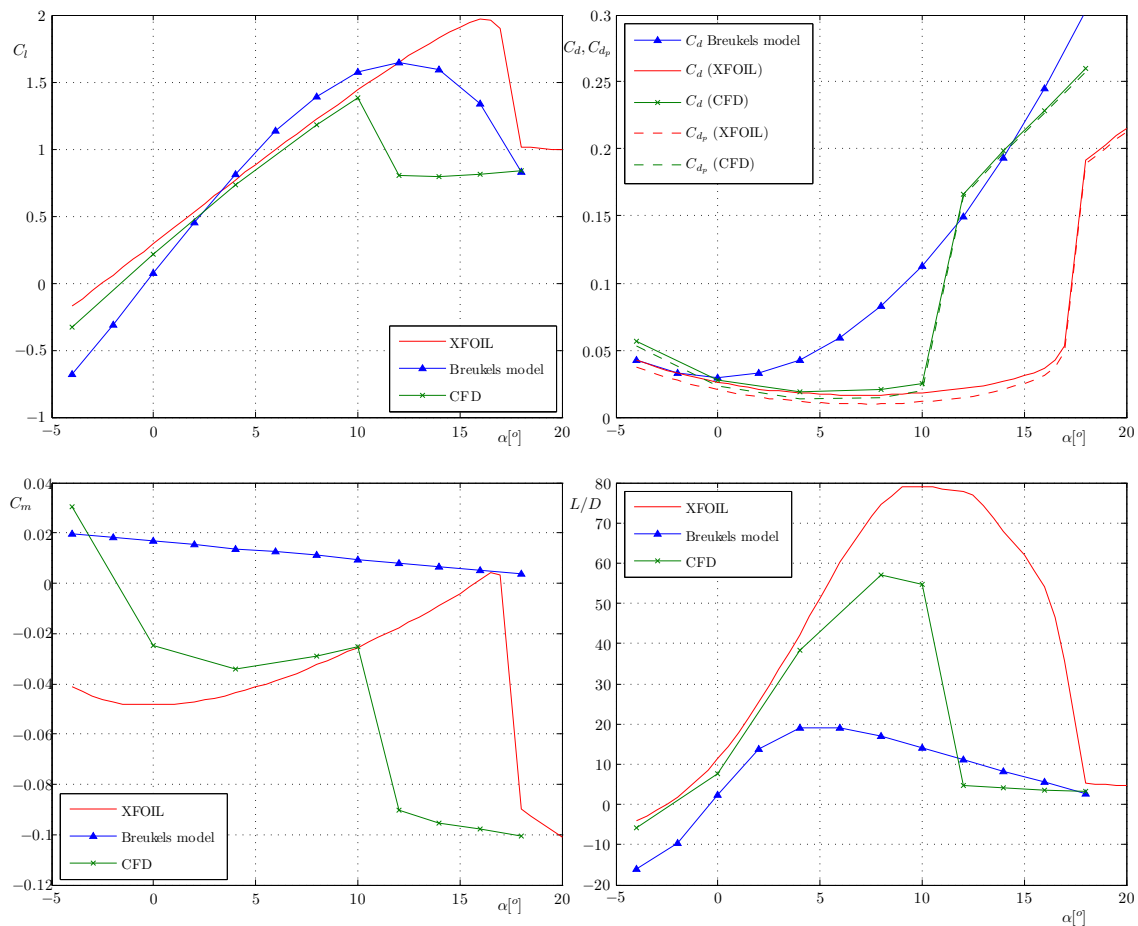


Figure 6.12: Lift, drag and moment curves of the tip profile (camber 1%, thickness 10%) of the DUT-MutinyV2 kite for $Re = 2.9 \cdot 10^6$ ($V_\infty = 15\text{m/s}$). In XFOIL simulations $n = 9$ is used.

The largest differences are visible in the moment coefficient curves, which are linear in the case of the regression model. This is a far too rough approximation. However, airfoil moment curves are not used in the new proposed tool and are therefore not of further interest.

Because of the significantly higher predicted drag, the maximum lift-to-drag ratio is a

factor 3.5 lower and reached approximately 6° earlier. Knowing that L/D is an important parameter for the performance of kites, suggests more accurate regression models are required.

XFOIL

Also the results of XFOIL are compared to those of Fluent, because XFOIL is much faster than high-fidelity CFD and could therefore be a source for future constructed regression models (or lookup tables).

XFOIL can handle small separation regions, but when the separation is getting larger or extends into the wake, the results are getting worse (Hepperle, 2007). XFOIL could therefore have difficulties with predicting the high Reynolds number flows around the strong curvatures of a single membrane airfoil. There is also a practical disadvantage when using XFOIL for LEI airfoils. In theory it is possible to place the panels on the real camber lines of the LEI kite profile, which exists of a round leading edge tube and a single sail profile. However XFOIL requires the profiles to be defined with a lower sail and an upper sail and all panels must be placed in downstream direction. Therefore a geometrical change to the original profile is required. The extent in which a geometry can be adapted is limited; when the geometry is badly defined, problems with convergence can occur.

First a geometrical conversion is applied in order to satisfy the requirements of XFOIL, see Figure 6.14. The one used by the kite design software 'Surfplan' is applied. It uses mathematical equations to change the original foil shape to a shape which can be loaded in XFLR5. The mathematical description of this geometrical change applied by Surfplan is described by (this is confidential information provided by David Aberdeen, the creator of SurfPlan): "The new lower surface follows the leading edge tube around to 45 degrees on the back half of the leading edge tube. From there, a Bezier curve is generated to join the leading edge tube to 25% chord on the sail line. Then, the lower surface continues to follow the sail profile, 0.25% below the upper sail."

The results are also visualized in Figure 6.11 and 6.12. XFOIL predicts a 10% higher $C_{L,max}$ at a 2° higher stall angle with respect to the CFD simulations. The simulations of the tip profile, which has only 1% camber, show significant higher differences for stall point: $C_{L,max} \approx 2$ when using XFOIL instead of $C_{L,max} \approx 1.4$ from the CFD simulations (at a 6° higher stall angle). The behavior of the linear range is approximately the same. In Figure 6.13, the velocity contours generated by Fluent simulations are compared with the predicted boundary layer area by XFOIL for several angles of attack. The boundary layer thickness given by XFOIL shows that even for large separation areas it is still able to predict the size of these areas, though at a later angle of attack.

All in all can be said that XFOIL is comparable to CFD calculations in predicting the airfoil behavior for both low and high angles of attack, and even beyond stall. Stall is however predicted later and at higher lift. XFOIL is however not the only tool that can be used for airfoil analysis and in future work other available methods should be explored.

Effect of Reynolds number

To see the effect of varying Reynolds number on airfoil aerodynamics, CFD simulations were performed for three different Reynolds numbers. From flight tests it is known that for the DUT-MutinyV2 kite apparent wind velocities during flight vary between 5-22m/s

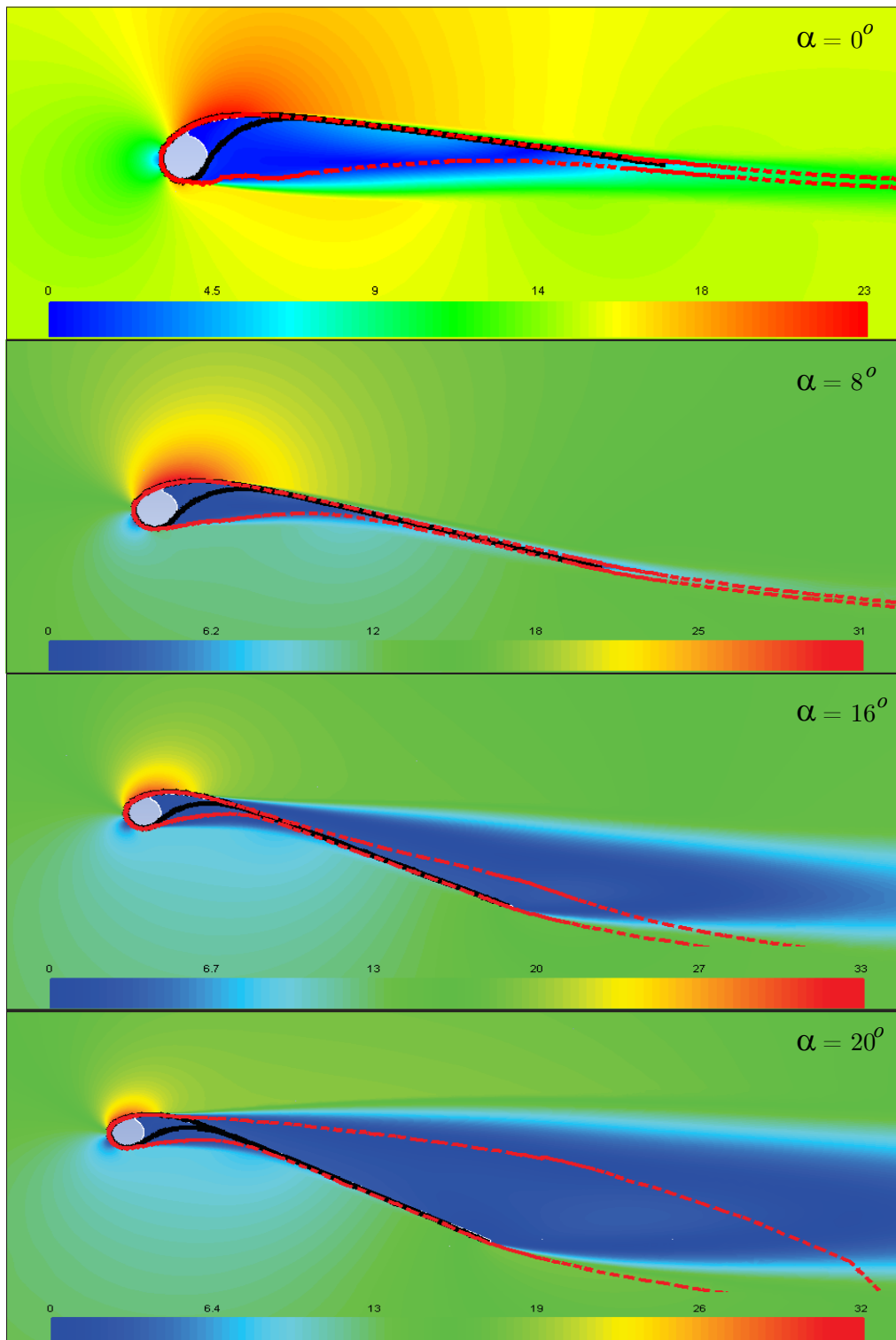


Figure 6.13: Predicted boundary layer by XFOIL and velocity contours from CFD simulations for the root profile of the DUT-MutinyV2 kite for $Re = 2.9 \cdot 10^6$.

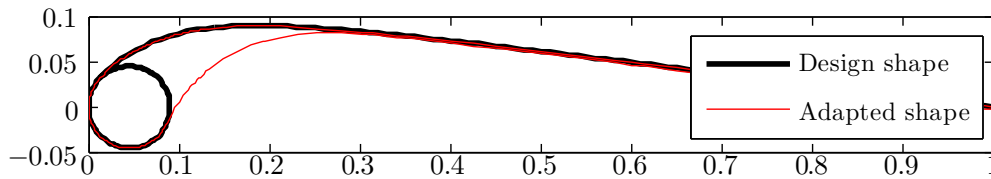


Figure 6.14: The geometrical conversions of the DUT-MutinyV2 root profile such that XFOIL can handle the shapes.

(Ruppert, 2010). The corresponding Reynolds numbers for the DUT-MutinyV2 root profile are $Re = 1 \cdot 10^6$ and $Re = 4.6 \cdot 10^6$. The results can be found in Figure 6.16, where also the results of XFOIL are included. Note that the CFD uncertainties of stall point predictions are higher, because less points are simulated.

XFOIL predicts only small changes in stall point, while in the CFD simulations there is a rapid shift between $Re = 1 \cdot 10^6$ and $Re = 2.9 \cdot 10^6$. After this shift no large changes occur, at least up till $Re = 4.6 \cdot 10^6$. It is clear that higher Reynolds numbers result in higher maximum stall and critical angle of attack. Since the stall point of the 3D wing analysis is strongly dependent on the 2D curves, significant changes can be expected when using XFOIL or CFD and different Reynolds numbers.

The use of polynomial regression models

Besides using XFOIL generated lift and drag curves it is possible to construct from given data a mathematical description of the lift, drag and moment coefficients for varying airfoil shapes, for which often a polynomial regression model is used. In order to find such a function, numerous airfoils need be analyzed. Performing experiments is very time consuming and often not feasible. For the highly turbulent flows around LEI kite profiles, XFOIL has a too late stall prediction, as shown in the previous section. Breukels (2011) used results of high-fidelity 2D CFD simulations to construct a polynomial regression model. There is however some room for improvement, especially regarding the efficiency of the process.

The polynomial regression model of Breukels depends on camber, thickness and angle of attack:

$$\begin{aligned} C_L &= f(\kappa, t, \alpha) \\ C_D &= f(\kappa, t, \alpha) \\ C_M &= f(\kappa, t, \alpha) \end{aligned} \quad (6.6)$$

In his simulations, Breukels measures the camber value of the deforming wing at 30% chord. This implies the assumption that maximum camber position is always located at 30% chord, independent of wing configuration. In reality the position of maximum camber can vary for deforming wings, which could result in different airfoil shapes and hence, different aerodynamic forces. How much the location of maximum camber changes during flight could be investigated and, if necessary, implemented in the fitted functions as an extra variable.

Another parameter which is not included in the fitted functions is the Reynolds number. Apparent velocities during flight can strongly vary and next to this, LEI kites have

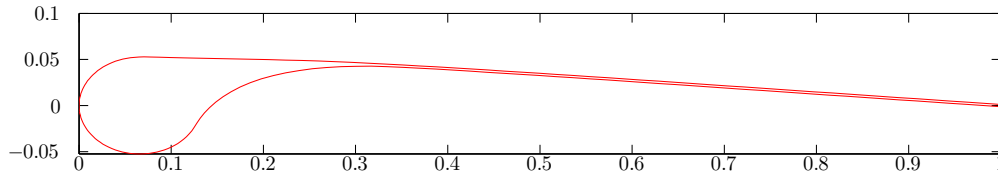


Figure 6.15: The tip profile of the DUT-MutinyV2 kite after geometrical conversion.

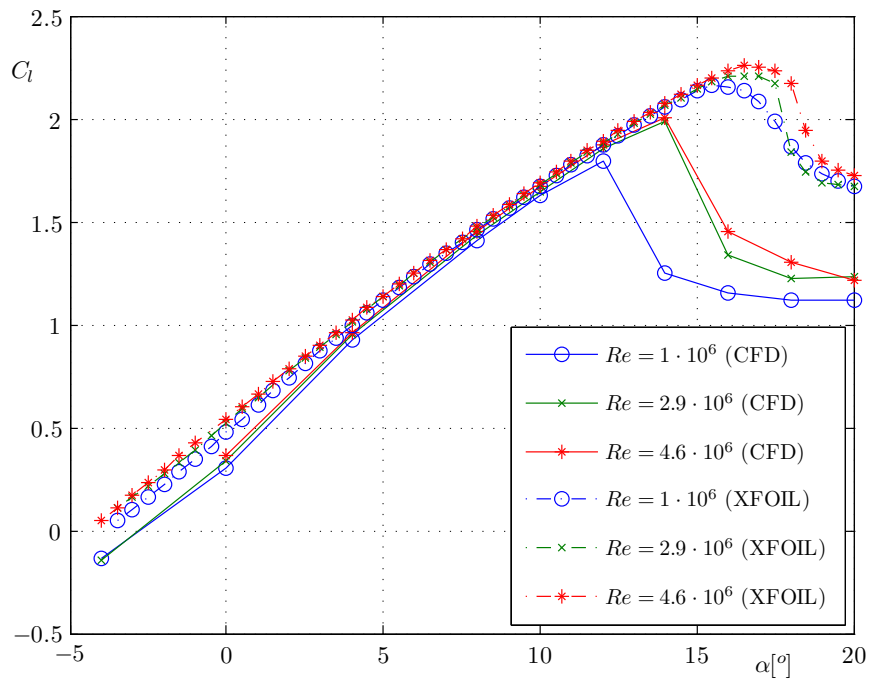


Figure 6.16: The effect of Reynolds number on lift prediction of CFD and XFOIL for the root profile of the DUT-MutinyV2 kite.

usually high taper ratios and thus strong spanwise variations in chord length. As a result viscous airfoil data is required for a range of Reynolds numbers. The Reynolds number can significantly influence $C_{l_{max}}$ and the critical angle of attack, as was shown in the previous section.

In future work the parameters for Reynolds number and position of maximum camber p could be added to the regression model:

$$\begin{aligned} C_L &= f(\kappa, t, Re, p, \alpha) \\ C_D &= f(\kappa, t, Re, p, \alpha) \\ C_M &= f(\kappa, t, Re, p, \alpha) \end{aligned} \tag{6.7}$$

This increases the required number of airfoil analyses, but makes the polynomial model more complete and therefore more accurate results can be expected in the proposed non-linear VLM.

In order to efficiently construct a polynomial function preferably a small amount of CFD analyses are performed, while ensuring an acceptable quality level. Similar to the conventional approach of wind tunnel experiments, Breukels used the One-Factor-at-A-Time (OFAT) approach. In this approach, one individual design variable is successively varied while the remaining design variables are kept at a baseline level. The largest possible test matrix is generated by OFAT and consists of all possible combinations of design variables. In typical experiments only a limited number of measurements is executed due to budget and time constraints. Therefore, it is often chosen to omit measurements that combine variations of several design variables (interactions), which might lead to a lower quality result. A more efficient approach is D-Optimal design (Montgomery, 2008). An extensive description of this 'measurement point distribution algorithm' is beyond the scope of this report, however it can be said that the algorithm efficiently determines the location of the new measurement points to construct a model which is within a predefined margin of error. Less simulations will be required therefore saving on time consuming processes such as CAD drawing, meshing and numerical solving.

Because regression models are of great importance for the aerodynamic load solver, an example is given for the construction of an interpolation function for C_L by using D-Optimal design. Similar to Breukels approach the variations are $15\% \leq t \leq 25\%$ and $0\% \leq \kappa \leq 12\%$. Assume that nothing is known about the order of the response³, therefore start with the simplest model which only has linear interactions.

1. Do a complete angle of attack sweep with small stepping for the baseline configuration e.g. $t = 15\%$, $\kappa = 0\%$.
2. Determine the order of the $C_L - \alpha$ curve. For the remaining angle of attack sweeps use only $\mathcal{O}(C_L - \alpha) + 1$ measurement points.
3. Determine the configurations at the boundaries of the function domain, that is all possible combinations of the extreme values of the used variables. In this case that would be $2^2 = 4$ combinations. For each of these boundaries an angle of attack sweep should be performed.

³In many cases, from experience or literature, there is already an idea of which order the interactions will be.

4. Construct from the available data an interpolation model. If only data at the boundaries is used D-Optimal design is equivalent to Full Factorial Design (Engelund et al., 1993), resulting in a linear interaction model.
5. Determine the error between a new non-used measurement point (configuration with angle of attack sweep) and the value at that point predicted by the model. The location of this point should be taken furthest away from the used data. For the linear interaction model this is at the center of the functional domain. In the example it would be: $t = 20\%$ and $\kappa = 6\%$.
6. If the error is too large increase the complexity of the model by increasing the order of the terms and interactions. With augmented D-Optimal design the number and locations of the new measurement points is determined.
7. Go back to step 4 and repeat until the error is sufficiently small.

In the work of Breukels (2011) all possible combinations of 4 camber values and 3 thicknesses are used ($\kappa = 0, 4, 8, 12\%$, $t = 15, 20, 25\%$), resulting in $4 \times 3 = 12$ configurations. Given that his $C_L - \alpha$ curve is of third order with respect to α , 4 measurement points are required (step 2) for each angle of attack sweep. Then, in total he used at least $12 \times 4 = 48$ measurement points. In his work he uses linear interactions of camber and quadratic interaction of thickness, therefore the model consists of 24 coefficients. With D-Optimal Design a same order model would be found by only 24 measurement points, which would a reduction of 50% in the number of CFD simulations. It might be that a few more measurement points are required to obtain a smaller margin of error, but there will still be a large reduction. This makes it definitely worthwhile using this approach.

6.2.2 Chordwise pressure distribution

The results of the non-linear VLM give a pressure distribution over the wing, both in span and chordwise direction. However, the chordwise pressure distribution of a VLM and 3D panel method for a wing with a LEI kite profile are unrealistic, since the resulting pressures represent inviscid flow that stays attached to the surface. How a more realistic pressure distribution can be found is discussed in this section.

There are several possibilities that can be used to determine the chordwise distribution:

- Use the method of Breukels (2011), which makes use of an assumed shape of the pressure distribution: This method has high analytical flexibility and requires small computational effort, though is very limited in predicting chordwise variations. Since these can have strong influence on the profile shape, a more accurate method shall be determined.
- Make a lookup table: This requires many CFD simulations with different profiles and angles of attack. It is unknown of what order the chordwise pressure variations as function of profile and flow parameters are, therefore large discrepancies can be expected when using interpolation function for the lookup tables.
- Make a polynomial regression model: In this case a number of chordwise points should be selected for which a polynomial model is constructed from generated CFD data. Again many CFD simulations would be required, and information of the CFD data will get lost when constructing models for a reduced number of chordwise points.

- Use XFOIL: This will require on-the-fly XFOIL calculations. As the rest of this section will demonstrate, this is a possibility which requires somewhat more computational power than the above discussed possibilities, but no preliminary work is required and the results are of high accuracy.

On-the-fly use of XFOIL

From the comparison with Fluent results it became clear that XFOIL predicts, with a margin of error, the same behavior as CFD simulations, only with delayed stall. Now assume that external 2D viscous data of the profiles is used, which can either be from a regression model or a lookup table. For each section the final effective angle of attack of the VLM calculation is known. If these angles would be used as input to an XFOIL analysis of the corresponding profile, the resulting lift values and pressure distribution will closely match the CFD results for a large range of angles of attack, see Figure 6.17. For small angles the over-pressure at the bottom side is gradually decreasing, instead of a more constant pressure region. Beyond the stall point ($\alpha = 14^\circ$) the differences between the shapes of pressure distributions significantly increase. Especially the pressure peak at the leading edge reaches less high values in CFD simulations.

XFOIL shows boundary layers that in a large extent correspond with the separated flow region of CFD calculations (Figure 6.13) and as a result also the shape of the pressure distribution is equivalent, only with a shift in angle of attack when stall occurs. A trick was applied to cope with this shift in stall angle. First the difference between the effective angle of attack and stall point in the 2D (external) viscous curve was measured. Then the pressure distribution is determined from XFOIL calculation at the angle of attack taken at the point with the same difference with respect to the predicted stall point of XFOIL. This way similar behavior is expected, therefore matching the shape of the pressure distribution with that of the location in the viscous curve. The result of using such a shift for angles of attack past stall is compared with the pressure distribution shape without this shift, see Figure 6.18. The pressure distributions are scaled to match the generated lift of the CFD calculation. Indeed, the scaled pressure distribution of XFOIL at $\alpha = 18^\circ$ more closely match the CFD results than the distribution at $\alpha = 16^\circ$. This is mainly caused by the changes in upper side pressure, which corresponds to the fact that the thick boundary layer at $\alpha = 18^\circ$ closely match the separated flow region of the CFD simulations. The relative standard deviation of the difference between the scaled distributions and CFD data is respectively for $\alpha = 16^\circ$ and $\alpha = 18^\circ$ approximately 6% and 4%. Compared with the deviations for low and medium angles of attack, on average 9% and 1%, this difference is considered so small that the shift in angle of attack around stall is not worth taking the effort. Especially, when considering that, for this shift, it is required to generate a lift curve in XFOIL to find the stall angle, which would mean extra computation effort.

Load distribution and scaling procedure

As was already shown in Figure 6.18 the chordwise pressure distribution initially corresponds to the lift and drag of the XFOIL analysis. These lift and drag values are however different than the results of the complete wing analysis by the non-linear VLM, where downwash significantly alters spanwise predictions in lift and drag. This section explains how the chordwise pressure distribution from XFOIL is scaled to the results of the non-

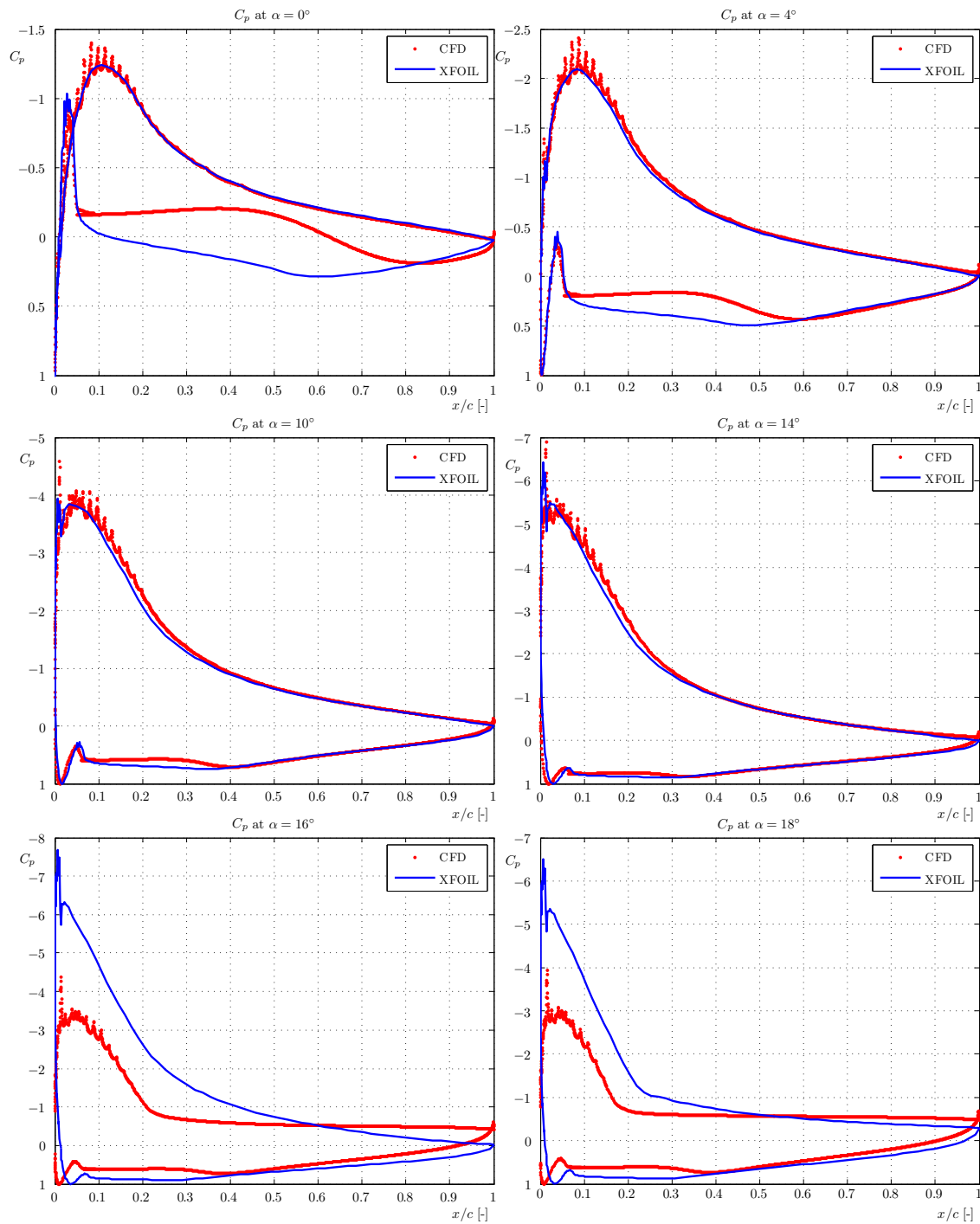


Figure 6.17: Pressure distributions for several angles of attack for a typical kite profile (DUT-MutinyV2 root profile).

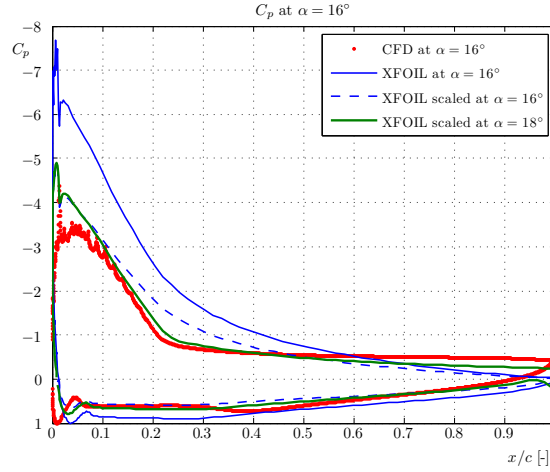


Figure 6.18: Pressure distributions scaled to same total lift.

linear VLM analysis. Furthermore, the distribution of the aerodynamic forces over the required number of nodes is explained. A visualization of the complete aerodynamic solver is sketched in Figure 6.19.

In contrast to Breukels method, in which there is pressure distribution shape constructed for 5 chordwise points (see Figure 6.20), this method can reduce the found pressure distribution in XFOIL to a desired number of chordwise points. XFOIL typically uses between 100-250 panels; none of the information about the pressure distribution shape will get lost as long as the number of chordwise elements in the deformation model within the FSI solver is less than the amount of chordwise XFOIL panels. More on reduction of information for the interaction of the FSI components is discussed in Section 6.2.2.

The resulting pressures at a desired number of i chordwise points can be obtained by integration. The obtained pressures from XFOIL analysis are defined perpendicular to the panel. Therefore, integration is performed both parallel (\hat{t}) as perpendicular (\hat{n}) to the flow. Then the chordwise lift and drag force components F_{L_i} and F_{D_i} are defined as the sum of the mean average of each integrated interval over upper and lower side:

$$F_{L_i} = \frac{\int_i^{i+1} \vec{p}_{upper} \cdot \hat{n} \left(\frac{x}{c} \right) d \left(\frac{x}{c} \right)}{\left(\frac{x_{i+1}}{c} \right) - \left(\frac{x_i}{c} \right)} - \frac{\int_i^{i+1} \vec{p}_{lower} \cdot \hat{n} \left(\frac{x}{c} \right) d \left(\frac{x}{c} \right)}{\left(\frac{x_{i+1}}{c} \right) - \left(\frac{x_i}{c} \right)} \quad (6.8)$$

$$F_{D_i} = \frac{\int_i^{i+1} \vec{p}_{upper} \cdot \hat{t} \left(\frac{x}{c} \right) d \left(\frac{x}{c} \right)}{\left(\frac{x_{i+1}}{c} \right) - \left(\frac{x_i}{c} \right)} - \frac{\int_i^{i+1} \vec{p}_{lower} \cdot \hat{t} \left(\frac{x}{c} \right) d \left(\frac{x}{c} \right)}{\left(\frac{x_{i+1}}{c} \right) - \left(\frac{x_i}{c} \right)} \quad (6.9)$$

Figure 6.20 shows this integration procedure for the components perpendicular to the flow. The resultant pressure Δp is the pressure difference between the lower and upper airfoil surface: $\Delta p = p_{lower} - p_{upper}$.

Because the total section lift resulting from the pressure distribution is not equal to the section lift L of the 3D analysis, the pressures are scaled accordingly, such that:

$$\sum_{i=1}^{n-1} cF_{L_i} = L \quad (6.10)$$

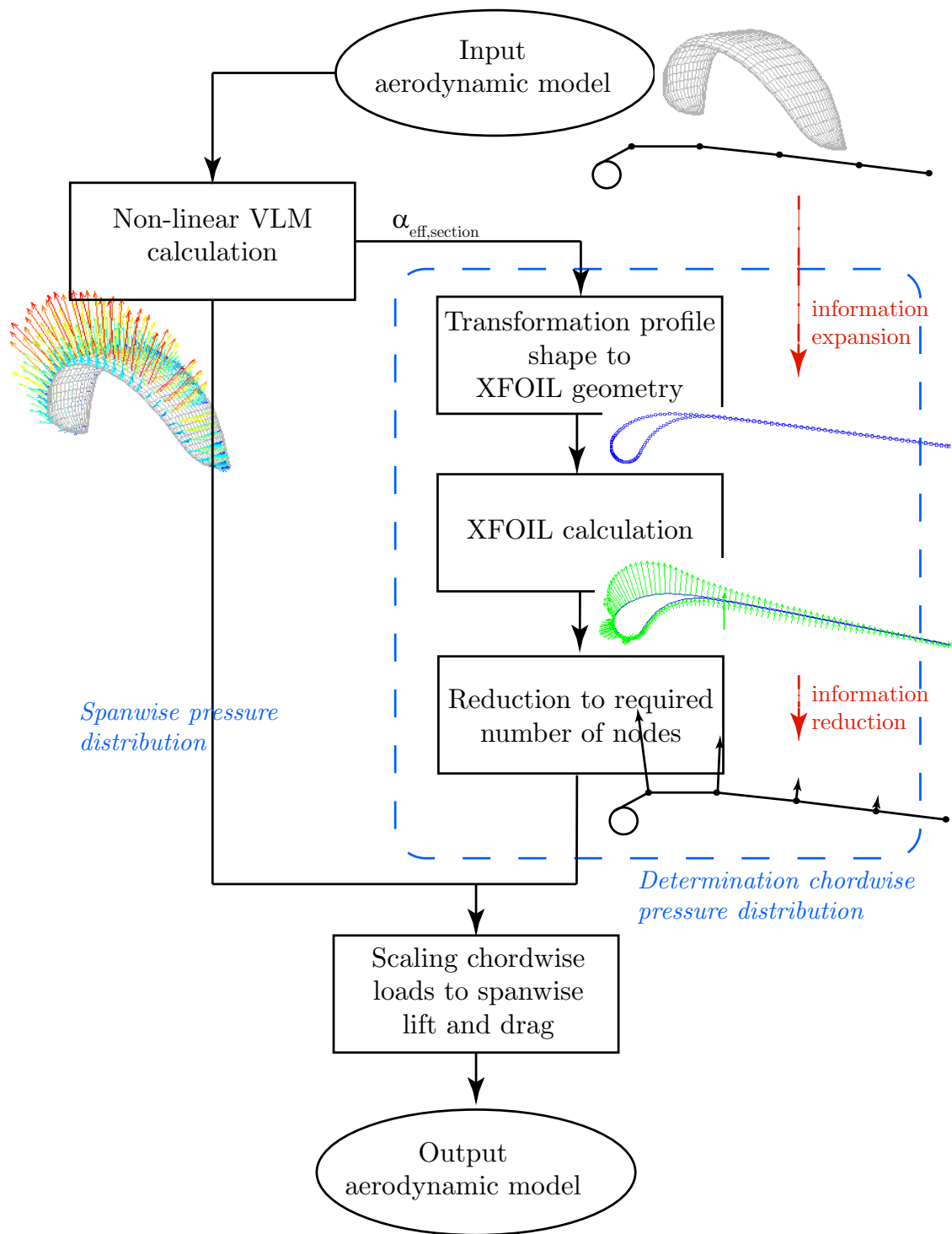


Figure 6.19: Illustration of the required procedure for determining the chordwise pressure distribution with XFOIL.

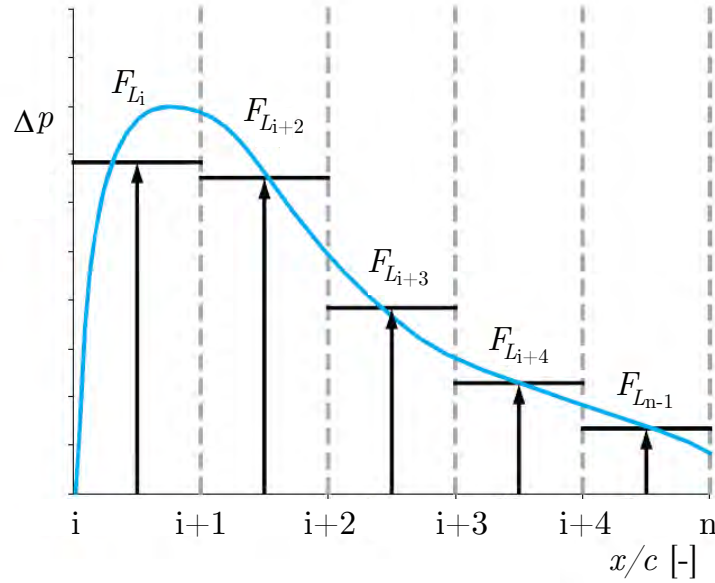


Figure 6.20: Integration procedue.

Both lift and drag components are scaled with this factor, therefore the shape of the pressure distribution remains intact to this moment.

Next, the drag components have to be scaled to the total section drag D from the 3D analysis, which includes both profile as induced drag. As a result the shape of pressure distribution will change. The scaling factor b follows from:

$$\sum_{i=1}^{n-1} b(cF_{D_i}) = D \quad (6.11)$$

Applying the lift and drag in this manner, ensures that the relative variations over the chord remain the same.

The now scaled pressure distribution results in a moment, which differs from the moment that follows from the external viscous profile data. This is partly because the XFOIL pressure distribution is used instead of the unknown distribution of the viscous profile data and partly because induced drag is not included in a 2D viscous analysis. The latter reason has however little effect on the total generated moment because drag is generally a factor 5-15 times lower and has a small moment arm compared to lift forces.

Expansion-reduction of chordwise loads

An important note should be made to the reduction of information about the pressure distribution, of which a visualization is made in Figure 6.19. Reduction is applied because more information is acquired than required i.e. the large amount of chordwise nodes used by XFOIL is not required for the input of the deformation model. Using the same, low number of panels in XFOIL's viscous analysis is generally not possible. XFOIL needs sufficient information about the airfoil shape to be able to converge the iteratively calculations of boundary layer properties.

The relatively large amount of nodes of the chordwise pressure distribution resulting from XFOIL simulations is obtained by giving an input of airfoil shape. This airfoil shape is based on the to-be-analyzed shape for the aerodynamic load model that is generated by the deformation model in the FSI solver. The input to the aerodynamic model, generally contains less chordwise points than which is required for the airfoil shape in XFOIL. For example, both FSI solvers from Breukels (2011) as Bosch (2012a) used only 5 chordwise points.⁴ This shortage of information is filled up by assuming an airfoil shape based on the very limited amount of information available (indicated in the Figure with 'information expansion').

This reduction and expansion of information about the geometrical and aerodynamic properties, seems an inefficient approach. It is however required to comply with the criteria that apply to the different used programs in the FSI solver, consisting of a deformation model, VLM, XFOIL and external data source (model). And in this way, there is high flexibility in what kind of discretization can be used in the FSI solver and how the pressure distribution shape can change as function of angle of attack and profile geometry. A way to avoid this reduction-expansion procedure is to use an airfoil database or regression model.

Effect on computation time

The computation times for obtaining the chordwise pressure distribution is mainly determined by the viscous-inviscid interaction calculations of XFOIL. The scaling of the chordwise pressure loads are relatively simple operations and have minor impact on computation time. This follows from the fact that similar scaling principles are used in Breukels' aerodynamic model, which only requires in total 10ms when implemented in Matlab.

The computation time of an XFOIL calculation for one angle of attack can strongly vary with airfoil discretization, flow case and settings for the iterative process. In Table 6.2 computation times for a range of angles of attack are given. For this a timer was implemented in the XFLR5 plug-in version of XFOIL. The computation time is mainly determined by the number of iterations and was on average roughly 160ms, but showed peaks up to 440ms for low angles of attack. These correspond to an airfoil discretization of 100 panels.

For comparison the required number of iterations for both the plug-in as the stand-alone version are given. For most angles of attack the number of iterations were equivalent, except for the low angles of attack. Then the XFLR5 plug-in had troubles with convergence or did not converge at all for angles close to zero, while the stand-alone version had no troubles at all. This shows that with proper settings computation times are similar for all angles of attack. Further, it was found that the chance that convergence occurs after more than 50 iterations is small.

With respect to the total computation time of the new method, the implementation of on-the-fly-use of XFOIL strongly increases computation time. Considering a typical model of a LEI kite has 25-40 spanwise stations⁵, each requiring one XFOIL calculation

⁴Note that the FEM of Bosch (2012a) was only a demonstration model and was mainly restricted in chordwise elements because he uses the aerodynamic model of Breukels (2011). When employed in future work the proposed FSI solver could use many more chordwise elements.

⁵The DUT-MutinyV2 kite, discussed in Section 6.3, has 32 spanwise stations.

Table 6.2: Required computational effort for XFOIL viscous-inviscid calculations for a LEI kite profile with 200 panels.

Angle of attack	Computation time [ms]	XFOIL iterations:	
		XFLR5 plug-in	stand-alone
0°	-	-	22
2°	440	48	22
4°	160	15	18
8°	150	14	17
12°	160	16	13
16°	170	19	18

of 150ms, computation times are increased by 3.8-6.0 seconds. The total degrees of freedom are in this case between 400-800 (panels). Mark that it is assumed the wing is unsymmetrical. For symmetrical wings the required XFOIL calculations reduce with 50%.

6.3 Simulation results of a LEI kite

A kite, with which the DUT KitePower group has performed many test flights, is simulated with the proposed aerodynamic tool in this thesis.

6.3.1 DUT-MutinyV2 kite

The design shape of the DUT-MutinyV2 kite is used as input for the simulation. The export option in Surfplan is used to convert the drawing to a XFLR5 project file containing the wing and profiles, see Figure 6.21. Then a refinement of the tips was made, to better match the simulated wings with the design shape. Struts are not incorporated in the simulation. It was observed that between the root and the last strut, the shape of the profile was nearly constant (less than 1% difference in camber and thickness), therefore the small variations are neglected and the profile is assumed to be constant in this region. The root and tip profile (Figure 6.14 and 6.15) were also used in the analyses in previous sections. The tip profile is assumed to be constant over the entire tip surface. The corresponding aerodynamic curves can be found in Appendix G. Parameters of the kite are given in Table 6.3. For span and chordwise paneling 32×20 panels are used, corresponding to a total of 640 panels.

6.3.2 Experimental data from flight test

Experimental data for this kite is available from tests from the DUT KitePower group and were post-processed in Ruppert (2010). For this case some remarks have to be made. Next to the simplifications to the wing geometry, it is not accounted for deformations caused by the varying flight conditions, because it is very difficult to obtain geometrical information via measurements. Therefore the comparison neglects aeroelastic behavior

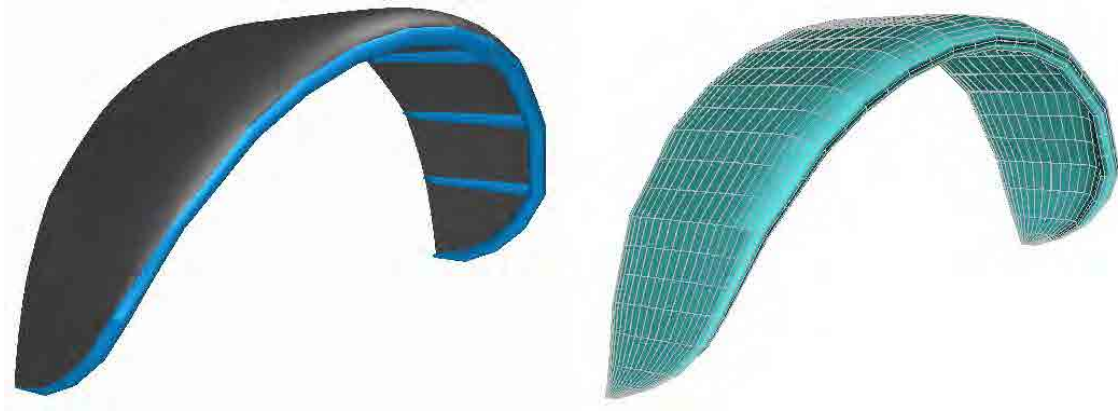


Figure 6.21: Left: design shape from the kite design tool Surfplan. Right: Discretized kite in XFLR5.

and is thus not a 'true' comparison, though it can already give some indication of the quantities that are generated with the new tool.

The scatter of the data visualizes the uncertainties but not the errors due to GPS, IMU (Inertial Measurement Unit), wind ground meter measurements, wind model and winch sensors. These devices and models were all required to determine the angle of attack and resultant force C_R , which is defined as:

$$C_R = \sqrt{C_L^2 + C_D^2} \quad (6.12)$$

A correction for tether drag is included, based on the work of Argatov et al. (2009). Here C_L and C_D are the lift and drag coefficient of the entire kite system, thus the drag generated by the bridle and KCU is not corrected for.

Table 6.3: DUT-MutinyV2 kite parameters.

Parameter	Value
Airfoils	Root profiles: $t = 9\%$, $\kappa = 5\%$ (fig. 6.21) Tip profile: $t = 10\%$, $\kappa = 1\%$ (fig. 6.15)
Reynolds number	$2.9 \cdot 10^6$
Projected wing span	6.6 m
Root chord length	2.72 m
Projected surface area	16.5 m^2
Aspect ratio	4.8

6.3.3 Comparison of results

The results from the simulations of the DUT-MutinyV2 kite are compared with the experimental data and with the aerodynamic model of Breukels. Only the results of the

VLM (version MG_b) are given. The results of the 3D panel method are omitted, because it has problems with the strong curvature and small panels at the tip. The predicted values were very sensitive for small changes in discretization, up to the point where the entire lift curve shifted several degrees and lift slope increased with more than a factor 2. After testing numerous types of discretization, *it was concluded the 3D panel method is not suitable for handling LEI kites*. Also version AK is not recommended to use for this case due to the difficulties with determining induced angles for wings with strong dihedral. As mentioned in Section 5.4.3, version MG_b predicts more realistic lift and drag distributions. The computation times of the simulations varied between 150-200ms.

Resultant force curve

COMPARE FOTOOS OF FLIGHT, WITH CAD DRAWING. The resultant force as function of angle of attack can be seen in Figure 6.22.

When considering the results of the nonlinear VLM, it is clear that the use of XFOIL viscous airfoil data has almost no influence on the resultant forces compared to the standard VLM, which is expected because of the late stall predictions in airfoil data (Section 6.2).

There is definitely coherence between the methods based on Breukels regression model/CFD data and the experimental data, especially the cases where 1 iteration is used. There is however a significant difference between the lift slopes. The deviations can be caused by:

- Errors in experimental data: both forces and angles of attack can be lower or higher.
- No correction for deformation changes during flight. The profile significantly changes as a result of the pressure forces. It is however unclear whether this increases or decreases lift. Also spanwise camber can change due to local variations in structural stresses and aerodynamic forces. An increase in spanwise camber could reduce the effective area resulting in lower forces.
- Modeling errors: the presence of struts is neglected, which might disturb the flow, such that less lift is generated. Next to this, (viscous) 3D effects are not accounted for and could result in large differences in lift slope, which was also seen in the case of winglets (Section 5.4.4).
- Wrong correction for tether drag. However, even without the corrections the deviations were significant.

It is unclear which reason(s) is dominant for the difference in lift slope.

Comparison with Breukels' aerodynamic model

A comparison is made between the simulated values and the aerodynamic model of Breukels (discussed in Chapter 3). His model is rebuild in Matlab, where the local angle of attack of Equation 4.8 is used. The 3D correction is not implemented, because it is questionable whether it improves the model, according to Breukels himself (stated by Bosch (2012a); see more on this in Section 3.1.4). The resultant force curves are also given in Figure 6.22.

The lift slope is much larger than non-linear VLM predicts, which corresponds to the fact that only 2D theory is used in Breukels model. From finite wing theory follows that lift slope decreases for decreasing aspect ratio. Correspondingly, also the spanwise

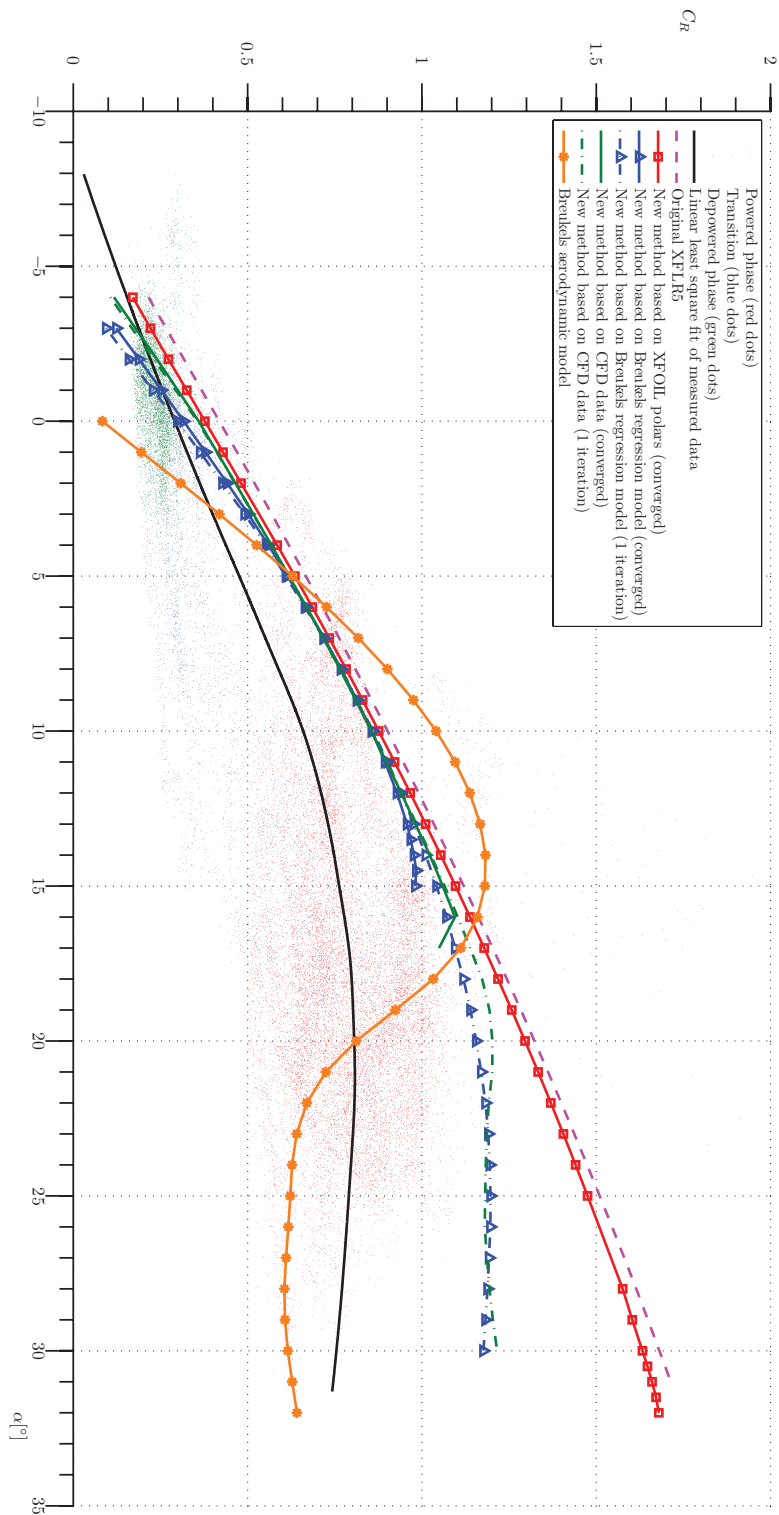


Figure 6.22: Resultant force versus angle of attack for VLM2 (MG_b) with free wake. The black line is obtained from the scattered experimental data by a weighted linear least square method.

lift distribution is significantly different than those predicted by the non-linear VLM, as depicted in Figure 6.23. This is of high importance for aeroelastic simulation. Further mark that Breukels model does not incorporate induced drag, and has therefore much lower drag prediction.

Spanwise distributions

The spanwise distributions of lift, normal force, total drag and profile drag are shown in Figure 6.23. The wiggles in the lift distribution originate from the discrete variations in dihedral angle, which are also present in the real kite. The normal forces show nice smooth behavior. The peaks at the tips can be caused by problems in the Trefftz-plane calculations of XFLR5 for arc shaped wings. These are not visible when inspecting the panel forces at the tips, as shown in Figure 6.24. These show the more gradual reduction of lift towards the tips. Just beyond stall, at $\alpha = 15^\circ$, the lift distribution shows a stall region at the root. Correspondingly, profile (viscous) drag increases at the root. However, the induced drag shows unrealistically low values at this location, which is also caused by the corrupted Trefftz-plane calculations. These problems in the far-field-analysis should be fixed or a panel force integration for out-of-plane wings could be used.

Effect of tip root profile

Two profiles were used for this model, where the tip profile only covered the tip surface after the last strut. To see whether having a different tip profile influences total lift, the profile was replaced with the root profile. The wing had now one continuous profile. As a result, the entire lift curve shifted approximately 0.02 higher, which is small considering that lift values are between 0.4 and 1.1.

For a static load case of a design shape with almost constant profile over most of the wing up to the tip surface, the assumption of having a constant profile is justified. However, when dynamic load cases are considered, where the shape is deformed under load, this assumption could lead to significant different behavior prediction at the tip.

Prediction beyond stall

Extreme angles of attack can repeatedly occur at certain spanwise sections during flight, for instance when giving strong steering inputs and during jelly fishing. It is therefore important that the aerodynamic solver can give solutions for these extreme angles. From Figure 6.25 it follows that the effect of the number of iterations has large influence on the predicted range of angle of attacks. The curves show that with the nonlinear VLM a solution is found for all angles of attack, including angles far beyond stall, when using 1 iteration (under the condition the 2D viscous data was sufficient). The values at angles before stall are almost not affected by the number of iterations, opposed to the behavior after stall. The low number of converged solutions at the angles of attack beyond stall is most probably because no relaxation method is applied. Using a well-refined relaxation process can largely improve convergence, including convergence speed. Relaxation is however not yet implemented in the current software due to time constraints.

The discontinuous behavior of the converged solution for the CFD data based simulations correspond to the abrupt 2D stall behavior of the profiles. It follows that from these simulations the 3D stall behavior will correspond to the 2D stall behavior of the profiles,

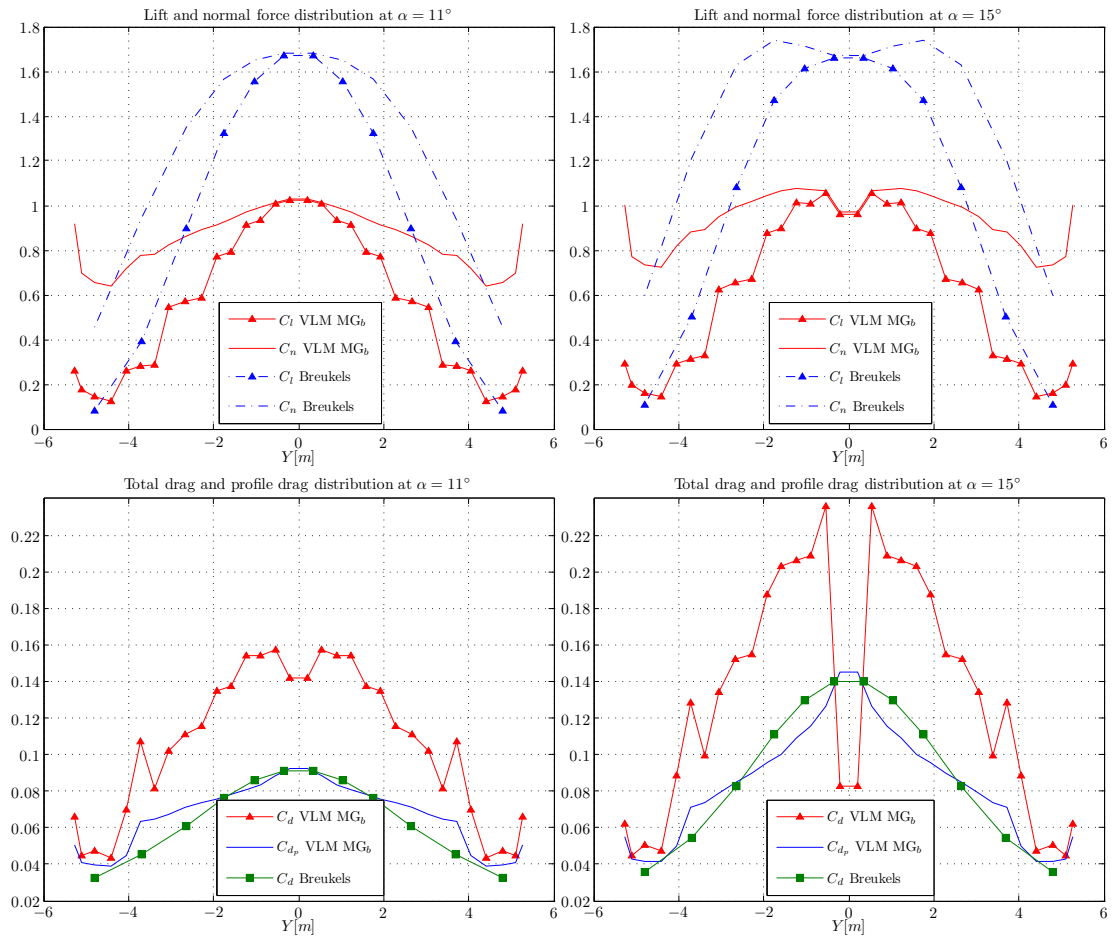


Figure 6.23: Spanwise distribution plots for the DUT-MutinyV2 kite for angle of attack before and beyond stall. For the angle shift corrections in VLM MG_b the polars generated from Breukels regression models are used. The Y coordinate is measured in the direction of the arc.

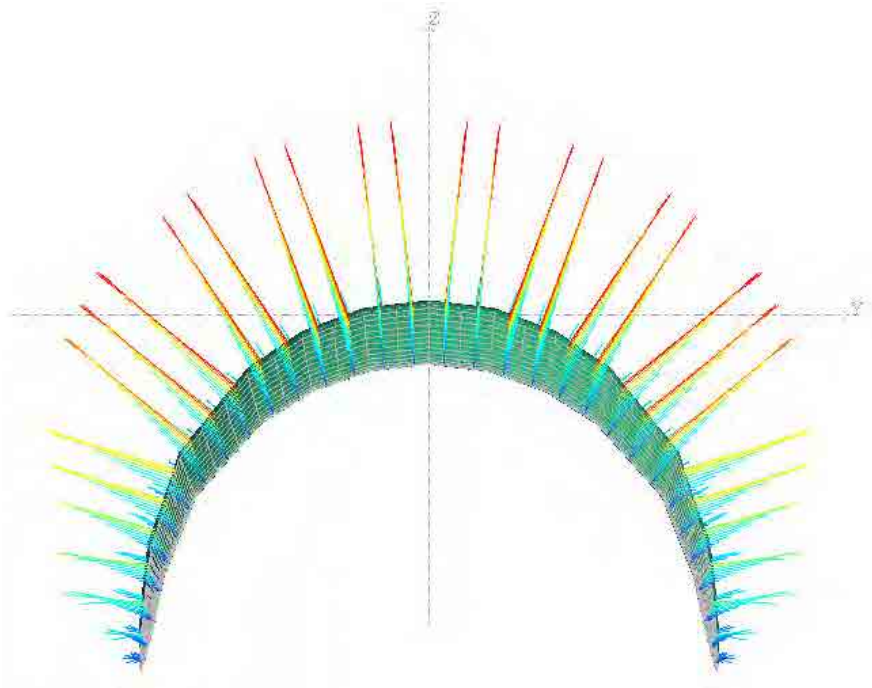


Figure 6.24: Panel force distribution over the DUT-MutinyV2 kite at $\alpha = 11^\circ$.

while in reality separation is strongly three dimensional and can result in complete different 3D stall behavior. Lower accuracy should therefore be expected for the angles of attack beyond stall.

Whether the converged solution or using only 1 iteration is most accurate cannot be determined at this stage, because of the mentioned uncertainties and the lack of a relaxation method. In principle, a converged solution should have higher accuracy, because the lift correction is based on itself and therefore inherently requires iteration.

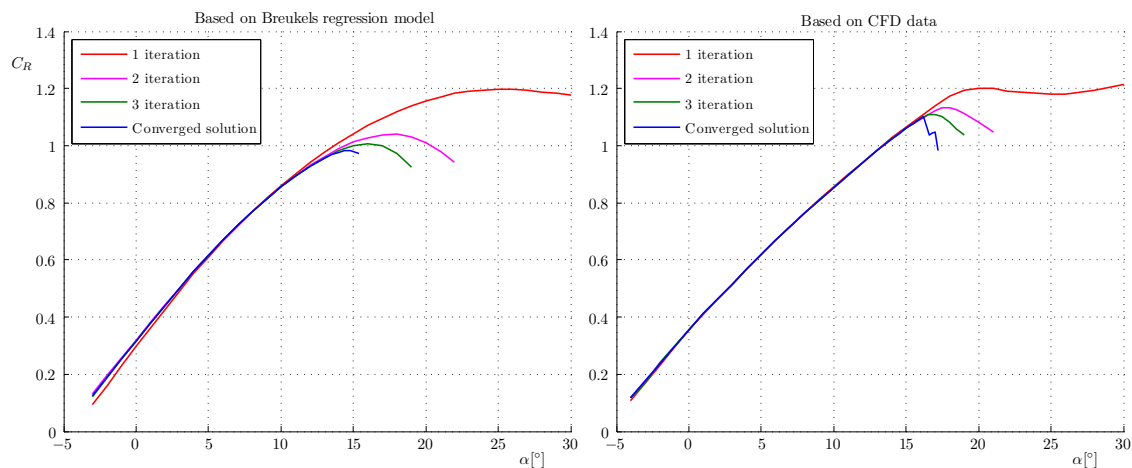


Figure 6.25: Resultant force versus angle of attack for VLM2 (MG_b) with free wake. The black line is obtained from the scattered experimental data by a weighted linear least square method.

6.4 Computation times

In this report a new tool is developed to determine the aerodynamic loads for a given geometry. This chapter dealt with the difficulties that arise when applying the method to LEI kites. In this section the computation time of the aerodynamic load solver is discussed and an estimation is given for the case where the new tool is implemented in the latest developed aeroelastic solver.

6.4.1 Aerodynamic load solver

The total computational effort of the aerodynamic load solver for a given geometry consists of:

- Determination airfoil data, viscous and inviscid
- Non-linear VLM calculation
- Determination chordwise pressure distribution
- Scaling pressure distribution

An indication of the computation times for each of the components of the current aerodynamic load solver is given in Table 6.4. If airfoil data is obtained from lookup tables or regression models, calculation times are in the order of milliseconds (knowing that the complete aerodynamic model of Breukels took 10ms when implemented in Matlab (Bosch, 2012b)). Each nonlinear VLM calculation took approximately 180ms for a LEI kite with 640 panels. When using XFOIL for the chordwise pressure loads, computation times strongly increase: by estimation this would take 4800ms (for each of the 32 spanwise sections about 150ms). The scaling of the chordwise pressure distribution to the obtained sectional lift and drag values from the 3D analysis is negligible regarding computation time. Therefore the resulting total computation time is about 5 seconds.

It follows that the required viscous XFOIL calculation takes 96% of the total computation time. This is such a large part, that ways should be found to reduce the effort for

Table 6.4: Estimation of computation times for the components of the aerodynamic solver for a model of 640 panels with 32 spanwise sections.

Component	Computation time [ms]
Generating airfoil data (viscous and inviscid)	<10
Non-linear VLM calculation	180
Chordwise loads from XFOIL	4800
Scaling	<10

finding realistic chordwise loads. The following approaches are suggested:

- Save the pressure loads for certain airfoil shapes and angles of attack in a database/lookup-table. This could even be implemented as a smart algorithm: for every XFOIL calculation the database grows, up to the point where XFOIL calculations are no longer required. In that case computation times of the aerodynamic model could be reduced to only 200ms, considering a nonlinear VLM calculation takes roughly 180ms and minor effort is required for the remaining calculations.
- Use the pressure distribution shape used by Breukels (2011) or an extension/adaption of it. The accuracy is expected to be lower, because of the limited possibilities to vary distribution shape. How much the chordwise loads differ between Breukels model and those generated by XFOIL should however be investigated.
- Make the algorithm more efficient.
- Avoid calculation of all spanwise section. The variations in chordwise loads between spanwise sections might be small enough to use interpolation techniques.
- Use other viscous airfoil analysis programs, which are faster than XFOIL.

6.4.2 Estimation for the aeroelastic solver

Considering the FSI solver of Bosch (2012a), the consequence of using the new software in his FSI solver is having higher computation times. Given that the relation between FEM and aerodynamic load computation time is approximately 10:1, an estimation is made of the computation times, as given in Table 6.5. Clearly, the addition of on-the-fly-use of XFOIL has major impact on the applicability of the tool. When compared to the use of high-fidelity 3D CFD simulations, the computation times are however still very small. In the work of Wachter (2008) one 3D CFD simulation took about 1 week, using 12 processors. This shows that it is very impractical to incorporate such a method in FSI simulations.

Table 6.5: Estimation times of the aeroelastic solver of Bosch (2012a) using the current (Breukels) and new aerodynamic model. On-the-fly-use of XFOIL is abbreviated with 'OX'. Average time steps of 4.5ms are assumed.

Computation times	Nonlinear VLM		Breukels model
	with OX	without OX	
real-time factor	1100×	65×	25×
60s simulation (hours)	18.9	1.1	0.4

Conclusions

During the performed research, the goal was to develop a model, which can predict the aerodynamic loads within the framework of aeroelastic simulations of leading edge inflated kites.

The New Tool A non-linear potential flow method is proposed, where viscous corrections on both lift and drag are implemented by using airfoil data of the analyzed wing. The method combines the capability of a VLM and 3D panel method to incorporate effects of finite, non-planar wings with the capability of viscous airfoil analysis to predict non-linear effects, including stall. The method is implemented in the user-friendly software XFLR5.

Validation From validation on several wing configurations the following conclusions can be drawn:

- The method shows significant improvement on the standard VLM and 3D panel method, primarily in predicting non-linear lift forces and the ability to predict stall. Errors are typically between 5% and 15% with respect to windtunnel data.
- Because of the high variety in used wing configurations and flow cases for validation, it is concluded that the capabilities of the new method extend far beyond serving as aerodynamic load model for leading edge inflated kites. It is at least interesting in almost all cases where a standard VLM or 3D panel method is used.
- The method is not able to predict the strong influence of winglets on lift and drag at low Reynolds numbers, because it does not model 3D viscous effects.
- The nonlinear 3D panel method has similar accuracy to the VLM for flat wings, but the VLM has higher accuracy for arc shaped wings.

In general, it is seen that the applied lift corrections are too high in the linear regime and too low in the non-linear regime. This shows that this method, where viscous effects are implemented on basis of 2D theory, has its limitations with respect to predicting the in-reality-occurring 3D aerodynamic effects.

The significantly higher computation times for the 3D panel method, together with the above conclusions, make the VLM more attractive to use for all wing configurations,

except when both an upper and lower surface pressure distribution are required, since these can only be given by a 3D panel method.

LEI Kites From comparison with real test flight data, the impression is given that the new method predicts realistic behavior of LEI kites. However, structural deformations during flight were not included in the simulation, which makes comparison difficult.

Significant improvement is obtained in predicting the aerodynamic loads with respect to the currently most advanced aerodynamic method used in dynamic kite models (Breukels, 2011). The new method is more realistic, because of its capability to incorporate effects of finite wings and its higher flexibility in predicting chordwise pressure distributions.

The computation time for determining the aerodynamic loads of an LEI kite with the new approach is approximately 5 seconds, consisting of 96% for the determination of the chordwise pressure distribution with XFOIL. Less than 0.2 seconds is required for the non-linear VLM calculation. This tool can be incorporated in a FSI kite model to analyze pumping cycles and simulate load cases for kite design. For both applications a 60 second real-time simulation is required, this will cost roughly 19 hours of computation time. When a simpler chordwise load model is used, simulation times are reduced to 1 hour. Regarding the performance of the developed software, which is also illustrated in Figure 7.1, it can be concluded that it has higher fidelity with respect to competitive aerodynamic methods used in dynamic kite modeling, while maintaining acceptable computation times. Therefore, the developed method is able to significantly increase the accuracy of the current FSI models that simulate flight dynamics and aeroelastic phenomena of LEI kites. Furthermore, it can be used as a basis or validation of lower resolution models.

Concluding, it can be said that the developed method is very promising for future work and fosters a new generation of kite models that improve development of AWE systems. The applicability of the tool extends however much further than kites alone, as is shown by the variety of wing configurations in the validation cases.

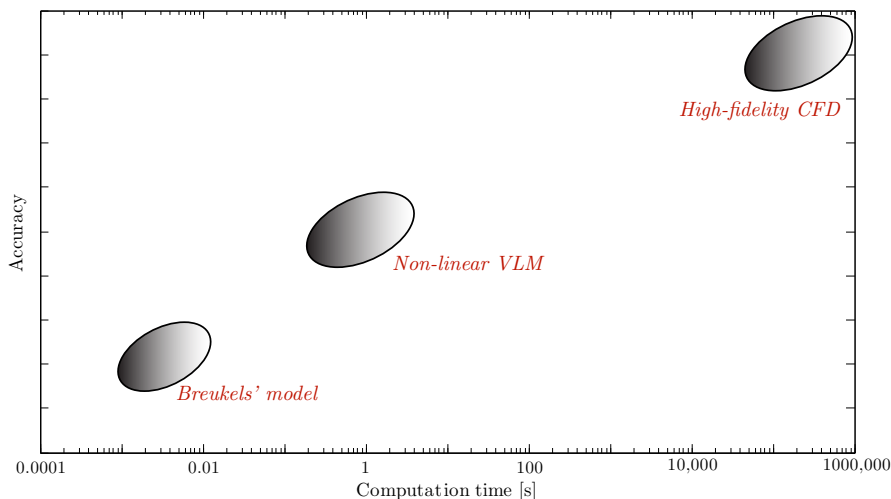


Figure 7.1: Performance of the new method.

Recommendations

The recommendations follow from the challenges of integrating the non-linear VLM in an aeroelastic model.

Currently, only symmetrical wing configurations can be built in XFLR5. From inspection in the code, it followed that adapting the code to handle unsymmetrical geometries should not be too difficult.

Iterative solving with the non-linear potential flow method generally results in diverged solutions for angles of attack beyond stall. The use of a relaxation method should be evaluated.

When polynomial regression models are used as viscous airfoil database, they should be implemented in the algorithm. For the static cases considered in this report, all polars were manually generated. Furthermore, the regression model of Breukels could be adapted and extended in the ways explained in this report. Validation for 2D CFD simulations would give insight in the predicted errors.

Some peculiarities in the standard VLM calculations could be investigated and, if possible, improved e.g. discretization errors near the root, erroneous Trefftz-plane calculations and strange peaks near the tips.

When on-the-fly-use of XFOIL is desired, it should be implemented in the code. Attention should be paid when configuring XFOIL, to ensure and speed up convergence.

An approach should be found to transform the output geometry from the deformation model to an input geometry of the aerodynamic model. Likewise, a vice versa transformation is required after aerodynamic analysis.

References

- Abbott, I., Von Doenhoff, A., & Stivers Jr, L. (1945). *Summary of airfoil data* (Tech. Rep.).
- Agten, M. (2012). Aerodynamic analysis of wings in airborne wind energy applications. *Master of Science Thesis, Faculty of Aerospace Engineering, Delft University of Technology*.
- Airplay Kitesailing. (2009). *Kite*. <http://www.airplaykitesailing.com/?file=kop8.php>. (Accessed 5 July 2012)
- Alblas, L. (2009). *Studenten wubbo ockels ontwerpen recordbrekende hydrokite*. <http://www.lr.tudelft.nl/nl/actueel/agenda/event/detail/studenten-wubbo-ockels-ontwerpen-recordbrekende-hydrokite/>.
- Anderson, J. (1980). Numerical lifting line theory applied to drooped leading-edge wings below and above stall. *Journal of Aircraft*, 17, 898-904.
- Anderson, J. (2001). *Fundamentals of aerodynamics* (3rd ed.). McGraw-Hill, USA.
- Argatov, I., Rautakorpi, P., & Silvennoinen, R. (2009). Estimation of the mechanical energy output of the kite wind generator. *Renewable Energy*, 34(6), 1525-1532.
- Baldwin, G. (2008). *Kite power for heifer internationals overlook farm*. Unpublished doctoral dissertation, Worcester Polytechnic Institute.
- BBC. (2012). *Kiteboarding to replace windsurfing at 2016 Rio Olympics*. www.bbc.co.uk/sport/0/olympics/17980607.
- Bonne, U. (2010). Power generation with high-flying kites, sky sails or wings. *Natural Energy Laboratory of Hawaii Authority*.
- Bosch, A. (2012a). Finite element analysis of a kite for power generation. *Master of Science Thesis, Faculty of Aerospace Engineering, Delft University of Technology*.
- Bosch, A. (2012b). *Personal communication*. (Researcher, ASSET institute, Delft University of Technology)

- Bosch, A., Schmehl, R., Tiso, P., & Rixen, D. (2012). Dynamic nonlinear aeroelastic model of a kite for power generation. *submitted to AIAA Journal of Guidance, Control and Dynamics*.
- Breukels, J. (2011). An engineering methodology for kite design. *PhD Thesis, Delft University of Technology*.
- Bungart, M. (2009). Fluid-struktur kopplung an einem ram-air-kiteschirm. *Master of Science Thesis, Stuttgart University*.
- Canale, M., Fagiano, L., & Milanese, M. (2007). Power kites for wind energy generation. *IEEE Control Systems Magazine*, 27(6), 25-38.
- Carqueija, P. F. P., Eca, L. R. da Cunha de, Gaunaa, M., Carvalho Gato, L. M. de, & Campos Henriques, J. C. de. (2010). Aerodynamic Investigations of a High-altitude Wind Energy Extraction System. *Dissertation, Mechanical Engineering, Riso National Laboratory, Denmark*.
- CFD-Online. (2011a). *Turbulence modeling*. http://www.cfd-online.com/Wiki/Turbulence_modeling. (Accessed 20 Feb 2012)
- CFD-Online. (2011b). *Y plus wall distance estimation*. http://www.cfd-online.com/Wiki/Y_plus_wall_distance_estimation. (Accessed 20 September 2012)
- CFD-Online. (2012). *Direct numerical simulation (dns)*. [http://www.cfd-online.com/Wiki/Direct_numerical_simulation_\(DNS\)](http://www.cfd-online.com/Wiki/Direct_numerical_simulation_(DNS)). (Accessed 31 July 2012)
- Chatzikonstantinou, T. (1989). Numerical analysis of three-dimensional non rigid wings. *AIAA, Aerodynamic Decelerator Systems Technology Conference, 10th, Cocoa Beach, FL*.
- Chatzikonstantinou, T. (1993). Recent advances in the numerical analysis of ram air wings: The three dimensional simulation code 'para3d'. *RAeS/AIAA Aerodynamic Decelerator Systems Technology Conference and Seminar, 12th, London, United Kingdom*, 13-23.
- Coenen, E., Veldman, A., & Patrianakos, G. (2000). Viscous-inviscid interaction method for wing calculations. *Proc Euro. Congr. Comp. Meth. in Appl. Sc. and Eng., ECCO-MAS 2000*.
- Cohn, D. (2006). Windmills in the sky. *San Francisco: Wired News*.
- Cyberiad. (1981). *Airfoil: NACA 0012*. www.cyberiad.net/library/airfoils/foildata/n0012c1.htm. (Accessed 20 April 2012)
- Diehl, M., & Houska, B. (2009). Windenergienutzung mit schnell fliegenden flugdrachen: eine herausforderung für die optimierung und regelung wind power via fast flying kites: a challenge for optimization and control. *at-Automatisierungstechnik*, 57(10), 525-533.
- Drela, M., & Giles, M. (1987). Viscous-inviscid analysis of transonic and low reynolds number airfoils. *AIAA journal*, 25(10), 1347-1355.

- Drela, M., & Youngren, H. (2011). *AVL Overview*. web.mit.edu/drela/Public/web/avl/. (Accessed 20 December 2011)
- EnerKite. (2012). *Mobile airborne wind energy system ek30*. <http://www.enerkite.com/EK30.html>. (Accessed 10 July 2012)
- Engelund, W., Stanley, D., Lepsch, R., McMillin, M., & Unal, R. (1993). Aerodynamic configuration design using response surface methodology analysis. *NASA STI/Recon Technical Report A, 94*, 10718.
- Evolution Kiteboarding. (2008a). *Kite advantages and disadvantages*. <http://www.kiteboardingevolution.com/kite-advantages.html>. (Accessed 3 July 2012)
- Evolution Kiteboarding. (2008b). *The kiteboarding kite*. <http://www.kiteboardingevolution.com/kiteboarding-kite.html>. (Accessed 3 July 2012)
- Fechner, U. (2012). *Personal communication*. (PhD researcher kite power control and electronics, Delft University of Technology)
- Fechner, U., & Schmehl, R. (2012). High level control and optimization of kite power systems. *Proceedings of 8th PhD Seminar on Wind Energy in Europe*.
- Furey, A., & Harvey, I. (2007). Evolution of neural networks for active control of tethered airfoils. *Advances in Artificial Life*, 746-755.
- Furey, A., & Harvey, I. (2008). Adaptive behavioural modulation and hysteresis in an analogue of a kite control task. *From Animals to Animats 10*, 509-518.
- Gal-Rom, Y., & Raveh, D. (2011). Simplified aerostructural static model for inflated wings. *AIAA journal*, 49(6), 1180-1190.
- Garner, H. C., Rogers, E. W. E., Acum, W. E. A., & Maskell, E. C. (1966). Subsonic Wind Tunnel Wall Corrections. *AGARD (Advisory Group for Aerospace Research & Development), North Atlantic Treaty Organization*.
- Garrard, W., Center, A. H. P. C. R., & Minnesota, U. of. (1995). *Inflation analysis of ram air inflated gliding parachutes*. Army High Performance Computing Research Center.
- Gaunaa, M., Carqueija, P. F. P., Réthoré, P. E., & Sørensen, N. N. (2010). A computationally efficient method for determining the aerodynamic performance of kites for wind energy applications. *Risø National Laboratory, Denmark*.
- Groot, S. de. (2010). Modelling the dynamics of an arc-shaped kite for control law design. *Master of Science Thesis, Faculty of Aerospace Engineering, Delft University of Technology*.
- Hassan, G. (2011). Market status report high altitude wind energy. *GL Garrard Hassan Deutschland GmbH*.
- Heil, M., Hazel, A., & Boyle, J. (2008). Solvers for large-displacement fluid-structure interaction problems: segregated versus monolithic approaches. *Computational Mechanics*, 43(1), 91-101.

- Hepperle, M. (2007). *Designing an airfoil*. <http://www.mh-aerotoools.de/airfoils/methods.htm>.
- Hess, J., & Smith, A. (1962). *Calculation of non-lifting potential flow about arbitrary three-dimensional bodies* (Tech. Rep.). DTIC Document.
- Heuvel, J. van den. (2010). Improving performance and safety of kitesailing. *Master of Science Thesis, Faculty of Aerospace Engineering, Delft University of Technology*.
- Horsten, B. J. C., & Veldhuis, L. L. M. (2009). A new hybrid method to correct for wind tunnel wall- and support interference on-line. *World Academy of Science, Engineering and Technology, vol. 58*.
- Houska, B. (2009). Internal paper: A 9dof kite model.
- Jones, R. T. (1946). Wing Plan Forms for High-Speed Flight. *NACA Technical Note 1033, Langley Memorial Aeronautical Laboratory, Langley Field, Washington*.
- Joseph, D. (2003). Viscous potential flow. *Journal of Fluid Mechanics, 479*, 191-197.
- Kalro, V., Aliabadi, S., Garrard, W., Tezduyar, T., Mittal, S., & Stein, K. (1997). Parallel finite element simulation of large ram-air parachutes. *International journal for numerical methods in fluids, 24*(12), 1353-1369.
- Katz, J., & Plotkin, A. (1991). *Low-speed aerodynamics - from wing theory to panel methods*. San Diego State University.
- Kitepower. (2012). <http://www.kitepower.eu/>.
- KitesurfingSchool. (2000). *Kite designing, kite making*. http://www.kitesurfingschool.org/kite.htm#Sled_Boosting. (Accessed 4 July 2012)
- Knappskog, H. (2011). *Nonlinear control of tethered airfoils: Path-following control of tethered airfoils*. Unpublished doctoral dissertation, Norwegian University of Science and Technology.
- LabS55. (2011). *Ampyx power: Airborne wind energy competitive with fossil fuels*. www.labs55.nl/unit_28-29.html. (Accessed 20 October 2011)
- Laddermill kites wind energy. (2011). www.windenergy1.com/. Energy Guide Wind. (Accessed 17 October 2011)
- Lingard, J. (1995). Ram-air parachute design. In *Precision aerial delivery seminar, 13th aiaa aerodynamic decelerator systems technology conference, clearwater beach*.
- Lock, R., & Williams, B. (1987). Viscous-inviscid interactions in external aerodynamics. *Progress in Aerospace Sciences, 24*(2), 51-171.
- Low turbulence wind tunnel. (n.d.). <http://www.lr.tudelft.nl>. Delft University of Technology. (Accessed 5 September 2012)
- Loyd, M. (1980). Crosswind kite power. *Journal of Energy, 4*(3), 106-111.
- Mack, L. (1984). *Boundary-layer linear stability theory* (Tech. Rep.). DTIC Document.

- Makani Power. (2011). *Update: First unconstrained flight*. www.makanipower.com/company/news/page/2. (Accessed 10 October 2011)
- Maskew, B. (1987). Program VSAERO Theory Document. *NASA Contractor Report 4023*.
- Maughmer, M., & Coder, J. (2010). *Comparisons of theoretical methods for predicting airfoil aerodynamic characteristics* (Tech. Rep.). DTIC Document.
- Melin, T. (2000). A vortex lattice matlab implementation for linear aerodynamic wing applications. *Master's Thesis, Royal Institute of Technology (KTH)*.
- Menter, B. (1989). *Turbulence modeling for engineering flows*. Research and Development Fellow, Ansys, Inc.
- Menter, F. (1992). Improved two-equation $k - \omega$ turbulence models for aerodynamic flows. *NASA STI/Recon Technical Report N, 93*.
- Miller, A., Müller, M., Neumann, S., Würz, W., Harich, A., & Flysurfer, D. (2007). Numerische untersuchung der aerodynamischen kräfte an einem flügelement mit unterbrochenem hinterkantenschlitz. *Studienarbeit IAG, Universität Stuttgart*.
- Montgomery, D. (2008). *Design and analysis of experiments*. John Wiley & Sons Inc.
- Mulder, J., Staveren, W. van, Vaart, J. van der, & Weerdt, E. de. (2006). Flight dynamics lecture notes. *TU Delft*.
- Munk, M. M. (1923). The minimum induced drag of aerofoils. *NACA Technical Report R-121*.
- Ockels, W. (2001). Laddermill, a novel concept to exploit the energy in the airspace. *Aircraft design, 4*(2-3), 81-97.
- Paraschivoiu, I. (2003). *Subsonic aerodynamics*. Presses inter Polytechnique.
- Pealinck, R. (2012). *Personal communication*. (Flysurfer R&D team)
- Ruppert, M. (2010). Development and validation of a real time pumping kite model. *Master of Science Thesis, Faculty of Aerospace Engineering, Delft University of Technology*.
- Schlichting, H., & Gersten, K. (2000). *Boundary-layer theory*. Springer Verlag.
- Schmehl, R. (2012a). Kiting for wind power. *Wind Systems, 7*, 36-43.
- Schmehl, R. (2012b). *Renewable energy, kite power*. (TEDx Delft conference)
- Schmitt, F. (2007). About boussinesq's turbulent viscosity hypothesis: historical remarks and a direct evaluation of its validity. *Comptes Rendus Mécanique, 335*(9), 617-627.
- Schwoll, J. (2012). Finite element approach for statically loaded inflatable kite structures. *Master of Science Thesis, Faculty of Aerospace Engineering, Delft University of Technology*.

- Sheldahl, R., & Klimas, P. (1981). *Aerodynamic characteristics of seven symmetrical airfoil sections through 180-degree angle of attack for use in aerodynamic analysis of vertical axis wind turbines* (Tech. Rep.). Sandia National Labs., Albuquerque, NM (USA).
- Sieberling, S., & Ruitkamp, R. (2011). The powerplane an airborne wind energy system conceptual operations. *Ampyx Power, The Hague*.
- SkySails. (2012a). *Skysails marine*. <http://www.skysails.info/english/>. (Accessed 4 July 2012)
- SkySails. (2012b). *Skysails power*. <http://www.skysails.info/english/power/>. (Accessed 10 July 2012)
- Skywalk GmbH. (2008). *Ram-air wing*. (Via Master of Science Thesis Aart de Wachter)
- Slater, J. (2008). *Uncertainty and error in cfd simulations*. <http://www.grc.nasa.gov/WWW/wind/valid/tutorial/errors.html>. NPARC Alliance.
- Slingshot. (2009). *Slingshot TURBO3*. <http://www.slingshot.com.br/kites.htm>. (Accessed 3 July 2012)
- Smith, S. C. (1996). A Computational and Experimental Study of Nonlinear Aspects of Induced Drag. *NASA Technical Paper 3598, Ames Research Center, Moffett Field, California*.
- Stokes, G. (1851). On the effect of the internal friction of fluids on the motion of pendulums. *Transactions of the Cambridge Philosophical Society*, 9, 8.
- Stull, R. (2000). *Meteorology: For scientists and engineers: a technical companion book with ahrens' meteorology today*. Brooks/Cole.
- Terink, E. (2009). Kiteplane flight dynamics. *Master of Science Thesis, Faculty of Aerospace Engineering, Delft University of Technology*.
- Tinling, B. E., & Kolk, W. R. (1951). The effects of mach number and reynolds number on the aerodynamic characteristics of several 12-percent-thick wings having 35° of sweep-back and various amounts of camber. *National Advisory Committee for Aeronautics, Washington*.
- Tiobe programming community index*. (2009). <http://www.tiobe.com/index.php/content/paperinfo/tpci/index.html>. (Retrieved 3 August 2011)
- Van Ingen, J. (2008). The en method for transition prediction. historical review of work at tu delft. *38th Fluid Dynamics Conference and Exhibit, Seattle, Washington*.
- Veldhuis, L. L. M. (2012a). Aircraft Aerodynamics. *AE4130 lecture slides, Faculty of Aerospace Engineering, Delft University of Technology*.
- Veldhuis, L. L. M. (2012b). *Personal communication*. (Aerodynamics, Delft University of Technology)

- Vos, W. (2006). The verification and validation of preliminary cfd results for the construction of an a priori aerodynamic model. *Master of Science Thesis, Faculty of Aerospace Engineering, Delft University of Technology*.
- Wachter, A. de. (2008). Deformation and aerodynamic performance of a ram-air wing. *Master of Science Thesis, Faculty of Aerospace Engineering, Delft University of Technology*.
- Wikipedia. (2006). *Leading edge inflatable kite*. [http://en.wikipedia.org/wiki/Stall_\(flight\)](http://en.wikipedia.org/wiki/Stall_(flight)). (Accessed 6 August 2012)
- Wikipedia. (2007). *Leading edge inflatable kite*. <http://en.wikipedia.org/wiki/File:LEI-Kite.jpg>. (Accessed 3 July 2012)
- Williams, P., Lansdorp, B., & Ockels, W. (2007a). Flexible tethered kite with moveable attachment points, part i: Dynamics and control. *AIAA Atmospheric Flight Mechanics Conference*.
- Williams, P., Lansdorp, B., & Ockels, W. (2007b). Flexible tethered kite with moveable attachment points, part ii: State and wind estimation. *AIAA Atmospheric Flight Mechanics Conference*.
- Williams, P., Lansdorp, B., Ruiterkamp, R., & Ockels, W. (2008). Modeling, simulation, and testing of surf kites for power generation. *No. AIAA, 6693*.
- Wirsing, E. (1999). De prestaties van het profiel naca642a015 gemeten in drie verschillende windtunnelconfiguraties. *Master of Science Thesis, Faculty of Aerospace Engineering, Delft University of Technology*.
- XFLR5. (2011). Analysis of foils and wings operating at low reynolds numbers. *Guidelines for XFLR5 v6.03*.
- XtremeSport. (2008). *Kite surfing leading edge inflatables versus foil*. <http://xtremesport4u.com/extreme-water-sports/kite-surfing-leading-edge-inflatables-versus-foil/>. (Accessed 3 July 2012)
- Yen, S. C., & Fei, Y. F. (2011). Winglet dihedral effect on flow behavior and aerodynamic performance of NACA0012 wings. *Journal of Fluids Engineering, vol. 133*.
- Zhu, Y., Moreau, M., Accorsi, M., Leonard, J., & Smith, J. (2001). Computer simulation of parafoil dynamics. *16th AIAA Aerodynamic Decelerator Systems Technology Conference*.

Power kites and their applications

Since kites already exist for thousands of years there are countless numbers of different shaped kites, each shape serving a certain purpose. However in this thesis there is a focus on high performance kites used for clean energy generation. Performance is here defined as the ability of a kite to transport wind energy to a controlled system e.g. a ship or a generator. For clean energy generation it is always strived for to obtain as much energy as possible, and therefore the power produced by a kite should be as high as possible. Therefore these kites are often called power or traction kites. The concept of clean energy generating kites is relatively new compared to the expanding market of sport kites, where large gains in performance are booked in the past decades. Since in sport kiting it is also often desired to have high amounts of power, there is often large coherence between shapes of sport kites and those used for energy generation. In this section an overview of high performance kite applications is given, where briefly is described what the main differences in kite design and performances are. Before doing this a description is given on the two main type of kites used for high performance applications.

A.0.3 Foil kites vs LEI kites

There are two main types of kites used for these applications: foil kites and LEI kites, respectively also named ram-air kites and tube kites (see Figure A.1 and A.2).

Foil kites are hollow wings made of 2 layers of soft fabric which have openings at the stagnation point on the leading edge, allowing them to fill with air and thereby giving the kite its airfoil shape. The control and power lines of a foil kite are not attached directly to the kite but attach instead to a wide series of smaller lines which are attached to many points on the kite, forming what is called a bridle. The bridle maintains the desired shape of the kite and also provides better flight control.

Opposed to foil kites, LEI kites consist of a single skin, also called canopy, and is connected to inflatable bladders providing structural stiffness. The bladders are surrounded by protective tubes of Dacron and other reinforcements are used in high-wear or high-load areas. LEI kites require a less complex bridle than foil kites, because of the pressurized tubes.

Originally only the C-kite existed, see Figure A.3, which has square corners and forms a deep C-shaped arc when flying (Evolution, 2008a). These kites do not have a bridle,



Figure A.1: See through impression of the construction of a ram air wing (Skywalk, 2008).



Figure A.2: A LEI kite where the inflated leading edge and struts make the kite more rigid than a ram air kite (Wikipedia, 2007).

but are only connected to the four corners of the kite (with an optional fifth safety line). Later several Supported Leading Edge (SLE) kites were introduced, which use a bridle system to better maintain the shape of the kite. The most famous SLE is the BOW kite, see Figure A.4: these kites have a concave trailing edge and have a shallower arc in planform and therefore look flatter. These features allow the kite's angle of attack to be altered more and thus adjust the amount and range of power being generated to a much greater degree than previous LEI's, which has been a significant improvement in safety.

Foil kites have significant less profile drag than LEI kite profiles, because they don't have the large flow separation area behind the round LE. As a result foil kites have generally higher lift-to-drag ratio (L/D). LEI kites have however much more depower and a better recovery after strong maneuvering. For more detailed descriptions on pros and cons of LEI and foil kites, see Evolution (2008a), Evolution (2008b) and XtremeSport (2008).

A.0.4 Sport kites

Kites are most famous for their use for recreational purposes and currently the kite industry is dominated by sport kites. Many competitions are held in which there are several disciplines mainly involving speed and airtime. Each sport and discipline requires its own specific kite properties; in this section the interaction between design and performance in kitesports is considered.

For *skydiving* ram air wings are used of which the primary function is to quickly and safely decelerate the fall of the skydiver to a speed at which he can land. Mainly rectangular shaped wings are used that contain large opening cells to decrease opening time of the canopy. It should be strong enough to absorb the shock of the opening and depending on discipline it should have a certain glide ratio making it possible to fly horizontal distances. For BASE-jumping, canopy formation- and accuracy-flying which are generally safer to operate because they are less prone to dive rapidly with relatively small control inputs and they glide more slowly. These medium performance canopies

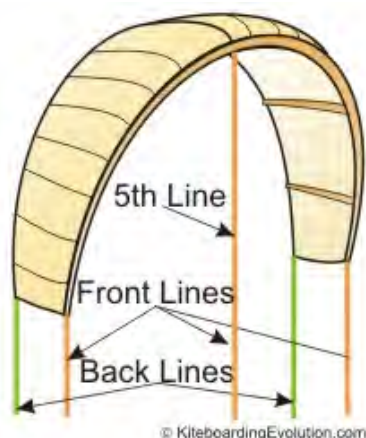


Figure A.3: A C-kite with two back and two front lines (Evolution, 2008b).

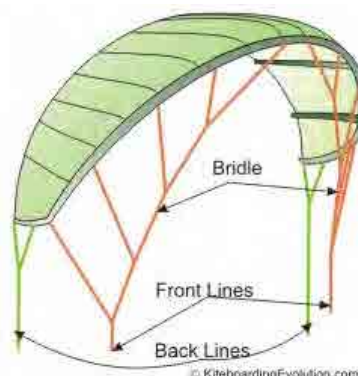


Figure A.4: The most popular SLE kite: the BOW kite, which has a concave trailing edge (Slingshot, 2009).

typically have a less-efficient glide ratio. In BASE-jumping larger opening cells are used to decrease opening time of the canopy. High performance canopies are tapered or elliptical and respond faster to control input, therefore often chosen by experienced skydivers.

Ram air wings are also used for *paragliding*, in which it is possible to increase in height by using the currents of rising air. Therefore highly efficient airfoils and planform shapes are required. A disadvantage of these wings is the high sensitivity to turbulent air. A variant of paragliding is speed riding for which the wings are much smaller and stable.

Sports involving kites near the surface can be roughly split up in land kites and surf kites. In *kitebuggying* mainly ram air wings are used, because of their high impact resistance. Also for *snow kiting* foil kites are used, moreover due to their easy and quick deployment and no pump is required. In *kitebuggying* the pilot sits in a buggy and is connected to a kite which generates the power to move around. Speeds can go up to 100km/h and therefore medium to high aspect ratios are used. Buggy jumping is also possible, for which larger kites or higher aspect ratio kites can be used. Another land kite sport is: snowboarders or skiers use kites to ride or jump in snow covered areas. Mainly foil kites are used due to their easy and quick deployment and no pump is required. LEI kites are used in a lesser extent, they are however considered safer since they are more rigid and have large depower.

Probably the most booming and popular kite sport is *kitesurfing*. It has even replaced windsurfing in the Olympic Games 2016. Initially foil kites were used, but nowadays almost only LEI kites are produced for this sport, because of their good water relaunchability and depower performance. Another important reason why LEI kites are so popular for kite surfing is because of Sled Boosting: due to a moving center of pressure the tow point moves in the same direction, which for the lift growth phase ($0 < \alpha < \alpha_{(C_{L,max})}$) means the angle of attack further increases getting even more lift, while for the decline phase ($\alpha > \alpha_{(C_{L,max})}$) the angle of attack decreases and therefore decelerating lift loss. In terms of the rider this means they can jump easier and higher (KitesurfingSchool, 2000). Several disciplines exist, each having its own specific requirements on board and kite shape. For freestyle high manoeuvrability is desired and therefore often C-shape kites are



Figure A.5: Top left: kitebuggying, top right: paragliding, bottom left: skydiving, bottom right: kitesurfing.

used. For course racing upwind performance is important, hence higher aspect ratio kites are used which have a higher L/D ratio. In wave riding the kite should have constant pulling force and therefore a built-in angle of attack (twist) can be used.

To a somewhat lesser degree kites are used for *sailing*. Slowly the interest for ships propelled by kites is growing and even contests between kite sailers are turning up.

A.0.5 Kite propelled marine systems

The first and currently only kite powered product available for industrial use is the kite propelled marine vessel, see Figure A.6. The german company SkySails sold a few of these systems, which use ram air kites with a size up to 320m^2 . Because of their size they are relatively slow, however the combination of having a large surface area, flying the kite crosswind (read below) and using efficient profiles with large lift coefficient these kites can produce up to 2MW of power in favorite wind conditions (SkySails, 2012a). This way a cargo ship can save ten tons of oil a day, reduce their fuel cost with 10-35% and significantly lower emissions.

There are companies developing kite systems for sailboats and yachts, see Figure A.7. 'Airplay Kitesailing' uses 25m^2 LEI kites on a catamaran (Airplay, 2009). They state that the advantage of using kites instead of conventional sails is simply higher speed, resulting from four factors:

- A kite flies at higher altitude, where there is more wind.
- Using crosswind motion the apparent wind speed is higher and thus higher forces can be achieved.



Figure A.6: A cargo ship propelled by a kite from the company SkySails.

- There is no righting moment resulting from the kite, thus its surface area can be larger than a sail.
- Because the kite slightly lifts the boat out of the water drag is reduced.

An extensive analysis on kiteboating/kitesailing was performed by Heuvel (2010).

A more conceptual idea is the 'Hydrokite' developed at Delft University of Technology, see Figure A.8. It is a new sustainable approach to reach high speeds over water. The system consists of three main components: the kite, cabin and keel. The kite provides both lift and propulsion, while the keel assures grip on the water. Inside the cabin, which would fly at 15m above the water, the pilots control and navigate the Hydrokite to a top speed of 90km/h. Considering this speed and a cabin for two pilots it was calculated a BOW kite of about 157m² at altitudes between 100-150m is required (Alblas, 2009).

Other kite powered energy concepts

The DUT KitePower project described in the previous section is one of the power kite systems for wind energy generation and distinguishes itself from other existing systems by the airborne kite control mechanism. In the last decade the number of companies involved in kite power energy systems has increased from 5 up to 50. Shortly some of these systems will be discussed.

SwissKitePower is a collaborative research and development project between three academic, non-profit institutions and Alstom Switzerland. Their prototype demonstrated



Figure A.7: Kitesailing or kiteboating on a catamaran (Airplay, 2009).



Figure A.8: A conceptual idea to travel over water: the Hydrokite.

in August 2009 is very similar to the DUT KitePower project. At that time they were also using a LEI kite with an airborne kite control unit. Currently they are testing and investigating new kite designs.

The University of Turin (Politecnico di Torino) initiated the *KiteGen* project, also a pumping kite system but with some different characteristics. Instead of one tether and an airborne control pod two lines are used which are connected between two electric drives fixed on the ground and the bridle system of the kite. The flight of the kite is controlled by regulating the pulling force on each line. This way this system has more cable drag, but does not require a heavy control unit in the air. Their current prototype system generates up to 40kW using a 10m² foil kite (Canale et al., 2007).



Figure A.9: The 21m² high performance foil kite used by EnerKite (EnerKite, 2012).

The german company *EnerKite* has a pumping kite system in which, just as *KiteGen*, also two winches are used. For the 30kW rated power system a 5kg weighing 21m² foil kite is used. It is specially designed to have maximized performance and power at minimized weight. In Figure A.9 it can be seen that it is BOW like shaped, has a complex bridle system and many ribs to maintain an efficient profile over the span of the wing. No large deformation dents at the leading edge can be seen, indicating the profile is carefully designed such that stagnation pressure does not excessively deforms the profile. Further it appears as a slender wing (high aspect ratio). The combination of high aspect ratio and efficient profile design indicate the kite most probably has a high L/D . (EnerKite, 2012)

Skysails not only has a kite propulsion system for ships, but also a pumping kite system of which the currently functional model has an installed generator power of 55kW. Their 20m² foil kite, shown in Figure A.11, has also BOW-like characteristics with an aspect ratio of approximately 2.5 and is automatically controlled by an airborne kite control unit. Instead of air vents over the whole span two large vents near the center provide the required internal pressure. Currently they are developing a 1MW demonstrator model where the kite will have a sail area of approximately 400m² and an aspect ratio of approximately 2.7. The company will focus on offshore applications where the systems is

installed on floating platforms that can be anchored at depths down to 700m, see Figure A.10. Conventional wind turbines are not cost effective at depths beyond 40m, because they require a solid foundation. (SkySails, 2012b)



Figure A.10: A conceptual offshore kite powered wind farm of SkySails Power (SkySails, 2012b).



Figure A.11: The foil kite used by SkySails Power with two large air inlets near the center (SkySails, 2012b).

Also a combination of the beforementioned kite powered ship propulsion and energy generation is possible. By incorporating a pumping kite system of which the energy is fed to electrical engines a ship could be indirectly propelled by a kite. Two systems that use this kind of technique for the propulsion of a ship are the 'Laddermill ship project' (Ecolution) and the 'KiteNav' project.

Appendix B

Example of conventional kite design: 'designing the DUT power kites'

To get an impression which considerations are involved during a kite design process this section describes the main design features of the kite used in the TUD KitePower system. It will give an indication of how a conventional kite design process works.

Currently there are four kites which were used for the KitePower system, three having a surface area of 25m^2 and one of 14m^2 .

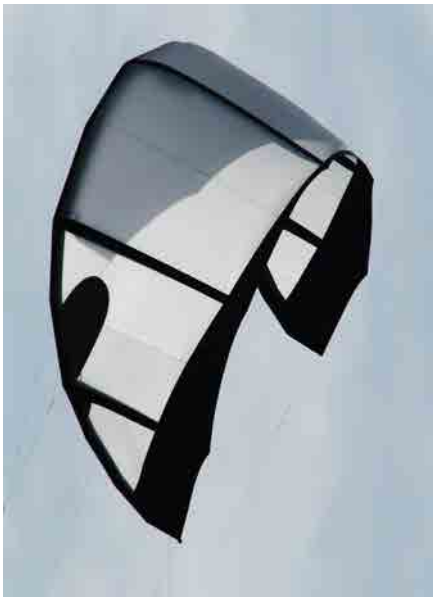


Figure B.1: The first kite of the TUD KitePower system, the 25m^2 TUD-MutinyV1.

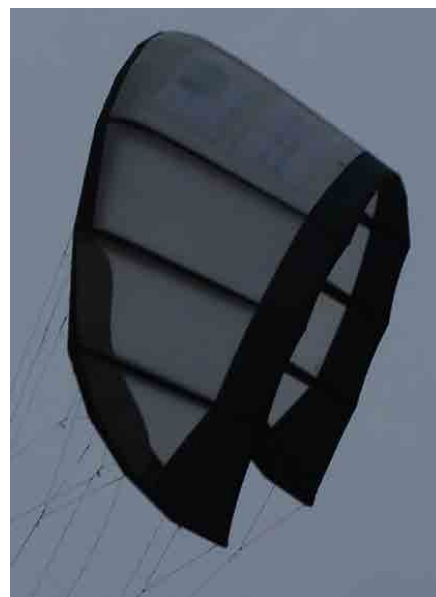


Figure B.2: The 25m^2 TUD-MutinyV2 kite has more curvature, an extra strut and a less sharp corner at the TE around the tip.

B.1 MutinyV1 25m²

The first kite was a standard 25m² kite of the brand Mutiny, see Figure B.1. A LEI kite was chosen to have high structural stiffness. It is a BOW kite and therefore has desirable stall behavior and depower capability. The vertical surfaces at the tips make the kite stable and maneuverable. Initially the only adaptation was the number of bridle points. Next to the shape of the kite its behavior is strongly dependent on the bridle system, which was extensively described by Heuvel (2010). Primarily it supports the kite such that it maintains the desired shape. Secondly it determines the amount of depower a kite can have, see Figure B.4. The amount of depower is on the one hand determined by the bridle system, specifically the working line of the power lines, and on the other hand by the position of the aerodynamic center. This is the point at which the pitching moment coefficient for the airfoil does not vary with angle of attack. When having minimum tension in the steering lines and the kite has stopped rotating, the total moment has become zero. This means the moments caused by the aerodynamic forces, the weight and the force in the power and steering lines are in balance. Thus to increase maximum depower either the aerodynamic center should be more to the rear and/or bottom or the working line of the power lines should be placed more to the front and/or top. In the case of the TUD-Mutiny-V1 depowering is provided by both using forward placement of the bridles and, due to the bow like shape, a good rearward placement of the aerodynamic center. The design of the bridle system incorporates pulleys to allow for relative change in line length between two connected bridle lines when pitch angle is changed (e.g. during a depower maneuver). This is required for kites with high out-of-plane planforms.

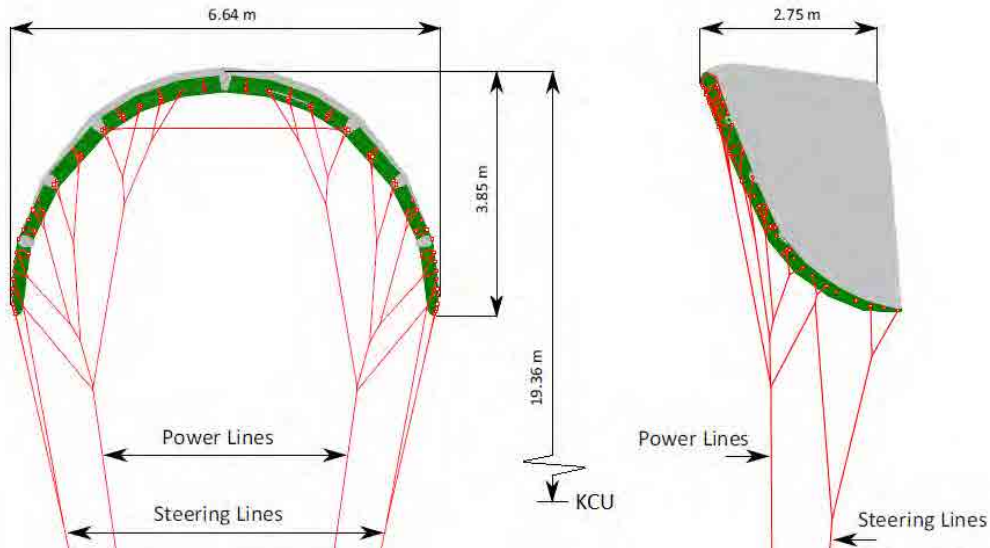


Figure B.3: CAD representation of the TUD-Mutiny-V2 (Schwoll, 2012).

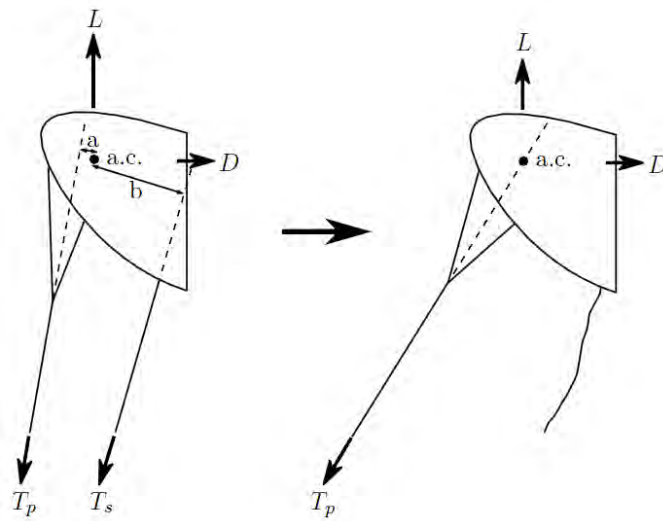


Figure B.4: A kite can be depowered until the working line of the power lines goes through the aerodynamic center (Heuvel, 2010).

B.2 MutinyV2 25m²

To increase depower the LE of the second version, the TUD-Mutiny-V2 (Figure B.2 and B.3), had slightly more curvature making it possible to place the power lines to the front, while maintaining the same LE tension between the bridle point connections. It also meant more surface area at the tips increasing manoeuvrability and side-window launching capability. A different bridle was used, which gave more rigidity to the structure and better prevented collapse. Furthermore an extra strut prevented flapping of the canopy at the tips and gave more rigidity to the structure. The sharp TE corner at the tips caused flapping of the canopy, see Figure 2.12, and was removed in the second Mutiny kite. To further reduce flapping of the canopy glass fiber reinforcements were placed on the canopy at the TE.

B.3 GenetrixV1 Hydra 14m²

Though depower and rigidity were increased in the second version these were still important properties of which improvement was desirable. Therefore an additional kite was purchased, the 14m² Genetrix Hydra, see Figure B.5. This kite has a lower camber factor, which is the ratio between the out of plane deflection and the projected span of the wing (this makes the kite look flatter looking from the front). Having a lower camber factor is equivalent to having a relative larger projected area (or higher projected aspect ratio) and therefore it generates more lift per total surface area and thus higher traction force. Another advantage is the possibility to use knots instead of pulleys in the bridle: knots perform better in preventing buckling of the LE, described by Heuvel (2010). Furthermore, all struts were reinforced with carbon fiber rods to increase stiffness.



Figure B.5: An additional kite was acquired to verify whether a lower camber factor and higher aspect ratio positively influenced performance. This kite is a $14m^2$ Genetrix Hydra.

B.4 GenetrixV2 $25m^2$

The performance of the Genetrix Hydra was found to be very satisfying and therefore it was used as the basis for the third $25m^2$ -sized DUT PowerKite. A new design feature was implemented: a bulging LE, see Figure B.6. Instead of adding more struts, this feature should preserve a constant profile between struts. Again knots were used in the bridle system and extra reinforcements of Dacron and plastic patches at the TE should reduce canopy flapping. In the first tests it was noticed the kite steers less aggressive, which was expected because the kite has low camber and therefore little vertical surface to steer. It was also verified that the high projected aspect ratio of the kite results in a higher loading, while having much depower.



Figure B.6: The Genetrix 25m² contains a bulging LE to preserve a more constant profile over the wing.

Theory of aerodynamic methods

C.1 General theories

C.1.1 Kutta-Joukowski theorem and Kutta-condition

The Kutta-Joukowski theorem determines the lift (per unit span) of an airfoil section by determining the circulation in a region of potential flow:

$$L' = \rho_{\infty} V_{\infty} \Gamma_{\infty} \quad (\text{C.1})$$

Here ρ_{∞} and V_{∞} are the undisturbed flow properties. Circulation Γ_{∞} is determined as the line integral:

$$\Gamma_{\infty} \equiv - \oint_c \vec{V} \cdot d\vec{s} \quad (\text{C.2})$$

around a path c far from and enclosing the airfoil.

For potential flow over an airfoil an infinite amount of solutions is possible. The value of circulation can be anything and therefore it is not defined where the stagnation points are located. In real life flow the rear stagnation point for a body with a sharp trailing edge is located at that trailing edge. This condition is known as the Kutta-condition and implies which value the circulation should have to satisfy this condition. The fact that this rear stagnation point is at the trailing edge is a result of viscosity, hence the Kutta-condition incorporates an important effect of viscosity while maintaining the advantages that potential flow offers.

$$\Gamma_{\infty} \equiv - \oint_c \vec{V} \cdot d\vec{s} = - \iiint_S (\nabla \times \vec{V}) \cdot d\vec{s} \quad (\text{C.3})$$

Circulation is directly related to vorticity by Stokes' theorem, see Equation C.3. Circulation implies presence of vorticity and hence, rotational flow; a property which should not be present in potential flows. The Kutta-Joukowski theorem can still be valid however. As can be seen in Equation C.2 is defined as an integral along a closed contour and therefore does not contain information about the contents within that contour. Now consider the elementary potential flow of a free vortex, see Figure C.1. A free vortex is irrotational and velocity is inversely proportional to the radius. It is irrotational everywhere, except

at the center where it has infinite strength. If now such a vortex can be placed such that the center is within the airfoil, the flow is everywhere irrotational and therefore potential flow theory is applicable.

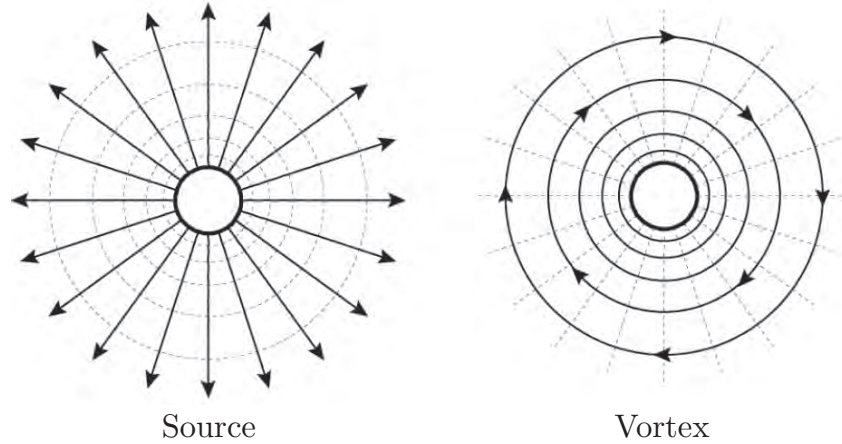


Figure C.1: Visualization of two elementary flows, which can be used to describe the flow around an airfoil. The source has radially directed induced velocity vectors, while the vortex has induced velocities in the tangential direction.

C.1.2 Vortex filament, Biot-Savart law and Helmholtz's vortex theorems

We expand the concept of a 2D point vortex to 3D: the vortex filament. A vortex filament can be curved and induces a flow field in the surrounding space. The filament with length $A \leq l \leq B$ has constant circulation Γ and induces a velocity at a distance \vec{r} of:

$$\vec{V} = \int_A^B \frac{\Gamma}{4\pi} \frac{d\vec{l} \times \vec{r}}{|\vec{r}|^3} \quad (\text{C.4})$$

This equation is the Biot-Savart law. Helmholtz's vortex theorems state that strength of a vortex filament is constant along its length. Furthermore, he states the filament cannot end in a fluid; it must extend to the boundaries of the fluid (which can be $\pm\infty$) or form a closed path. These theorems were important building blocks for lifting line theory and the vortex lattice method.

C.2 Thin airfoil theory

Thin Airfoil Theory (TAT) is a 2D method which predicts forces, pressures and moments on thin cambered airfoils, therefore it does not take thickness into account.

A vorticity distribution is placed on the airfoil camberline as shown in Figure C.2. This distribution will be a solution of Laplace's equation such that the camber line becomes a streamline of the flow and such that the Kutta condition is satisfied at the trailing edge. The boundary conditions are satisfied if the vortex induced velocities cancel the free-

stream velocity component normal to the airfoil (Anderson, 2001). The latter is defined as

$$w'(s) = V_\infty \left(\alpha - \frac{dz}{dx} \right) \quad (\text{C.5})$$

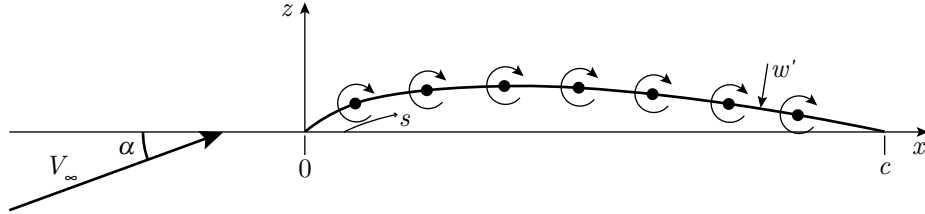


Figure C.2: Vorticity distribution on the camberline of a thin airfoil.

The velocity induced at location x due to the vorticity at location ξ is assumed to be equal to the induced velocity at the same x location due to a vortex projected on the x axis (see Figure C.3). This is because the camber line of a thin airfoil is close to the chord line. Vortex singularity is used to determine the induced velocity by means of the Biot-Savart law. Combining this with the flow tangency BC, the integral relation of thin airfoil theory is obtained as

$$\frac{1}{2\pi} \int_0^c \frac{\gamma(\xi) d\xi}{x - \xi} = V_\infty \left(\alpha - \frac{dz}{dx} \right) \quad (\text{C.6})$$

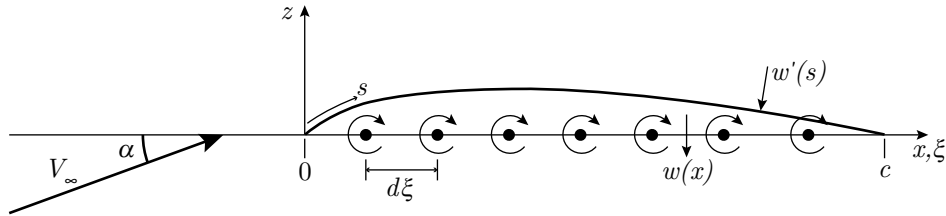


Figure C.3: Projected vorticity distribution on the x axis of thin airfoil's camberline.

Here, γ represents the strength of the vortex street. With the integral relation, airfoils can also be designed for a desired pressure distribution. This is called the thin airfoil inverse design method. By a Fourier series representation of γ , the use of polar coordinates and trigonometric relations, the unknown constants become

$$\begin{aligned} A_0 &= \alpha - \frac{1}{\pi} \int_0^\pi \frac{dz}{dx} d\theta_0 \\ A_n &= \frac{2}{\pi} \int_0^\pi \frac{dz}{dx} \cos n\theta_0 d\theta_0 \end{aligned} \quad (\text{C.7})$$

With these expressions, the pressure difference between upper and lower surface, the lift coefficient and moment coefficient about the leading edge can be determined as

$$C_{p_l} - C_{p_u} = 4 \left(A_0 \cos \frac{\theta_0}{2} + \sum_1^w A_n \sin n\theta_0 \right) \quad (\text{C.8})$$

$$C_l = \pi (2A_0 + A_1) \quad (\text{C.9})$$

$$C_m = - \left[\frac{C_l}{4} + \frac{\pi}{4} (A_1 - A_2) \right] \quad (\text{C.10})$$

C.3 2D panel method

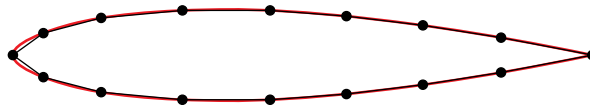


Figure C.4: Discretization of a 2D airfoil section using a panel method.

Before getting into 3D numerical wing analysis methods it is useful to understand 2D numerical methods. In such methods a distribution of singularities is solved for a specified shape, see figure 3.10. In combination with a uniform stream, the singularities produce the flow over a given body. These singularities can consist of elementary potential flows, such as sources, sinks, doublets and vortices. Most common is to use a combination of both source (σ) and vortex (γ) panels, which basically simulate respectively airfoil thickness and circulation (instead of vortices also doublets are used). Lets assume the airfoil is discretized in a number of panels (as can be seen in Figure 3.10) which contain these two singularities. Each of these singularities induce a velocity potential at a predefined point of each panel, the control points. In order to satisfy the boundary condition of zero normal velocity at the control point the potential at that point due to all the panels should be equal to the normal velocity component of the freestream:

$$V_{\infty,n} + V_n = 0 \quad (\text{C.11})$$

where V_n is the summation of induced normal velocities of all panels. For panel i this can be written as:

$$V_{n,i} = \sum_{j=1}^N A_{ij} \cdot \sigma_j + \sum_{j=1}^N B_{ij} \cdot \gamma_j + C_i \cdot V_{\infty} = 0 \quad (\text{C.12})$$

where the coefficients (A_{ij}, B_{ij}) represent the influence of panel j distribution strengths on the control point of panel i and represents the freestream influence. All coefficients are functions of the geometry of the section i.e. due to orientation and spacing of panels. The resulting system can be written in matrix form, see Equation C.13. To complete the system the Kutta-condition is used: the tangential velocities leaving at the trailing edge panel have equal magnitude. This gives a system of linear equations which allow the

solution for the required distribution strengths to be found.

$$\begin{bmatrix} A_{1,1} & \dots & A_{1,N} \\ \vdots & \ddots & \vdots \\ A_{N,1} & \dots & A_{N,N} \\ B_{1,1} & \dots & B_{1,N} \\ \vdots & \ddots & \vdots \\ B_{N,1} & \dots & B_{N,N} \end{bmatrix} \begin{bmatrix} \sigma_1 \\ \vdots \\ \sigma_N \\ \gamma_1 \\ \vdots \\ \gamma_N \end{bmatrix} = \begin{bmatrix} C_1 \\ \vdots \\ C_N \\ C_1 \\ \vdots \\ C_N \end{bmatrix} \cdot (-V_\infty) \quad (\text{C.13})$$

Once the distribution strengths have been calculated, surface tangential velocities at the center of each panel can be calculated and then surface pressure coefficients by

$$C_{p,i} = 1 - \left(\frac{V_i}{V_\infty} \right)^2 \quad (\text{C.14})$$

The panel method as described in this section is named a 'first-order' method because it assumes a constant value of singularity over a given panel. Higher order methods can also be used; for a more thorough discussion of panel methods, see Katz & Plotkin (1991) and Anderson (2001).

C.3.1 2D boundary layer correction

A relatively efficient way of introducing the effects of viscosity into calculations on airfoils is by adding the effects of a boundary layer to the potential flow solution in an iterative manner, also known as viscous-inviscid interaction. The inviscid outer flow region serves as input to the boundary layer equations from which a quantity known as the displacement thickness can be determined. With this quantity the wall streamlines are displaced to obtain a correction on the potential flow solution of the pressure field, see Figure 3.10. Another option to displace the streamlines is to use a source contribution on the contour of such strength that a normal velocity v_n is generated:

$$v_n = \frac{d}{dx} (U\delta^*) \quad (\text{C.15})$$

Here x is in the direction of the panel, U is the local outer flow velocity and δ^* the displacement thickness. The advantage of this procedure is that the geometry of the airfoil remains the same through all iterations (Veldhuis, 2012a).

These boundary layer correction methods produce results that for most cases of engineering interest compare well with experiment and this at much lower computational cost than Navier-Stokes simulations. Furthermore, viscous-inviscid interaction methods give clear insight into the behavior of the boundary layer since the integral thicknesses are immediately available (Coenen et al., 2000).

C.4 Lifting line theory

For the circulation lift theory of Kutta-Joukowski, an infinite wing span was assumed, such that there were no spanwise variations in the lift force distribution. LLT corrects

this 2D theory by incorporating a finite wing section. One of them is the appearance of a starting vortex once the wing starts moving upstream, as shown in figure 3.4. This vortex is equal in magnitude as the bound vortex, but in the opposite direction of rotation. According to LLT, the wing is considered to be a single vortex line, at which the bound vortex is bound to. Next to this, the wing tips generate so called tip vortices, resulting in a closed system, which is a result of the conservation of circulation (Kelvin's circulation theorem). This tip vortex is the key to LLT. If the change in lift distribution is known at a given lift section, it is possible to predict how that section influences the lift over its neighbors: the vertical induced velocity (called upwash/downwash ω) can be quantified using the velocity distribution within a vortex, and related to a change in effective angle of attack over the neighboring sections. For a rectangular wing the spanwise lift distribution is highest at the root and gradually decreases to zero towards the tips.

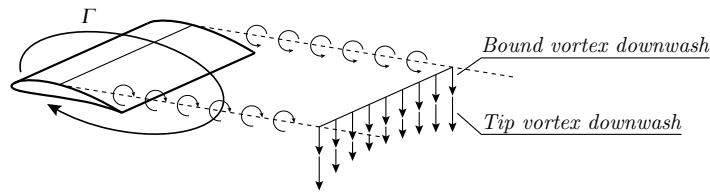


Figure C.5: Downwash distribution of a finite straight wing due to the bound vortex (constant) and the tip vortices (parabolic).

As a result of the tip vortices, additional downwash is added to the already present downwash due to the bound vortex. The resulting system is illustrated in Figure C.5. The equally distributed downwash comes from the bound vortex and the parabolic distribution increasing towards the wing tips is a result of the tip vortices. Since this holds for a rectangular shaped wing, changing this shape results in a different downwash distribution. An elliptical shaped wing equally distributes the extra downwash due to tip vortices, such that the total downwash is also constant along the wing span. The downwash magnitude increases towards the wing tips increasing the induced drag. The total induced drag D_i is determined as:

$$D_i = \rho V_\infty \int_{tip}^{tip} \Gamma \sin(\alpha_i) dy \quad (\text{C.16})$$

where α_i is the induced angle defined by $\alpha_i = \sin^{-1} \left(\frac{\omega_i}{V_\infty} \right)$.

Airfoil section validation

This appendix contains the simulation results of 4 different airfoil sections used for the validation cases, performed with XFOIL and obtained from literature.

D.1 NACA - 64₂(A)015

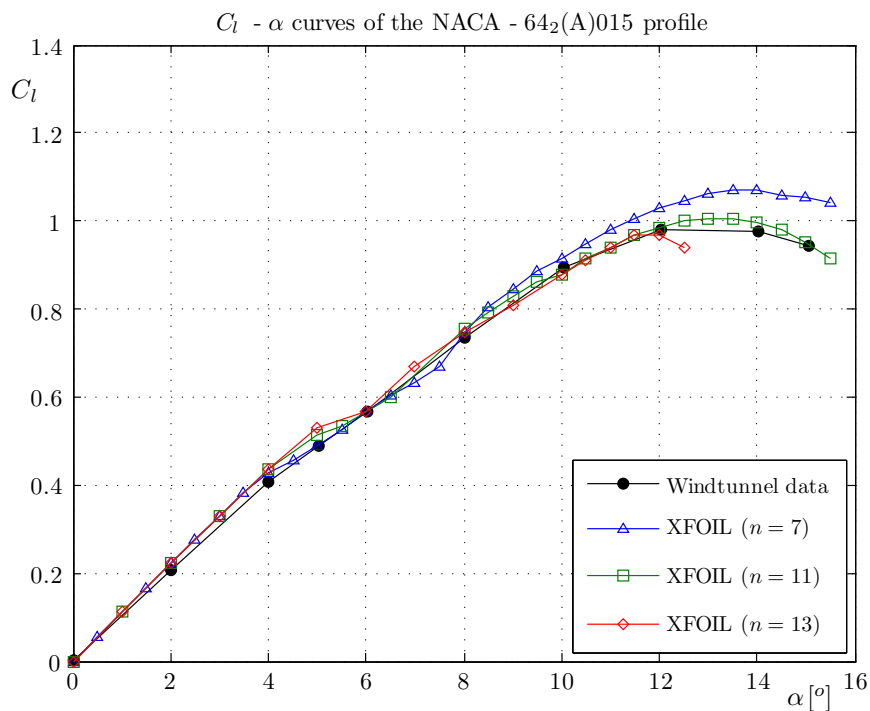


Figure D.1: The $C_l - \alpha$ curves obtained from windtunnel experiments and XFOIL simulations with 3 different values of n for the NACA - 64₂(A)015 profile used for the flat wing configuration where $Re = 1.0 \cdot 10^6$.

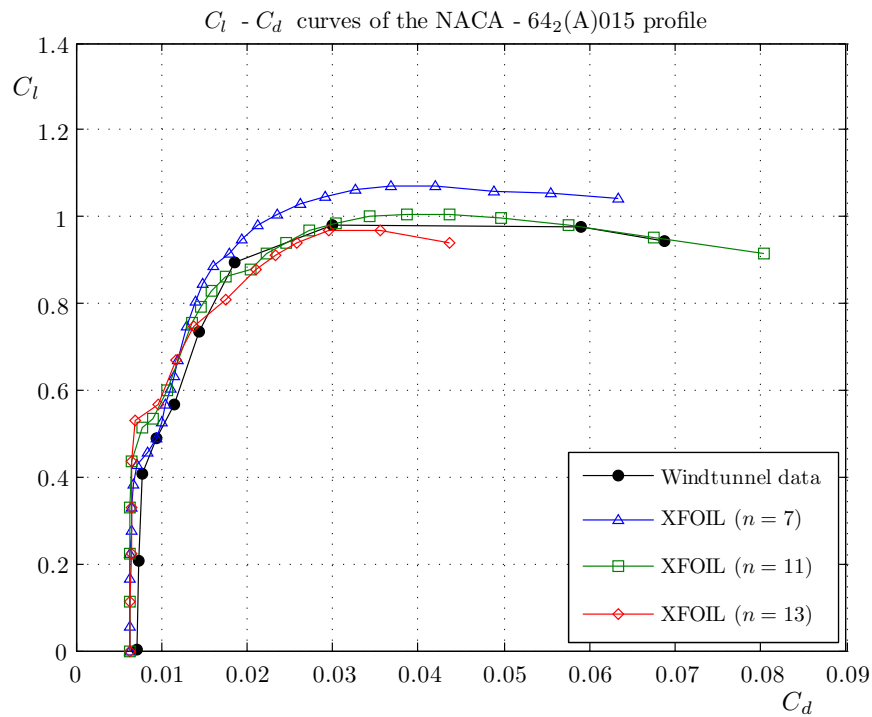


Figure D.2: The $C_l - C_d$ curves obtained from windtunnel experiments and XFOIL simulations with 3 different values of n for the NACA - 64₂(A)015 profile used for the flat wing configuration where $Re = 1.0 \cdot 10^6$.

D.2 NACA - 65₁(A)012

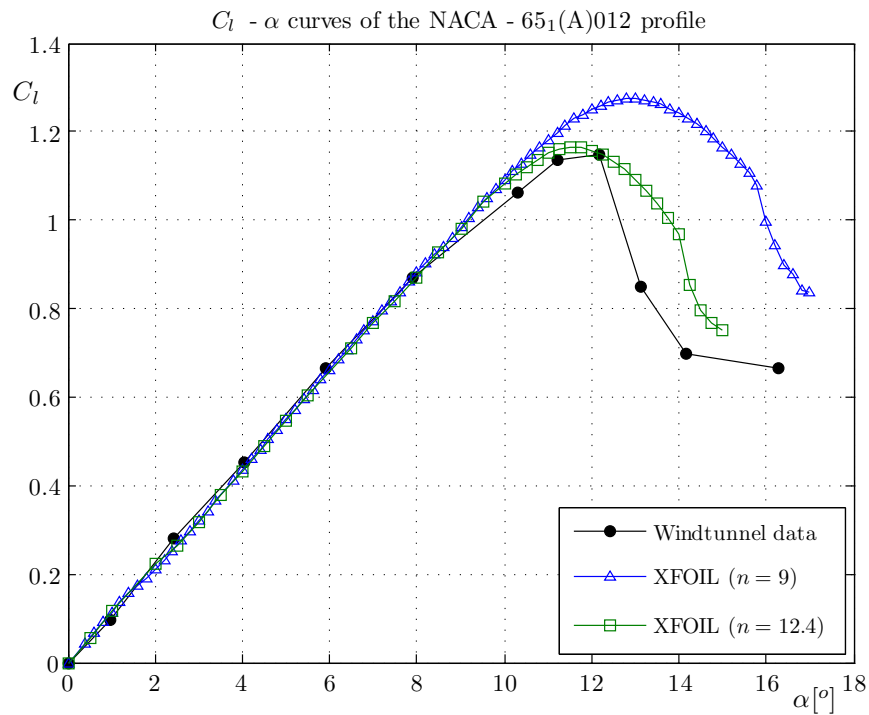


Figure D.3: The $C_l - \alpha$ curves obtained from windtunnel experiments and XFOIL simulations with 2 different values of n for the NACA - 65₁(A)012 profile used for the swept wing configurations where $Re = 3.0 \cdot 10^6$.

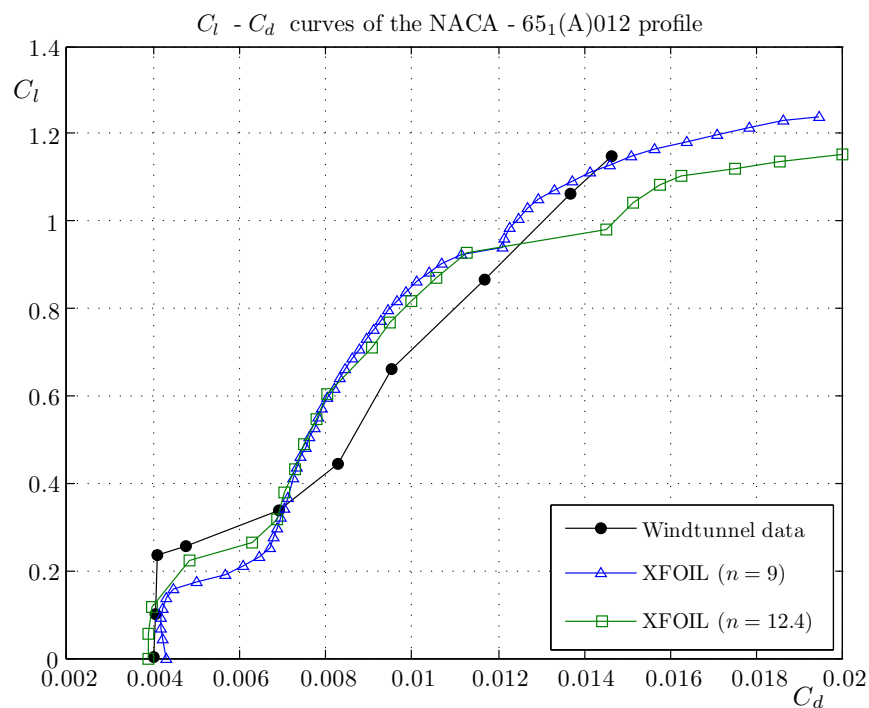


Figure D.4: The $C_l - C_d$ curves obtained from windtunnel experiments and XFOIL simulations with 2 different values of n for the NACA - 65₁(A)012 profile used for the swept wing configurations where $Re = 3.0 \cdot 10^6$.

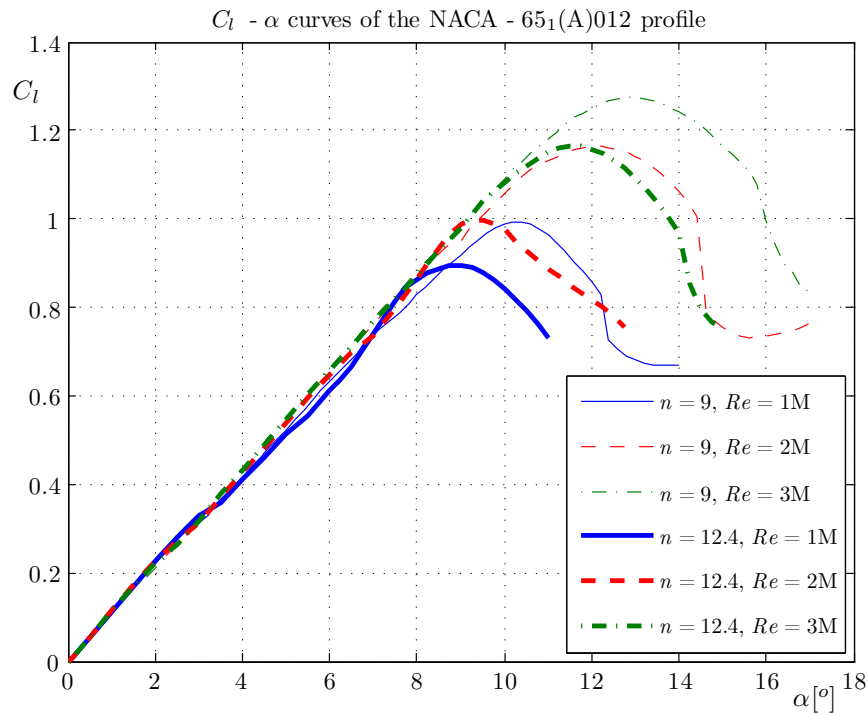


Figure D.5: The $C_l - \alpha$ curves obtained from XFOIL simulations with 2 different values of n for the NACA - 65₁(A)012 profile used for the swept wing configurations where $Re = (1.0 - 3.0) \cdot 10^6$.

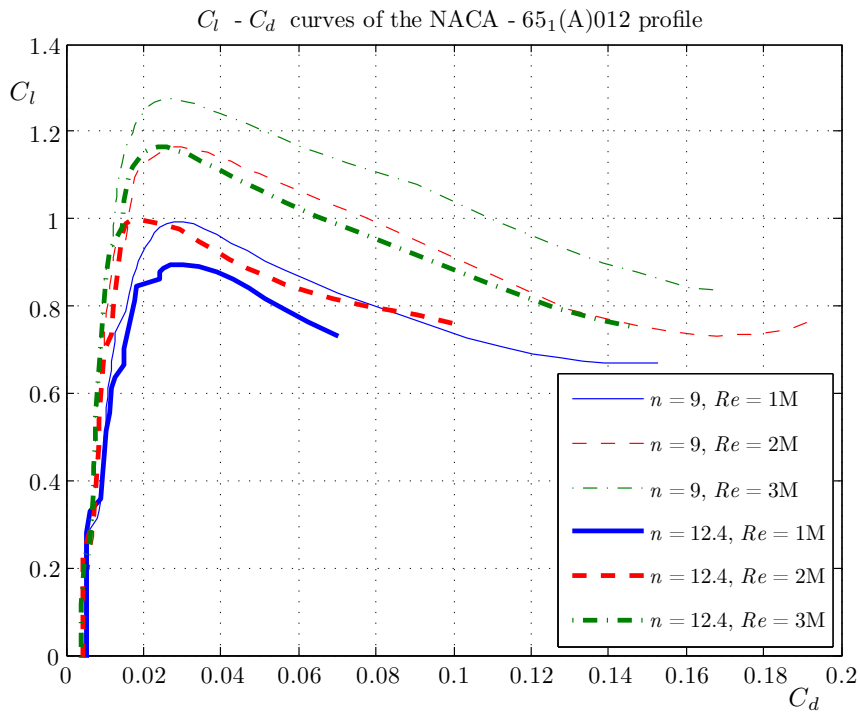


Figure D.6: The $C_l - C_d$ curves obtained from XFOIL simulations with 2 different values of n for the NACA - 65₁(A)012 profile used for the swept wing configurations where $Re = (1.0 - 3.0) \cdot 10^6$.

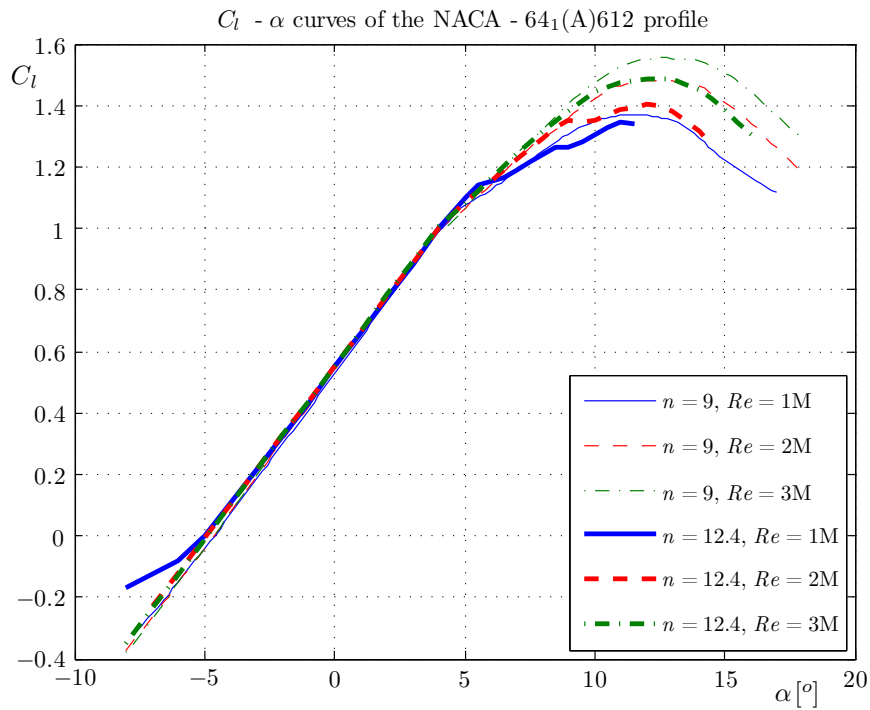
D.3 NACA - 64₁(A)612

Figure D.7: The $C_l - \alpha$ curves obtained from XFOIL simulations with 3 different values of n for the NACA - 64₁(A)612 profile used for the swept wing configurations where $Re = (1.0 - 3.0) \cdot 10^6$.

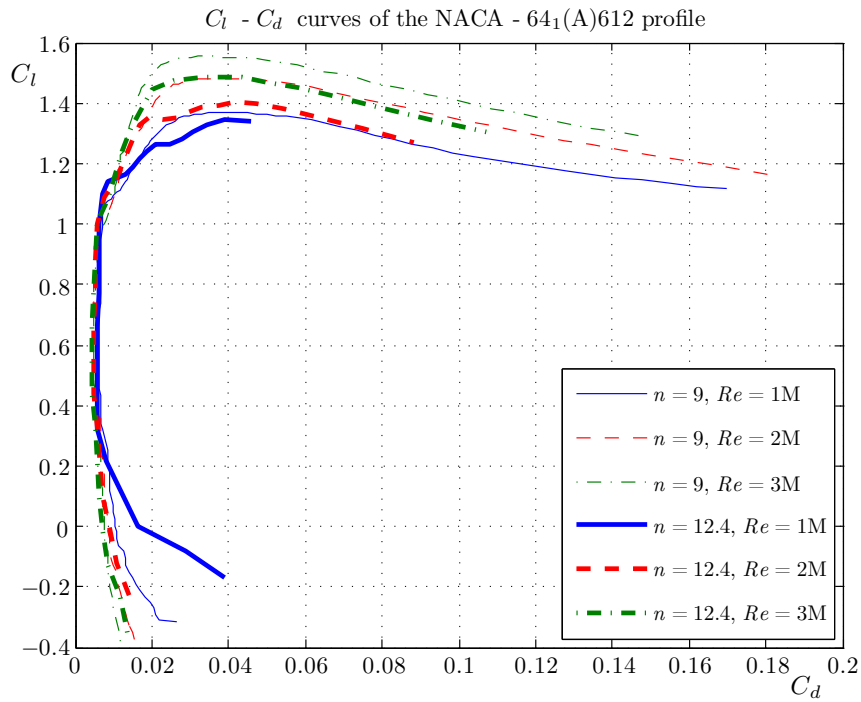


Figure D.8: The $C_l - C_d$ curves obtained from XFOIL simulations with 3 different values of n for the NACA - 64₁(A)612 profile used for the swept wing configurations where $Re = (1.0 - 3.0) \cdot 10^6$.

D.4 NACA - 0012

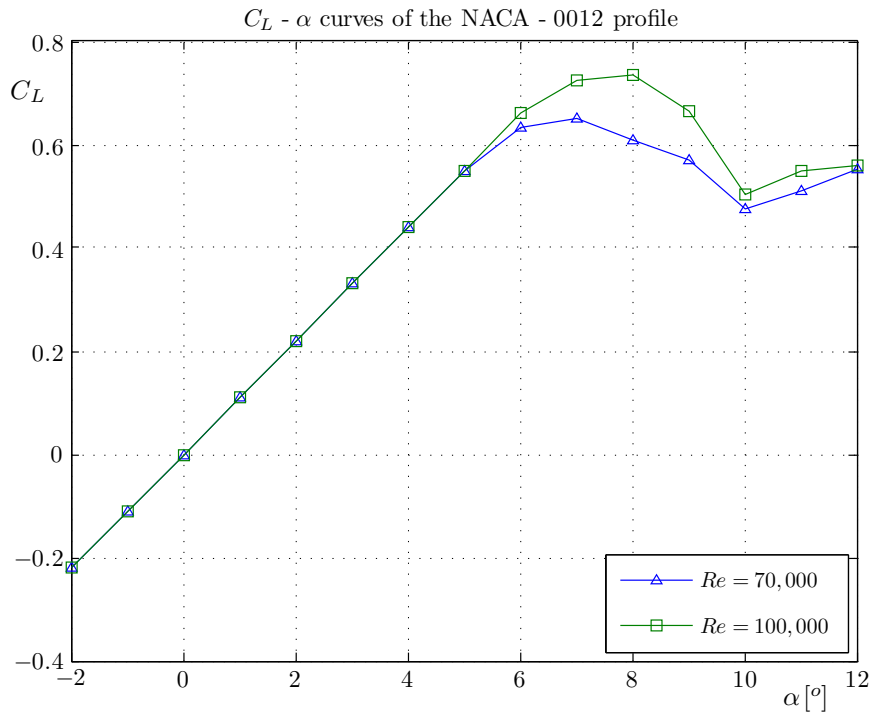


Figure D.9: The $C_L - \alpha$ curves obtained from Cyberiad (1981) for the NACA - 0012 profile used for the winglet configuration where $Re = 80 \cdot 10^3$.

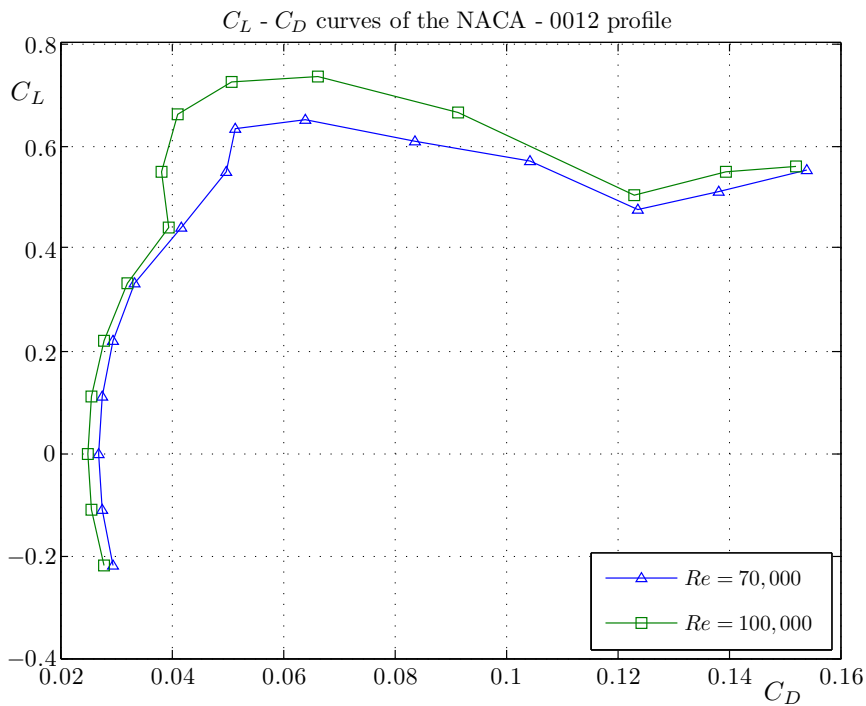


Figure D.10: The $C_L - C_d$ curve obtained from Cyberiad (1981) for the NACA - 0012 profile used for the winglet configuration where $Re = 80 \cdot 10^3$.

D.5 NACA - 64-418

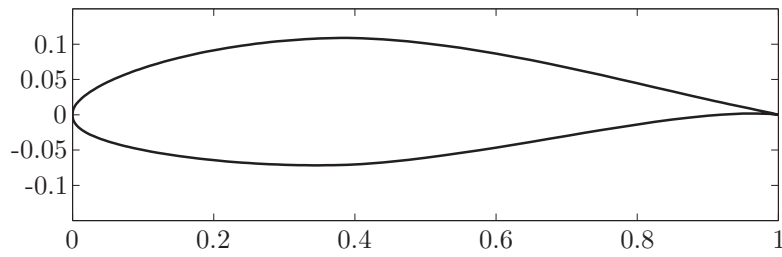


Figure D.11: The NACA - 64-418 airfoil section used for the arc shaped kite.

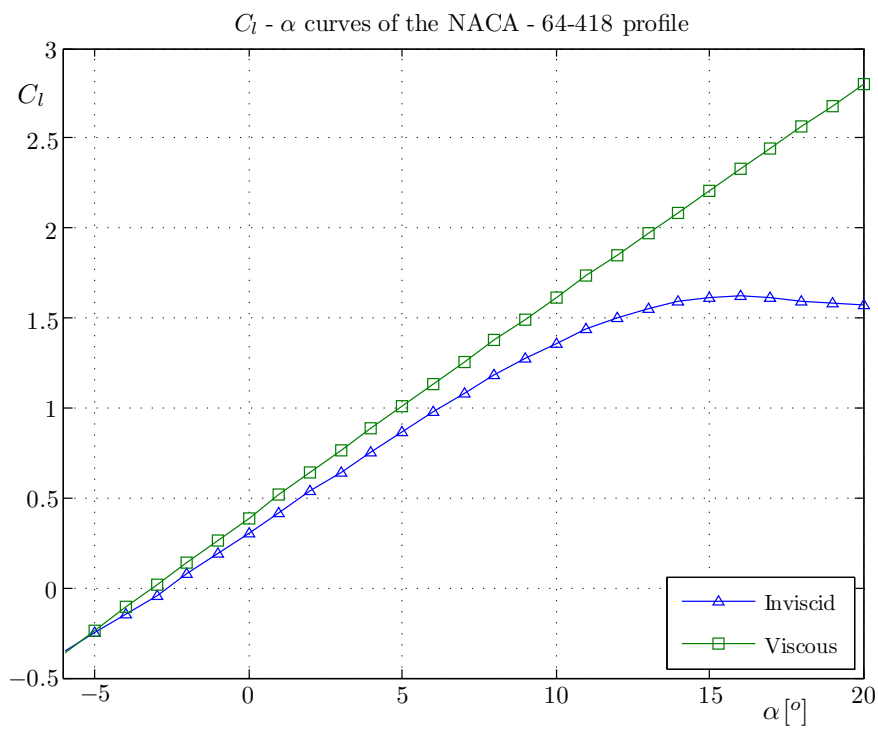


Figure D.12: The inviscid and viscous $C_l - \alpha$ curves obtained from Gaunaa et al. (2010) for the NACA - 64-418 profile used for the arc shaped kite where $Re = 6 \cdot 10^6$.

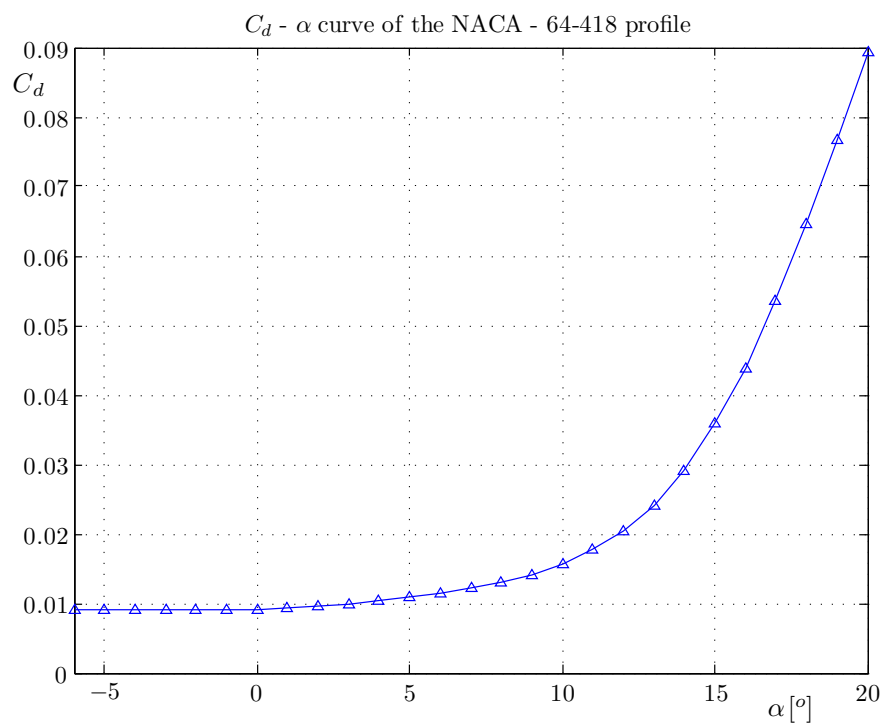


Figure D.13: The $C_d - \alpha$ curve obtained from Gaunaa et al. (2010) for the NACA - 64-418 profile used for the arc shaped kite where $Re = 6 \cdot 10^6$.

VLM/3D panel method validation

This appendix contains the simulation results of each validation case performed with 4 different versions of the adapted XFLR5 program. A trade-off procedure is performed on these results, as explained in section 5.3.

E.1 Flat wing

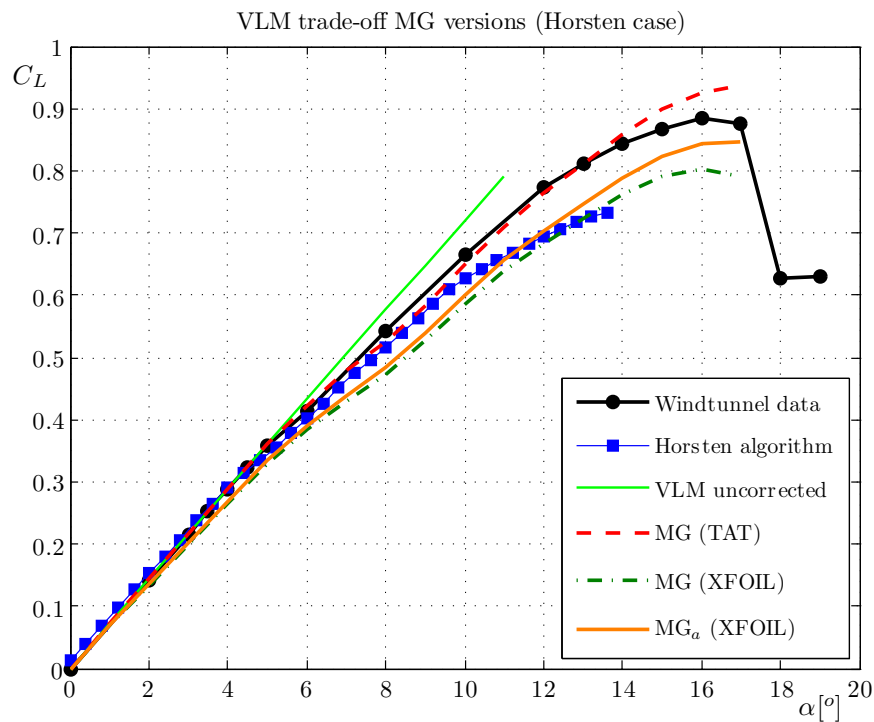


Figure E.1: The $C_L - \alpha$ curves obtained from windtunnel experiments and XFLR5 simulations (VLM MG versions) for the flat wing where $Re = 1.0 \cdot 10^6$.

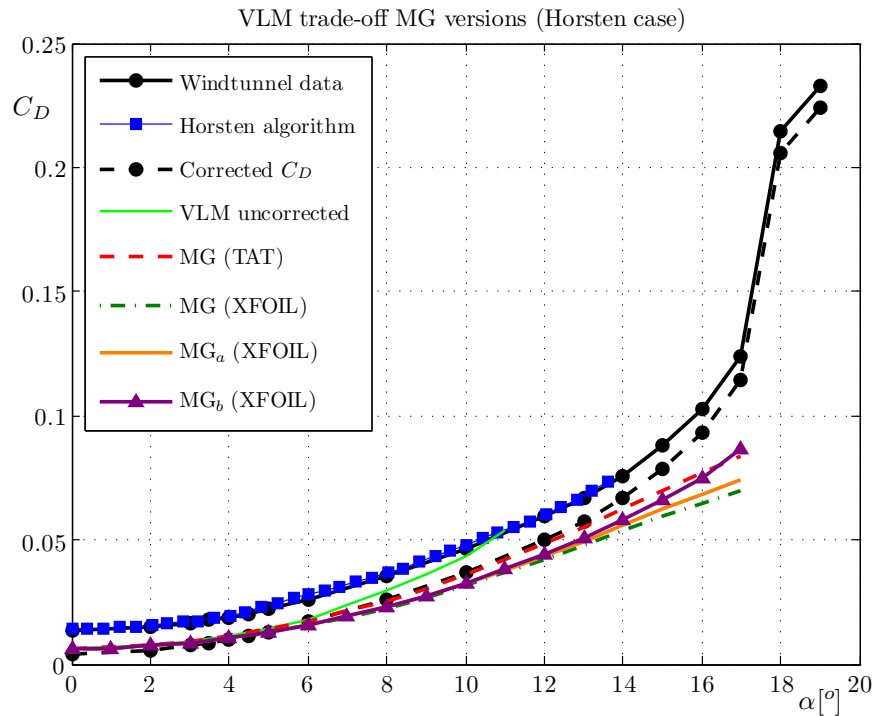


Figure E.2: The $C_D - \alpha$ curves obtained from windtunnel experiments and XFLR5 simulations (VLM MG versions) for the flat wing where $Re = 1.0 \cdot 10^6$.

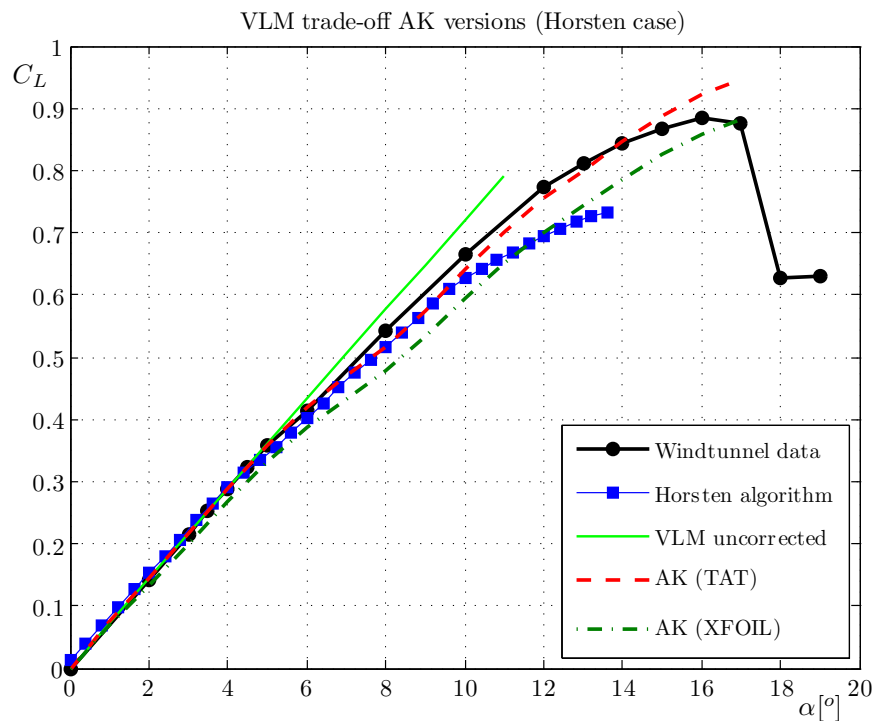


Figure E.3: The $C_L - \alpha$ curves obtained from windtunnel experiments and XFLR5 simulations (VLM AK versions) for the flat wing where $Re = 1.0 \cdot 10^6$.

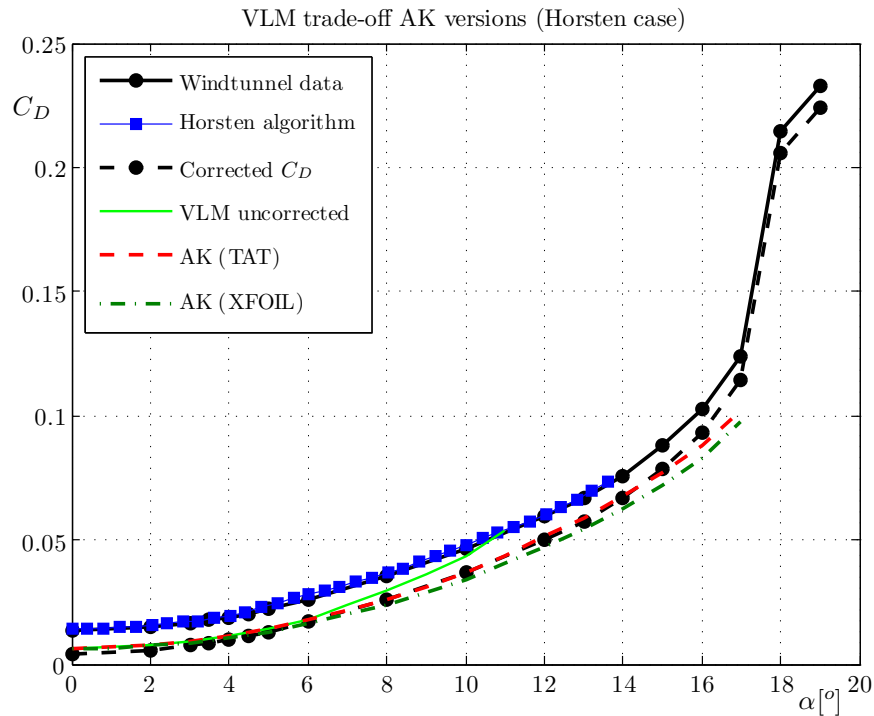


Figure E.4: The $C_D - \alpha$ curves obtained from windtunnel experiments and XFLR5 simulations (VLM AK versions) for the flat wing where $Re = 1.0 \cdot 10^6$.

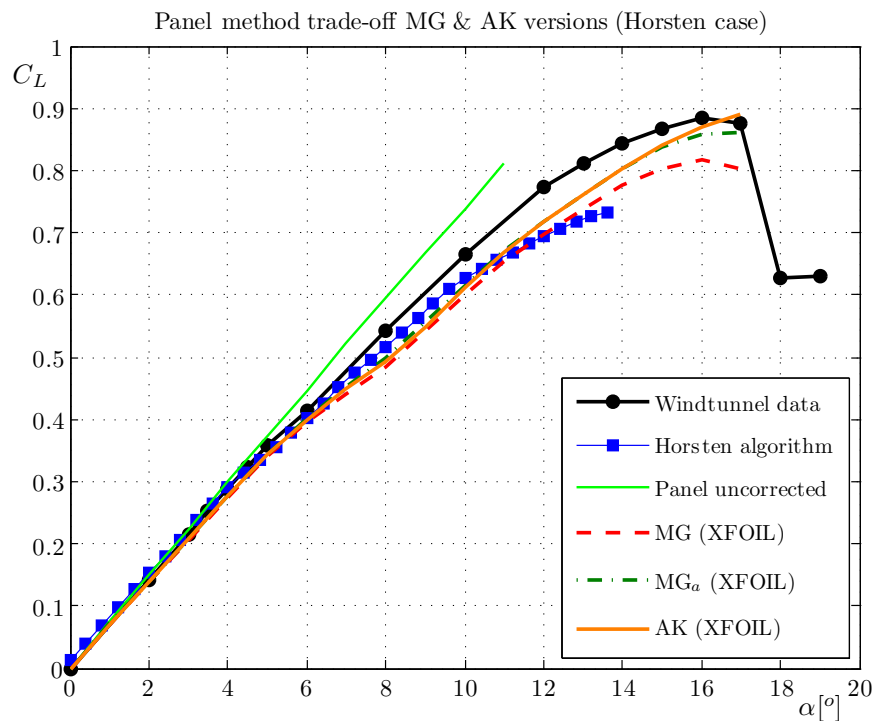


Figure E.5: The $C_L - \alpha$ curves obtained from windtunnel experiments and XFLR5 simulations (Panel versions) for the flat wing where $Re = 1.0 \cdot 10^6$.

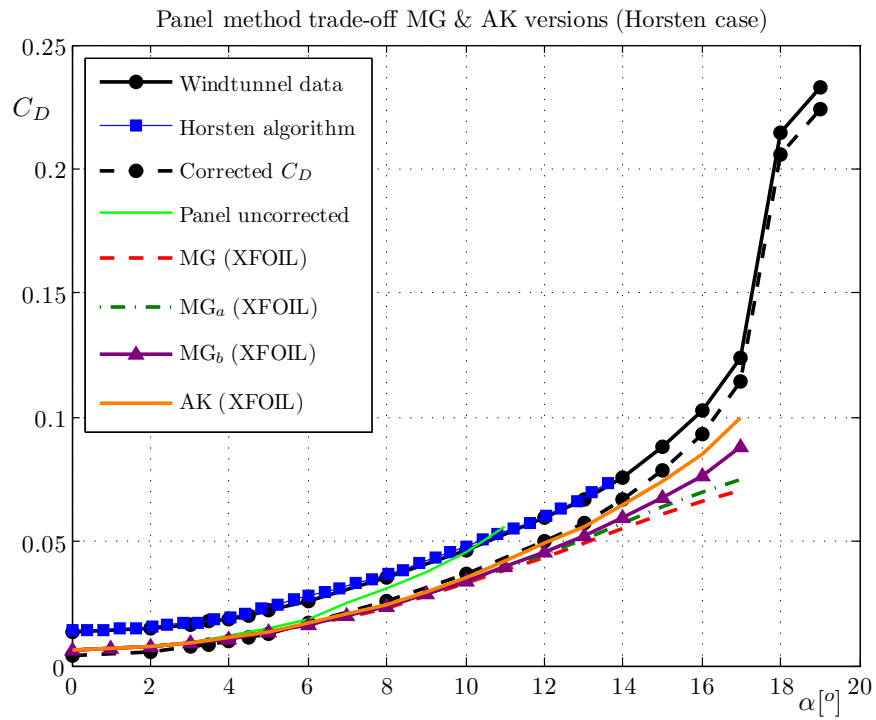


Figure E.6: The $C_D - \alpha$ curves obtained from windtunnel experiments and XFLR5 simulations (Panel method versions) for the flat wing where $Re = 1.0 \cdot 10^6$.

E.2 Swept wing AR5_012

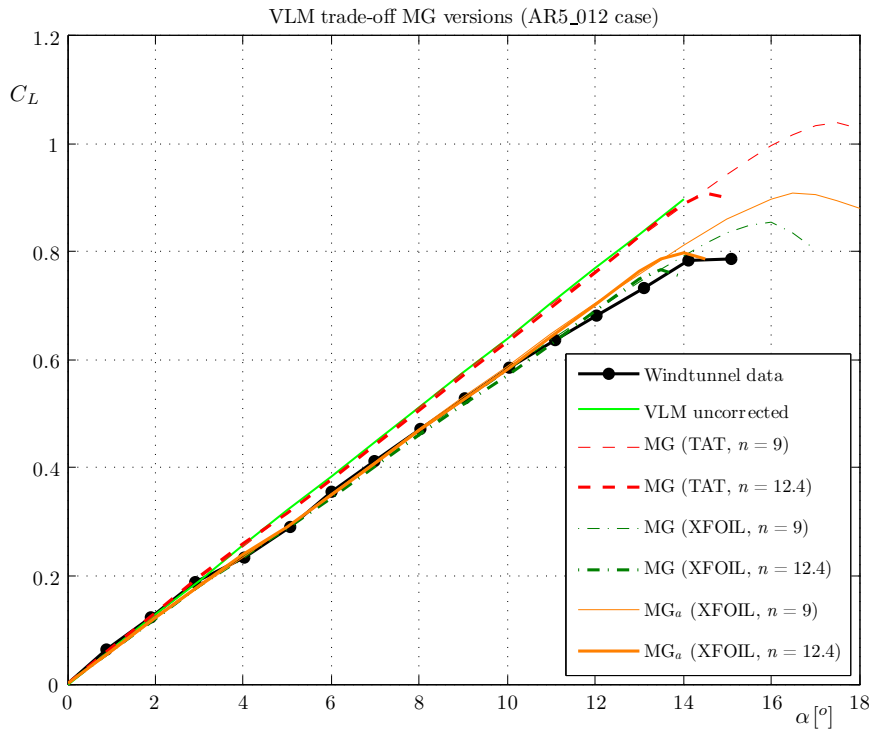


Figure E.7: The $C_L - \alpha$ curves obtained from windtunnel experiments and XFLR5 simulations (VLM MG versions) for the AR5_012 wing where $Re = 2.0 \cdot 10^6$.

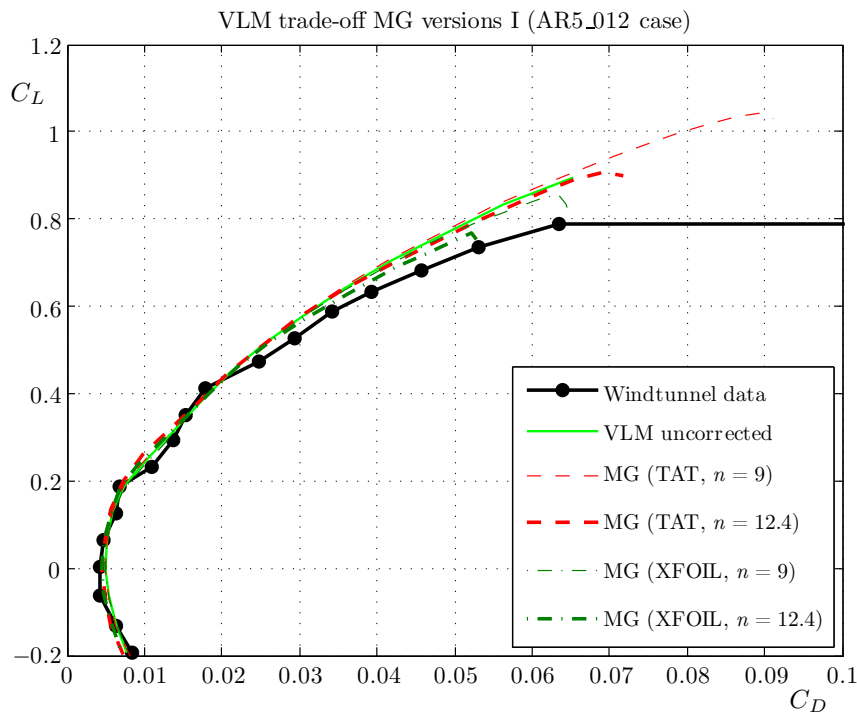


Figure E.8: The $C_L - C_D$ curves obtained from windtunnel experiments and XFLR5 simulations (VLM MG versions) for the AR5_012 wing where $Re = 2.0 \cdot 10^6$.

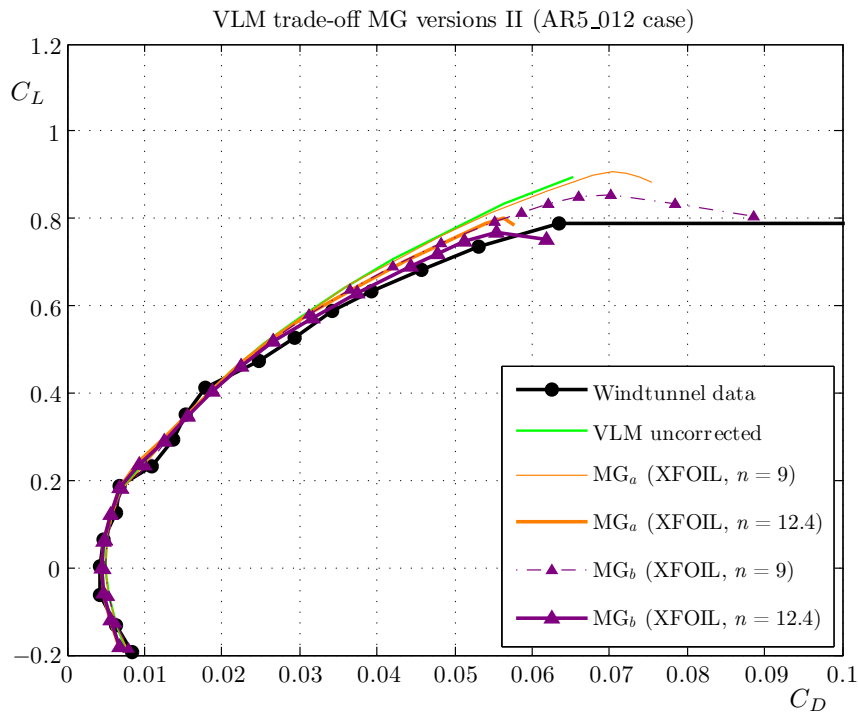


Figure E.9: The $C_L - C_D$ curves obtained from windtunnel experiments and XFLR5 simulations (VLM MG versions) for the AR5_012 wing where $Re = 2.0 \cdot 10^6$.

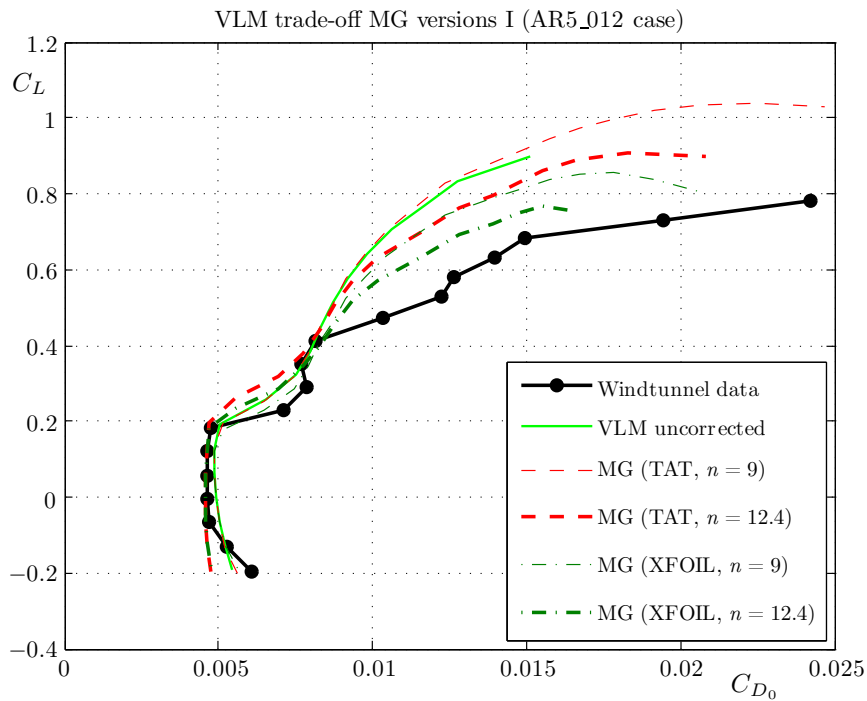


Figure E.10: The $C_L - C_{D_0}$ curves obtained from windtunnel experiments and XFLR5 simulations (VLM MG versions) for the AR5_012 wing where $Re = 2.0 \cdot 10^6$.

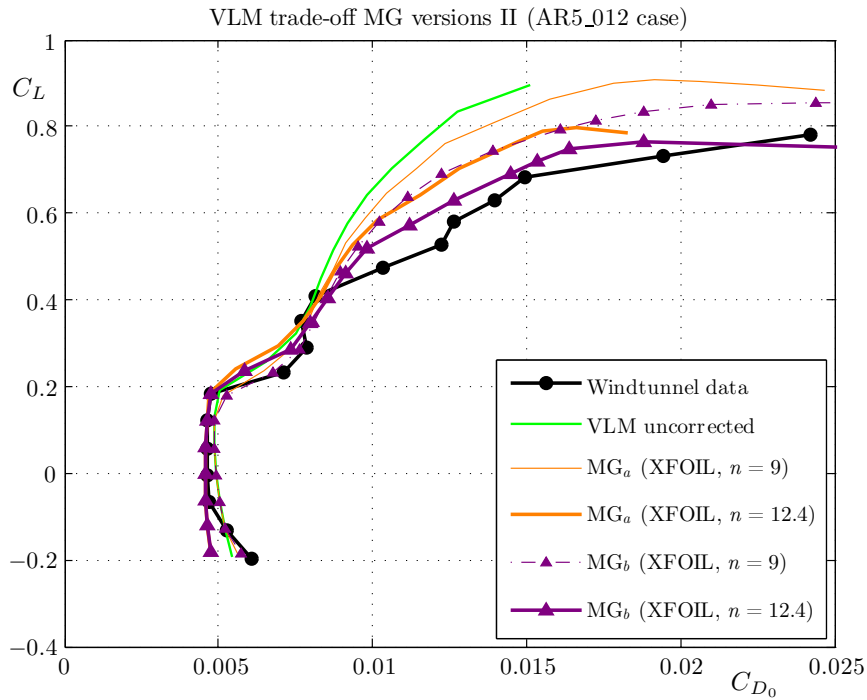


Figure E.11: The $C_L - C_{D_0}$ curves obtained from windtunnel experiments and XFLR5 simulations (VLM MG versions) for the AR5_012 wing where $Re = 2.0 \cdot 10^6$.

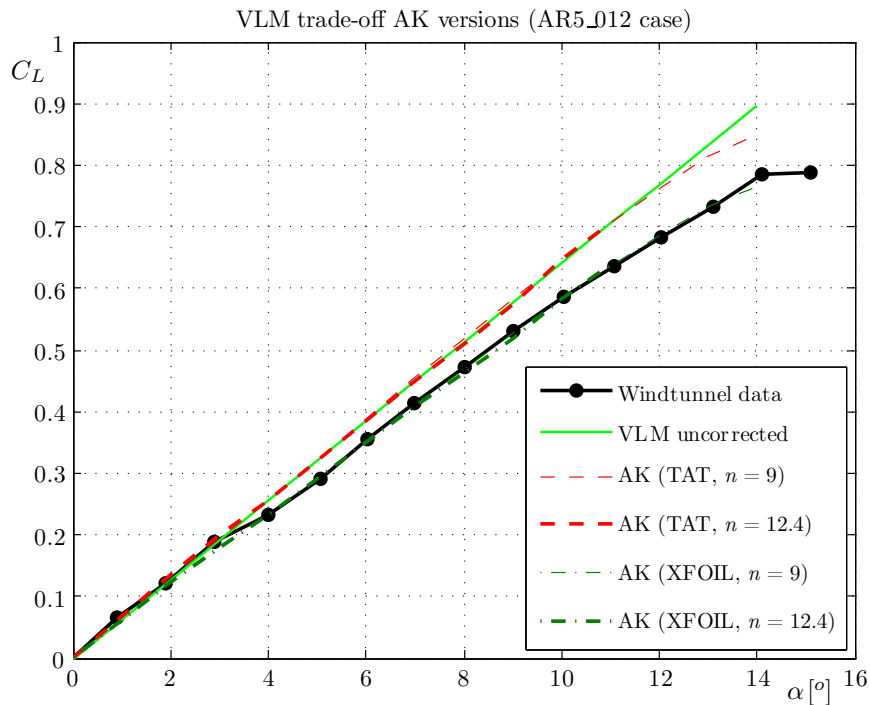


Figure E.12: The $C_L - \alpha$ curves obtained from windtunnel experiments and XFLR5 simulations (VLM AK versions) for the AR5_012 wing where $Re = 2.0 \cdot 10^6$.

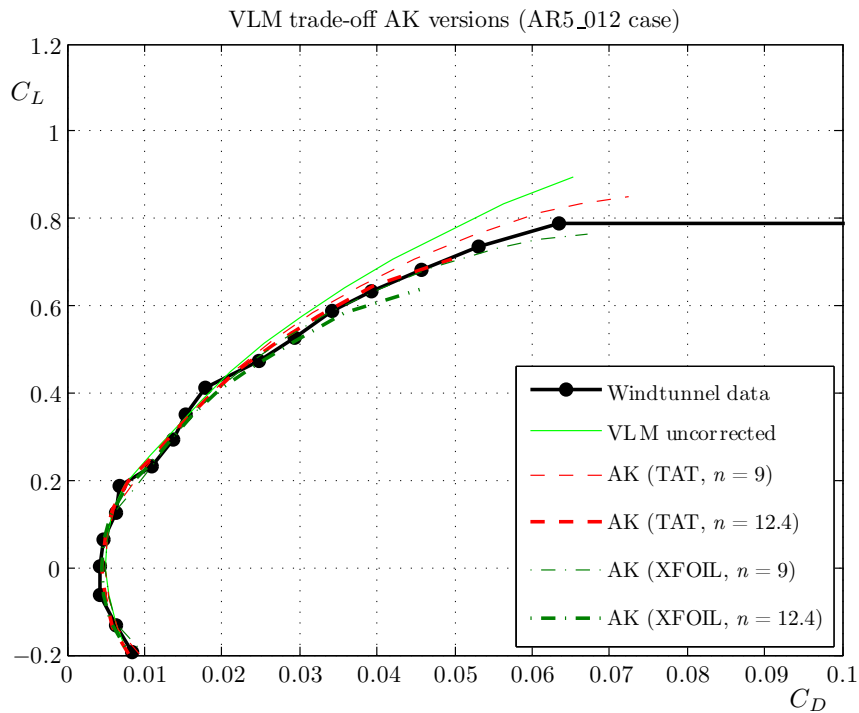


Figure E.13: The $C_L - C_D$ curves obtained from windtunnel experiments and XFLR5 simulations (VLM AK versions) for the AR5_012 wing where $Re = 2.0 \cdot 10^6$.

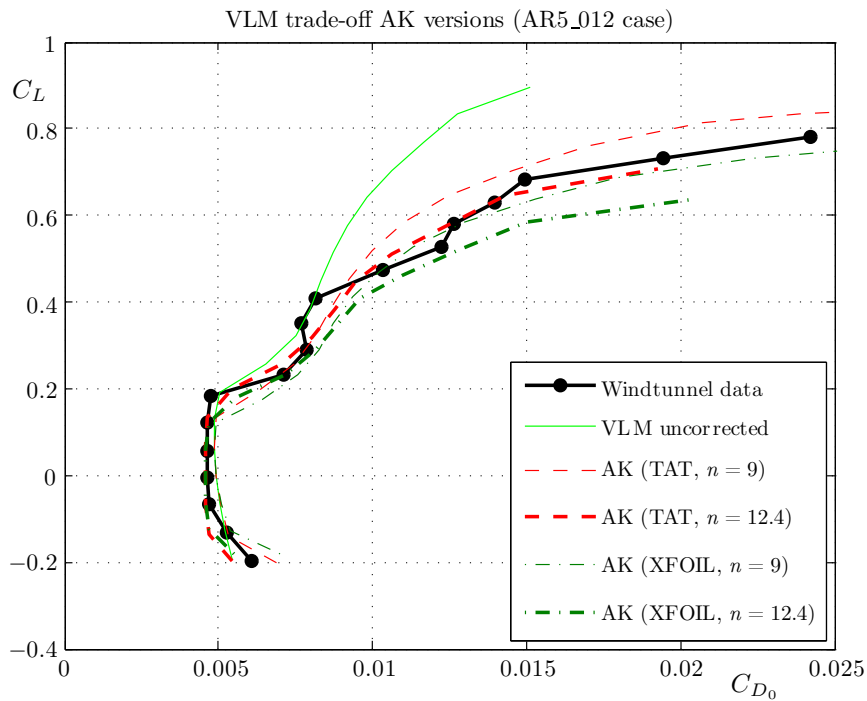


Figure E.14: The $C_L - C_{D_0}$ curves obtained from windtunnel experiments and XFLR5 simulations (VLM AK versions) for the AR5_012 wing where $Re = 2.0 \cdot 10^6$.

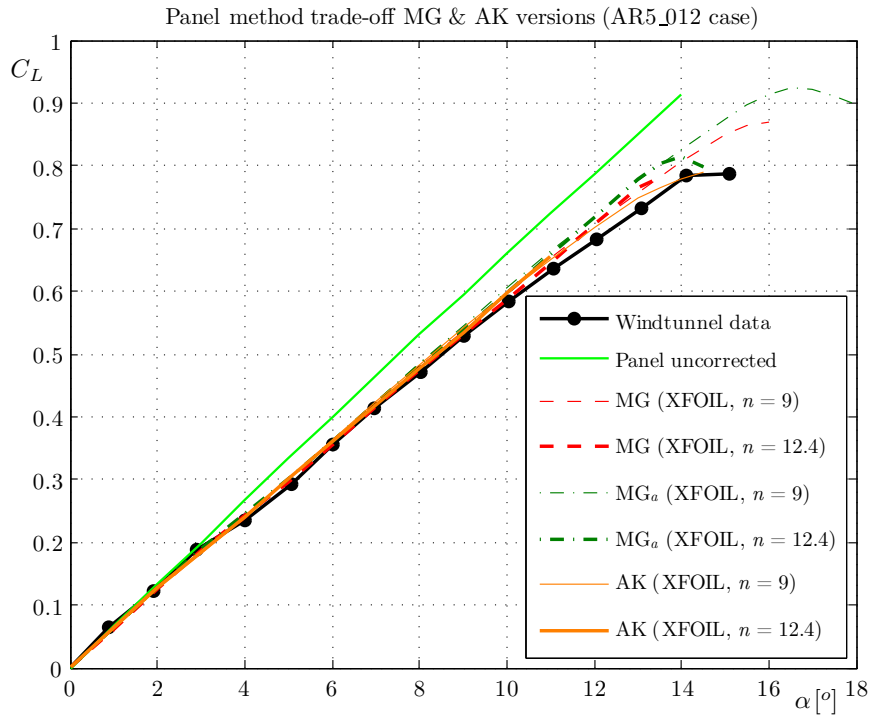


Figure E.15: The $C_L - \alpha$ curves obtained from windtunnel experiments and XFLR5 simulations (Panel method versions) for the AR5_012 wing where $Re = 2.0 \cdot 10^6$.

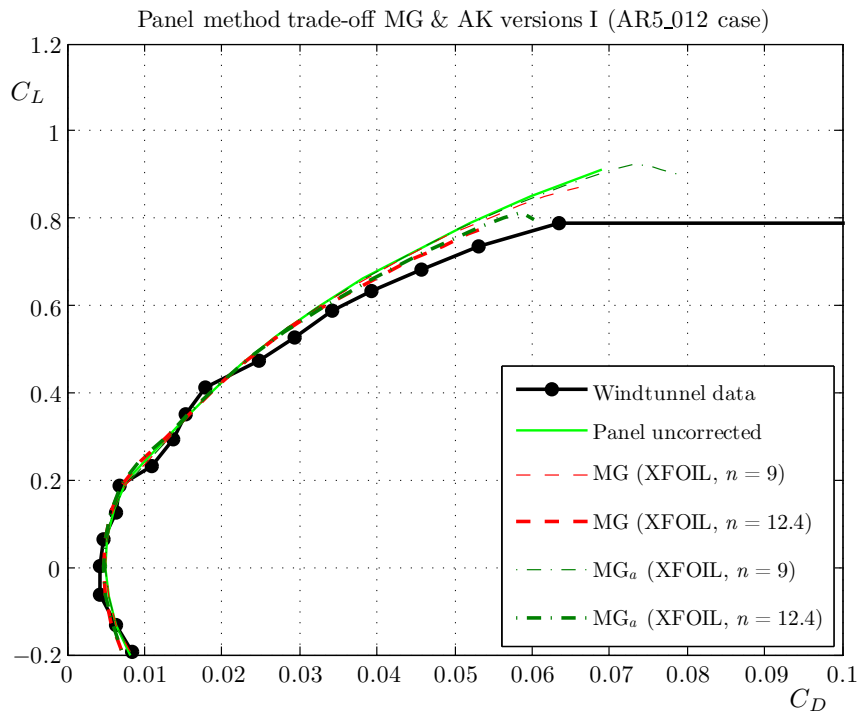


Figure E.16: The $C_L - C_D$ curves obtained from windtunnel experiments and XFLR5 simulations (Panel method versions) for the AR5_012 wing where $Re = 2.0 \cdot 10^6$.

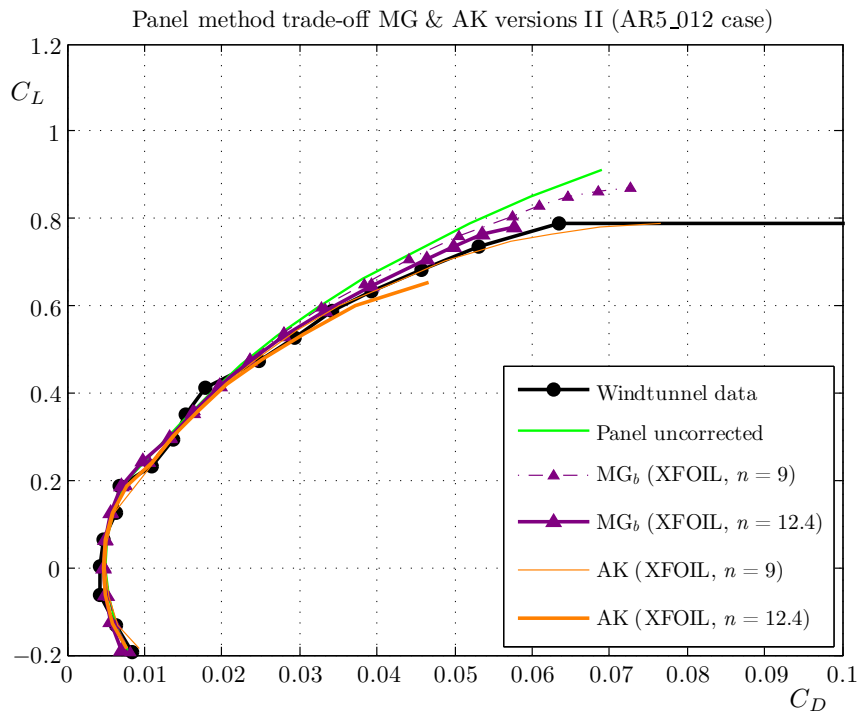


Figure E.17: The $C_L - C_D$ curves obtained from windtunnel experiments and XFLR5 simulations (Panel method versions) for the AR5_012 wing where $Re = 2.0 \cdot 10^6$.

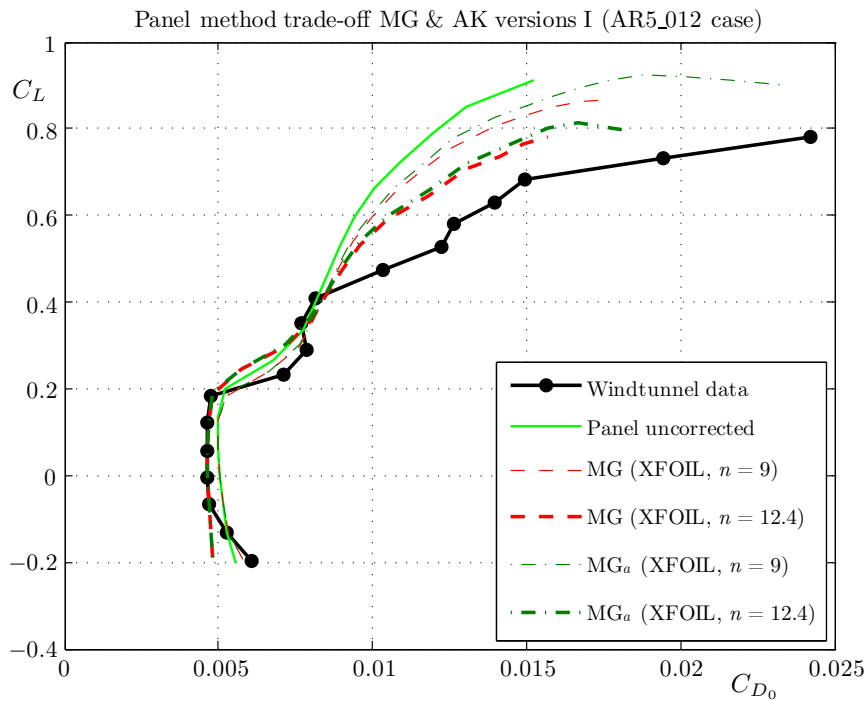


Figure E.18: The $C_L - C_{D_0}$ curves obtained from windtunnel experiments and XFLR5 simulations (Panel method versions) for the AR5_012 wing where $Re = 2.0 \cdot 10^6$.

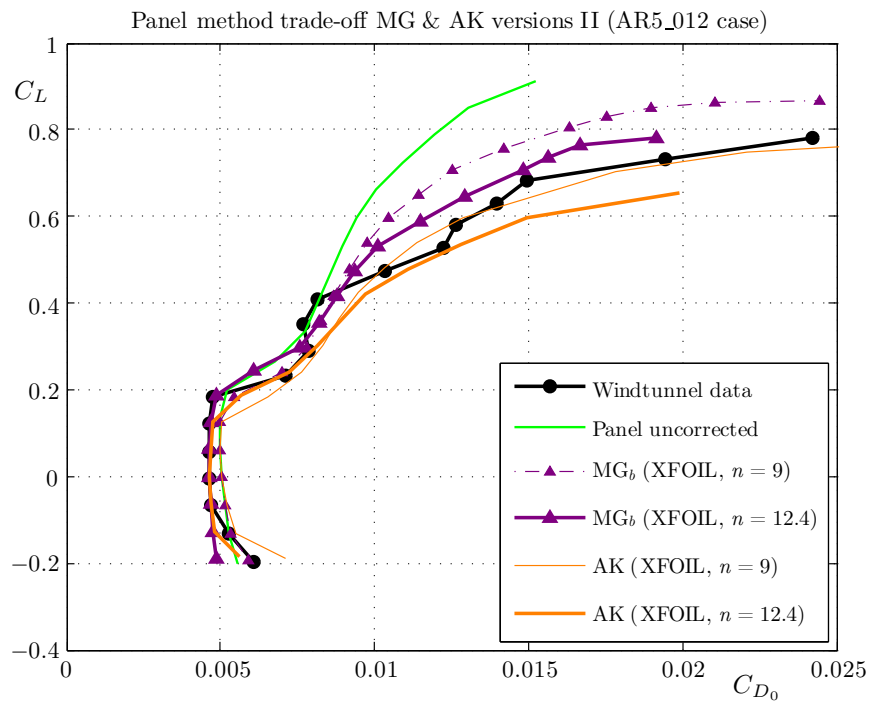


Figure E.19: The $C_L - C_{D_0}$ curves obtained from windtunnel experiments and XFLR5 simulations (Panel method versions) for the AR5_012 wing where $Re = 2.0 \cdot 10^6$.

E.3 Swept wing AR5_612

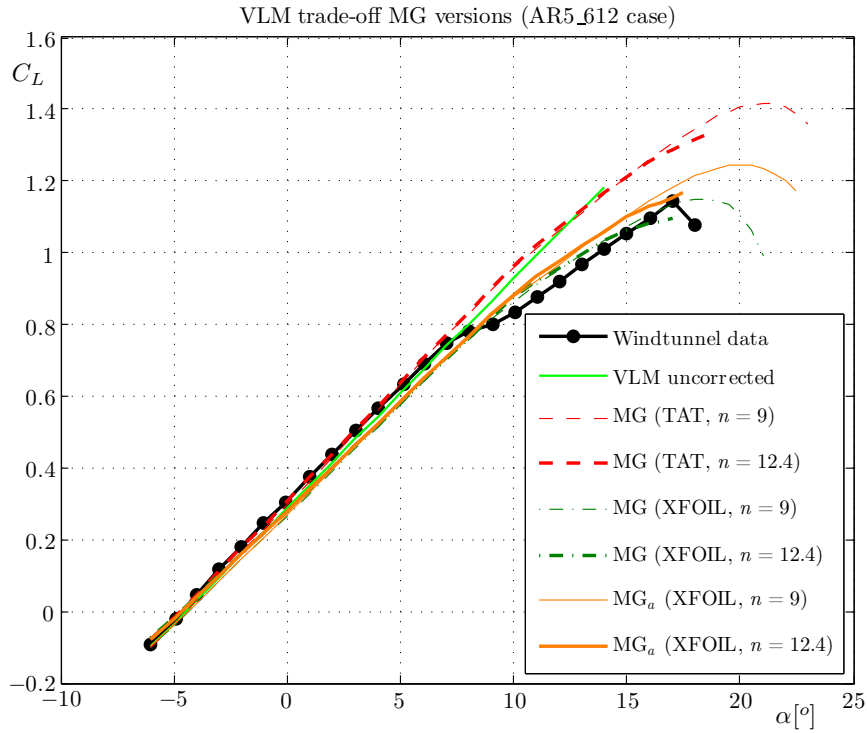


Figure E.20: The $C_L - \alpha$ curves obtained from windtunnel experiments and XFLR5 simulations (VLM MG versions) for the AR5_612 wing where $Re = 2.0 \cdot 10^6$.

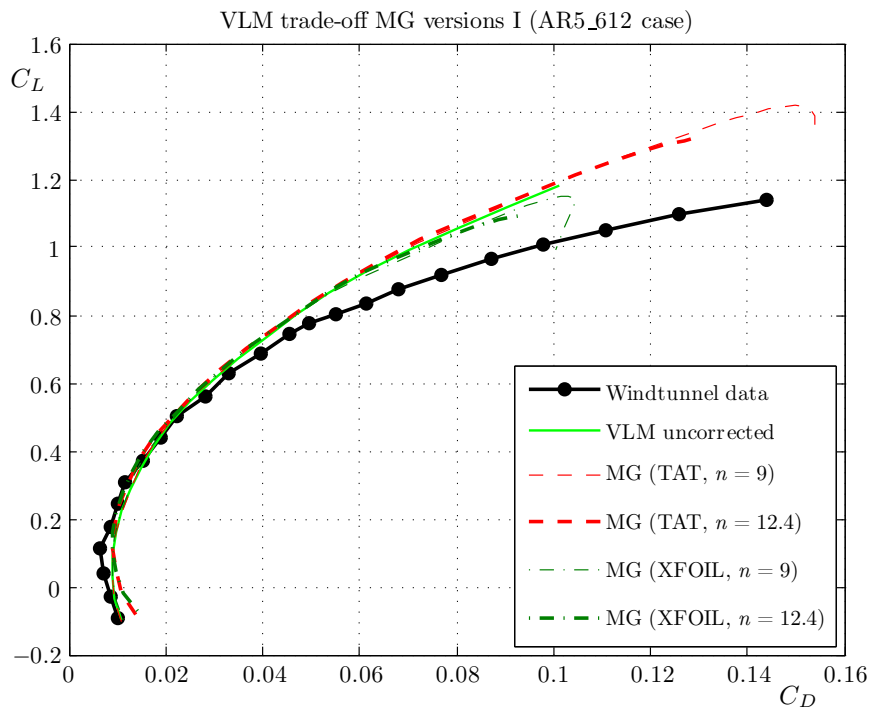


Figure E.21: The $C_L - C_D$ curves obtained from windtunnel experiments and XFLR5 simulations (VLM MG versions) for the AR5_612 wing where $Re = 2.0 \cdot 10^6$.

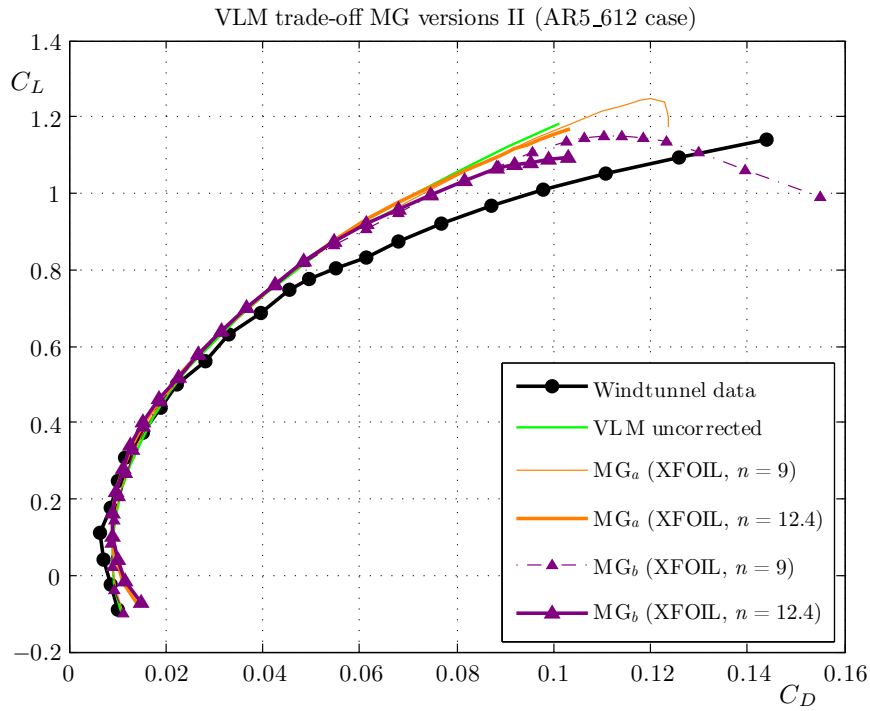


Figure E.22: The $C_L - C_D$ curves obtained from windtunnel experiments and XFLR5 simulations (VLM MG versions) for the AR5_612 wing where $Re = 2.0 \cdot 10^6$.

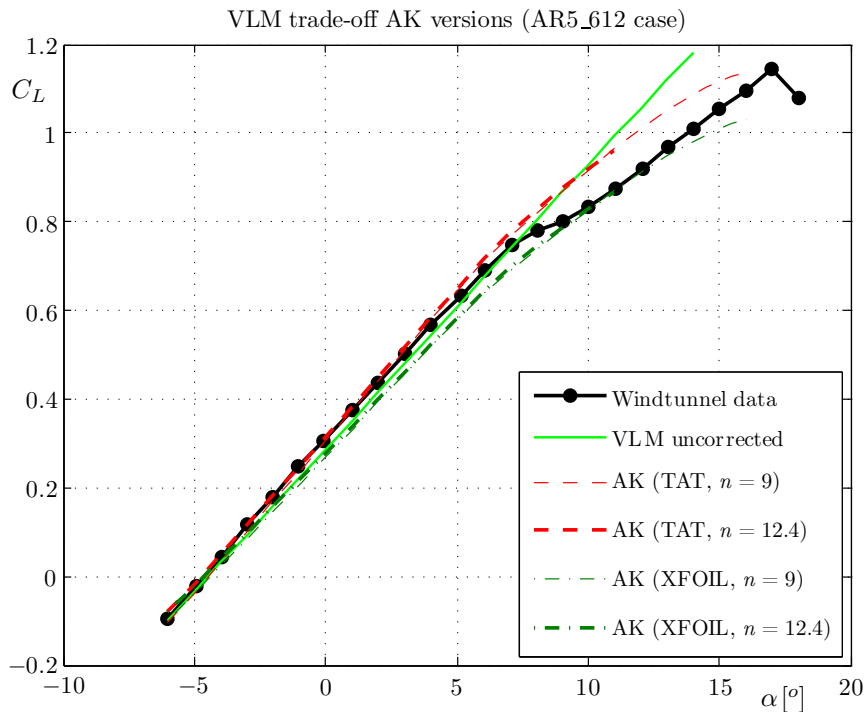


Figure E.23: The $C_L - \alpha$ curves obtained from windtunnel experiments and XFLR5 simulations (VLM AK versions) for the AR5_612 wing where $Re = 2.0 \cdot 10^6$.

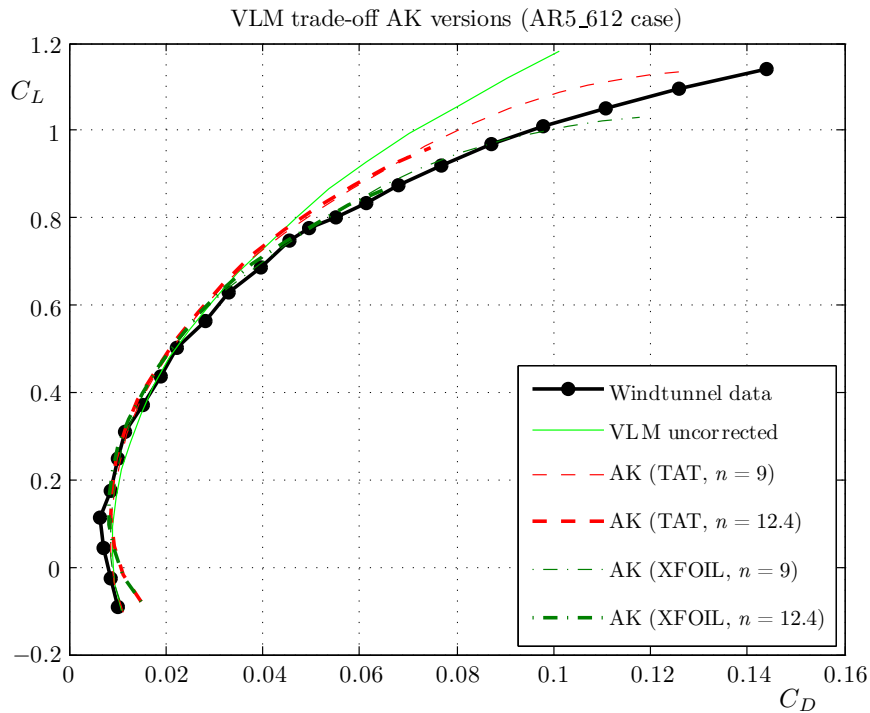


Figure E.24: The $C_L - C_D$ curves obtained from windtunnel experiments and XFLR5 simulations (VLM AK versions) for the AR5_612 wing where $Re = 2.0 \cdot 10^6$.

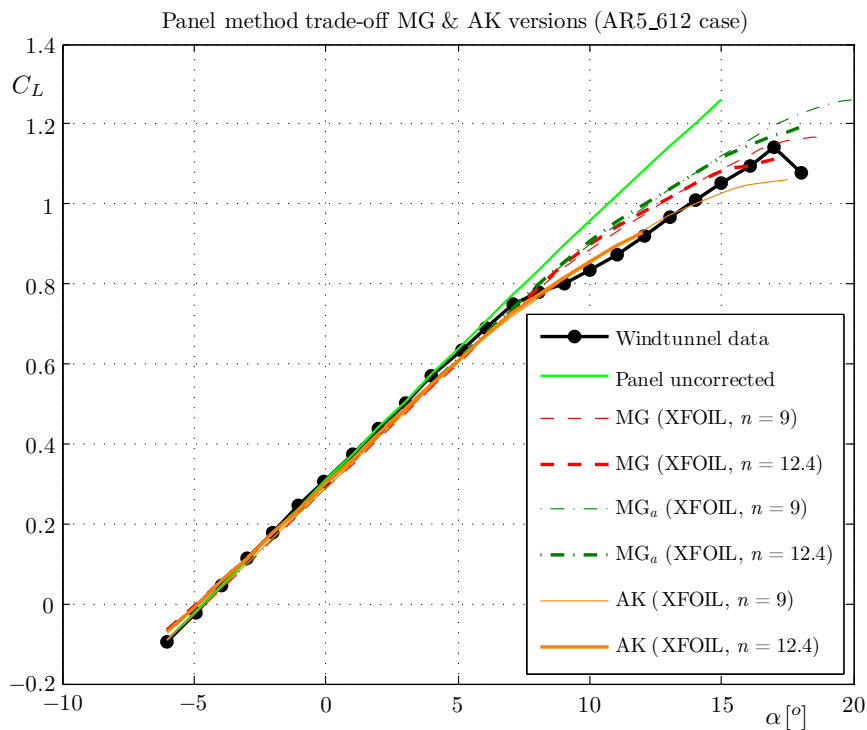


Figure E.25: The $C_L - \alpha$ curves obtained from windtunnel experiments and XFLR5 simulations (Panel method versions) for the AR5_612 wing where $Re = 2.0 \cdot 10^6$.

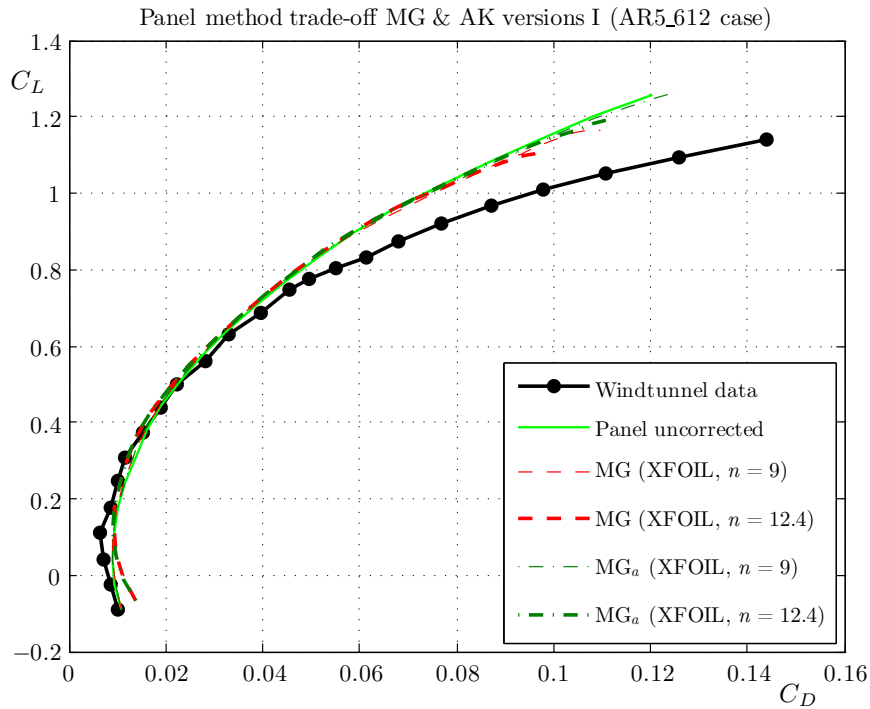


Figure E.26: The $C_L - C_D$ curves obtained from windtunnel experiments and XFLR5 simulations (Panel method versions) for the AR5_612 wing where $Re = 2.0 \cdot 10^6$.

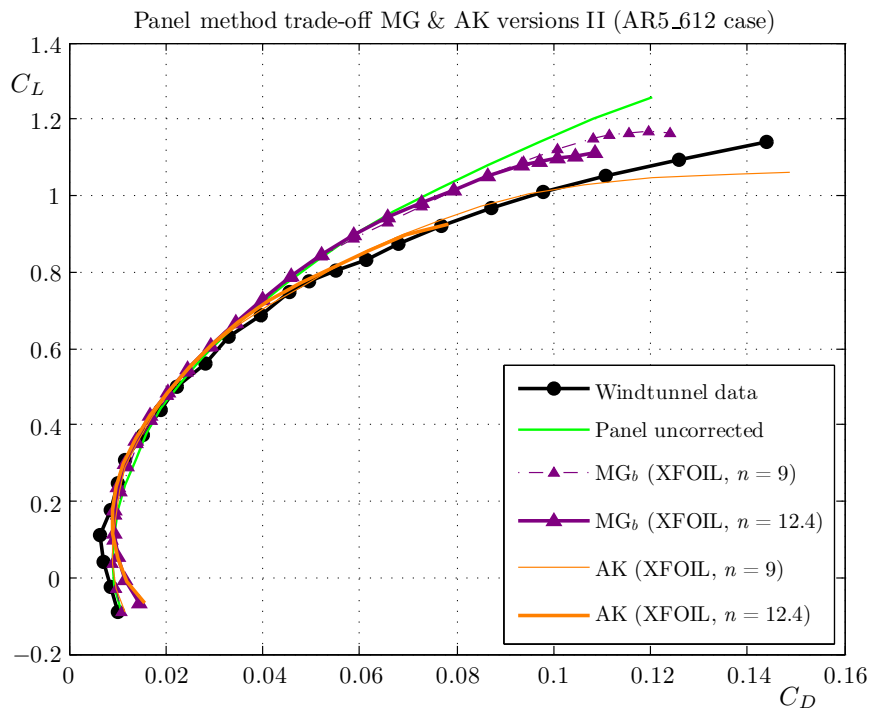


Figure E.27: The $C_L - C_D$ curves obtained from windtunnel experiments and XFLR5 simulations (Panel method versions) for the AR5_612 wing where $Re = 2.0 \cdot 10^6$.

E.4 Swept wing AR10_012

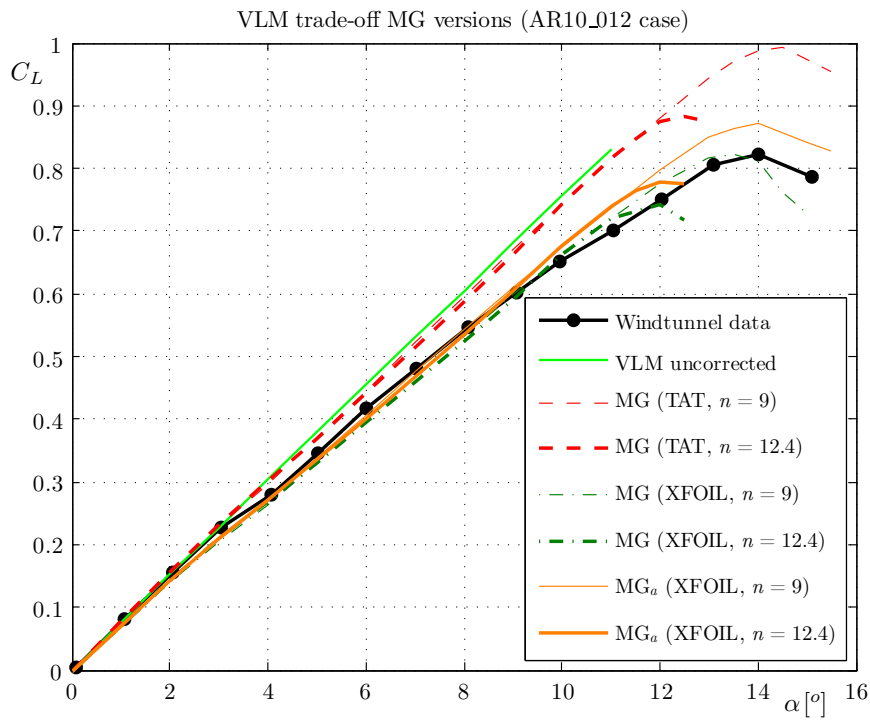


Figure E.28: The $C_L - \alpha$ curves obtained from windtunnel experiments and XFLR5 simulations (VLM MG versions) for the AR10_012 wing where $Re = 2.0 \cdot 10^6$.

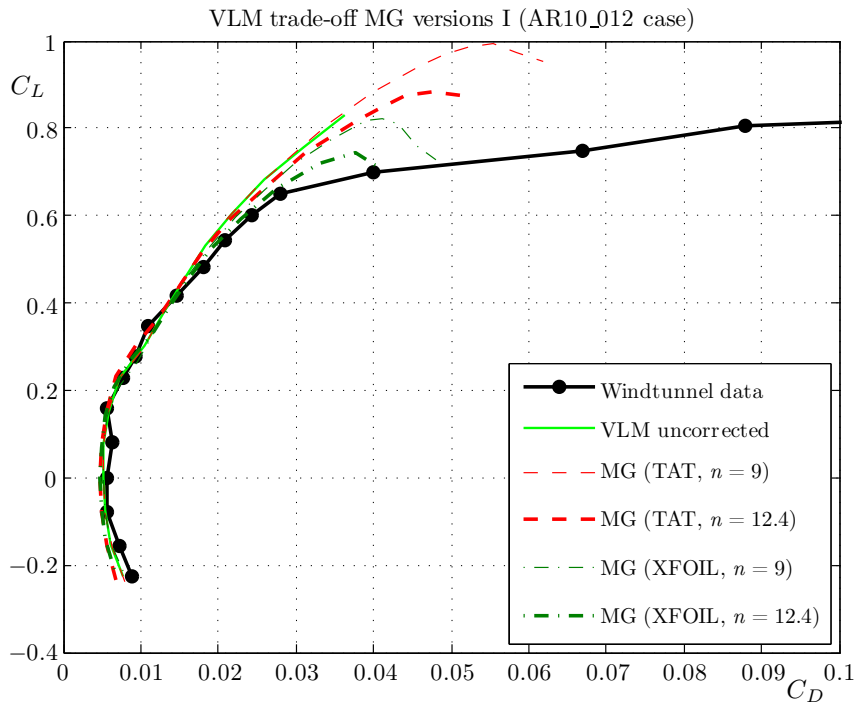


Figure E.29: The $C_L - C_D$ curves obtained from windtunnel experiments and XFLR5 simulations (VLM MG versions) for the AR10_012 wing where $Re = 2.0 \cdot 10^6$.

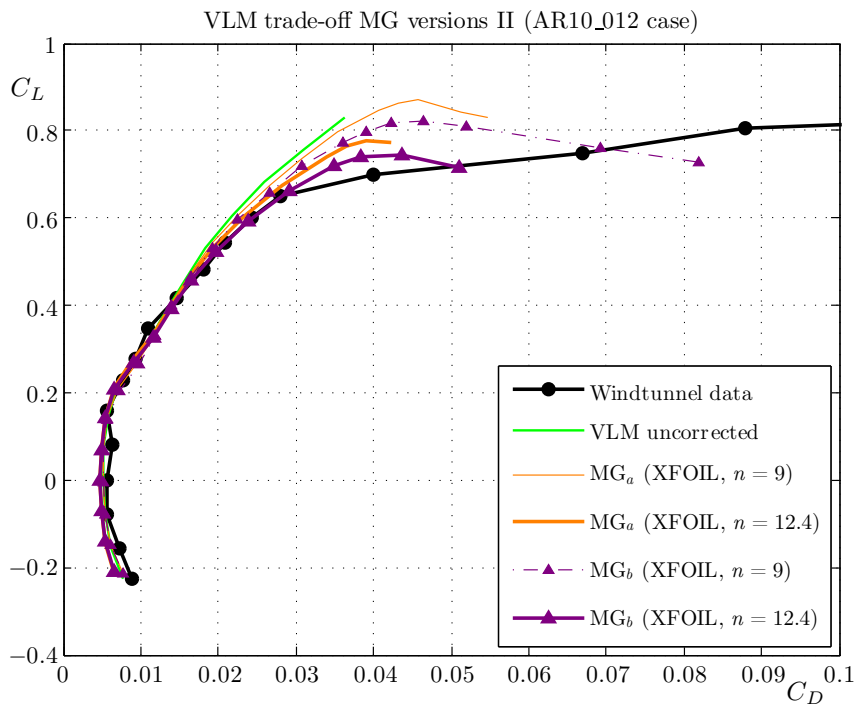


Figure E.30: The $C_L - C_D$ curves obtained from windtunnel experiments and XFLR5 simulations (VLM MG versions) for the AR10_012 wing where $Re = 2.0 \cdot 10^6$.

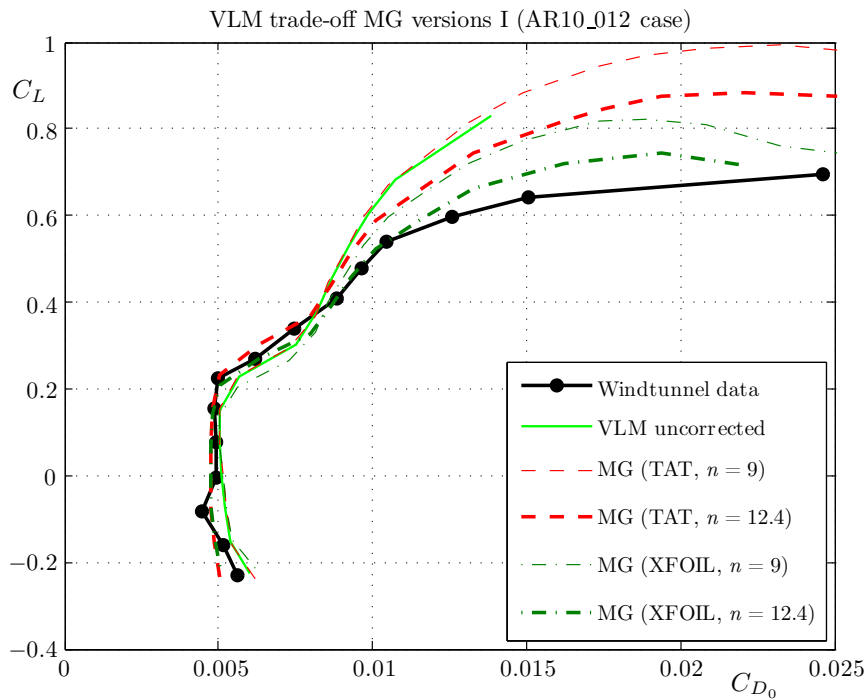


Figure E.31: The $C_L - C_{D_0}$ curves obtained from windtunnel experiments and XFLR5 simulations (VLM MG versions) for the AR10_012 wing where $Re = 2.0 \cdot 10^6$.

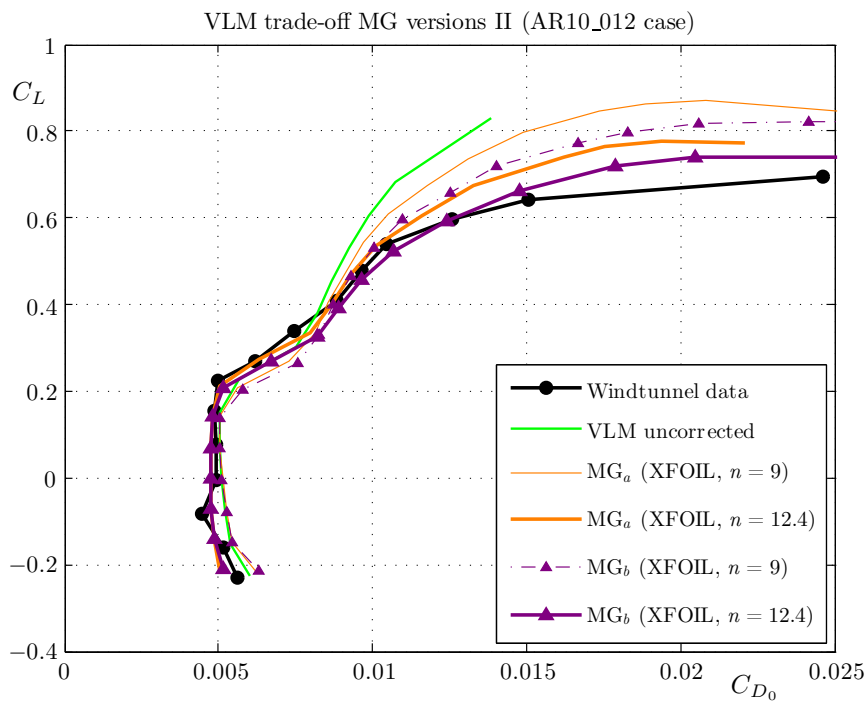


Figure E.32: The $C_L - C_{D_0}$ curves obtained from windtunnel experiments and XFLR5 simulations (VLM MG versions) for the AR10_012 wing where $Re = 2.0 \cdot 10^6$.

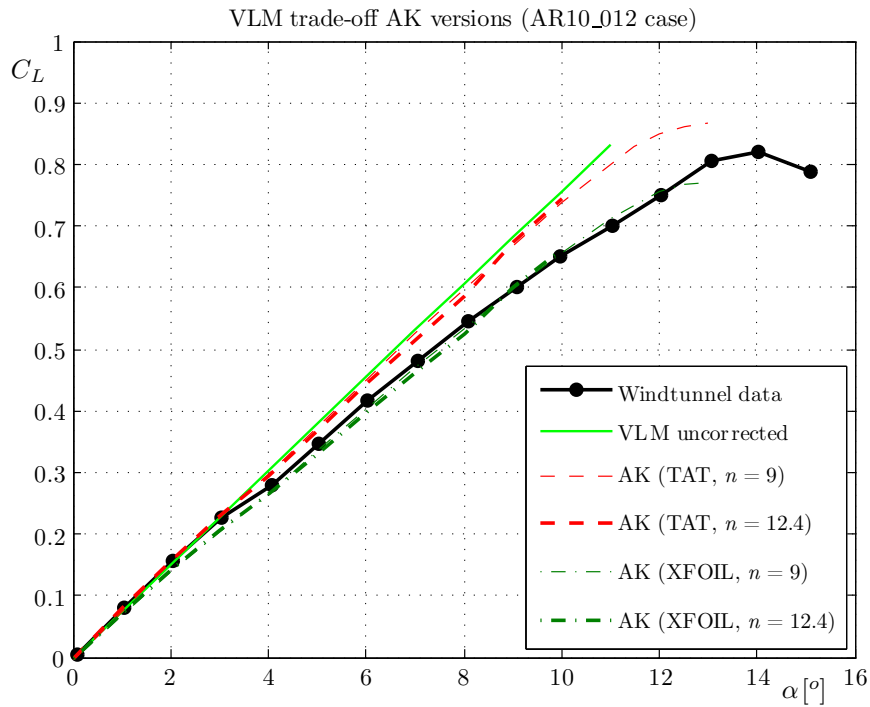


Figure E.33: The $C_L - \alpha$ curves obtained from windtunnel experiments and XFLR5 simulations (VLM AK versions) for the AR10_012 wing where $Re = 2.0 \cdot 10^6$.

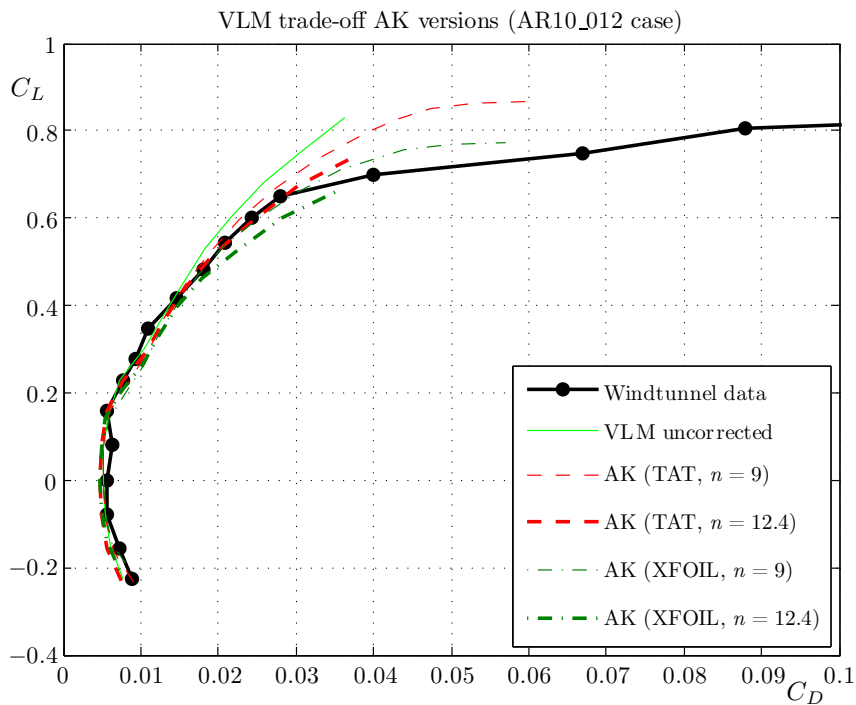


Figure E.34: The $C_L - C_D$ curves obtained from windtunnel experiments and XFLR5 simulations (VLM AK versions) for the AR10_012 wing where $Re = 2.0 \cdot 10^6$.

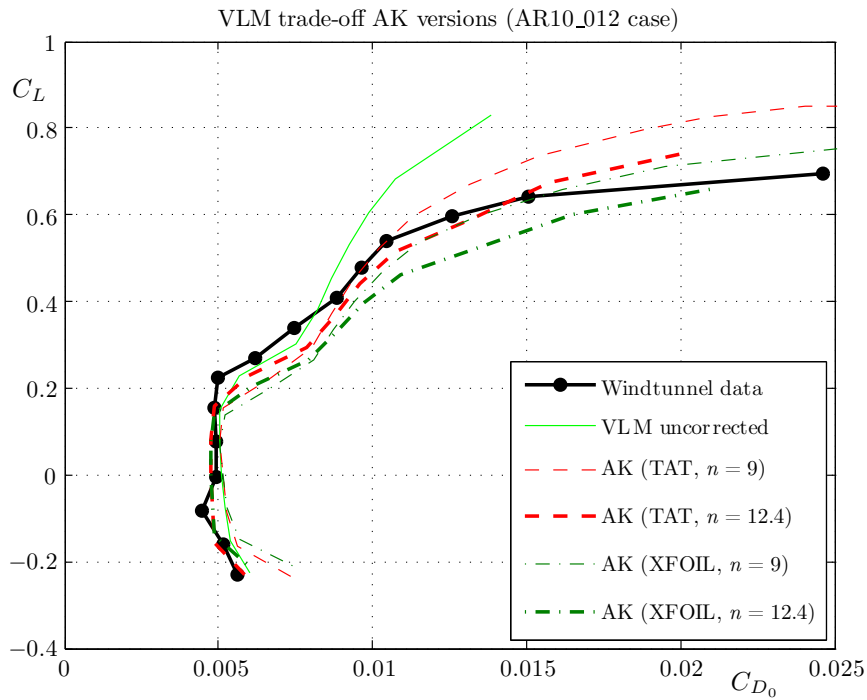


Figure E.35: The $C_L - C_{D_0}$ curves obtained from windtunnel experiments and XFLR5 simulations (VLM AK versions) for the AR10_012 wing where $Re = 2.0 \cdot 10^6$.

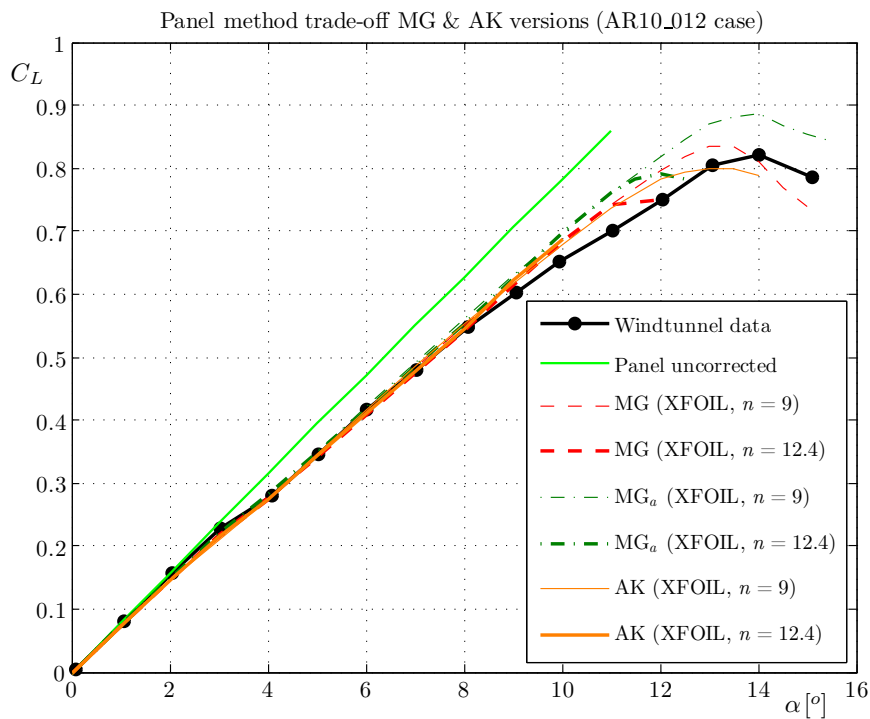


Figure E.36: The $C_L - \alpha$ curves obtained from windtunnel experiments and XFLR5 simulations (Panel method versions) for the AR10_012 wing where $Re = 2.0 \cdot 10^6$.

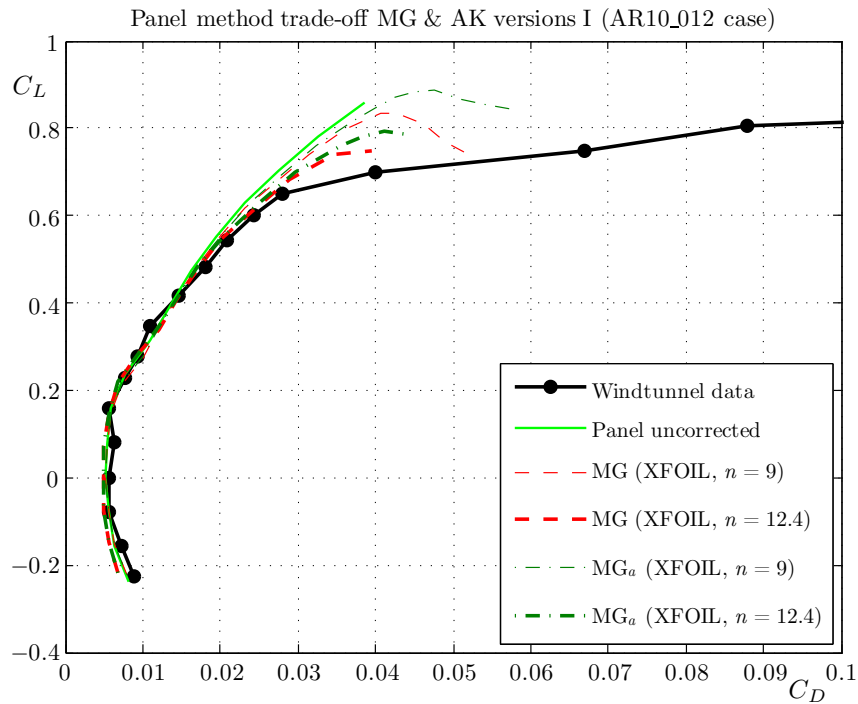


Figure E.37: The $C_L - C_D$ curves obtained from windtunnel experiments and XFLR5 simulations (Panel method versions) for the AR10_012 wing where $Re = 2.0 \cdot 10^6$.

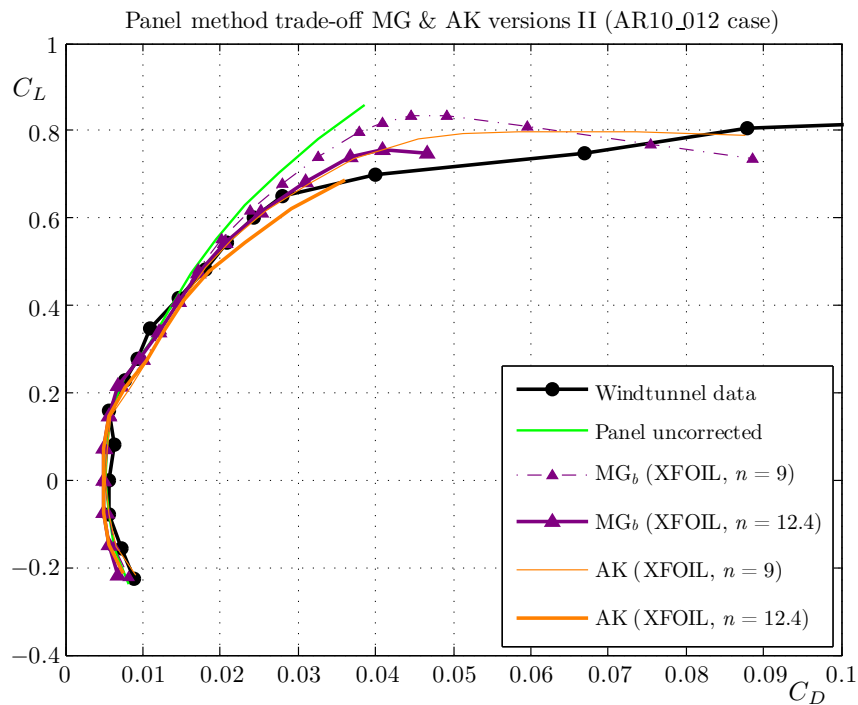


Figure E.38: The $C_L - C_D$ curves obtained from windtunnel experiments and XFLR5 simulations (Panel method versions) for the AR10_012 wing where $Re = 2.0 \cdot 10^6$.

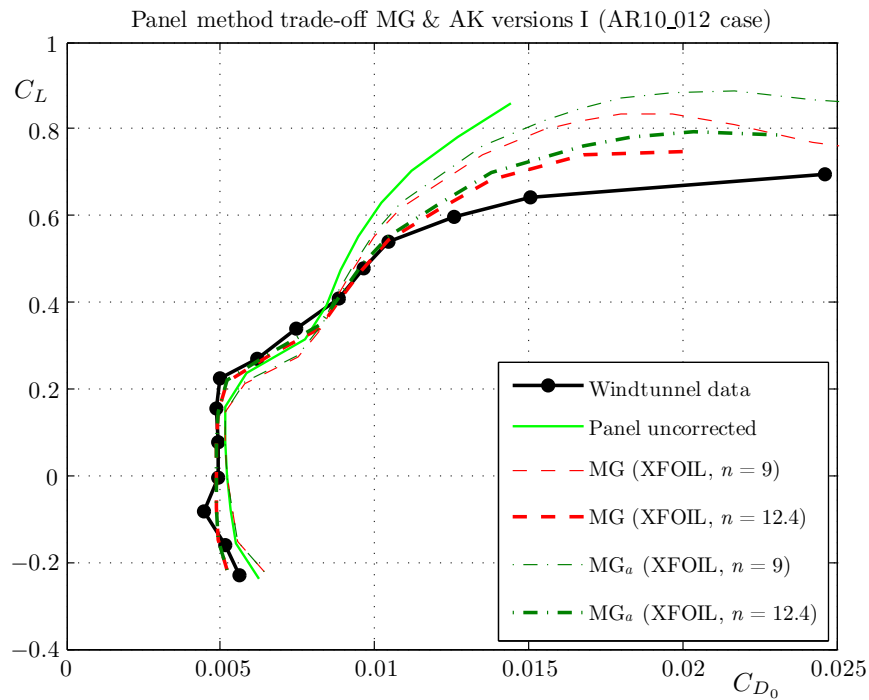


Figure E.39: The $C_L - C_{D_0}$ curves obtained from windtunnel experiments and XFLR5 simulations (Panel method versions) for the AR10_012 wing where $Re = 2.0 \cdot 10^6$.

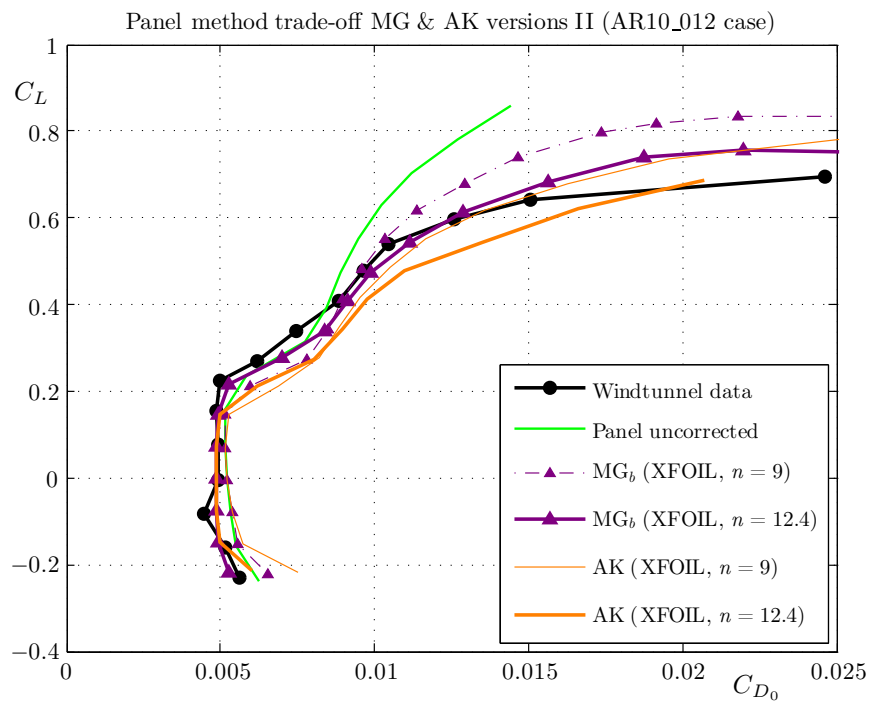


Figure E.40: The $C_L - C_{D_0}$ curves obtained from windtunnel experiments and XFLR5 simulations (Panel method versions) for the AR10_012 wing where $Re = 2.0 \cdot 10^6$.

E.5 Swept wing AR10_612

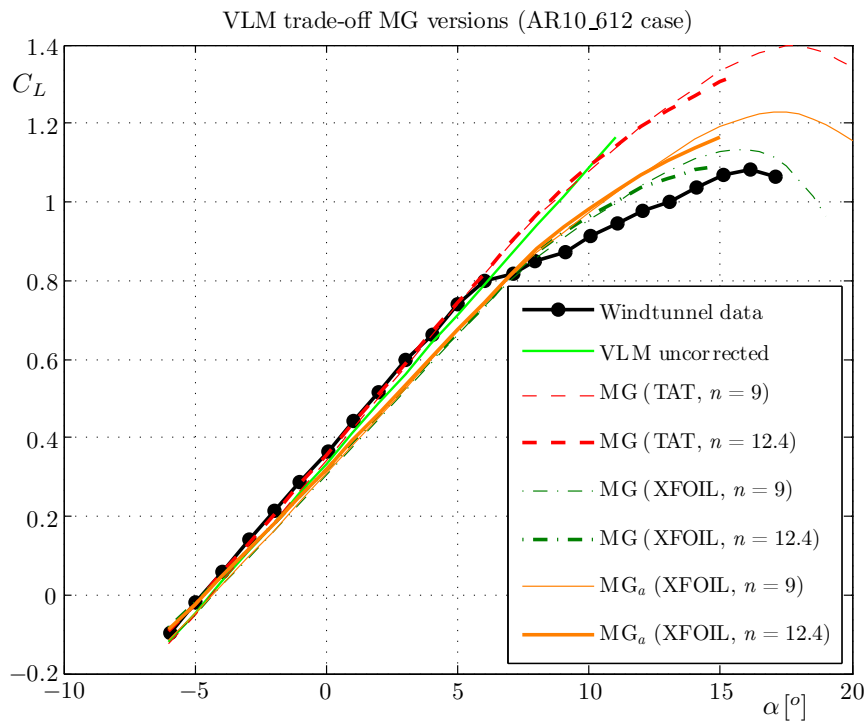


Figure E.41: The $C_L - \alpha$ curves obtained from windtunnel experiments and XFLR5 simulations (VLM MG versions) for the AR10_612 wing where $Re = 2.0 \cdot 10^6$.

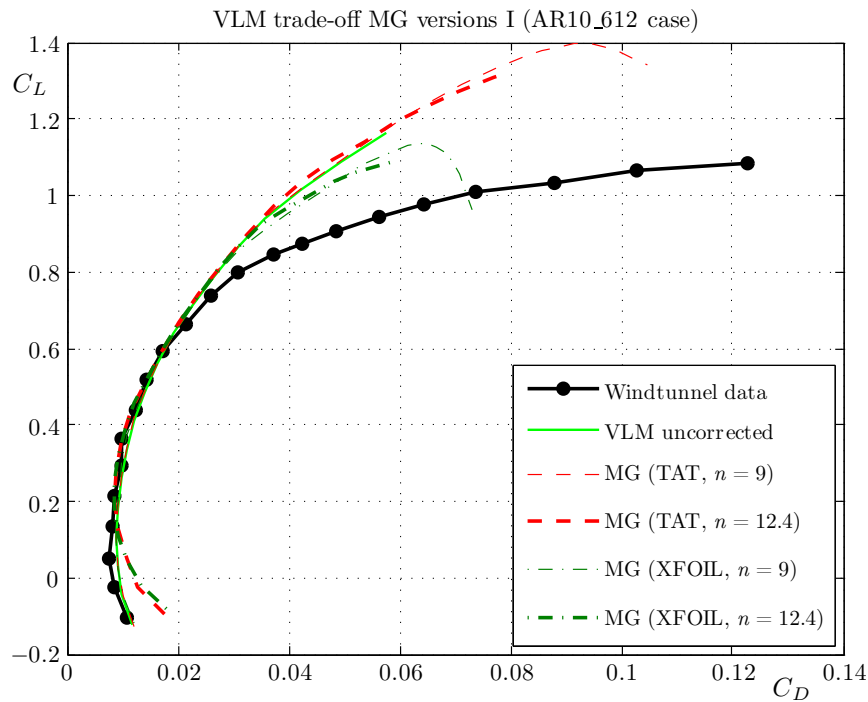


Figure E.42: The $C_L - C_D$ curves obtained from windtunnel experiments and XFLR5 simulations (VLM MG versions) for the AR10_612 wing where $Re = 2.0 \cdot 10^6$.

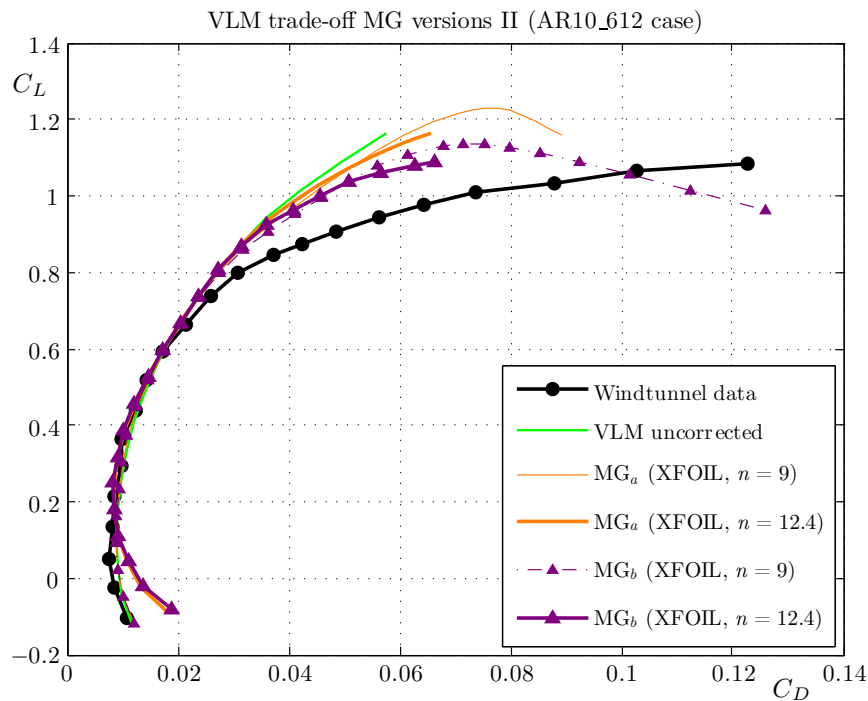


Figure E.43: The $C_L - C_D$ curves obtained from windtunnel experiments and XFLR5 simulations (VLM MG versions) for the AR10_612 wing where $Re = 2.0 \cdot 10^6$.

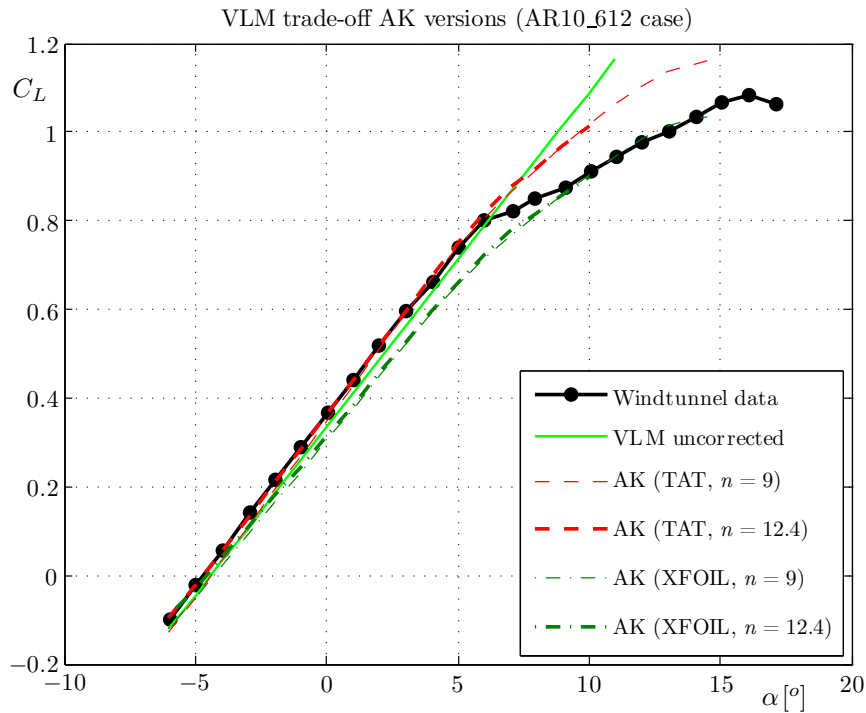


Figure E.44: The $C_L - \alpha$ curves obtained from windtunnel experiments and XFLR5 simulations (VLM AK versions) for the AR10_612 wing where $Re = 2.0 \cdot 10^6$.

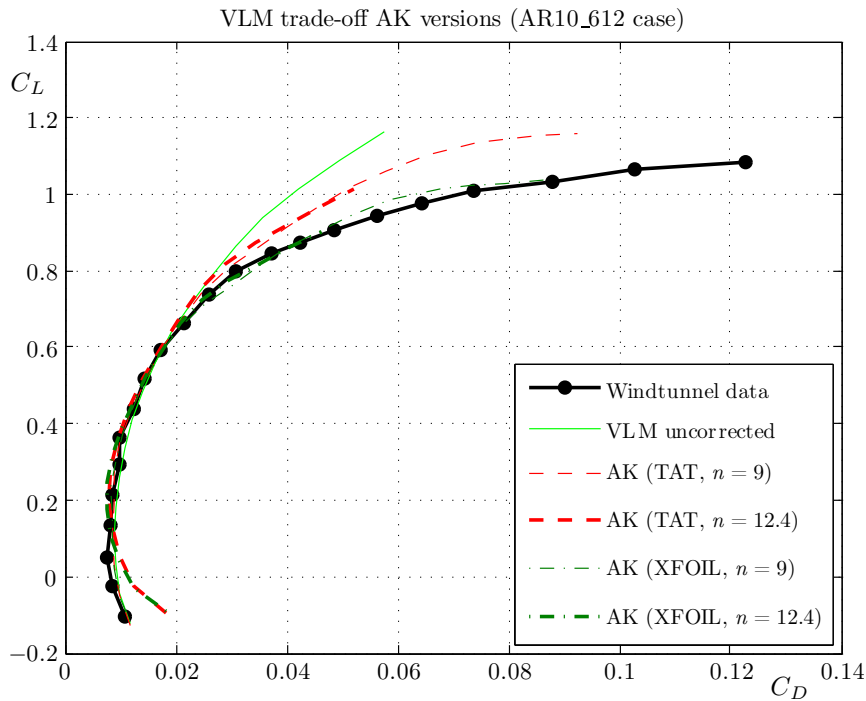


Figure E.45: The $C_L - C_D$ curves obtained from windtunnel experiments and XFLR5 simulations (VLM AK versions) for the AR10_612 wing where $Re = 2.0 \cdot 10^6$.

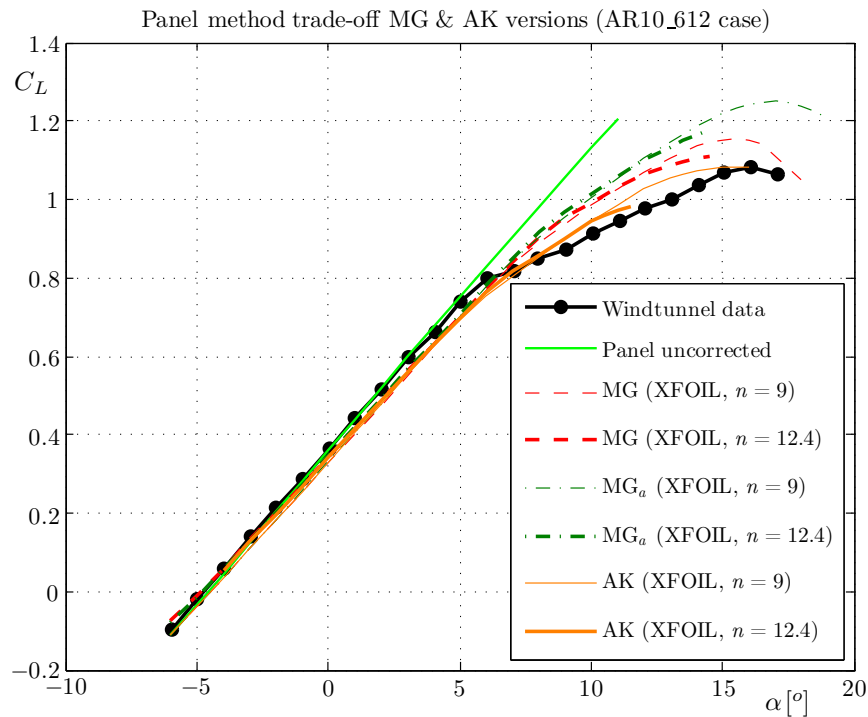


Figure E.46: The $C_L - \alpha$ curves obtained from windtunnel experiments and XFLR5 simulations (Panel method versions) for the AR10_612 wing where $Re = 2.0 \cdot 10^6$.

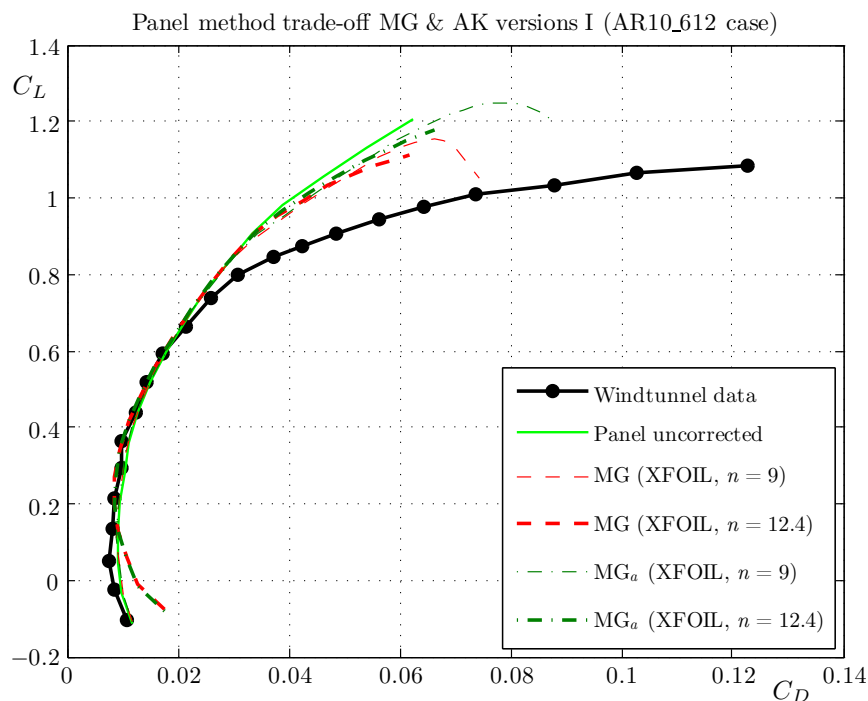


Figure E.47: The $C_L - C_D$ curves obtained from windtunnel experiments and XFLR5 simulations (Panel method versions) for the AR10_612 wing where $Re = 2.0 \cdot 10^6$.

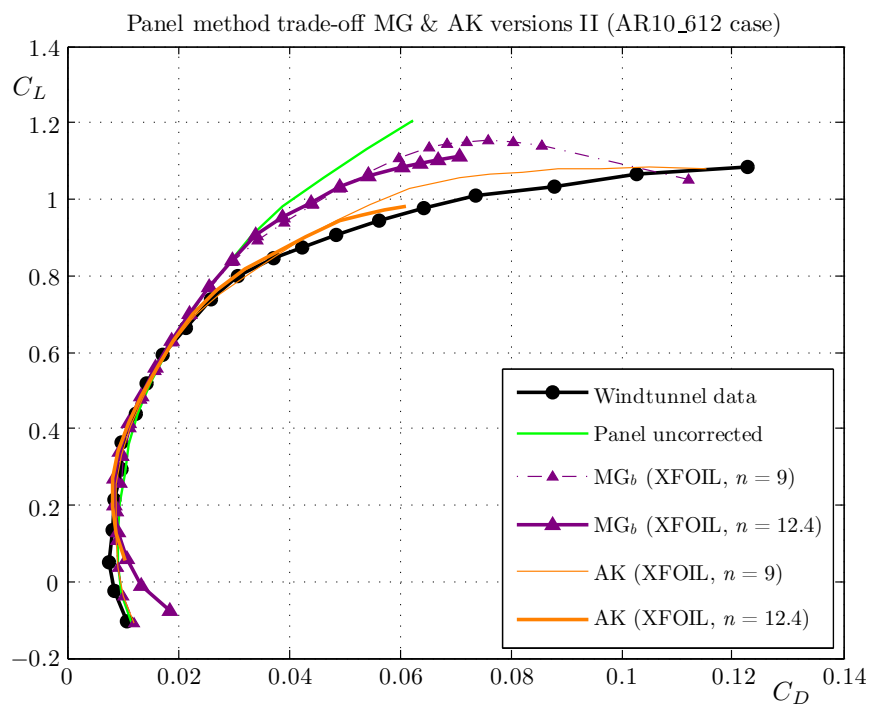


Figure E.48: The $C_L - C_D$ curves obtained from windtunnel experiments and XFLR5 simulations (Panel method versions) for the AR10_612 wing where $Re = 2.0 \cdot 10^6$.

Simulation results final versions

This appendix contains the remaining simulation results (see section 5.4) of the validation cases performed with the versions MG_b and AK of the adapted XFLR5 program.

F.1 Flat wing

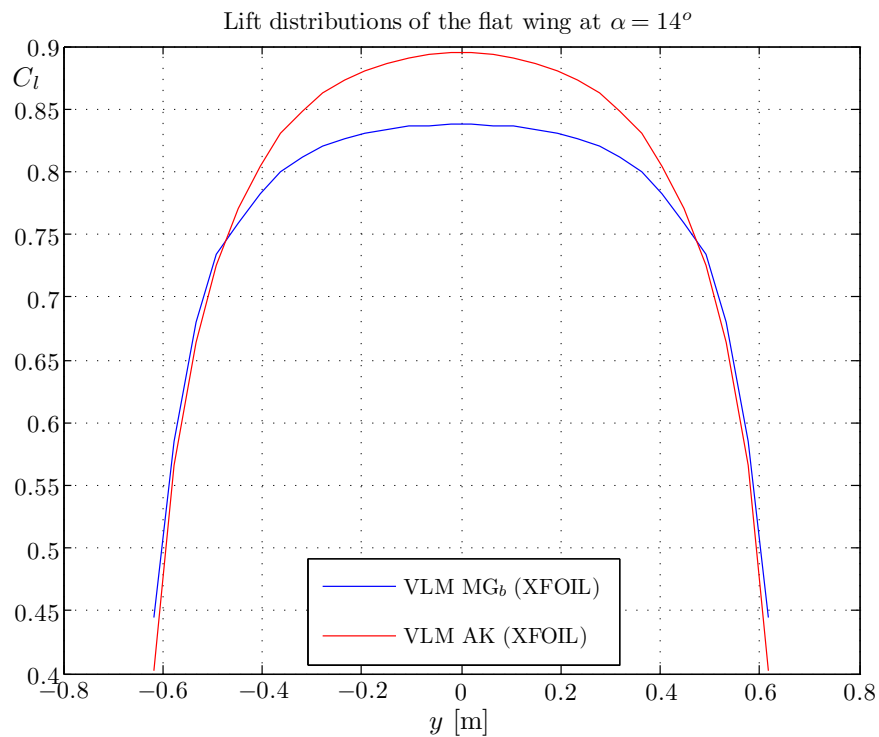


Figure F.1: The $C_l - y$ distribution obtained from XFLR5 simulations for the flat wing with $\alpha = 14^\circ$.

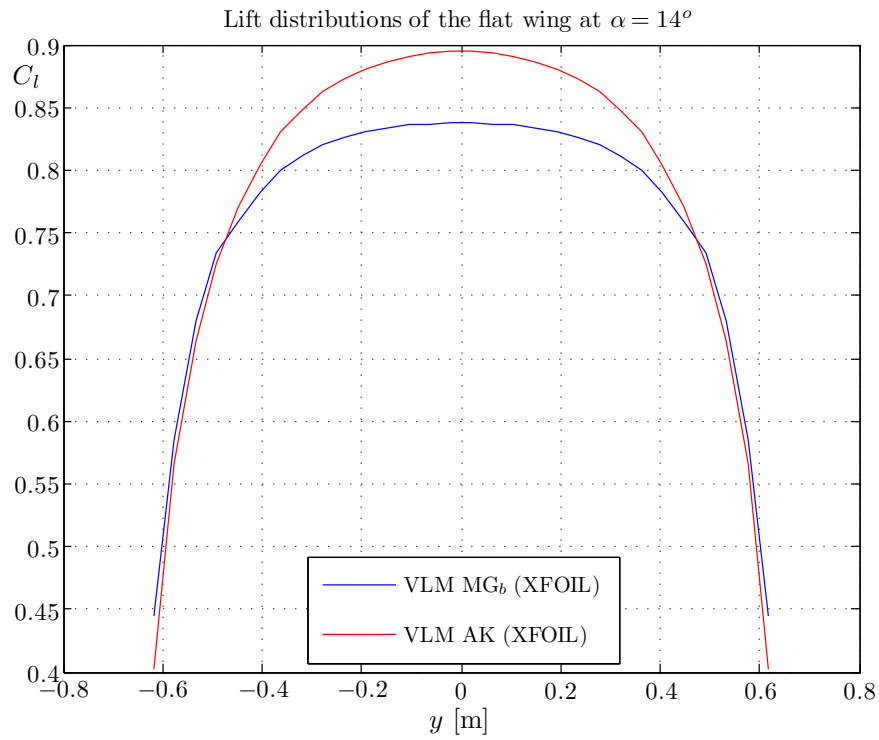


Figure F.2: The $\alpha_s - y$ distribution obtained from XFLR5 simulations for the flat wing with $\alpha = 14^\circ$.

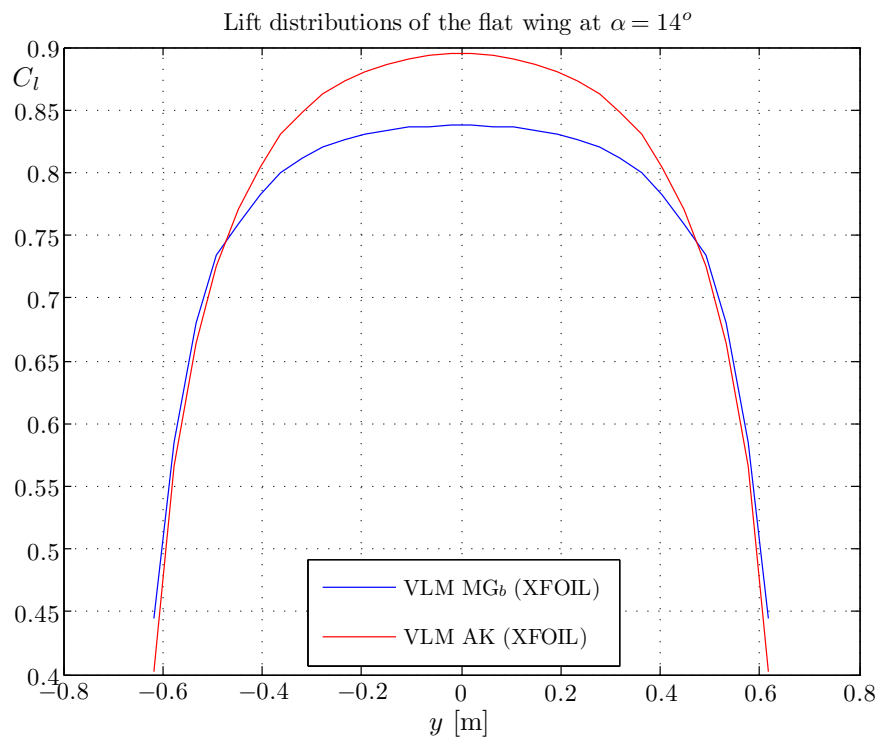


Figure F.3: The $\alpha_{eff} - y$ distribution obtained from XFLR5 simulations for the flat wing with $\alpha = 14^\circ$.

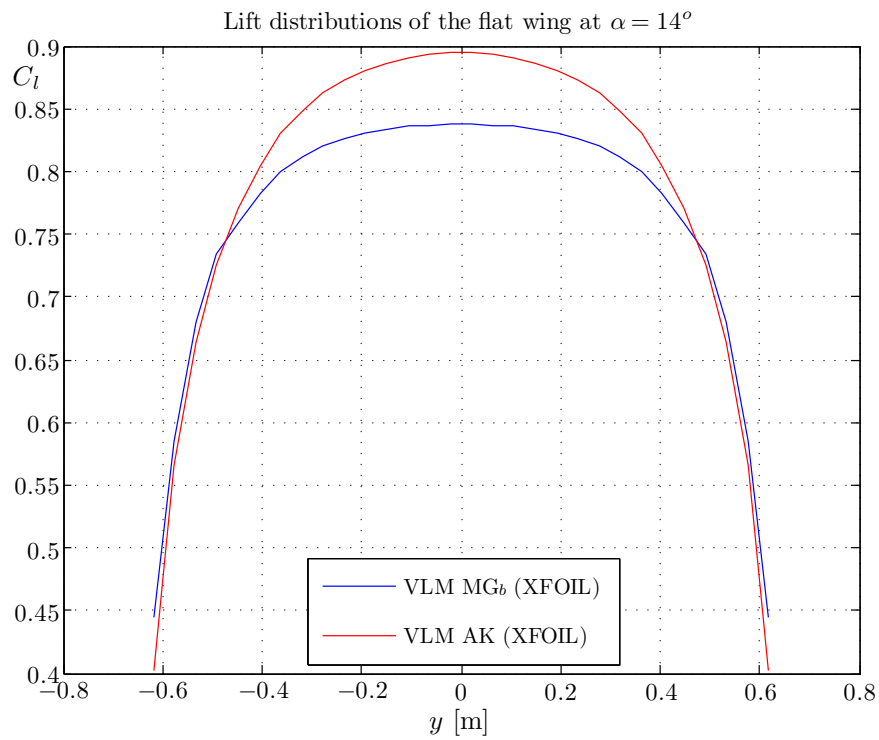


Figure F.4: The $C_{d_0} - y$ distribution obtained from XFLR5 simulations for the flat wing with $\alpha = 14^\circ$.

F.2 Swept wing AR5_012

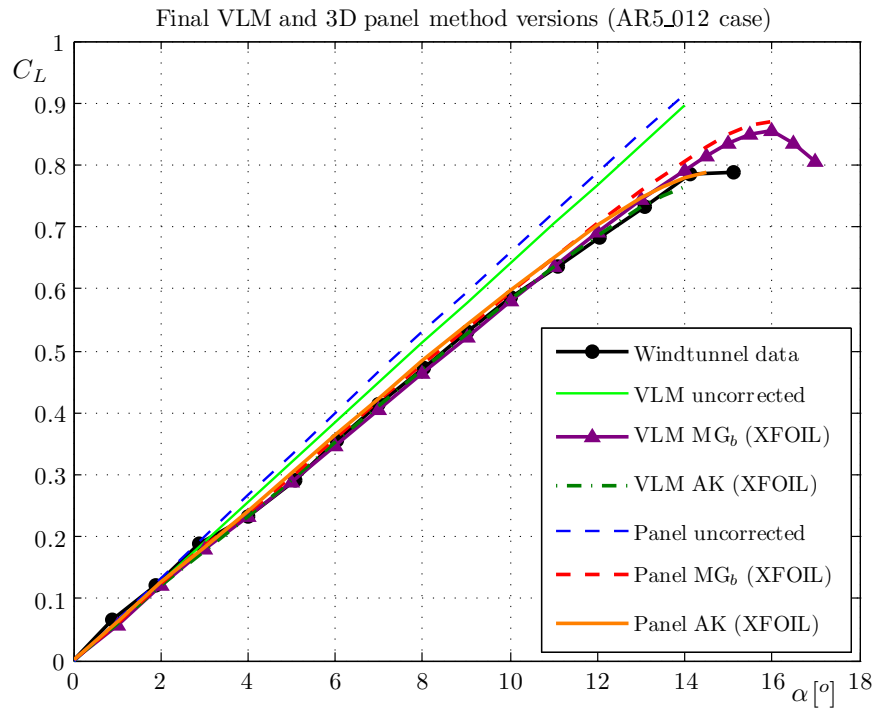


Figure F.5: The $C_L - \alpha$ curve obtained from windtunnel experiments and XFLR5 simulations of the AR5_012 wing where $Re = 2.0 \cdot 10^6$.

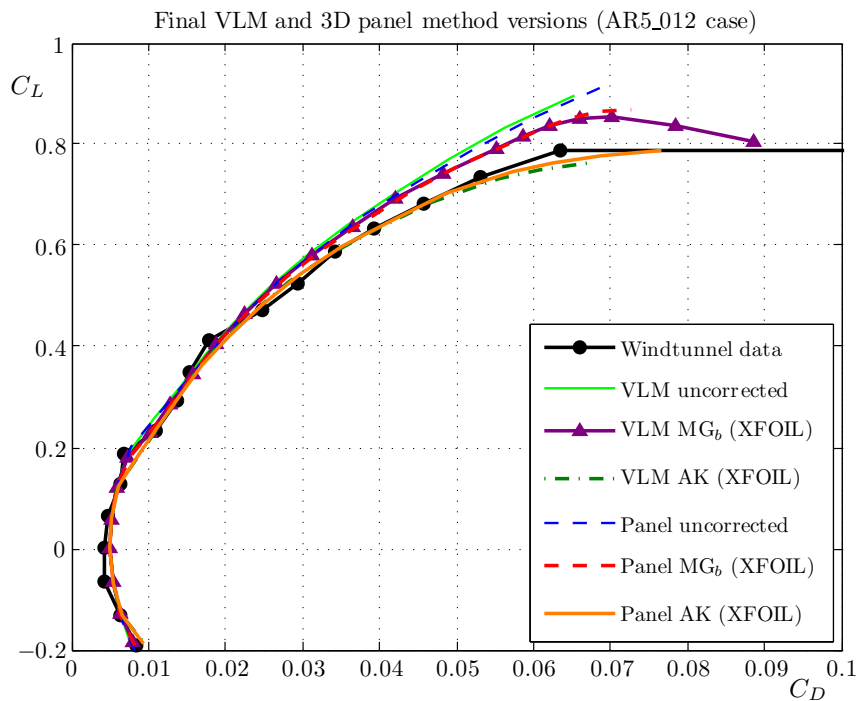


Figure F.6: The $C_L - C_D$ curve obtained from windtunnel experiments and XFLR5 simulations of the AR5_012 wing where $Re = 2.0 \cdot 10^6$.

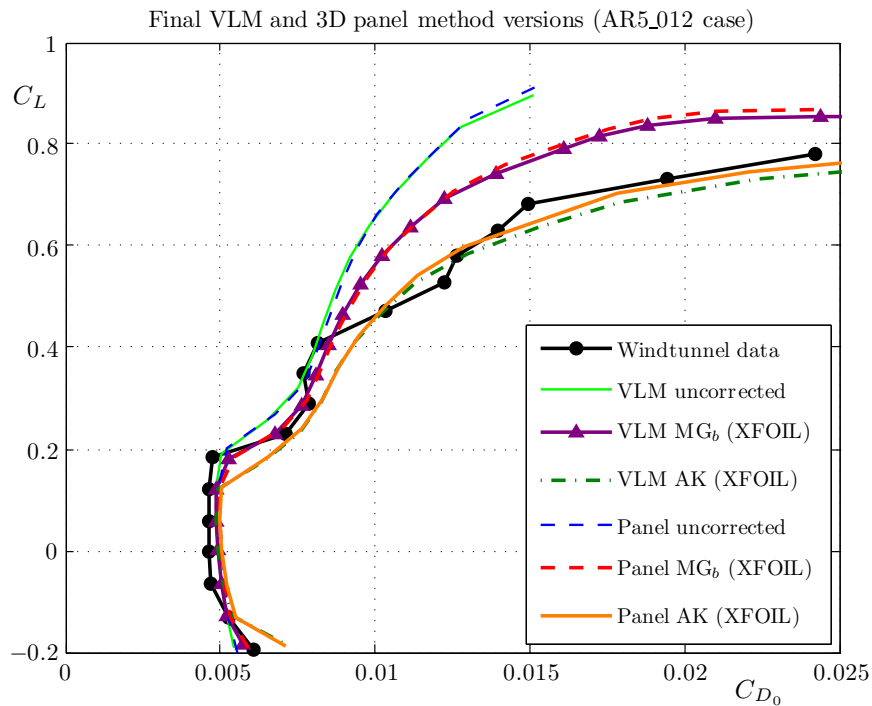


Figure F.7: The $C_L - C_{D_0}$ curve obtained from windtunnel experiments and XFLR5 simulations of the AR5_012 wing where $Re = 2.0 \cdot 10^6$.

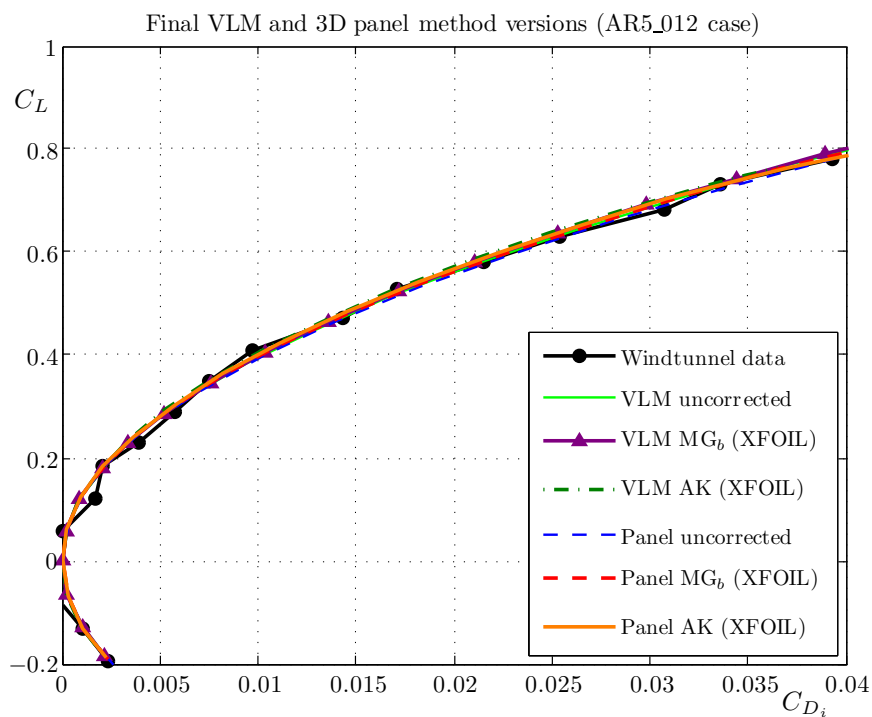


Figure F.8: The $C_L - C_{D_i}$ curve obtained from windtunnel experiments and XFLR5 simulations of the AR5_012 wing where $Re = 2.0 \cdot 10^6$.

F.3 Swept wing AR5_612

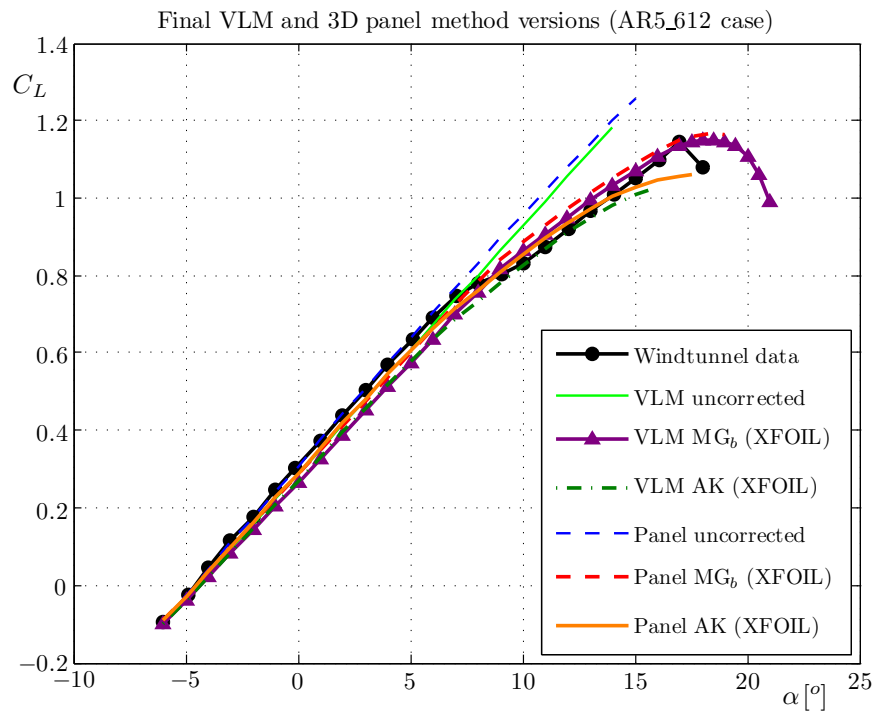


Figure F.9: The $C_L - \alpha$ curve obtained from windtunnel experiments and XFLR5 simulations of the AR5_612 wing where $Re = 2.0 \cdot 10^6$.

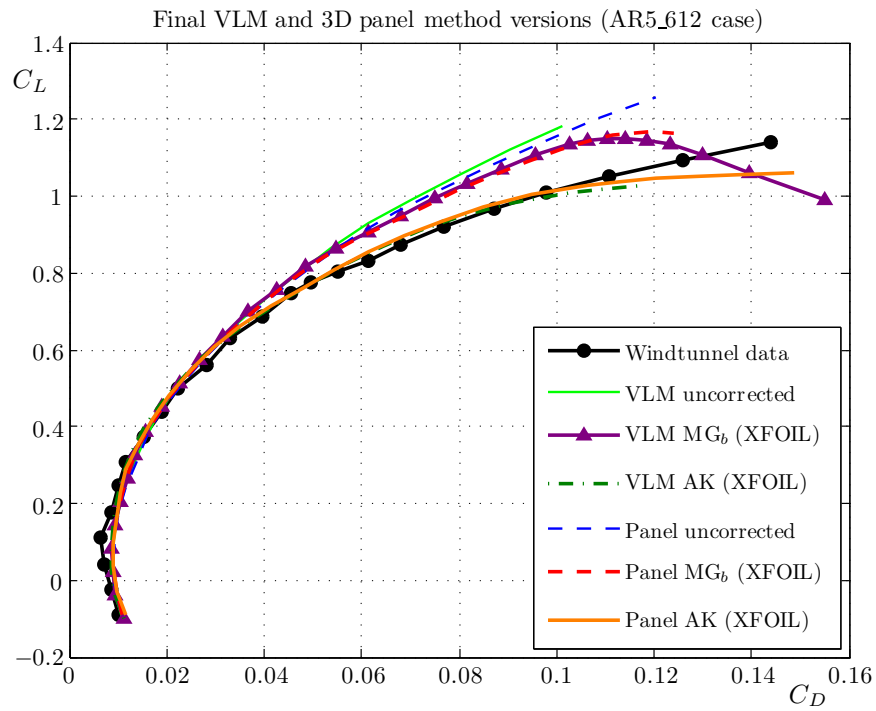


Figure F.10: The $C_L - C_D$ curve obtained from windtunnel experiments and XFLR5 simulations of the AR5_612 wing where $Re = 2.0 \cdot 10^6$.

F.4 Swept wing AR10_612

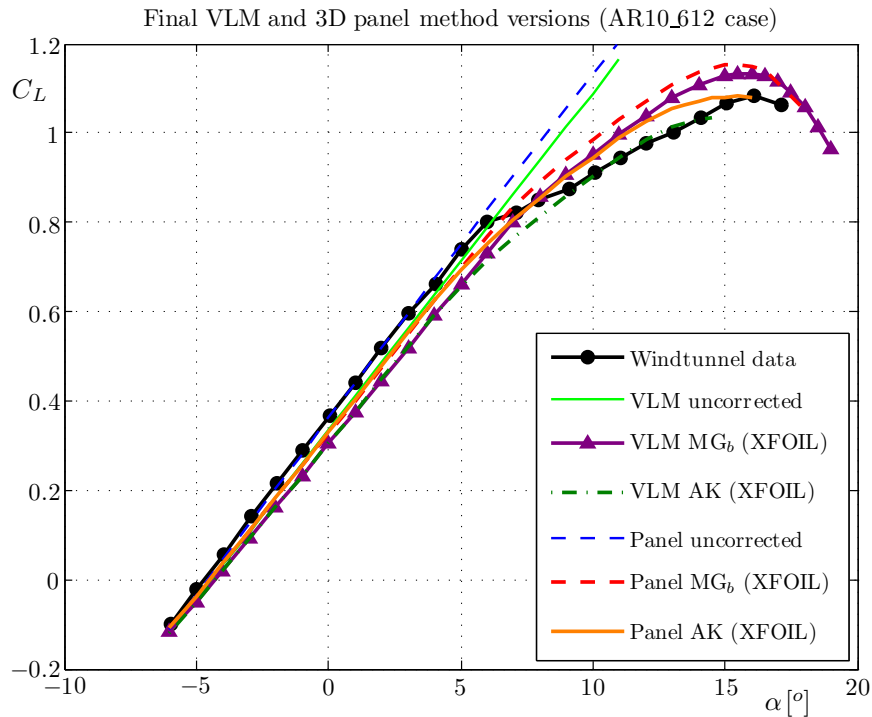


Figure F.11: The $C_L - \alpha$ curve obtained from windtunnel experiments and XFLR5 simulations of the AR10_612 wing where $Re = 2.0 \cdot 10^6$.

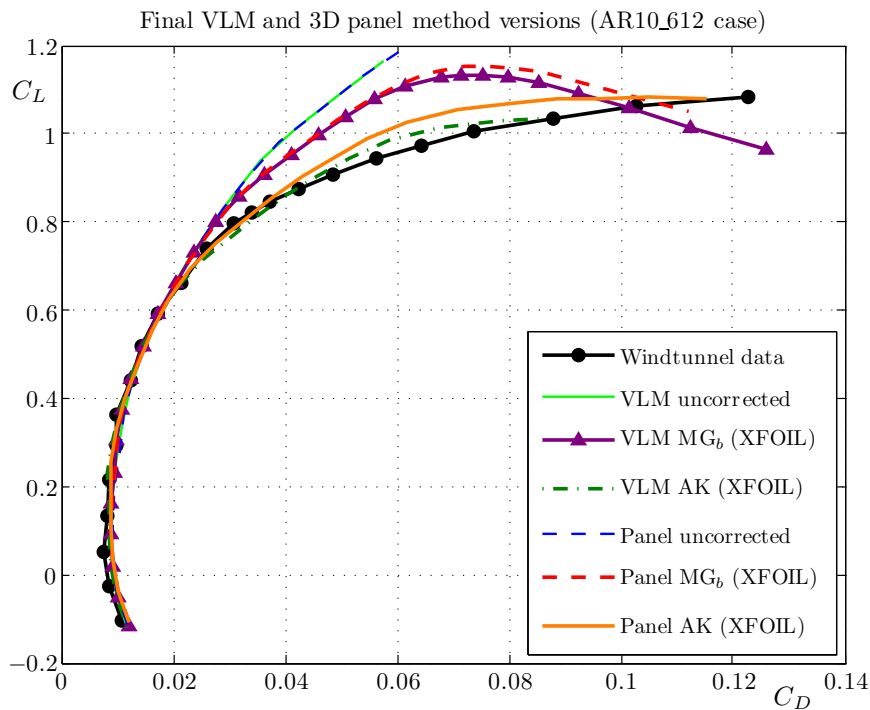


Figure F.12: The $C_L - C_D$ curve obtained from windtunnel experiments and XFLR5 simulations of the AR10_612 wing where $Re = 2.0 \cdot 10^6$.

F.5 Arc shaped kite

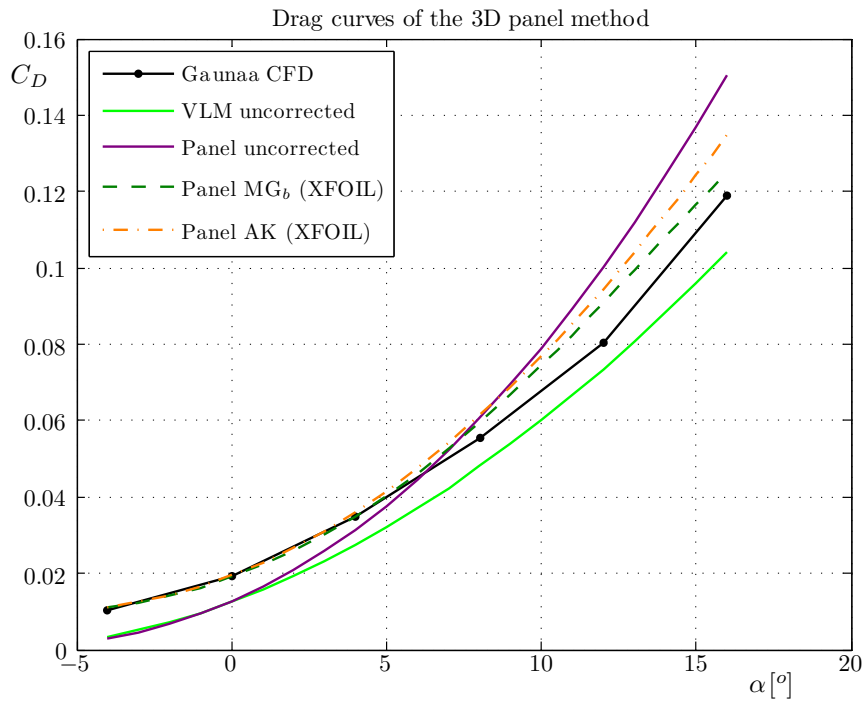


Figure F.13: Comparison of $C_D - \alpha$ curves obtained from simulations of the arc shaped kite.

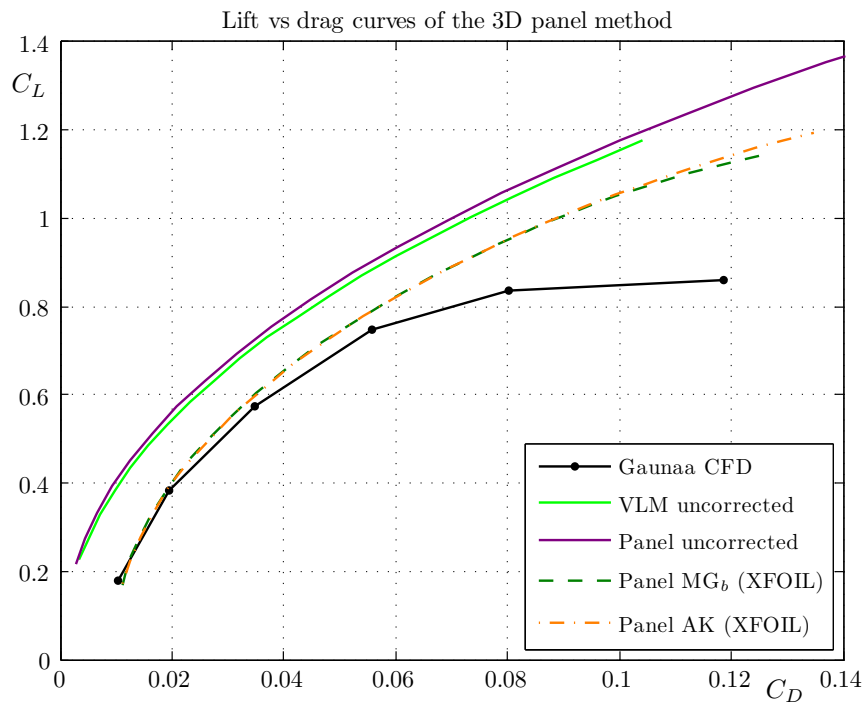


Figure F.14: Comparison of $C_L - C_D$ curves obtained from simulations of the arc shaped kite.

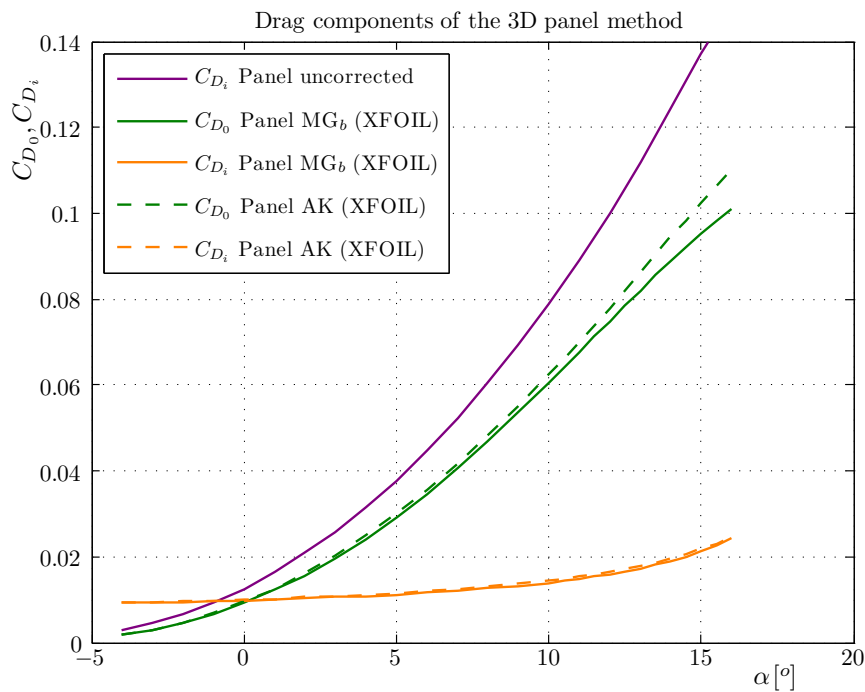


Figure F.15: Comparison of C_D , C_{D_0} and C_{D_i} as function of α curves obtained from simulations of the arc shaped kite.

Fluent mesh properties

The mesh densities were defined as follows: The elements between 0.5 chord in front of the leading edge and 2 chords behind the trailing edge have a maximum size of 10cm. The second density area starts 1.5 chord in front of the leading edge and ends 5 chords behind the trailing edge and has elements not larger than 30cm. The rest of the domain has a maximum element size of 2m.

For the grid adaption based on pressure coefficient and TI, a threshold of 0.02 is set in both cases.

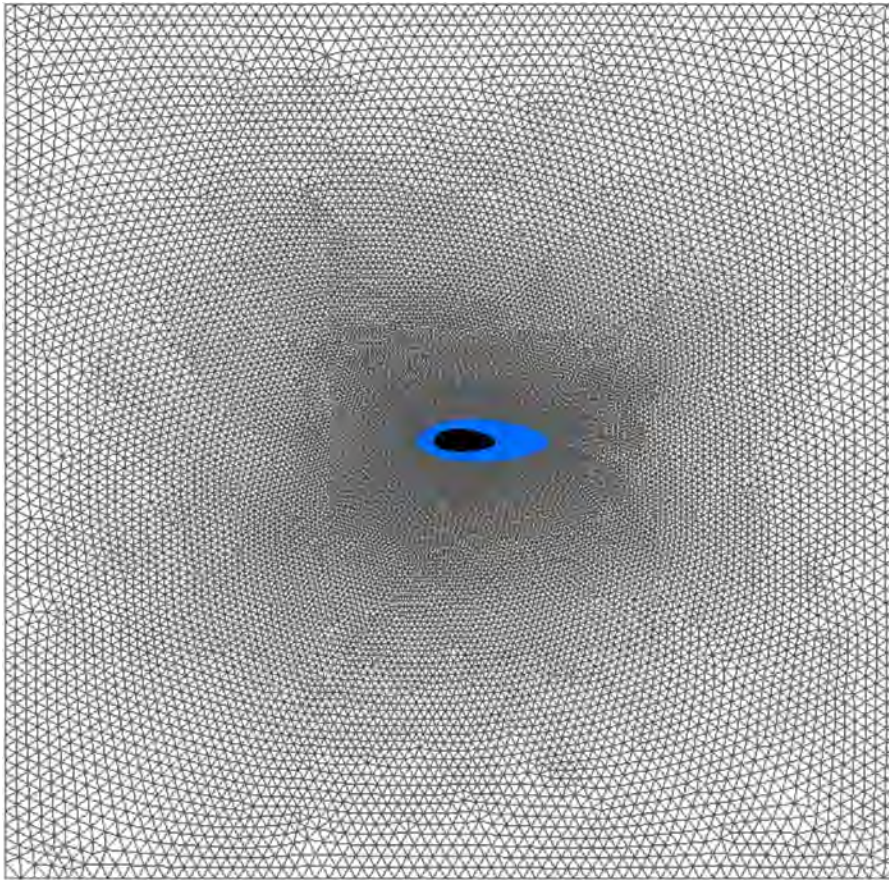


Figure G.1: The shown mesh shows the gradually growing cells towards the boundaries.

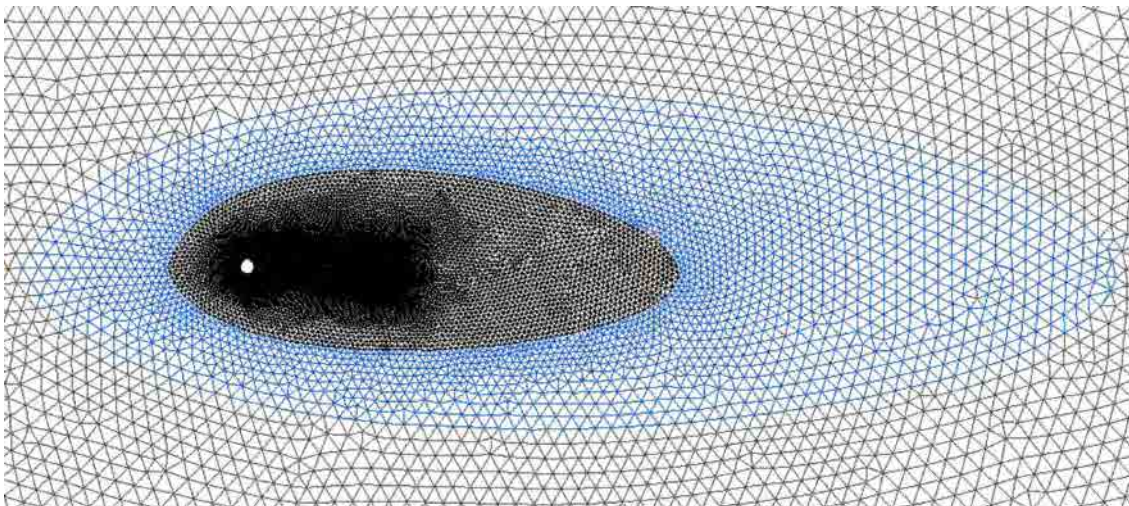


Figure G.2: The use of different mesh densities to obtain an efficient mesh.

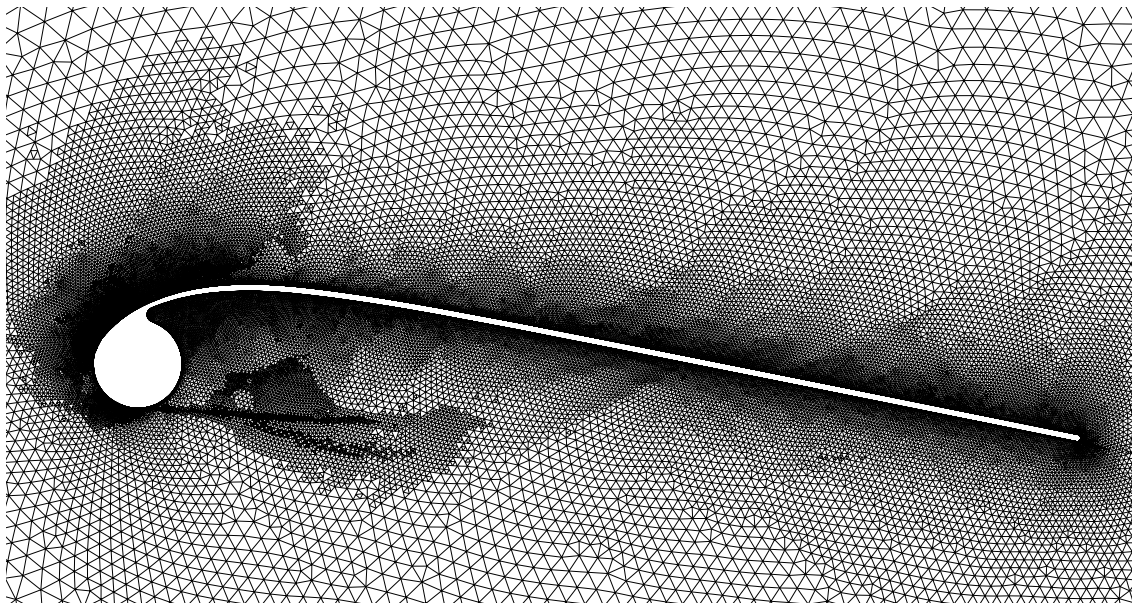


Figure G.3: The resultant mesh after two grid adaptations.

List of Figures

1.1	A kite power system can be seen as an evolution of a wind turbine (Schmehl, 2012b).	2
1.2	Aeroelastic models are required to capture the interaction between fluid and structural dynamics.	2
2.1	High altitude wind power in The Netherlands (<i>KitePower</i> , 2012).	6
2.2	Two airborne wind energy kite concepts of which the Makani M1 is a rigid kiteplane with generators on board (Makani, 2011) and the Laddermill consists of flexible kites with a generator on the ground (<i>Laddermill Kites Wind Energy</i> , 2011).	6
2.3	A pumping kite system using crosswind by flying Figures-of-eight (Groot, 2010).	8
2.4	Powering and depowering of the kite by changing the pitch angle resulting from a difference in lengths of the steering lines and power lines (Bosch, 2012a).	9
2.5	The power production of six consecutive pumping cycles with the 20kW prototype system (Bosch et al., 2012).	9
2.6	Definition of angle of attack and slide slip angle in the body-fixed reference frame.	10
2.7	Forces and velocities on a kite in crosswind motion (Breukels, 2011).	11
2.8	System layout of the current system at DUT KitePower (<i>KitePower</i> , 2012).	13
2.9	The KCU without protection cover shows that the micro winches greatly determine the size of the pod (<i>KitePower</i> , 2012).	14
2.10	Left: Prototype of the 10kW PowerPlane design (LabS55, 2011). Middle: DUT-MutinyV2 LEI kite (Bosch, 2012a). Right: Ram-air wing of EnerKite (EnerKite, 2012).	16
2.11	The bridles and lines of a LEI play an important part in the dynamic behavior (Slingshot, 2009).	17
2.12	The TUD-MutinyV1 has a sharp trailing edge corner near the tip causing flapping of the canopy.	20
2.13	Two types of aeroelastic solvers: flow and displacement equations can be solved simultaneous (monolithic) or separately (partitioned).	20
2.14	Currently available models that simulate kite dynamics.	21
2.15	A typical lift curve including a linear regime and a nonlinear regime (Wikipedia, 2006).	24
3.1	Side view of a wing section.	30

3.2	A schematic representation of the modeled pressure distribution (Breukels, 2011).	31
3.3	The values for the weight factors $w_i + u_i a$ for different values of airfoil moment coefficient C_M (Breukels, 2011).	31
3.4	Development of a closed circulation vortex system behind a finite wing section.	32
3.5	An overview of the discussed aerodynamic analysis methods. Breukels' method is omitted, because it uses fractions of both VLM as CFD. Also nonlinear potential flow is omitted here, because the unsteady and full potential equation contain respectively time and density differential terms, while in this report these effects are neglected in the modeling of kite aeroelastics.	35
3.6	Top view of a semi-span wing illustrating the vortex lattice method using horseshoe vortices.	38
3.7	Top view of a semi-span wing illustrating VLM using ring vortices.	38
3.8	Lay-up of a 3D wing using VLM.	39
3.9	Lay-up of a three-dimensional wing using a panel method.	40
3.10	The thickness of the boundary layer is added to the airfoil geometry.	41
3.11	The relative position of the new method, a nonlinear VLM/3D panel method, with respect to other available aerodynamic methods.	44
3.12	Levels of fidelity used in fluid-structure interaction computations.	45
4.1	Definition of the effective angle of attack, induced angle of attack and effective lift vector.	48
4.2	Angle shift correction method on 2D lift polars to account for viscous effects in a 3D analysis.	49
4.3	Correction methods concerning viscous and thickness effects using thin airfoil theory and a 2D panel method for a 3D VLM and panel method.	51
4.4	Flow diagram of the adapted XFLR5 program structure.	54
4.5	Two dimensional airflow acting on an airfoil with a local angle of attack α .	55
4.6	Perpendicular velocity vector projected on the wing dihedral.	56
4.7	Effect of the number of panels on the error with respect to the finest grid and computational time for the flat wing case (see Section 5.2.1), using inviscid calculations. The computational times correspond to the average over an angle of attack sweep of 21 steps.	59
4.8	Placement of wake direction with (bottom) and without (top) using the tilted geometry setting.	60
4.9	Inviscid lift curves of the two VLM's and 3D panel method for the flat wing case.	61
5.1	Flat wing configuration in XFLR5.	65
5.2	A symmetrical NACA - 65 ₁ (A)012 and cambered NACA - 64 ₁ (A)612 airfoil section used for the swept wing configurations.	66
5.3	Swept wing configuration in XFLR5, with $A = 10$, $\Lambda = 35^\circ$ and a highly cambered profile.	67
5.4	Oil flow patterns during a windtunnel test on five different wing configurations, considering a baseline wing and added winglets under various dihedral angles at $\alpha = 15^\circ$ and $Re = 80,000$.	68
5.5	Circular arc shaped kite configuration in XFLR5, used to validate the method of Gaunaa.	69
5.6	Error of the linear and non-linear region for 2 different n -values of all versions for the swept wing configurations.	72
5.7	Option tree of available methods for each program version.	73
5.8	Trade-off criteria used for validation.	74
5.9	Error of the linear and non-linear region of the lift and drag curves of all VLM versions for all validation cases.	74
5.10	Error of the linear and non-linear region of the lift and drag curves of all 3D panel method versions for all validation cases.	75
5.11	Error of the location and value of $C_{L_{max}}$ of all VLM and 3D panel method versions for all validation cases, including the number of reached stall points.	75

5.12	The $C_L - \alpha$ curves obtained from wind tunnel experiments and XFLR5 simulations of the flat wing where $Re = 1.0 \cdot 10^6$	76
5.13	The $C_D - \alpha$ curves obtained from wind tunnel experiments and XFLR5 simulations of the flat wing where $Re = 1.0 \cdot 10^6$	77
5.14	The $C_L - \alpha$ curves obtained from wind tunnel experiments and XFLR5 simulations of the swept AR10_012 wing where $Re = 2.0 \cdot 10^6$	78
5.15	The $C_L - C_D$ curves obtained from wind tunnel experiments and XFLR5 simulations of the swept AR10_012 wing where $Re = 2.0 \cdot 10^6$	78
5.16	The $C_L - C_{D_0}$ curves obtained from wind tunnel experiments and XFLR5 simulations of the swept AR10_012 wing where $Re = 2.0 \cdot 10^6$	79
5.17	The $C_L - C_{D_i}$ curves obtained from wind tunnel experiments and XFLR5 simulations of the swept AR10_012 wing where $Re = 2.0 \cdot 10^6$	79
5.18	MAD of the linear and non-linear region of the lift curves of the uncorrected XFLR5 version and adapted versions for all validation cases.	80
5.19	MAD of the linear region of the drag (total, profile and induced part) curves of the uncorrected XFLR5 version and adapted versions for all validation cases.	80
5.20	MAD of the non-linear region of the drag (total, profile and induced part) curves of the uncorrected XFLR5 version and adapted versions for all validation cases.	81
5.21	Normalized error of the value and location of $C_{L_{max}}$ of version MG_b for all validation cases.	82
5.22	Normalized error of the value and location of $C_{L_{max}}$ of version AK for all validation cases.	82
5.23	The $C_l - y$ and $\alpha_s - y$ distributions obtained from XFLR5 simulations (original, MG_b and AK) for the AR10_012 wing with $\alpha = 6^\circ$ and $\alpha = 13.3^\circ$	83
5.24	The $\alpha_{eff} - y$ and $C_d - y$ distributions obtained from XFLR5 simulations (original, MG_b and AK) for the AR10_012 wing with $\alpha = 6^\circ$ and $\alpha = 13.3^\circ$	84
5.25	The lift, drag and induced drag curves obtained from wind tunnel experiments and XFLR5 simulations of the winglet configuration with ($\Gamma = 90^\circ$) and without winglet for $Re = 80,000$	86
5.26	Comparison of $C_L - \alpha$ curves obtained from simulations of the arc shaped kite.	88
5.27	Comparison of $C_D - \alpha$ curves obtained from simulations of the arc shaped kite.	89
5.28	Comparison of $C_L - C_D$ curves obtained from simulations of the arc shaped kite.	89
5.29	Comparison of $L/D - \alpha$ curves obtained from simulations of the arc shaped kite.	90
5.30	Comparison of C_D , C_{D_0} and C_{D_i} as function of α curves obtained from simulations of the arc shaped kite.	90
5.31	The $C_l - y$ and $C_d - y$ distributions obtained from simulations of the arc shaped kite with $\alpha = 0^\circ$ and $\alpha = 16^\circ$	91
5.32	Comparison of $C_L - \alpha$ curves obtained from simulations of the arc shaped kite.	92
5.33	Comparison of $L/D - \alpha$ curves obtained from simulations of the arc shaped kite.	92
5.34	Convergence and accuracy of C_L vs number of iterations of the flat wing for $\alpha = 16^\circ$	93
5.35	Induced angle distribution (VLM AK (XFOIL)) of the flat wing for $\alpha = 16^\circ$	94
6.1	A zoom-in on the two dimensional grid around the center profile of the DUT-MutinyV2 kite.	98
6.2	The sharp corner between the leading edge tube and canopy is modeled with a finite radius arc to simplify boundary layer meshing.	99
6.3	The prism mesh at the trailing edge.	99
6.4	Contours of pressure coefficient for the DUT-MutinyV2 center profile at $\alpha = 4^\circ$ and $Re = 2.9 \cdot 10^6$	100

6.5	Contours of turbulence intensity for the DUT-MutinyV2 center profile at $\alpha = 4^\circ$ and $Re = 2.9 \cdot 10^6$	100
6.6	Residuals during iteration. Left: $\alpha = 0^\circ$, right: $\alpha = 10^\circ$	103
6.7	Iterative behavior of lift and drag coefficient for a kite profile with thickness 9% and camber 5% at an angle of attack of 10°	104
6.8	Effect of the number of cells on lift, drag and moment coefficients, using a kite profile with 9% thickness and 5% camber at $\alpha = 0^\circ$	105
6.9	Lift and drag coefficients for increasing domain size. The difference is taken with respect to the values for the largest domain.	106
6.10	Iterative behavior of different values for TI and length scale.	107
6.11	Lift, drag and moment curves of the root profile (camber 5%, thickness 9%) of the DUT-MutinyV2 kite for $Re = 2.9 \cdot 10^6$ ($V_\infty = 15m/s$). In XFOIL simulations $n = 9$ is used.	109
6.12	Lift, drag and moment curves of the tip profile (camber 1%, thickness 10%) of the DUT-MutinyV2 kite for $Re = 2.9 \cdot 10^6$ ($V_\infty = 15m/s$). In XFOIL simulations $n = 9$ is used.	110
6.13	Predicted boundary layer by XFOIL and velocity contours from CFD simulations for the root profile of the DUT-MutinyV2 kite for $Re = 2.9 \cdot 10^6$	112
6.14	The geometrical conversions of the DUT-MutinyV2 root profile such that XFOIL can handle the shapes.	113
6.15	The tip profile of the DUT-MutinyV2 kite after geometrical conversion.	114
6.16	The effect of Reynolds number on lift prediction of CFD and XFOIL for the root profile of the DUT-MutinyV2 kite.	114
6.17	Pressure distributions for several angles of attack for a typical kite profile (DUT-MutinyV2 root profile).	118
6.18	Pressure distributions scaled to same total lift.	119
6.19	Illustration of the required procedure for determining the chordwise pressure distribution with XFOIL.	120
6.20	Integration procedue.	121
6.21	Left: design shape from the kite design tool Surfplan. Right: Discretized kite in XFLR5.	124
6.22	Resultant force versus angle of attack for VLM2 (MG_b) with free wake. The black line is obtained from the scattered experimental data by a weighted linear least square method.	126
6.23	Spanwise distribution plots for the DUT-MutinyV2 kite for angle of attack before and beyond stall. For the angle shift corrections in VLM MG_b the polars generated from Breukels regression models are used. The Y coordinate is measured in the direction of the arc.	128
6.24	Panel force distribution over the DUT-MutinyV2 kite at $\alpha = 11^\circ$	129
6.25	Resultant force versus angle of attack for VLM2 (MG_b) with free wake. The black line is obtained from the scattered experimental data by a weighted linear least square method.	130
7.1	Performance of the new method.	134
A.1	See through impression of the construction of a ram air wing (Skywalk, 2008).	146
A.2	A LEI kite where the inflated leading edge and struts make the kite more rigid than a ram air kite (Wikipedia, 2007).	146
A.3	A C-kite with two back and two front lines (Evolution, 2008b).	147
A.4	The most popular SLE kite: the BOW kite, which has a concave trailing edge (Slingshot, 2009).	147
A.5	Top left: kitebuggying, top right: paragliding, bottom left: skydiving, bottom right: kitesurfing.	148
A.6	A cargo ship propelled by a kite from the company SkySails.	149
A.7	Kitesailing or kiteboating on a catamaran (Airplay, 2009).	149
A.8	A conceptual idea to travel over water: the Hydrokite.	149
A.9	The $21m^2$ high performance foil kite used by EnerKite (EnerKite, 2012).	150

A.10	A conceptual offshore kite powered wind farm of SkySails Power (SkySails, 2012b).	151
A.11	The foil kite used by SkySails Power with two large air inlets near the center (SkySails, 2012b).	151
B.1	The first kite of the TUD KitePower system, the 25m ² TUD-MutinyV1.	153
B.2	The 25m ² TUD-MutinyV2 kite has more curvature, an extra strut and a less sharp corner at the TE around the tip.	153
B.3	CAD representation of the TUD-Mutiny-V2 (Schwoll, 2012).	154
B.4	A kite can be depowered until the working line of the power lines goes through the aerodynamic center (Heuvel, 2010).	155
B.5	An additional kite was acquired to verify whether a lower camber factor and higher aspect ratio positively influenced performance. This kite is a 14m ² Genetrix Hydra.	156
B.6	The Genetrix 25m ² contains a bulging LE to preserve a more constant profile over the wing.	157
C.1	Visualization of two elementary flows, which can be used to describe the flow around an airfoil. The source has radially directed induced velocity vectors, while the vortex has induced velocities in the tangential direction.	160
C.2	Vorticity distribution on the camberline of a thin airfoil.	161
C.3	Projected vorticity distribution on the x axis of thin airfoil's camberline.	161
C.4	Discretization of a 2D airfoil section using a panel method.	162
C.5	Downwash distribution of a finite straight wing due to the bound vortex (constant) and the tip vortices (parabolic).	164
D.1	The $C_l - \alpha$ curves obtained from windtunnel experiments and XFOIL simulations with 3 different values of n for the NACA - 64 ₂ (A)015 profile used for the flat wing configuration where $Re = 1.0 \cdot 10^6$	165
D.2	The $C_l - C_d$ curves obtained from windtunnel experiments and XFOIL simulations with 3 different values of n for the NACA - 64 ₂ (A)015 profile used for the flat wing configuration where $Re = 1.0 \cdot 10^6$	166
D.3	The $C_l - \alpha$ curves obtained from windtunnel experiments and XFOIL simulations with 2 different values of n for the NACA - 65 ₁ (A)012 profile used for the swept wing configurations where $Re = 3.0 \cdot 10^6$	167
D.4	The $C_l - C_d$ curves obtained from windtunnel experiments and XFOIL simulations with 2 different values of n for the NACA - 65 ₁ (A)012 profile used for the swept wing configurations where $Re = 3.0 \cdot 10^6$	167
D.5	The $C_l - \alpha$ curves obtained from XFOIL simulations with 2 different values of n for the NACA - 65 ₁ (A)012 profile used for the swept wing configurations where $Re = (1.0 - 3.0) \cdot 10^6$	168
D.6	The $C_l - C_d$ curves obtained from XFOIL simulations with 2 different values of n for the NACA - 65 ₁ (A)012 profile used for the swept wing configurations where $Re = (1.0 - 3.0) \cdot 10^6$	168
D.7	The $C_l - \alpha$ curves obtained from XFOIL simulations with 3 different values of n for the NACA - 64 ₁ (A)612 profile used for the swept wing configurations where $Re = (1.0 - 3.0) \cdot 10^6$	169
D.8	The $C_l - C_d$ curves obtained from XFOIL simulations with 3 different values of n for the NACA - 64 ₁ (A)612 profile used for the swept wing configurations where $Re = (1.0 - 3.0) \cdot 10^6$	170
D.9	The $C_l - \alpha$ curves obtained from Cyberiad (1981) for the NACA - 0012 profile used for the winglet configuration where $Re = 80 \cdot 10^3$	171
D.10	The $C_l - C_d$ curve obtained from Cyberiad (1981) for the NACA - 0012 profile used for the winglet configuration where $Re = 80 \cdot 10^3$	171
D.11	The NACA - 64-418 airfoil section used for the arc shaped kite.	172

D.12	The inviscid and viscous $C_l - \alpha$ curves obtained from Gaunaa et al. (2010) for the NACA - 64-418 profile used for the arc shaped kite where $Re = 6 \cdot 10^6$.	172
D.13	The $C_d - \alpha$ curve obtained from Gaunaa et al. (2010) for the NACA - 64-418 profile used for the arc shaped kite where $Re = 6 \cdot 10^6$.	173
E.1	The $C_L - \alpha$ curves obtained from windtunnel experiments and XFLR5 simulations (VLM MG versions) for the flat wing where $Re = 1.0 \cdot 10^6$.	175
E.2	The $C_D - \alpha$ curves obtained from windtunnel experiments and XFLR5 simulations (VLM MG versions) for the flat wing where $Re = 1.0 \cdot 10^6$.	176
E.3	The $C_L - \alpha$ curves obtained from windtunnel experiments and XFLR5 simulations (VLM AK versions) for the flat wing where $Re = 1.0 \cdot 10^6$.	176
E.4	The $C_D - \alpha$ curves obtained from windtunnel experiments and XFLR5 simulations (VLM AK versions) for the flat wing where $Re = 1.0 \cdot 10^6$.	177
E.5	The $C_L - \alpha$ curves obtained from windtunnel experiments and XFLR5 simulations (Panel versions) for the flat wing where $Re = 1.0 \cdot 10^6$.	177
E.6	The $C_D - \alpha$ curves obtained from windtunnel experiments and XFLR5 simulations (Panel method versions) for the flat wing where $Re = 1.0 \cdot 10^6$.	178
E.7	The $C_L - \alpha$ curves obtained from windtunnel experiments and XFLR5 simulations (VLM MG versions) for the AR5_012 wing where $Re = 2.0 \cdot 10^6$.	179
E.8	The $C_L - C_D$ curves obtained from windtunnel experiments and XFLR5 simulations (VLM MG versions) for the AR5_012 wing where $Re = 2.0 \cdot 10^6$.	179
E.9	The $C_L - C_D$ curves obtained from windtunnel experiments and XFLR5 simulations (VLM MG versions) for the AR5_012 wing where $Re = 2.0 \cdot 10^6$.	180
E.10	The $C_L - C_{D_0}$ curves obtained from windtunnel experiments and XFLR5 simulations (VLM MG versions) for the AR5_012 wing where $Re = 2.0 \cdot 10^6$.	180
E.11	The $C_L - C_{D_0}$ curves obtained from windtunnel experiments and XFLR5 simulations (VLM MG versions) for the AR5_012 wing where $Re = 2.0 \cdot 10^6$.	181
E.12	The $C_L - \alpha$ curves obtained from windtunnel experiments and XFLR5 simulations (VLM AK versions) for the AR5_012 wing where $Re = 2.0 \cdot 10^6$.	181
E.13	The $C_L - C_D$ curves obtained from windtunnel experiments and XFLR5 simulations (VLM AK versions) for the AR5_012 wing where $Re = 2.0 \cdot 10^6$.	182
E.14	The $C_L - C_{D_0}$ curves obtained from windtunnel experiments and XFLR5 simulations (VLM AK versions) for the AR5_012 wing where $Re = 2.0 \cdot 10^6$.	182
E.15	The $C_L - \alpha$ curves obtained from windtunnel experiments and XFLR5 simulations (Panel method versions) for the AR5_012 wing where $Re = 2.0 \cdot 10^6$.	183
E.16	The $C_L - C_D$ curves obtained from windtunnel experiments and XFLR5 simulations (Panel method versions) for the AR5_012 wing where $Re = 2.0 \cdot 10^6$.	183
E.17	The $C_L - C_D$ curves obtained from windtunnel experiments and XFLR5 simulations (Panel method versions) for the AR5_012 wing where $Re = 2.0 \cdot 10^6$.	184
E.18	The $C_L - C_{D_0}$ curves obtained from windtunnel experiments and XFLR5 simulations (Panel method versions) for the AR5_012 wing where $Re = 2.0 \cdot 10^6$.	184
E.19	The $C_L - C_{D_0}$ curves obtained from windtunnel experiments and XFLR5 simulations (Panel method versions) for the AR5_012 wing where $Re = 2.0 \cdot 10^6$.	185
E.20	The $C_L - \alpha$ curves obtained from windtunnel experiments and XFLR5 simulations (VLM MG versions) for the AR5_612 wing where $Re = 2.0 \cdot 10^6$.	186
E.21	The $C_L - C_D$ curves obtained from windtunnel experiments and XFLR5 simulations (VLM MG versions) for the AR5_612 wing where $Re = 2.0 \cdot 10^6$.	186
E.22	The $C_L - C_D$ curves obtained from windtunnel experiments and XFLR5 simulations (VLM MG versions) for the AR5_612 wing where $Re = 2.0 \cdot 10^6$.	187

E.23	The $C_L - \alpha$ curves obtained from windtunnel experiments and XFLR5 simulations (VLM AK versions) for the AR5_612 wing where $Re = 2.0 \cdot 10^6$.	187
E.24	The $C_L - C_D$ curves obtained from windtunnel experiments and XFLR5 simulations (VLM AK versions) for the AR5_612 wing where $Re = 2.0 \cdot 10^6$.	188
E.25	The $C_L - \alpha$ curves obtained from windtunnel experiments and XFLR5 simulations (Panel method versions) for the AR5_612 wing where $Re = 2.0 \cdot 10^6$.	188
E.26	The $C_L - C_D$ curves obtained from windtunnel experiments and XFLR5 simulations (Panel method versions) for the AR5_612 wing where $Re = 2.0 \cdot 10^6$.	189
E.27	The $C_L - \dot{C}_D$ curves obtained from windtunnel experiments and XFLR5 simulations (Panel method versions) for the AR5_612 wing where $Re = 2.0 \cdot 10^6$.	189
E.28	The $C_L - \alpha$ curves obtained from windtunnel experiments and XFLR5 simulations (VLM MG versions) for the AR10_012 wing where $Re = 2.0 \cdot 10^6$.	190
E.29	The $C_L - C_D$ curves obtained from windtunnel experiments and XFLR5 simulations (VLM MG versions) for the AR10_012 wing where $Re = 2.0 \cdot 10^6$.	191
E.30	The $C_L - C_D$ curves obtained from windtunnel experiments and XFLR5 simulations (VLM MG versions) for the AR10_012 wing where $Re = 2.0 \cdot 10^6$.	191
E.31	The $C_L - C_{D_0}$ curves obtained from windtunnel experiments and XFLR5 simulations (VLM MG versions) for the AR10_012 wing where $Re = 2.0 \cdot 10^6$.	192
E.32	The $C_L - C_{D_0}$ curves obtained from windtunnel experiments and XFLR5 simulations (VLM MG versions) for the AR10_012 wing where $Re = 2.0 \cdot 10^6$.	192
E.33	The $C_L - \alpha$ curves obtained from windtunnel experiments and XFLR5 simulations (VLM AK versions) for the AR10_012 wing where $Re = 2.0 \cdot 10^6$.	193
E.34	The $C_L - C_D$ curves obtained from windtunnel experiments and XFLR5 simulations (VLM AK versions) for the AR10_012 wing where $Re = 2.0 \cdot 10^6$.	193
E.35	The $C_L - C_{D_0}$ curves obtained from windtunnel experiments and XFLR5 simulations (VLM AK versions) for the AR10_012 wing where $Re = 2.0 \cdot 10^6$.	194
E.36	The $C_L - \alpha$ curves obtained from windtunnel experiments and XFLR5 simulations (Panel method versions) for the AR10_012 wing where $Re = 2.0 \cdot 10^6$.	194
E.37	The $C_L - \dot{C}_D$ curves obtained from windtunnel experiments and XFLR5 simulations (Panel method versions) for the AR10_012 wing where $Re = 2.0 \cdot 10^6$.	195
E.38	The $C_L - \dot{C}_D$ curves obtained from windtunnel experiments and XFLR5 simulations (Panel method versions) for the AR10_012 wing where $Re = 2.0 \cdot 10^6$.	195
E.39	The $C_L - \dot{C}_{D_0}$ curves obtained from windtunnel experiments and XFLR5 simulations (Panel method versions) for the AR10_012 wing where $Re = 2.0 \cdot 10^6$.	196
E.40	The $C_L - \dot{C}_{D_0}$ curves obtained from windtunnel experiments and XFLR5 simulations (Panel method versions) for the AR10_012 wing where $Re = 2.0 \cdot 10^6$.	196
E.41	The $C_L - \alpha$ curves obtained from windtunnel experiments and XFLR5 simulations (VLM MG versions) for the AR10_612 wing where $Re = 2.0 \cdot 10^6$.	197
E.42	The $C_L - C_D$ curves obtained from windtunnel experiments and XFLR5 simulations (VLM MG versions) for the AR10_612 wing where $Re = 2.0 \cdot 10^6$.	198
E.43	The $C_L - C_D$ curves obtained from windtunnel experiments and XFLR5 simulations (VLM MG versions) for the AR10_612 wing where $Re = 2.0 \cdot 10^6$.	198
E.44	The $C_L - \alpha$ curves obtained from windtunnel experiments and XFLR5 simulations (VLM AK versions) for the AR10_612 wing where $Re = 2.0 \cdot 10^6$.	199
E.45	The $C_L - C_D$ curves obtained from windtunnel experiments and XFLR5 simulations (VLM AK versions) for the AR10_612 wing where $Re = 2.0 \cdot 10^6$.	199

E.46	The $C_L - \alpha$ curves obtained from windtunnel experiments and XFLR5 simulations (Panel method versions) for the AR10_612 wing where $Re = 2.0 \cdot 10^6$.	200
E.47	The $C_L - C_D$ curves obtained from windtunnel experiments and XFLR5 simulations (Panel method versions) for the AR10_612 wing where $Re = 2.0 \cdot 10^6$.	200
E.48	The $C_L - C_D$ curves obtained from windtunnel experiments and XFLR5 simulations (Panel method versions) for the AR10_612 wing where $Re = 2.0 \cdot 10^6$.	201
F.1	The $C_l - y$ distribution obtained from XFLR5 simulations for the flat wing with $\alpha = 14^\circ$.	203
F.2	The $\alpha_s - y$ distribution obtained from XFLR5 simulations for the flat wing with $\alpha = 14^\circ$.	204
F.3	The $\alpha_{eff} - y$ distribution obtained from XFLR5 simulations for the flat wing with $\alpha = 14^\circ$.	204
F.4	The $C_{d_0} - y$ distribution obtained from XFLR5 simulations for the flat wing with $\alpha = 14^\circ$.	205
F.5	The $C_L - \alpha$ curve obtained from windtunnel experiments and XFLR5 simulations of the AR5_012 wing where $Re = 2.0 \cdot 10^6$.	206
F.6	The $C_L - C_D$ curve obtained from windtunnel experiments and XFLR5 simulations of the AR5_012 wing where $Re = 2.0 \cdot 10^6$.	206
F.7	The $C_L - C_{D_0}$ curve obtained from windtunnel experiments and XFLR5 simulations of the AR5_012 wing where $Re = 2.0 \cdot 10^6$.	207
F.8	The $C_L - C_{D_i}$ curve obtained from windtunnel experiments and XFLR5 simulations of the AR5_012 wing where $Re = 2.0 \cdot 10^6$.	207
F.9	The $C_L - \alpha$ curve obtained from windtunnel experiments and XFLR5 simulations of the AR5_612 wing where $Re = 2.0 \cdot 10^6$.	208
F.10	The $C_L - C_D$ curve obtained from windtunnel experiments and XFLR5 simulations of the AR5_612 wing where $Re = 2.0 \cdot 10^6$.	209
F.11	The $C_L - \alpha$ curve obtained from windtunnel experiments and XFLR5 simulations of the AR10_612 wing where $Re = 2.0 \cdot 10^6$.	210
F.12	The $C_L - C_D$ curve obtained from windtunnel experiments and XFLR5 simulations of the AR10_612 wing where $Re = 2.0 \cdot 10^6$.	210
F.13	Comparison of $C_D - \alpha$ curves obtained from simulations of the arc shaped kite.	211
F.14	Comparison of $C_L - C_D$ curves obtained from simulations of the arc shaped kite.	212
F.15	Comparison of C_D , C_{D_0} and C_{D_i} as function of α curves obtained from simulations of the arc shaped kite.	212
G.1	The shown mesh shows the gradually growing cells towards the boundaries.	214
G.2	The use of different mesh densities to obtain an efficient mesh.	214
G.3	The resultant mesh after two grid adaptations.	215

List of Tables

2.1	System sensitivity to kite dynamics of the KitePower prototype system. . .	14
2.2	Characteristics of existing aeroelastic kite models.	26
5.1	Flat wing configuration parameters.	65
5.2	Four swept wings configuration parameters.	66
5.3	Baseline wing configuration parameters excluding winglets.	68
5.4	Kite configuration main parameters.	69
5.5	Discretization parameters used for the validation cases, where <i>cos</i> means cosine and <i>uni</i> is uniform.	70
5.6	Effect of the number of iterations on the computational time for the flat wing, using version MG_b	95
6.1	Domain size influence on the number of cells. The number of cells are determined after grid adaption. Increase factor is taken with respect to the smallest domain.	106
6.2	Required computational effort for XFOIL viscous-inviscid calculations for a LEI kite profile with 200 panels.	123
6.3	DUT-MutinyV2 kite parameters.	124
6.4	Estimation of computation times for the components of the aerodynamic solver for a model of 640 panels with 32 spanwise sections.	131
6.5	Estimation times of the aeroelastic solver of Bosch (2012a) using the current (Breukels) and new aerodynamic model. On-the-fly-use of XFOIL is abbreviated with 'OX'. Average time steps of 4.5ms are assumed.	132

